Volume 3 | 2013
ISSN 2231 – 0002 | EISSN 2231 – 0010

Physics Express

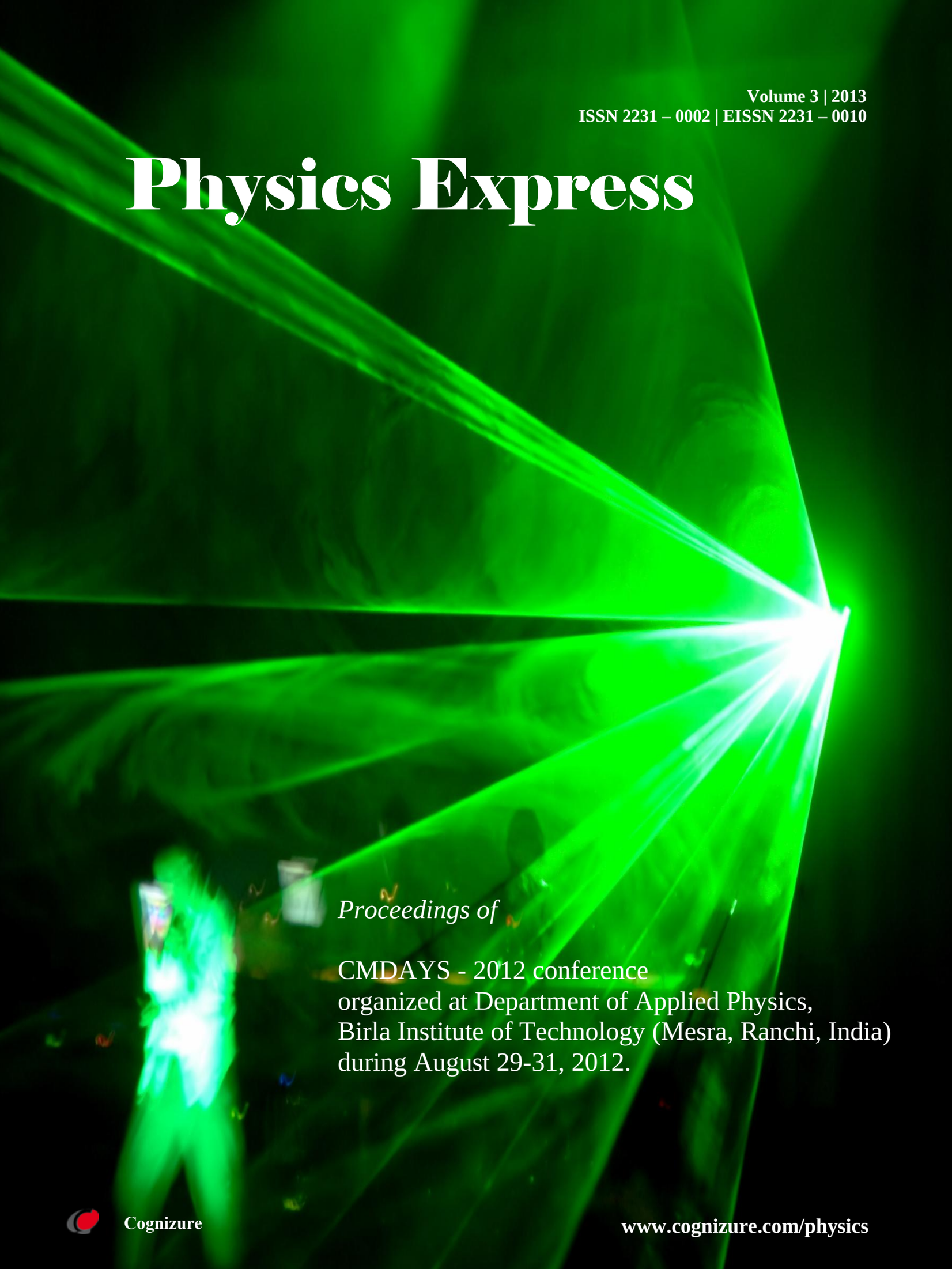

Proceedings of

CMDAYS - 2012 conference
organized at Department of Applied Physics,
Birla Institute of Technology (Mesra, Ranchi, India)
during August 29-31, 2012.

Cognizure

www.cognizure.com/physics

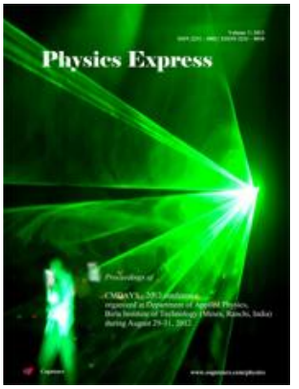

Physics Express

A special issue of selected articles presented in
CMDAYS - 2012 conference
organized at Department of Applied Physics,
Birla Institute of Technology (Mesra, Ranchi, India)
during August 29-31, 2012.

Table of Contents

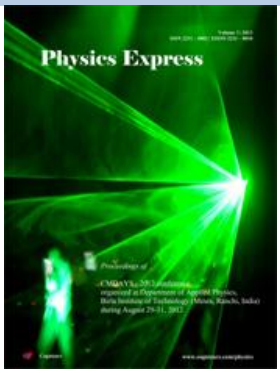

Editorial

The special issue on condensed matter physics from the CMDAYS - 2012 conference

S. K. Rout

Department of Applied Physics, Birla Institute of Technology, Mesra, Ranchi, 835215, Jharkhand, India

It is my pleasure to introduce this special issue of Physics Express on Condensed Matter Physics. This special issue contains the research articles presented in a National Conference on Condensed Matter Physics, the 20th CMDAYS, which is an annual three day conference on thrust areas in condensed matter physics, organized at Department of Applied Physics, Birla Institute of Technology (Mesra, Ranchi, India) during August 29-31, 2012.

CMDAYS serves the dual purpose of providing encouragement and fruitful academic deliberation among budding scientists and serves as a forum for participants from academia, government agencies and industry to report on research and development results, to interact, and to identify opportunities for cooperation in the fields of condensed matter physics, engineering and technology.

There were plenary talks by three successful and world renowned researchers, twelve invited lectures and more than three hundred contributed papers from experienced and young researchers in the field of condensed matter physics and allied areas of science and technology. This special issue on selected papers from CMDAYS 2012 contains extended versions of fourteen papers on both theoretical and experimental condensed matter physics.

The core element of this special issue, Condensed Matter Physics, which evolved from solid state physics, is one of the most important and fertile branches of contemporary physics. It is characterized by a multitude of workers, a variety of sub-areas, wide-spread influence on technical developments and rapid infiltration into interdisciplinary areas. The presented papers on condensed matter physics including nanomaterials and low dimensional systems, magnetism and magnetic materials, superconductivity, dielectrics, ferroelectrics, polymers, ceramics, composites, soft condensed matter, correlated systems, optoelectronics, thin films and devices, statistical and computational condensed matter physics were very interesting and worth publication in extended form for the progress of science. Interdisciplinary topics relevant to condensed matter are included for completeness.

In the article entitled "Tailoring the magnetocaloric properties of $Ni_{51}Mn_{34}In_{15}$ alloy by Ge and Si substitution for In" by Rahul Das, A. Perumal and A. Srinivasan, the effect of atomic substitution on the structural and magnetocaloric parameters of $Ni_{51}Mn_{34}In_{15}$ alloy has been investigated using powder X-ray diffraction and magnetization measurements. X-ray diffraction studies confirmed the existence of the martensitic phase in $Ni_{51}Mn_{34}In_{15}$ and $Ni_{51}Mn_{34}In_{14}Ge_1$ alloys, and austenitic phase in $Ni_{51}Mn_{34}In_{14}Si_1$ alloy at room temperature.

In the article entitled "Impedance spectroscopy and electrical conductivity studies on $(Bi_{0.5}Na_{0.5})_{0.92}Ba_{0.08}TiO_3$ ceramic" by Ansu Kumar Roy, Amrita Singh, Karishma Kumari, Ashutosh Prasad and Kamal Prasad, lead-free perovskite $(Bi_{0.5}Na_{0.5})_{0.92}Ba_{0.08}TiO_3$ (BNBT08) was prepared at 1160ºC/3h in air atmosphere by conventional high temperature solid state reaction ceramic fabrication technique. The crystal structure, microstructure, dielectric, piezoelectric properties, and ac conductivity of the sample were studied.

In the article entitled "Structural and electrical characteristics of nanocrystalline copper nickel oxide films formed by RF magnetron sputtering" by A. Sreedhar, M. Hari Prasad Reddy and S. Uthanna, nanocrystalline $CuNiO_2$ films were deposited on glass substrates by RF magnetron sputtering of $Cu_{50}Ni_{50}$ target at an oxygen partial pressure of $2x10^{-2}$ Pa, sputter pressure of 4 Pa and at various substrate bias voltages in the range from 0 to -90 V. The deposited films were characterized for chemical composition with energy dispersive X-ray analysis, crystallographic structure by X-ray diffraction, surface morphology using atomic force microscope and electrical properties by Hall measurement system.

In the article entitled "Crystal-field and molecular-field in ferromagnetic Mott-insulator $Y_2V_2O_7$ pyrochlore", A. Ali Biswas and Y. M. Jana simulated the observed thermal dependence of dc susceptibility χ of $Y_2V_2O_7$, and determined the CF parameters, CF energies and corresponding wave-functions, *g*-tensors of V^{4+} ions and anisotropy of the local magnetic susceptibility at V-site.

In the article entitled "Force induced unzipping of dsDNA: The solvent effect" by Amar Singh, Bhaskar Mittal and Navin Singh, the authors have investigated the effect of salt present in the solution, on the force induced unzipping of a heterogeneous dsDNA molecule using Peyrard Bishop and Dauxois (PBD) model.

In the article entitled "Synthesis and characterization of yellow light emitting $Na_5Dy(MoO_4)_4$ double molybdate phosphor" by S. Dutta, S. Som, R. K. Mukherjee and S. K. Sharma, sodium-dysprosium double molybdate $Na_5Dy(MoO_4)_4$ phosphor has been synthesized in order to achieve a novel long wavelength yellow light. The structural, optical and dielectric studies of this phosphor were investigated in detail. The thermoluminescence studies with computerized glow-curve deconvolution procedure were applied to gain complete insight of the kinetic behavior for the synthesized host matrix doped with Dy^{3+} ions.

In the article entitled "Comparative studies on magnetocrystalline anisotropy constant of $CoFe_{1.5}M_{0.5}O_4$, M=Al & Cr" by Lawrence Kumar, Pawan Kumar, Manoranjan Kar, the authors have done a detailed study on crystal structure and its correlation of the physical properties with different types of dopants. They have compared the properties of $CoFe_{1.5}Al_{0.5}O_4$ and $CoFe_{1.5}Cr_{0.5}O_4$ samples.

In the article entitled "DC electrical resistivity study of $YBa_2Cu_3O_{7-\delta}$ +x $BaTiO_3$-$CoFe_2O_4$ superconductor" by M. Sahoo and D. Behera, the electrical resistivity ρ (T) around the

superconducting transition of YBCO + x BTO-CFO (x = 0.0,0.2,0.4,0.6 wt. %) is presented.

In the article entitled "Theoretical study of velocity of sound in cuprates in normal state" by K. C. Bishoyi, S. P. Mohapatra and G. C. Rout, the authors address a microscopic theoretical calculation of temperature dependence of velocity of sound in cuprates in normal state in under-doped region. The effect of position of f-level, hybridization, the e-p coupling and AFM coupling are investigated to explain the sharp depression at Néel temperature and the suppression of velocity of sound in the low temperature AFM phase of the high-T_c system in normal phase.

In the article entitled "Effect of staggered field on the temperature dependent ultrasonic attenuation in cuprates", S. P. Mohapatra, K. C. Bishoyi and G. C. Rout present a microscopic theoretical model to study the effect of staggered magnetic field on the temperature dependent ultrasonic attenuation coefficient. The attenuation coefficient shows a sharp drop at the Néel temperature indicating an anti-ferromagnetic phase transition from high temperature paramagnetic to low temperature ferromagnetic phase as shown by ultrasound measurements on Tl-Ba-Ca-Cu-O.

In the article entitled "Spin susceptibility: A study of anomalies due to Kondo effect and f-electron correlation in HF systems" by P. C. Baral and G. C. Rout, the authors attempt to study the interplay between the Kondo effect and short range f-f correlations within the mean-field approximation. They investigated the momentum and frequency dependent dynamical spin susceptibility for HF systems. In particular, they compared the formation of the resonant spin excitations (resonance peaks) with the resonance peak in the inelastic neutron scattering (INS) experiment.

In the article entitled "Theoretical study of pseudogap effect on the interplay of SDW and superconductivity in cuprates", K. L. Mohanta, S. K. Panda, B. K. Raj and G. C. Rout assume the CDW and SDW interactions as pseudogaps and attempt to investigate their interplay with superconductivity by varying the model parameters of the high-T_c systems. The model calculation is applied to interpret the tunneling conductance data.

In the article entitled "Theoretical study of the interplay of spin-charge and orbital orderings in manganites" by Saswati Panda, P. Purohit and G. C. Rout, the authors consider the Kondo-Heisenberg interaction along with the JT distortion and CDW interaction as the extra mechanisms to account for the insulating phase just above T_c.

In the article entitled "First - principles calculations of electronic structure, optical properties and phase instability of potassium dihydrogen arsenate" by G. Sriprakash, S. N. Prabhava, K. P. Ramesh and K. Rukmani, the authors explain the phase instability, electronic band structure, optical properties and lattice dynamics in tetragonal KDA using DFT calculations. Further, reasons for deviation of KDA from linear relation (T_c- R) (shown by KDP like crystals) is also addressed. The calculations of the phononic modes at high pressure show an evidence of phase stability.

As convener of the CMDAYS-2012 and an Associate Editor of this journal, it is my pleasure to note the diverse and intense research activities in this area. It is expected that this special issue will be well received by the readers as a small sample of the current research on the condensed matter physics and related areas. We thank the participants for their contributions to the meeting and to this special issue.

Acknowledgments

I would like to thank authors, reviewers, and staff members of Physics Express journal's editorial office for their contributions and support to this special issue. I would like to express my sincere appreciation for support to the Institute of Physics (Bhubaneswar), Saha Institute of Nuclear Physics (Kolkata), DST (New Delhi), CSIR (New Delhi), DRDO (New Delhi), INSA (New Delhi), AICTE (New Delhi), BRNS (Mumbai) and other commercial sponsors and exhibitors for financial support.

I would like to offer my special thanks to the Vice Chancellor of Birla Institute of Technology, Mesra for providing the platform to organize this conference. I would like to thank Prof. D. Jairath, Head of the Department, for his guidance and support as and when required. Dr. Samrat Mukherjee, Co-convener, CMDAYS-2012, Dr. Rishi Sharma and all my colleagues from Department of Applied Physics, Birla Institute of Technology, Mesra, Ranchi, deserve special thanks for their hard work and whole hearted support for the success of the event.

Dr. Sanjeeb Kumar Rout
Convener
CMDAYS - 2012

Tailoring the magnetocaloric properties of $Ni_{51}Mn_{34}In_{15}$ alloy by Ge and Si substitution for In

Rahul Das*, A. Perumal, A. Srinivasan

Department of Physics, Indian Institute of Technology Guwahati, Guwahati – 781039, India

Author for correspondence: Rahul Das, email: d.rahul@iitg.ernet.in
Received 22 Aug 2012; Accepted 11 Oct 2012; Available Online 11 Oct 2012

Abstract

Effect of atomic substitution on the structural and magnetocaloric parameters of $Ni_{51}Mn_{34}In_{15}$ alloy has been investigated using powder X-ray diffraction and magnetization measurements. A small amount (1 at.%) of Silicon and Germanium substitution for Indium in $Ni_{51}Mn_{34}In_{15}$ alloy was done to perturb the inter atomic distances as well as electronic concentration of the alloy. This atomic substitution shifts the transition temperatures and hence the temperature at which the peak magnetic entropy change occurs in this alloy system. X-ray diffraction studies confirmed the existence of the martensitic phase in $Ni_{51}Mn_{34}In_{15}$ and $Ni_{51}Mn_{34}In_{14}Ge_1$ alloys, and austenitic phase in $Ni_{51}Mn_{34}In_{14}Si_1$ alloy at room temperature. The highest magnetic entropy change ΔS_M = 19.9 $Jkg^{-1}K^{-1}$ and refrigerant capacity RC = 35.9 Jkg^{-1} values are exhibited by the $Ni_{51}Mn_{34}In_{14}Si_1$ alloy at 279 K for a magnetic field change ΔH of 0 – 1.2 T.

Keywords: Magnetocaloric effect; Magnetic entropy change; Refrigerant capacity; Martensitic transformation; Alloys

1. Introduction

The urgent demand for developing energy saving, compact and environmental friendly magnetic refrigeration systems has propelled intensive search for new generation magnetic materials exhibiting large magnetocaloric effect (MCE) for low magnetic fields around room temperature. Most important refrigerant parameters are the magnetic entropy change (ΔS_M), refrigerant capacity (RC) and adiabatic temperature change (ΔT_{ad}). The large value of MCE near the martensitic transformation temperature has been reported in Ni-Mn-based ferromagnetic shape memory alloys (FSMAs), such as Ni–Mn–X (X= Ga, Sn, In, Sb) [1-4]. Generally, FSMAs have at least two phase transitions: a second-order magnetic phase transition at the Curie temperature (T_C) and a first-order structural phase transition at the martensitic start temperature (T_{MS}) [5-7]. As a result, they exhibit two types of MCE; a conventional (or direct) MCE around T_C and an inverse MCE around T_{MS}. Warburg, in 1881 reported for the first time that a sample of iron warmed up in an applied magnetic field due to conventional MCE (i.e. $\Delta T_{ad} > 0$ and $\Delta S_M < 0$) [8]. On the other hand, in an inverse MCE, the material under an applied magnetic field cools down (i.e. $\Delta T_{ad} < 0$ and $\Delta S_M > 0$) [9]. Since in Ni-Mn-based FSMAs a strong coupling exists between magnetism and structure, a large latent heat will be induced by the applied magnetic field during the first-order structural phase transition. Hence, these alloys are capable of exhibiting large ΔS_M and RC values suitable for use as magnetic refrigerants [4, 10]. In traditional Ni-Mn-based FSMAs such as Ni–Mn–Ga, ΔS_M as high as 86 $Jkg^{-1}K^{-1}$ has been reported [11]. However, this large ΔS_M is accompanied by a large thermal hysteresis gap of 10–20 K or higher and narrow (1–2 K) operating temperature range. Narrow operating temperature and large thermal or magnetic hysteresis gap exhibited by these materials are detrimental for technological applications. Recently, several groups have investigated Ga-free Ni-Mn-based FSMAs due to their large field induced shape memory effect and promising magnetic refrigerant properties. Peak ΔS_M of 35.8 $Jkg^{-1}K^{-1}$ and RC of 167 Jkg^{-1} have been reported for Ni-Mn-In alloy at 311 K (near the structural transition) for a magnetic field change (ΔH) of 0–5 T [12]. For Ni-Mn-In alloy, the thermal hysteresis gap can be ~ 20 K, which further widens with applied field [13]. It is well known that the transition temperatures and the MCE parameters can be tuned markedly by partial substitution of magnetic or nonmagnetic atoms in Ni–Mn–X (X= Ga, Sn, In, Sb) alloys [4, 14-16]. These additional atoms can perturb the atomic distances, mainly between Mn-Mn atoms, as well as the electronic concentration (*e/a* ratio) which are responsible for the exchange interaction and the degree of magnetic ordering [7, 17]. A large peak ΔS_M of 124 $Jkg^{-1}K^{-1}$ and RC of 158 Jkg^{-1} have been reported in Si substituted $Ni_{50}Mn_{35}In_{15}$ alloy at 239 K for an ΔH of 0 – 5 T [18]. *e/a* ratio as well as the magnetic moment coupling between Mn atoms also can be changed by varying the elemental composition of the alloy. Very recently, we have reported large ΔS_M and RC for low magnetic field change of Ni-Mn-In-Si alloy in which Ni was substituted for Mn [19]. Due to the large change in magnetic moment during the phase transitions, $Ni_{51}Mn_{34}In_{14}Si_1$ alloy exhibits a great perspective for MCE applications. In this work, we have investigated the effect of partial substitution of Si and Ge for In on the structural and magnetocaloric properties of $Ni_{51}Mn_{34}In_{15}$ alloy.

2. Experimental Details

Polycrystalline $Ni_{51}Mn_{34}In_{14}X_1$ (X = In, Si and Ge) ingots were prepared by conventional arc melting method using high purity elements in argon atmosphere. The final alloy ingots were obtained after repeated melting to ensure proper homogenization of the alloys. The net weight loss in the cast samples was found to be less than 2% of the initial

Table 1. Measured alloy composition, Martensite start temperature (T_{MS}), Curie temperature ($T_{C,A}$), change in magnetic entropy (ΔS_M), temperature at which maximum ΔS_M was obtained (T_{max}), refrigerant capacity (RC), and change in applied magnetic field (ΔH) of the parent, (X = In) and other two important alloys with X = Si and Ge.

Alloy ID	Composition from EDS	T_{MS} (K)	$T_{C,A}$ (K)	ΔS_M ($Jkg^{-1}K^{-1}$)	T_{max} (K)	RC (Jkg^{-1})	ΔH (T)
X = In	$Ni_{50.97}Mn_{33.45}In_{15.58}$	311	320	8.5	310	17.4	1.2
X = Si	$Ni_{50.69}Mn_{33.83}In_{14.07}Si_{1.41}$	278	294	19.9	279	35.9	1.2
X = Ge	$Ni_{50.31}Mn_{34.69}In_{13.83}Ge_{1.17}$	309	314	7.1	308	22.6	1.2

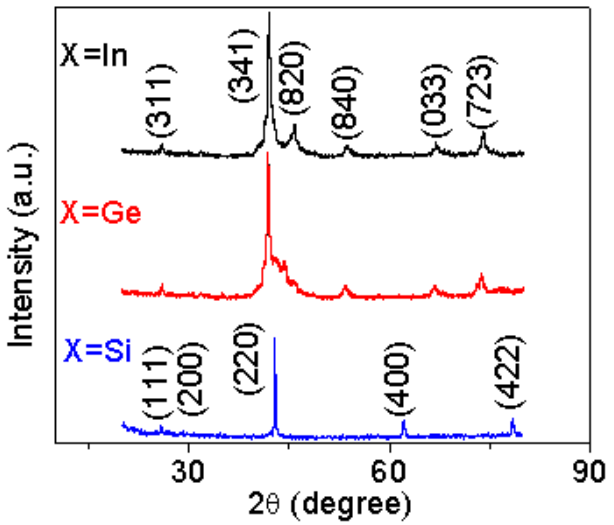

Figure 1. Room temperature XRD patterns of $Ni_{51}Mn_{34}In_{14}X_1$ alloys with X = In, Ge and Si.

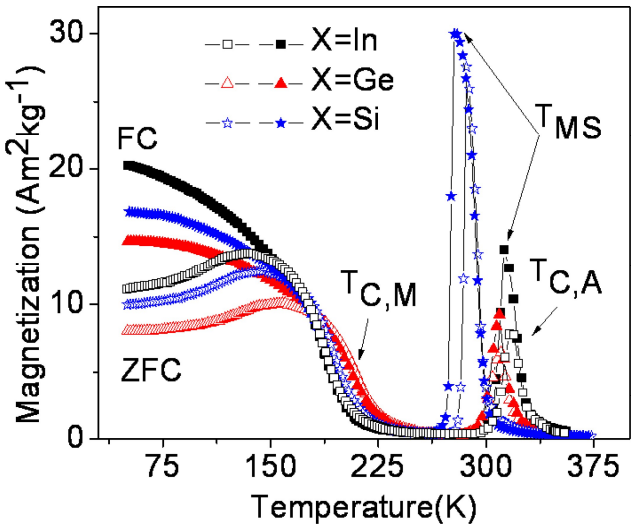

Figure 2. Temperature dependent magnetization curves of the $Ni_{51}Mn_{34}In_{14}X_1$ alloys with X = In, Ge and Si obtained at an applied field of 0.1 T. Filled and open symbols represent data during field-cooled (FC) and zero-field-cooled (ZFC), respectively. Curie temperature of martensitic phase ($T_{C,M}$), martensite start temperature (T_{MS}), and the Curie temperature of the austenite phase ($T_{C,A}$) are shown.

weight. The cast samples were sealed in quartz tube under a pressure of 10^{-3} Pa, annealed at 1173 K for 20 h and quenched in ice water. A part of the heat treated sample was crushed and used for structural analysis. A powder X-ray diffractometer (XRD, Rigaku TTRAX 18 kW) using Cu-K_α radiation (λ = 0.15406 nm) was used for structural analysis. Magnetic properties of the alloys were determined from magnetization measurements using a vibrating sample magnetometer (VSM, Lakeshore 7410). Composition of the alloy was verified using energy dispersive X-ray spectroscopy unit (EDS, Oxford) attached to a scanning electron microscope (SEM, Leo 1430 VP).

3. Results and Discussion

Room temperature XRD patterns as shown in Figure 1 indicate that at room temperature, $Ni_{51}Mn_{34}In_{15}$ and $Ni_{51}Mn_{34}In_{14}Ge_1$ alloys exist in martensitic phase (with orthorhombic unit cell) and the $Ni_{51}Mn_{34}In_{14}Si_1$ alloy in austenitic phase (with $L2_1$ structure). The overall composition of the alloys obtained from EDS analysis are summarised in Table 1. It can be seen that the final alloy composition is very close to the nominal (starting) composition of the respective alloys. Figure 2 depicts the temperature dependent magnetization (M-T) curves of the alloys obtained under an applied field of 0.1 T in zero-field-cooled (ZFC) and field-cooled (FC) conditions. For ZFC measurements, the samples were first cooled down to 50 K in the absence of magnetic field whereas for the FC measurements, the samples were cooled down from 375 K to 50 K in the presence of an external magnetic field. As the temperature is decreased from 375 K, magnetization first increases sharply due to the second order paramagnetic to ferromagnetic transformation and then abruptly decreases due to the first order austenite to martensite transformation. On further decreasing the temperature below 230 K, the samples exhibit a large increase in magnetization. This signifies the paramagnetic to ferromagnetic transition occurring in the martensite phase of the samples. Thus, all the alloys exhibit three characteristic temperatures, namely, Curie temperature of martensitic phase ($T_{C,M}$), martensite start temperature (T_{MS}), and the Curie temperature of the austenite phase ($T_{C,A}$). Below $T_{C,M}$ and in temperature interval $T_{MS}<T<T_{C,A}$, ferromagnetic order is observed and above $T_{C,A}$ paramagnetic behavior is observed. At low temperatures below 180 K the ZFC and FC curves separate from each other, indicating the irreversible nature in the magnetic property of the material. A hysteresis behavior, characteristic of a first order structural transition is also observed in M-T curves when the samples are thermally cycled. The strength of frictions encountered during the structural transformation can be characterized by the observed hysteresis gap. The frictions due to the rearrangements of domain and the motions of phase boundary are considered as most important factors affecting the hysteresis gap [20-22]. The hysteresis gap is determined by the temperature difference between the peak positions of the heating and cooling data. When Si is substituted for In, larger hysteresis of 8.5 K is observed, whereas Ge substitution results in a smaller hysteresis of 1.2 K. The characteristic

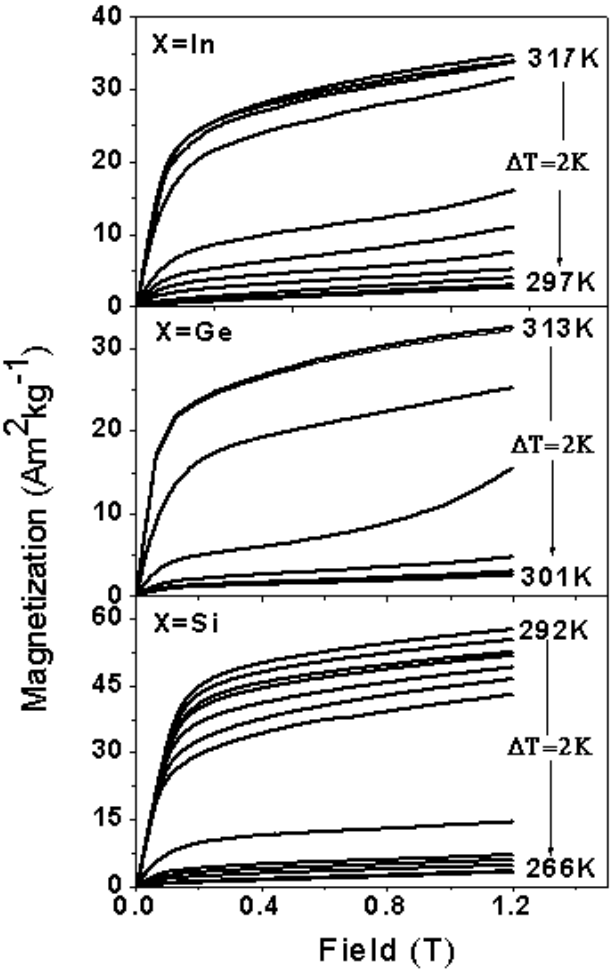

Figure 3. Isothermal magnetization curves obtained at 2 K temperature interval (ΔT) around Martensite start temperature for X = In, Ge and Si alloys.

temperatures $T_{C,A}$ and T_{MS} are defined as the temperatures at which dM/dT of ZFC and FC curves exhibit the minimum and maximum magnetization values, respectively. T_{MS} ($T_{C,A}$) of X = In, Ge and Si alloys are 311 K (320 K), 309 K (314 K) and 278 K (294 K), respectively. With the substitution of Ge and Si for In in $Ni_{51}Mn_{34}In_{15}$, both T_{MS} and $T_{C,A}$ are shifted to lower temperatures, but $T_{C,M}$ is shifted to higher temperatures. It has been reported [18] that T_{MS} and T_C decrease with an increase in *e/a* ratio in $Ni_{50}Mn_{35}In_{15-x}Si_x$ alloys. The *e/a* can be calculated from the concentration weighted sum of the valence electrons of the constituent atoms, such as Ni, Mn, In and Si/Ge, using the relation [23],

$$\frac{e}{a}=\frac{10Ni_{at.\%}+7Mn_{at.\%}+3In_{at.\%}+4(Si/Ge)_{at.\%}}{Ni_{at.\%}+Mn_{at.\%}+In_{at.\%}+(Si/Ge)_{at.\%}} \quad (1)$$

where 10 ($3d^8$, $4s^2$), 7 ($3d^5$, $4s^2$), 3 ($5s^2$, $5p^1$) and 4 ($3s^2$, $3p^2$)/($4s^2$,$4p^2$) are the valence electrons per atom for Ni, Mn, In, and Si/Ge atoms, respectively. The values of *e/a* are 7.91, 7.92 and 7.92 for In, Ge and Si substituted samples, respectively, which is in good agreement with the earlier reports [18]. Due to the smaller atomic radius of Ge (0.152 nm) and Si (0.146 nm) than that of In (0.2 nm), the Mn-Mn distance calculated from the corresponding unit cell vary from

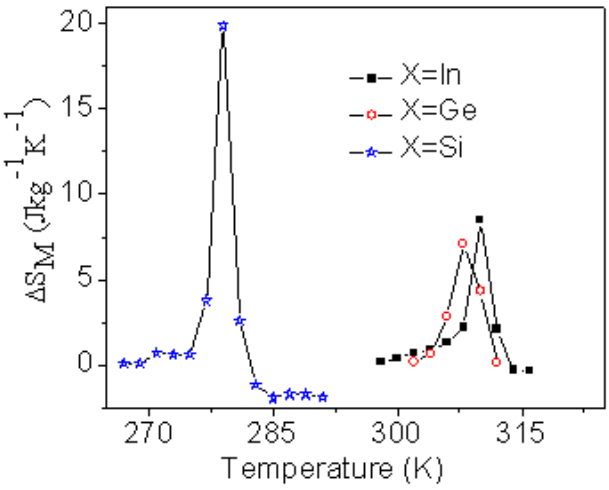

Figure 4. Temperature dependence of magnetic entropy change (ΔS_M) obtained under 1.2 Tesla field in $Ni_{51}Mn_{34}In_{14}X_1$ (X =In, Ge and Si) alloys.

0.535 nm for $Ni_{51}Mn_{34}In_{15}$ alloy to 0.539 nm ($Ni_{51}Mn_{34}In_{14}Ge_1$) and 0.422 nm ($Ni_{51}Mn_{34}In_{14}Si_1$). Comparing this data with the composition and characteristic temperatures listed in Table 1 can help in understanding the influence of atomic radius of the substituting atom on the shift in the characteristic temperatures. Figure 3 shows another interesting feature, i.e., the magnitude of the change in magnetization (ΔM) at structural transition decreases and increases with the substitution of Ge and Si, respectively. These variations are exactly opposite to the variation in Mn-Mn distance upon Ge and Si substitution, and hence the magnetic properties of Ni–Mn–X alloys are primarily determined by the Mn atoms which show an exchange interaction via conduction electrons [7]. A larger ΔM can produce a larger Zeeman energy, as a result of which a field-induced structural transformation over a wide temperature range can be expected [24]. Based on this idea, a detailed investigation on the magnetic properties, metamagnetic behavior and MCE of $Ni_{51}Mn_{34}In_{14}X_1$ (X = In, Si and Ge) alloy was carried out. ΔS_M and RC were calculated from the isothermal magnetization $(M\text{-}H)_T$ data using the following relations [12,25],

$$\Delta S_M(T)_H=\int_0^H\left(\frac{\partial M(T)}{\partial T}\right)_H dH \quad (2)$$

$$RC=\int_{T_1}^{T_2}\Delta S_M(T)_H\,dT \quad (3)$$

ΔS_M calculated from $(M\text{-}H)_T$ curves as a function of increasing magnetic field from 0 to 1.2 T at different temperatures have been obtained at 2 K interval near the T_{MS} of the respective alloys is shown in Figure 4. By integrating the area under the $\Delta S_M(T)$ curves over the full width at half maximum, RC values were obtained. Peak ΔS_M (RC) value corresponding to $Ni_{51}Mn_{34}In_{15}$, $Ni_{51}Mn_{34}In_{14}Ge_1$, and $Ni_{51}Mn_{34}In_{14}Si_1$ samples are 8.5 $Jkg^{-1}K^{-1}$ (17.4 Jkg^{-1}), 7.1 $Jkg^{-1}K^{-1}$ (22.6 Jkg^{-1}) and 19.9 $Jkg^{-1}K^{-1}$ (35.9 Jkg^{-1}), respectively. The highest ΔS_M and RC values are exhibited by the $Ni_{51}Mn_{34}In_{14}Si_1$ alloy at 279 K. $Ni_{51}Mn_{34}In_{14}Ge_1$ alloy

shows comparatively high RC but lowest ΔS_M around room temperature (308 K). The highest ΔS_M is clearly related to the $(\partial M/\partial T)_H$ term in equation (2). For 0.1 T applied magnetic field, $Ni_{51}Mn_{34}In_{14}Si_1$ alloy exhibits the highest value of $(\partial M/\partial T)_H$ of 6.6 $Am^2kg^{-1}K^{-1}$, among the three alloy compositions. Moreover, the highest hysteresis gap of 8.5 K observed in $Ni_{51}Mn_{34}In_{14}Si_1$ alloy is far less than the value of 20 K reported for Ni-Mn-In alloy [13]. These results indicate that favourable combination of MCE parameters near room temperature can be achieved in Ni-Mn-In alloys by appropriate atomic substitution for In.

4. Conclusions

Variation of ΔS_M and RC near T_{MS} in $Ni_{51}Mn_{34}In_{14}X_1$ (X =In, Ge and Si) alloys for ΔH of 0–1.2 T has been determined. The largest value of ΔS_M (RC) obtained was 19.9 $Jkg^{-1}K^{-1}$ (35.9 Jkg^{-1}) for $Ni_{51}Mn_{34}In_{14}Si_1$ alloy at 279 K, which is just below the ambient temperature. $Ni_{51}Mn_{34}In_{15}$ and $Ni_{51}Mn_{34}In_{14}Ge_1$ alloys show comparatively smaller peak ΔS_M and RC values just above ambient temperature. These experimental results indicate that atomic substitution provides a means for improving and tailoring the MCE properties of Ni-Mn-In alloys. So, this alloy is a better magnetic refrigerant material as compared to expensive rare earth based materials and other potentially toxic alloys containing As and Sb.

Acknowledgments

Financial assistance from Council of Scientific and Industrial Research [project No: 03(1236)/12/EMR-II] and infrastructural facilities provided by the DST [SR/S2/CMP-19/2006 and SR/FST/PII-020/2009] are gratefully acknowledged.

References

1. A. A. Cherechukin, T. Takagi, M. Matsumoto, V. D. Buchel'nikov, Phys. Lett. A 326 (2004) 146.
2. T. Krenke, M. Acet, E. F. Wassermann, X. Moya, L. Mañosa, and A. Planes, Phys. Rev. B 73 (2006) 174413.
3. A. Planes, L. Manosa, and M. Acet, J. Phys: Condens. Matter 21 (2009) 233201.
4. I. Dubenko, M. Khan, A. K. Pathak, B. R. Gautam, S. Stadler, and N. Ali, J. Magn. Magn. Mater. 321 (2009) 754.
5. Y. Sutou Y. Imano, N. Koeda, T. Omori, R. Kainuma, K. Ishida and K. Oikawa, Appl. Phys. Lett. 85 (2004) 4358.
6. X. G. Zhao, C. C. Hsieh, J. H. Lai, X. J. Cheng, W. C. Chang, W. B. Cui, W. Liu and Z. D. Zhang, Scripta Mater. 63 (2010) 250.
7. A. K. Pathak, I. Dubenko, J. C Mabon, S. Stadler, and N. Ali, J. Phys. D: Appl. Phys. 42 (2009) 045004.
8. E. Warburg, Ann. Phys. Chem. (Leipzig) 13 (1881) 141.
9. P. J. von Ranke, N. A. de Oliveira, B. P. Alho, E. J. R. Plaza, V. S. R. de Sousa, L. Caron, and M. S. Reis, J. Phys.: Condens. Matter 21 (2009) 056004.
10. E. Brück, J. Phys. D: Appl. Phys. 38 (2005) R381.
11. M. Pasquale, C. P. Sasso, L. H. Lewis, L. Giudici, T. Lograsso, and D. Schlagel, Phys. Rev. B. 72 (2005) 094435.
12. A. K. Pathak, M. Khan, I. Dubenko, S. Stadler, and N. Ali, Appl. Phys. Lett. 90 (2007) 262504.
13. T. Krenke, E. Duman, M. Acet, E. F. Wassermann, X. Moya, L. Mañosa, A. Planes, E. Suard, and B. Ouladdiaf, Phys. Rev. B. 75 (2007) 104414.
14. B. Gao, J. Shen, F. X. Hu, J. Wang, J. R. Sun, and B. G. Shen, Appl. Phys. A 97 (2009) 443.
15. T. Krenke, E. Duman, M. Acet, X. Moya, L. Mañosa, and A. Planes, J. Appl. Phys. 102 (2007) 033903.
16. V. K. Sharma, M. K. Chattopadhyay, A. Khandelwal, and S. B. Roy, Phys. Rev. B. 82 (2010) 172411.
17. P. J. Brown, A. Y. Bargawi, J. Crangle, K. U. Neumann, and K. R. A. Ziebeck, J. Phys.: Condens. Matter 11 (1999) 4715.
18. A. K. Pathak, I. Dubenko, S. Stadler and N. Ali, J. Phys. D: Appl. Phys. 41 (2008) 202004.
19. R. Das, A. Perumal and A. Srinivasan, IEEE Trans. Magn. 47 (2011) 2463.
20. F. X. Hu, J. Wang, J. Shen, B. Gao, J. R. Sun, and B. G. Shen, J. Appl. Phys. 105 (2009) 07A940.
21. Y. Deng, and G. S. Ansell, Acta Metall. Mater. 38 (1990) 69.
22. W. H. Wang, J. L. Chen, Z. H. Liu, G. H. Wu, and W. S. Zhan, Phys. Rev B 65 (2001) 012416.
23. B. Bao, Y. Long, J. F. Duan, P. J. Shi, G. H. Wu, R. C. Ye, Y. Q. Chang, J. Zhang, C. B. Rong, J. Appl. Phys. 103 (2008) 07B335.
24. B. Gao, F. X. Hu, J. Shen, J. Wang, J. R. Sun, and B. G. Shen, J. Magn. Magn. Mater. 321 (2009) 2571.
25. A. M. Tishin and Y. I. Spichkin, The Magnetocaloric Effect and its Applications, IOP, Bristol (2003).

Cite this article as:

Rahul Das *et al.*: **Tailoring the magnetocaloric properties of $Ni_{51}Mn_{34}In_{15}$ alloy by Ge and Si substitution for In.** *Phys. Express* 2013, **3**: 13

Impedance spectroscopy and electrical conductivity studies on $(Bi_{0.5}Na_{0.5})_{0.92}Ba_{0.08}TiO_3$ ceramic

Ansu Kumar Roy[a], Amrita Singh[a], Karishma Kumari[a], Ashutosh Prasad[a,*], Kamal Prasad[b]

[a] *University Department of Physics, T. M. Bhagalpur University, Bhagalpur- 812007, India*
[b] *Centre for Applied Physics, Central University of Jharkhand, Ranchi-835205, India*

[*] *Author for correspondence: Ashutosh Prasad, email: apd.phy@gmail.com*
Received 20 Jul 2012; Accepted 2 Oct 2012; Available Online 2 Oct 2012

Abstract

Lead-free perovskite $(Bi_{0.5}Na_{0.5})_{0.92}Ba_{0.08}TiO_3$ (BNBT08) was prepared at 1160ºC/3h in air atmosphere by conventional high temperature solid state reaction ceramic fabrication technique. The crystal structure, microstructure, dielectric, piezoelectric properties, and ac conductivity of the sample were studied. X-ray diffraction data confirmed the formation of a single phase tetragonal unit cell. Williamson-Hall plot was used to calculate the lattice-strain and the apparent particle size. The crystallite-size was found to be ~18 nm. The experimental relative density of BNBT08 was found to be ~96-97% of the theoretical one with an average grain size ~2.5 μm. Room temperature dielectric constant and dielectric loss tangent at 1 kHz were found to be equal to 1100 and 0.105, respectively. Longitudinal piezoelectric charge coefficient of the poled sample under a dc electric field of about 2.5 kV/mm applied for 15 minutes at 80°C in a silicone oil bath was found to be equal to 112 pC/ N. The high value of dielectric constant, relatively low loss factor, and high piezoelectric charge coefficient of the test ceramic sample showed the candidature for its usefulness in various electronic and other sensor/actuator applications. The Nyquist plots and conductivity studies showed the NTCR character of BNBT08. Jump Relaxation Model (JRM) was found suitable in explaining the mechanism of charge transport in BNBT08. The ac conductivity data provided apparent activation energy, and density of states at Fermi level. Activation/binding energies associated with different types of conductivity have been evaluated and the results have been analyzed in detail.

Keywords: Ceramics; Electronic materials; Dielectric properties; Piezoelectric; Electrical properties; Hopping conduction

1. Introduction

In recent years, lead-free piezoelectric ceramics have attracted considerable attention as important piezoelectric materials because of their outstanding advantages in free control atmosphere and no lead pollution. Hence, a large body of work has been reported in the last decade on the development of lead-free piezoceramics in the quest to replace Lead Zirconate Titanate (PZT) as the main material for electromechanical devices such as actuators, sensors, and transducers. In specific but narrow ranges of application the new materials appear adequate, but are not yet suited to replace PZT and other lead-based materials on a broader basis from application point of view. $(Bi_{0.5}Na_{0.5})$-TiO_3 composition (abbreviated to BNT) is one of important lead-free piezoelectric materials with perovskite structure discovered by Smolenskii et al. in 1960 [1]. As $(Bi_{0.5}Na_{0.5})$-TiO_3 composition exhibits a strong ferroelectricity and high Curie temperature T_C ~ 320°C [2-4], it has been considered to be a good candidate of lead-free piezoelectric ceramics to replace the widely used lead-based piezoelectric materials. It reveals a very interesting anomaly of dielectric properties as a result of low temperature phase transition from the ferroelectric to the anti-ferroelectric phase near 200 °C. However, this material has a drawback of high conductivity to cause problems in poling process. To improve its properties, some modifications on BNT composition have been performed. It has been reported that BNT-based compositions modified with $BaTiO_3$, $NaNbO_3$, $BiFeO_3$, $Bi_2O_3{\cdot}Sc_2O_3$ or La_2O_3 [5-10] showed improved piezoelectric properties and easier treatment in poling process compared with those of pure BNT ceramics. Among them, BNT–$BaTiO_3$ (abbreviated to BNBT) was more interesting owing to an existence of a rhombohedral (F_R)-tetragonal (F_T) morphotropic phase boundary (MPB). Takenaka and other researchers reported that the $(Bi_{0.5}Na_{0.5})_{0.94}Ba_{0.06}TiO_3$ composition near the MPB has relatively high piezoelectric properties [11-16]. An extensive literature survey revealed that no attempt, to the best of our knowledge, has so far been made to understand the conduction mechanism in BNBT*x* using impedance spectroscopy technique. It is with these views that the structural, microstructural, dielectric, polarization, piezoelectric, electric impedance and ac conductivity studies of $(Bi_{0.5}Na_{0.5})_{0.92}Ba_{0.08}TiO_3$ (abbreviated as BNBT08) ceramic i.e., very near MPB composition has been undertaken in the present work. Also, an attempt has been made to explain the conduction mechanism in BNBT08 using complex impedance and electric modulus spectroscopy techniques.

2. Experimental Details

Polycrystalline ceramic samples of $(Bi_{0.5}Na_{0.5})_{0.92}Ba_{0.8}TiO_3$ were prepared by a high- temperature solid-state reaction technique using oxides: Bi_2O_3, Na_2CO_3, $BaCO_3$and TiO_2 (Hi-Media) having purity more than 99.5%, in a suitable stoichiometry. The above ingredients were mixed thoroughly, first, in air and then in methanol medium using agate mortar and pestle. The oxide mixtures were first calcined at 1170ºC for about 3h in an alumina crucible. Adding a small amount of polyvinyl alcohol (PVA) as binder to the calcined powder, circular and rectangular disc shaped pellets were

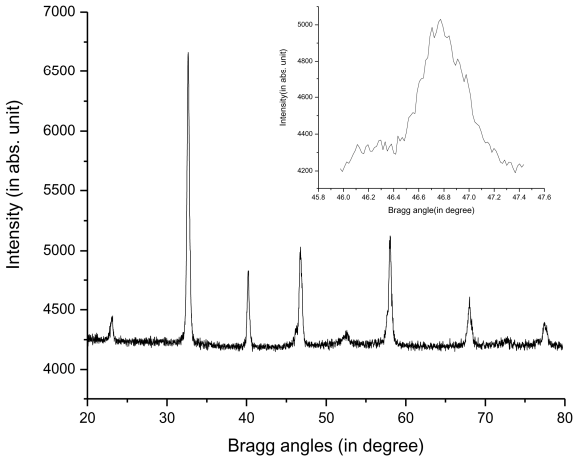

Figure 1. X-ray diffraction pattern of BNBT08 at room temperature. *Inset:* Expanded XRD pattern between 46º-47º.

fabricated by applying uniaxial pressure of 4-6 ton/square inch. Then the pellets were sintered at an optimized temperature of 1180 ºC for about 2 hr. to get a maximum density (~97% of the theoretical one).

The XRD spectra were observed on calcined powder of BNBT08 with an X-ray diffractometer (XPERT-PRO, Pan Analytical, USA) at room temperature, using CuK_α radiation (λ=1.5405 Å) over a wide range of Bragg angles ($20º \leq 2\theta \leq 80º$). The microstructure of the sintered pellet was studied at room temperature from the micrographs obtained by using a scanning electron microscope (JEOL-JSM840A). The frequency dependent dielectric constant (ε_r) and loss tangent (tanδ) at various temperatures and temperature dependent dielectric constant (ε_r) and loss tangent (tanδ) at various frequencies such as 100 Hz, 1 kHz, 10 kHz, 100 kHz and 1 MHz were measured using a computer-controlled LCR Hi-Tester (HIOKI 3532-50, Japan) on a symmetrical cell of type Ag | ceramic | Ag, where Ag is a conductive paint coated on either side of the pellet. Longitudinal piezoelectric charge coefficient (d_{33}) of the poled ceramic sample under an applied dc electric field of about 2.5 kV/mm at 80°C in a silicone oil bath) was measured using a PM3500 d_{33}/d_{31} meter (KCF Technologies, USA).

3. Results and Discussion

3.1. Structural study

Figure 1 shows the XRD spectra of calcined BNBT08 powder. A standard computer program (POWD) was utilized for the XRD-profile analysis. Good agreement between the observed and calculated inter-planar spacing with no trace of any extra peaks due to the constituent oxides were found, thereby suggesting the formation of a single-phase compound with tetragonal structure. The lattice parameters were as follows: a=3.8509 Å and b=3.9057 Å and hence tetragonality of lattice (c/a) was found to be equal to 1.0142 when indexed in tetragonal system. The unit cell volume was estimated to be equal to 57.92 $Å^3$. Literature survey revealed that BNBT06 is very close to the morphotropic phase boundary composition where both tetragonal and

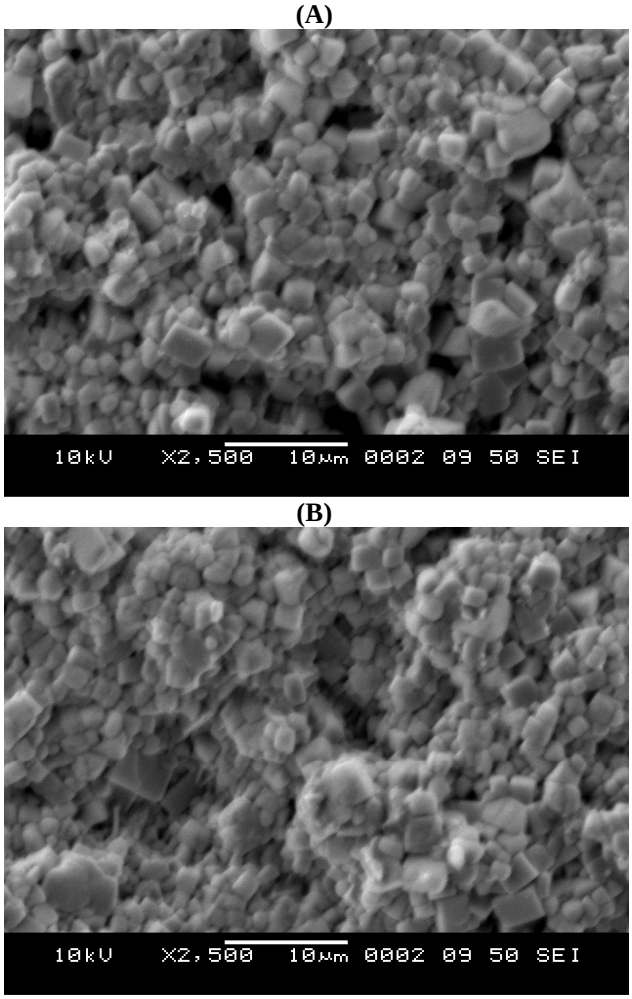

Figure 2. (A) & (B) SEM Micrographs of BNBT08 at 10µm magnification.

rhombohedral phases co-exist. The occurrence of tetragonal nature due to $BaTiO_3$ (BT) and also the rhombohedral nature due to BNT phase in BNBT08 is confirmed by the splitting of peak into two peaks (200) and (002) at 2θ values between 46º-47º. The crystallite size was estimated by analyzing the X-ray diffraction peak broadening using Scherrer equation

$$\beta = k\lambda/D \quad (1)$$

where D is the apparent crystallite size; β is the diffraction peak width at half intensity (FWHM); K is the Scherrer constant (~0.89). The term A in the Gaussian model in the form given below was applied to estimate the diffraction peak width at half maximum intensity.

$$I = I_0 + A/(\beta\sqrt{(\pi/2)}) \exp[-2\{(\theta-\theta_c)/\beta\}^2] \quad (2),$$

where A and θ_c are the area and centre of the curve, respectively. The apparent crystallite size was estimated to be of the order of 18 nm.

3.2. Microstructural study

Figures 2(A) and 2(B) show the SEM micrographs of BNBT08 observed in two different planes of the fractured surface at 10 µm magnification. Grain shapes are clearly visible, however showing slight porosity in the sample, thereby indicating the existence of polycrystalline microstructure.

(a)

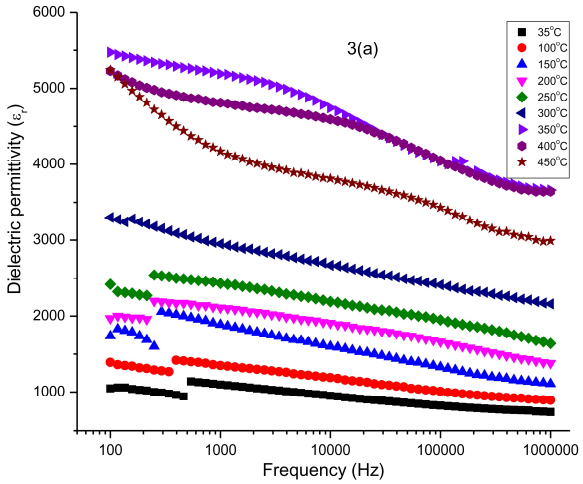

Figure 3(a). Variation of dielectric constant(ε_r) and loss tangent (tanδ) for BNBT08 with frequency at different temperatures.

(b)

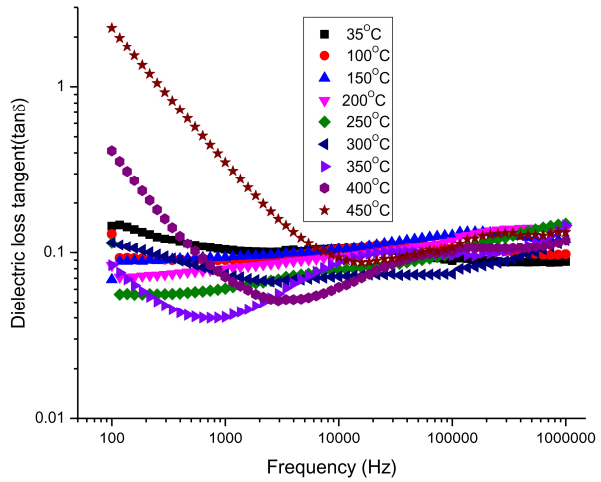

Figure 3(b). Variation of dielectric constant (ε_r) and loss tangent (tanδ) for BNBT08 with temperature at different frequencies.

Grains of unequal sizes appear to be distributed throughout the sample. The average grain size was estimated to be about 2.5 μm. Thus the ratio of grain size to apparent particle size of BNBT08 is found to be of the order of 100.

3.3. Relative density

The theoretical density for $(Bi_{0.5}Na_{0.5})_{0.92}Ba_{0.08}TiO_3$ was calculated using the following equation:

$$D= (W_1+W_2)/ (W1/D_1+ W_2/D_2) \quad (3)$$

where W_1 and W_2, are the weight percentages of the BNT and BT in the mixture, respectively; D_1 and D_2 are the densities of the BNT (=5.32g/cm^3) and BT (=6.02 g/cm^3), respectively. The theoretical density of BNBT08 was found to be equal to 5.37 g/cm^3. Apparent density of the sintered ceramic using Archimedes' principle was found to be equal to 5.26 g/cm^3. Thus, the relative density of the BNBT08 pellets was found to be of the order of 96-97%. The tolerance factor for BNBT08 ceramic was calculated by using Goldschmidt formula given by:

$$t= (R_a+R_b)/\sqrt{2}(R_b+R_o) \quad (4)$$

where R_a, R_b, and R_o are ionic radii of cation A, B and oxygen.

The value of t was found to be equal to 0.991651.

3.3. Dielectric study

The modified Debye equation related to a free dipole oscillating in an alternating field is expressed as

$$\varepsilon^*=\varepsilon(1-i\tan\delta)=\varepsilon_\infty+(\varepsilon_s-\varepsilon_\infty)/ [1+ (i\omega\tau)^{1-\alpha}] \quad (5)$$

Where ε_s and ε_∞ are the low- and high-frequency values of ε, ω (=2πf, f being the frequency of measurement) is the cyclic frequency, τ the relaxation time and α a measure of the distribution of relaxation time). A relatively high dielectric constant at low frequencies is a characteristic of a dielectric material. At very low frequencies ($\omega<<1/\tau$), dipoles follow the field and we have $\varepsilon\approx\varepsilon_s$. As the frequency increases ($\omega<1/\tau$), dipoles begin to lag behind the field and ε slightly decreases. When the frequency reaches the characteristic frequency ($\omega=1/\tau$), the dielectric constant drops (relaxation process) and at high frequencies ($\omega>>1/\tau$), dipoles can no longer follow the field and $\varepsilon\approx\varepsilon_\infty$. This behavior was observed in BNBT08, at least qualitatively. As can be seen in Figures 3(a) and 3(b), neither the dielectric constant nor the dielectric losses are significantly influenced by frequency (in the 100 Hz to 1MHz domain) suggesting a good homogeneity of the samples. It is observed that ε_r follows an inverse dependence on frequency, normally followed by almost all dielectric/ferroelectric materials. Dispersion with relatively high dielectric constant can be seen in the ε_r-f graph in the lower frequency region and dielectric constant drops at higher frequencies. Room temperature dielectric constant at 1 kHz was found to be ~1100. Further, as shown in Figure 3(b), the tanδ (f) plots showed almost frequency independence at different temperatures starting from the room temperature up to 300^{O}C, without showing any peak. On the other hand, the plots showed maxima and minima at 350^{O}C and above i.e. up to 450^{O}C, as well as minima shifting towards higher frequency side with increase in temperature. The minima shifted from 739 Hz to 16.247 kHz and maxima from 23 kHz to 291.189 kHz as the temperature was increased from 350^{O}C to 450^{O}C. The minima ranged from 0.040 to 0.086 and the corresponding maxima ranged from 0.102 to 0.130. At the same time, broadening of peaks with rise in frequency was observed, thereby showing high frequency dielectric dispersion, especially at large temperatures. In an attempt to explain the dielectric anomaly at low frequency and low temperatures, it would not be inappropriate to mention that mainly there are four types of polarization viz. (i) electronic (ii) ionic (iii) space charge or interfacial and (iv) dipolar. Out of these four, the first two contribute towards dielectric permittivity at higher frequencies and the latter two to that at lower frequencies. The imaginary part of dielectric permittivity, loss factor or tan δ is the electrical energy lost as heat in the polarization process in presence of an applied ac field. Dielectric loss is a function of frequency and temperature and is related to relaxation polarization in which a dipole is unable to follow the field

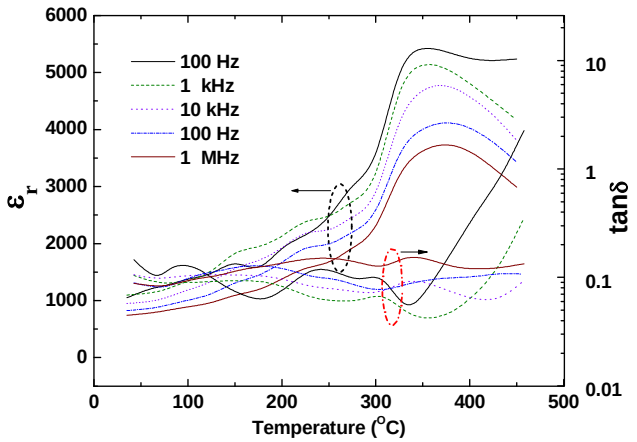

Figure 4. Variation of dielectric constant (ε_r) and loss tangent (tanδ) for BNBT08 with temperature at different frequencies.

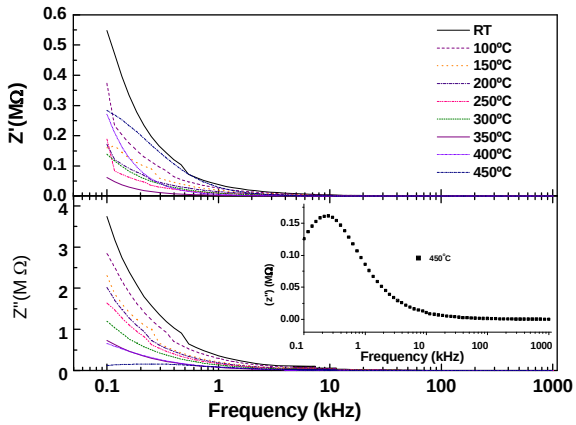

Figure 5. Frequency dependence of real (a) and imaginary (b) parts of impedance (Z*) of BNBT08 ceramic at indicated temperatures *Inset:* Frequency-dependence of imaginary part of impendence of BNBT08 at 450^{O}C.

variation without a measurable lag (hysteresis) on account of inherent frictional or damping forces of the rotating dipoles. Also, due to this change in polarization, a relaxation induced polarization current begins to flow in the dielectric which induces dielectric loss in the material. This lag of dipoles behind the field also led to slight decrease of dielectric constant. High dielectric loss tangent (~0.145) at 100 Hz and 35^{o}C is due to the domain wall motion in the ferroelectric region and it started diminishing up to the onset of anti-ferroelectric phase at the depolarizing temperature (T_d) and also up to 250^{o}C-300^{o}C and above 300^{o}C up to T_m (temperature for permittivity maximum) it goes up for all frequencies. This anomaly may be attributed to the reduction in domain wall contribution to dielectric loss, probably due to cation disorder by random distribution of Na^{+}, Bi^{3+} or Ba^{2+} at the A-site of the lattice. Beyond T_m, the electrical conductivity began to dominate resulting in sharp increase of dissipation factor/loss tangent (since $\sigma \propto \tan\delta$). This sharp increase in dielectric loss at about 450^{o}C may be attributed to the scattering of thermally activated charge carriers and some defects in the sample i.e., to the localized ionic conductivity. This type of dielectric dispersion with respect to increase in frequency may also be attributed to the structural disorder in the system. This sharp increase in loss tangent at least up to 2.5 at low frequency and 450^{o}C is endorsed by the appearance of a peak in Z″ vs. frequency drawn at 450^{o}C as shown in the *inset* of Figure 5. The merger of Z″ (as well as Z') at higher frequencies for all the temperatures indicates possible release of space charge polarization/accumulation at the boundaries of homogeneous phases in the applied external field.

In order to understand the physical nature of the dielectric anomaly in BNBT08, the temperature dependence of the real part of dielectric constant (ε_r) and loss tangent (tanδ) at various temperatures are plotted in Figure 4. All the plots show broad maxima at T_m (i.e. diffuse phase transition, DPT, where anti-ferroelectric to paraelectric phase transition takes place) near 348 ºC and another maxima at T_d (depolarization temperature, where ferroelectric to anti-ferroelectric phase transition takes place) at around 150 ºC. Further, it is seen that the plot corresponding to 100 Hz i.e., the minimum test frequency showed a sharply increasing trend at the highest chosen temperature (=450^{O}C), reaching the highest dielectric loss tangent value ~2.25. The broadening in the dielectric peak is a common feature in solid solutions which may be attributed to the presence of more than one cation (such as Na^{+}, Bi^{3+}, and Ba^{2+} at the A-site of the lattice in our case) in the sub-lattice that produce some kind of heterogeneity in the test material.

3.4. Piezoelectric study

Longitudinal piezoelectric charge coefficient (d_{33}) of the poled ceramic sample under an applied dc electric field of about 2.5 kV/mm at 80°C in a silicon oil bath was found to be ~112pC/N. Such a high value of d_{33} is due to the presence of a kind of morphotropic phase boundary (rhombohedral and tetragonal phases co-existing) in the BNBT08 composition. Transverse piezoelectric charge coefficient d_{31} was found to be ~12 pC/N Due to the limiting range of measurement of our poling instrument (which is only 5 kV) and coercivity of the material used, we had to take the thickness of the samples small (~1 mm or less). Consequently, we could get only a small amount of charge accumulation on the comparatively small perpendicular surface area, thereby yielding a smaller value of d_{31} in comparison with that of d_{33}, thus causing a discrepancy. On a naïve view, this anomaly may possibly be ascribed to the leakage of charge from the surface during manual adjustment of gap between the tips meant for d_{31} measurement in the instrument (d_{33}/d_{31} meter) or to other dominating factors causing the anomaly, not known to the authors at this point of time. Under the given condition, the hydrostatic charge coefficient d_h(= d_{33}+2 d_{31}) is found to be equal to 136 pC/N.

Figure 5 shows the frequency dependence of real and imaginary parts of complex impedance of BNBT08 at different temperatures. At each temperature the real as well as imaginary parts of impedance showed monotonic sharp exponential type of decrease for increasing frequencies below 450^{o}C. On the other hand, a peak was observed in Z″(f) plot corresponding to the data for 450^{o}C, as shown in the inset of the figure.

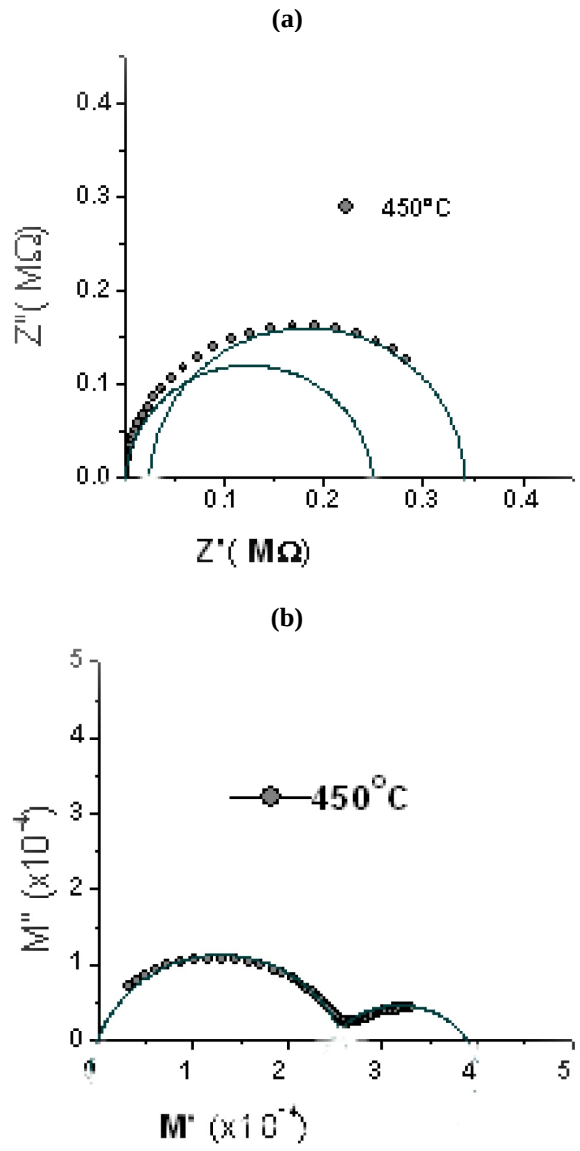

Figure 6. (a) & (b) Nyquist plots in the complex impedance and electric modulus planes, respectively for BNBT08 sample.

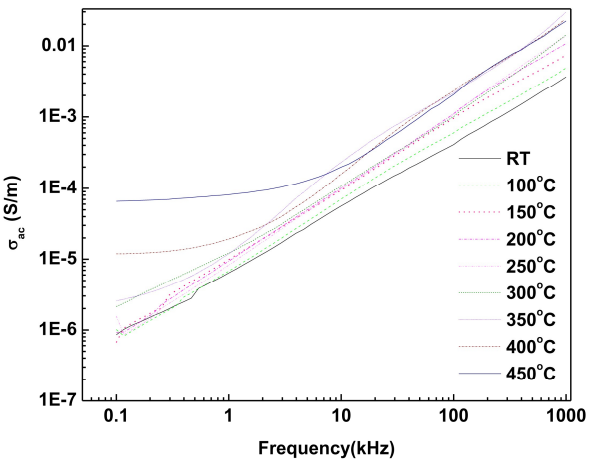

Figure 7. Dependence of ac conductivity with frequency at different indicated temperatures for BNBT08 ceramic.

3.5. Electrical impedance, electric modulus and ac conductivity studies

3.5.1. Electrical impedance analysis

As shown in Figure 6(a), two semicircular arcs or depressed circular arcs are seen in the complex impedance plane plot corresponding to a temperature of 450^{0}C, which can be explained on the basis of two parallel RC elements connected in series, one branch is associated with the grain and other with the grain-boundary of the sample. The arc of grain generally lies on a frequency range higher than that of grain-boundary, since the relaxation time τ (= $1/f_{max}$) for the grain-boundary is much larger than that of the bulk crystal. The Nyquist plot of Z" vs. Z' at 450^{o}C (Figure 6a) clearly revealed grain and grain-boundary peaks, thereby giving different values of R_s(=17.8Ω), R_g (=0.249MΩ), R_{gb} (=0.342MΩ), C_g (=1.872pF), and C_{gb} (=2.167nF). These data yield the grain and grain-boundary relaxation times equal to 0.466 μs and 0.741 ms, respectively. These data indicate the negative temperature coefficient of resistance (NTCR) behavior like those for semi conducting materials. The centers of the semi circles lie below the x-axis at an angle 'φ' (not shown in the plots for the sake of brevity), thereby indicating non-Debye type relaxation process in BNBT08. Further, the observed data indicate that the conduction in BNBT08 is predominant through grain boundary and thus it gives a scope for variety of device applications. It is observed that the magnitudes of both Z' and Z'' decrease with increase in frequency, thus indicating an increase in ac conductivity with rise in frequency.

3.5.2. Modulus spectrum analysis

In polycrystalline materials, impedance formalism emphasizes grain boundary conduction process, while bulk effects on frequency domain dominate in the electric modulus formalism. The use of modulus spectroscopy plot is particularly useful for separating the components with similar resistance but different capacitance. The other advantage of electric modulus formalism is that the electrode effect is suppressed. Due to the above reasons, complex electric modulus formalism was also adopted in the present case in order to see the different effects separately. Dielectric relaxation studies were carried out in the complex modulus M* formalism. Variation of real and imaginary parts of the electric modulus (M' and M″) as a function of frequency at various temperatures was studied. From the study it transpired that the value of M' increases from the low frequency towards a high frequency limit and the dispersion shifts to high frequency as temperature increases. However, for the sake of brevity, M'(f) and M″(f) plts have not been given in the paper. The Nyquist plot of M" vs. M' at 450^{o}C (Figure 6b) clearly revealed grain and grain-boundary peaks.

Figure 7 shows the log-log plot of ac electrical conductivity (σ_{ac}) versus frequency at different temperatures. It is observed from these plots (Figure 7) that in low temperature regime, ac conductivity increased with increase in frequency, thereby indicating dispersion of conductivity with frequency. With increase in temperature, dispersion in conductivity narrowed and all the curves for different frequencies appeared to merge at high temperatures, although they didn't merge completely. The activation energy for conduction was obtained using the Arrhenius relationship:

Table 1. AC /DC types of conductivity-based activation energies in low and high temperature ranges at different frequencies.

Temperature Ranges (^{O}C)	AC conductivity-based activation energies (in eV) at the indicated frequencies					DC conductivity-based activation energies (in eV) at the indicated temperature range	
	100 Hz	1 kHz	10 kHz	100 kHz	1 MHz	350^{O}C-450^{O}C	1.2548
35^{O}C-300^{O}C	0.0739	0.0871	0.0847	0.0639	0.0288		(r^2=0.99823)
r^2-values	0.7629	0.9264	0.9117	0.6658	0.5093		
325^{O}C-450^{O}C	0.7300	0.6040	0.1720	0.0855	0.1897		
r^2-values	0.8777	0.7135	0.7809	0.7711	0.8675		

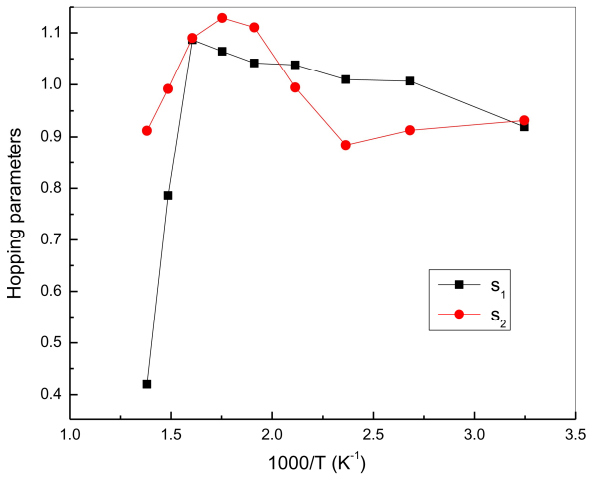

Figure 8. Temperature dependence of low (from 100 Hz up to54 kHz) and high (from 63 kHz up to 1 MHz) frequency hopping parameters (s_1&s_2) of BNBT08 ceramic.

$$\sigma_{ac} = \sigma_o \exp(-E_a / k_B T) \quad (6)$$

A linear least- squares- fit to the conductivity data to Eq. (6) gives the value of the apparent activation energy, E_a. The activation energy values for ac conductivity are found to increase with the increase in temperature as shown in Table 1. It is also observed that ac conductivity-based activation energy calculated at high frequency is lower than that at low frequency in the same temperature range. This is due to the fact that at low frequencies the overall conductivity is due to the mobility/transportation of charge carriers over long distance rather than from relaxation/ orientational mechanism, in which case charge mobility/ transportation is restricted to only the nearest neighboring lattice sites. The results will be further corroborated on the basis of hopping conduction in the explanations to follow.

In a bid to extend our frequency-dependent ac conductivity study, the Jonscher's power law as given below is to be used:

$$\sigma_{ac} = \sigma_o + A\omega^s \quad (7)$$

where σ_o is the frequency independent (electronic or dc) part of ac conductivity; s ($0 \le s \le 1$) is the index; ω is angular frequency of applied ac field and A [$= \pi N^2 e^2 / 6 k_B T (2\alpha)$] is a constant; e is the electronic charge; T is the temperature; α is the polarizability of a pair of sites and N is the number of sites per unit volume among which hopping takes place. Such a variation is associated with displacement of carriers which move within the sample by discrete hops of length R between randomly distributed localized sites. The term $A\omega^s$ can often be explained on the basis of two distinct mechanisms for carrier conduction: quantum mechanical tunneling (QMT) through the barrier separating the localized sites and correlated barrier hopping (CBH) over the same barrier. In these models, the exponent s is found to have two different trends with temperature and frequency. If the ac conductivity is assumed to originate from QMT, s is predicted to be temperature independent but is expected to show a decreasing trend with ω, while for CBH the value of s should show a decreasing trend with an increase in temperature. The exponent s has been found to behave in a variety of forms [18-20]. In general, the frequency dependence of conductivity does not follow the simple power relation as given above but follows a double power law [18-21] given as

$$\sigma_{ac} = \sigma_o + A\omega^{S_1} + B\omega^{S_2} \quad (8)$$

where σ_o is the same as in Eq. (7) i.e., the frequency independent (electronic or dc) part of ac conductivity. The exponent s_1 ($0 \le s_1 \le 1$) characterizes the low frequency region, corresponding to translational ion hopping and the exponent s_2 ($0 < s_2 < 2$) characterizes the high frequency region, indicating the existence of well localized relaxation/re-orientational process [21], the activation energy of which is ascribed to reorientation ionic hopping. Further, it may be inferred that the slope s_1 is associated with grain-boundary conductivity whereas s_2 depends on grain conductivity [22]. In the jump relaxation model (JRM) introduced by Funke [18] and extended by Elliot [19] to account for ionic conduction in solids, there is a high probability for a jumping ion to jump back (unsuccessful hop). However, if the neighborhood becomes relaxed with respect to the ion's position, the ion stays in the new site. The conductivity in the low frequency region is associated with successful hops. Beyond the low frequency region, many hops are unsuccessful, and as the frequency increases, more hops are unsuccessful. The change in the ratio of successful to unsuccessful hops results in dispersive conductivity. In the perovskite type oxide materials, presence of charge traps in the band gap of the insulator is expected. The JRM suggests that different activation energies are associated with unsuccessful and successful hopping processes. The frequency and temperature dependence of ac conductivity resembles that of hopping type conduction. Applying JRM to the frequency response of the conductivity for the present material, it was possible to fit the data to a double power law as given in Eq. (8). The temperature – dependent variations of the exponents, s_1 and s_2, are shown in Figure 8. From the plots it is manifested that s_1 assumes a maximum value ~1.06, which may be treated as ~1, keeping in

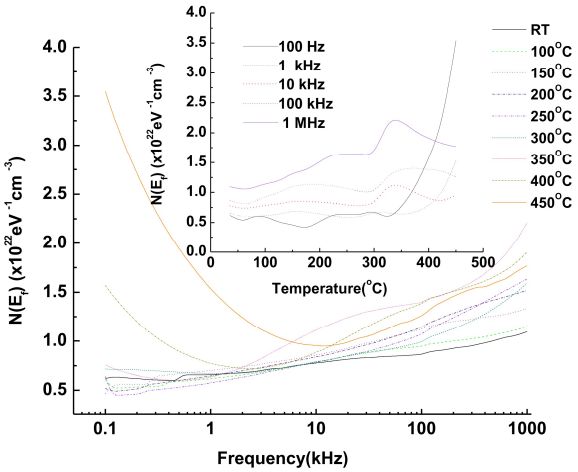

Figure 9. Frequency dependence of N (E_F) of BNBT08 ceramic at different temperatures. *Inset* shows the temperature dependence of N (E_F) at different frequencies.

view the largely scattered data points in the fitted curves (not shown in the paper for brevity sake). On the other hand, s_2 assumes maximum values ~1.13 with peak appearing near T_m (i.e., the anti-ferroelectric/paraelectric phase transition temperature). Recent literature has also endorsed that the exponent n (or s) is not limited to values below 1 [23,24], but no physical explanation to the existence of such a peak could be traced out from the literature.

Further, hopping conduction mechanism is generally consistent with the existence of a high density of states in the materials having band gap like that of a semiconductor. Due to localization of charge carriers, formation of polarons takes place and the hopping conduction may occur between the nearest neighboring sites. The low value of E_a may be due to the carrier transport through hopping between localized states in a disordered manner [25, 26]. The enhancement in conductivity with temperature may be considered on the basis that within the bulk, the oxygen vacancies due to the loss of oxygen are usually created during sintering and the charge compensation follows the Kröger -Vink equation [27]: $O_o \rightarrow \frac{1}{2}O_2 \uparrow + V_o^{\bullet\bullet} + 2e^{-1}$, which shows that free electrons are left behind in the process, making the material n-type. It may further be opined that lower high frequency ac activation energy than that at low frequency may possibly be due to the fact that at low frequencies the overall conductivity is due to the mobility/transportation of charge carriers over long distance rather than relaxation/orientational mechanism, in which case charge mobility/transportation is restricted to only the nearest neighboring lattice sites [28]. Since the energy required for the relaxation/orientational process is lower than that required for mobility of charge carriers over a long distance, hence the observed greater activation energy for conduction at lower frequency than for higher frequency, as referred earlier. In the light of the resulting frequency- and temperature-dependent ac conductivity data for BNBT08 ceramic sample it may be inferred that the applicability of CBH model of hopping is under question even in the lower frequency range (up to 54 kHz) while the JRM has shown its applicability in the entire frequency range.

In an attempt to find a more acceptable physical explanation to the experimental results, it is intended to apply Mott's Variable Range Hopping Conduction Model (VRHCM) [29] in future works. However, again the prohibiting condition is that the model has shown its suitability only in the lower temperature regions. Things are to be seen in the correct perception.

Lastly, the ac conductivity data have been used to evaluate the density of states at Fermi level $N(E_F)$ using the relation [30]:

$$\sigma_{ac}(\omega) = (\pi/3)e^2\omega k_B T\{N(E_F)\}2\alpha^{-5}\{\ln(f_o/\omega)\}^4 \quad (9)$$

where e is the electronic charge; f_o the phonon frequency (= 10^{13} Hz) and α (= 10^{10} m^{-1}) is the localized wave number. Figure 9 shows the frequency dependence of $N(E_F)$at different temperatures. It can be seen that each of the plots shows a minimum up to 300^{O}C after which the minimum starts disappearing and that the value of $N(E_F)$ decreases with the increasing frequency. Further, it is noted that the minima shift towards higher frequency side with the increasing value of $N(E_F)$ due to rise in temperature. The *inset* to Figure 9 shows temperature-dependent variation of $N(E_F)$ at different frequencies . The plots show peaks at and near T_d and a sharp increase beyond T_m and the anomaly is most pronounced at 100 Hz. The reasonably high values of $N(E_F)$ ($\sim 10^{21}$ $eV^{-1}cm^{-3}$) suggest that the hopping of charge carriers between the pairs of sites dominate the mechanism of charge transport in BNBT08.

Approximate values of dc conductivity of the test material were evaluated from the extrapolation of the plateau of the $\sigma_{ac}(\omega)$ plots up to ω=0 corresponding to 350^{O}C, 400^{O}C and 450^{O}C only. For temperature-dependent variation of dc conductivity following formula was used:

$$\sigma_{dc} = (\sigma_o / T)\exp(-E_a / k_B T) \quad (10)$$

from which the slope of the $\ln(\sigma_{dc*T})$ vs.10^3/T plot yielded the value of activation energy for dc conductivity (E_a) (=1.2548 eV), as given in Table 1.

4. Conclusions

Polycrystalline ceramic sample of $(Bi_{0.5}Na_{0.5})_{0.92}Ba_{0.08}TiO_3$ (BNBT08) was prepared by a conventional high-temperature solid state reaction technique at the sintering temperature of 1180°C. The formation of a single phase compound is confirmed by X-ray diffraction analysis which shows that the BNBT08 material is near morphotropic phase boundary composition where rhombohedral and tetragonal both phases co-exist. SEM micrograph of the sintered ceramic pellet shows dense and homogeneous packing of grains. Room temperature dielectric constant and loss tangent at 1 kHz are found to be ~1100 and 0.105, respectively. Longitudinal Piezoelectric charge coefficient (d_{33}) of the poled ceramic sample is found to be ~112 pC/N. The high value of dielectric constant, relatively low loss factor and high piezoelectric charge coefficient of the test ceramic sample showed the candidature for its usefulness in various electronic and other sensor applications. Complex impedance and electric modulus spectroscopic analyses showed the dielectric relaxation in the material to be of non-Debye type. The Nyquist plots and conductivity studies showed the NTCR character of BNBT08. The Correlated Barrier Hopping Model

(CBHM) (of course with a few modifications and limitations) and Jump Relaxation Model (JRM), in low and high frequency ranges, respectively, were found suitable in explaining the mechanism of charge transport in BNBT08. The ac conductivity data provided the minimum hopping length, apparent activation energy, and density of states at Fermi level. Activation/binding energies associated with different types of conductivity including hopping type have been evaluated and the results have been analyzed in detail.

Acknowledgements

The present work was supported by the Department of Science and Technology, New Delhi under Grant No.SR/S2/CMP-017/2008.

References

1. G. A. Smolenskii, V. A. Isupov, A. I. Agranovskaya, N. N. Krainik, Sov. Phys. Solid State 2 (1961) 2651.
2. T. Takenaka, H. Nagata, J. Eur. Ceram. Soc. 25 (2005) 2693.
3. C. Peng, J. F. Li, W. Gong, Mater. Lett. 59 (2005) 1576.
4. A. Sasaki, T. Chiba, Y. Mamiya, E. Otsuki, Jpn. J. Appl. Phys. 38 (1999) 5564.
5. J. Suchanicz, M. G. Gavshin, A. Y. Kudzin, and C. Kus., J. Mater. Sci. 36 (2001) 1981.
6. N. Ichinose, K. Udagawa, Ferroelectrics 169 (1995) 317.
7. T. Takenaka, K. Sakata, K. Toda, Ferroelectrics 106 (1990) 375.
8. Y Li., W. Chen, J. Zhou, Q. Xu, H. Sun, R. Xu, Mater. Sci. Eng. B 112 (2004) 5.
9. 9. G. O Jones, P. A. Thomas, Acta Crystallogr. B. 58 (2002) 168.
10. J. A. Zvirgzds, P. P. Kapostins, J. V. Zvirgzde, T. V. Krunzina, Ferroelectrics 40 (1982) 75.
11. S-E Park., K. S. Hong, J. Mater. Res. 12 (1997) 2152.
12. J-R. Gomah-Pettry, S. Said, P. Marchet, J-P. Mercurio, J. Eur. Ceram. Soc. 24 (2004) 1165.
13. BJ Chu, DR Chen, GR Li, QR Yin, J. Eur. Ceram. Soc. 22 (2002) 2115.
14. M. Chen, Q. Xu, BH Kim, BK Ahu, W. Chen, Mater. Res. Bull. 43 (2008) 1420.
15. RZ Zuo, C. Ye, XS Fang, JW Li, J. Eur. Ceram. Soc. 28 (2008) 871.
16. T. Gopal Reddy, B. Rajesh Kumar, T. Subba Rao, J. Altaf Ahmad, Int. J. Appl. Eng. Res. 6 (2011) 571.
17. An American National Standard IEEE Standard on Piezoelectricity, ANSI/IEEE Std. 176 (1987) 273.
18. K. Funke, Prog. Solid State Chem. 22 (1993) 111.
19. SR Elliot, Adv. Phys. 36 (1987) 135.
20. A. Pelaiz-Barranco, M. P. Gutierrez-Amador, A. Huanosta, R. Valenzuela, Appl. Phys. Lett. 73 (1998) 2039.
21. A. A. Youssef Ahmed, Z. Naturforsch. 57a (2002) 263.
22. R. Rizwana, T. Radha Krishna, A. R. James, P. Sarah, Cryst. Res. Technol. 42 (2007) 699.
23. A. N. Papathanassiou, I. Sakellis, Grammatikakis, Appl. Phys. Lett. 91 (2007) 122911.
24. H. M. El. Mallah, Acta Phys. Pol. A 122 (2012) 174.
25. Shail Upadhyay, Ashok Kumar Sahu, Devender Kumar and Om Prakash, J. Appl. Phys. 84 (1998) 828.
26. K. Prasad, C. K. Suman, R. N. P. Choudhary, Adv. Appl. Ceram. 105 (2006) 258.
27. F. A. Kröger, H. J. Vink, Solid State Phys. 3 (1956) 307.
28. S. Mahboob, G Prasad and G. S. K, Bull. Mater. Sci. 29 (2006) 35.
29. N. F. Mott, E. A. Davis, Electronic Processes in Non-crystalline Materials, Clarendon Press, Oxford (1979) p. 20.
30. M. A. M. Seyam, Appl. Surf. Sci. 181 (2001) 128.

Cite this article as:

Ansu Kumar Roy *et al.*: **Impedance Spectroscopy and Electrical Conductivity Studies on $(Bi_{0.5}Na_{0.5})_{0.92}Ba_{0.08}TiO_3$ Ceramic.** *Phys. Express* 2013, **3**: 14

Structural and electrical characteristics of nanocrystalline copper nickel oxide films formed by RF magnetron sputtering

A. Sreedhar*, M. Hari Prasad Reddy, S. Uthanna

Department of Physics, Sri Venkateswara University, Tirupati - 517 502, India

Author for correspondence: A. Sreedhar, email: ademsreedhar1985@gmail.com
Received 27 Aug 2012; Accepted 23 Oct 2012; Available Online 23 Oct 2012

Abstract

Copper-nickel-oxide ($CuNiO_2$) thin films have been deposited on glass substrates by RF magnetron sputtering of an equimolar copper nickel alloy target ($Cu_{50}Ni_{50}$) at a fixed oxygen partial pressure of $2x10^{-2}$ Pa and at different substrate bias voltages in the range from 0 to -90 V. The X-ray diffraction studies revealed that single phase nanocrystalline $CuNiO_2$ thin films were achieved at substrate bias voltage ≥ -30 V. The crystallite size of the films increased from 2.2 to 2.5 nm with increase of substrate bias voltage from 0 to -60 V. The grain size of the films increased from 80 to 95 nm with increase of substrate bias voltage from 0 to -60 V. The films formed at substrate bias voltage of -60 V exhibited low electrical resistivity of 1.5 Ωcm, Hall mobility 19 $cm^2V^{-1}sec^{-1}$ and hole concentration of $2x10^{17}$ cm^{-3}.

Keywords: RF magnetron sputtering; Thin films; Structure; Electrical properties

1. Introduction

Copper oxide has two different oxidation states namely cupric oxide (CuO) and cuprous oxide (Cu_2O). Out of these two oxides, Cu_2O is an attractive material to the researchers because of p-type semiconductor with a direct band gap of 2 eV. It finds potential applications due to nontoxicicity, abundance and low production cost. Copper oxide films were used as humidity sensors, electrochromic devices [1] and thin film heterojuction solar cells [2-4]. Doping of nickel into copper oxide enhances the p-type conductivity by introducing the shallow acceptor level in Cu_2O [5]. Nickel oxide is also a p-type material since charge transfer takes place from nickel vacancies. NiO films also find applications such as smart windows and electrochromic devices [6, 7]. Yang et al. [8] reported on the copper doped p-type NiO films for heterojunction diode applications. Miyata et al. [9] achieved p-type copper-nickel oxide thin films by RF magnetron sputtering using Cu_2O - NiO powder targets. He et al. [10] have studied the electrochromic properties of $Cu_xNi_{1-x}O$ films deposited by sol-gel dip coating. Chen et al. [11] reported the variation of electrical and optical properties with the copper doping concentration from 0 to 18.2 at.% in the NiO thin films by RF magnetron sputtering process for transparent conductor applications. Moghe et al. [12] investigated copper doped nickel oxide films grown by spray pyrolysis and observed enhanced optical absorption in the visible region and decrease in the electrical resistivity. Kikuchi et al. [13] reported the structural and electrical properties of Ni-doped copper oxide films deposited by pulsed laser deposition by varying the nickel concentration from 0 - 20 at.%. Zhao et al. [14] studied the structural, morphological and optical and electrochromic properties of copper doped nickel oxide films formed by electrochemical deposition method. In the present investigation, an attempt is made in the preparation of $CuNiO_2$ films by sputtering of equimolar $Cu_{50}Ni_{50}$ target using RF magnetron sputtering. The films were deposited at various substrate bias voltages. The deposited films were characterized for chemical composition, crystallographic structure, surface morphology and electrical properties. The influence of substrate bias voltage on the physical properties was systematically studied and the results are reported.

2. Experimental Details

Copper nickel oxide thin films have been deposited onto glass substrates by radio frequency (RF) magnetron sputtering of equimolar copper nickel alloy ($Cu_{50}Ni_{50}$) target (50 mm dia. and 3 mm thick). The sputter chamber with 50 liters volume was evacuated using a rotary pump and diffusion pump combination to produce base pressure of $5x10^{-4}$ Pa. Pressure in the sputtering chamber was measured using digital Pirani - Penning gauge combination. Argon and oxygen were used as sputter and reactive gases during the deposition of the films. The sputter and reactive gases were controlled by two Aalborg mass flow controllers. The target to substrate distance maintained during the deposition was 50 mm. The sputter power applied to the target was 100 W by using Advance Energy RF generator (13.56 MHz). The films were deposited at constant oxygen partial pressure of $2x10^{-2}$ Pa, sputter pressure of 4 Pa and at various the substrate bias voltages in the range from 0 to -90 V. The duration of deposition of the films was 90 min. The sputter deposition parameters fixed during the growth of the films are given in Table 1. The deposited copper nickel oxide films were characterized for chemical composition, crystallographic structure, surface morphology and electrical properties. The film thickness was measured by Veeco Dektak depth profilometer (model 150). The chemical composition of the films was determined with energy dispersive X-ray analysis (Oxford instruments Inca Penta FET x 3) attached to the scanning electron microscope (Carl Zeiss, model EVO MA 15). The crystallographic structure of the films was analyzed by using the X-ray diffraction taken on Bruker D8 Advance Diffractometer using monochromatic CuK_α radiation source with wavelength λ = 0.15406 nm. The surface morphology of the films was

Table 1. Deposition parameters maintained during the preparation of $CuNiO_2$ films.

Sputter target	: $Cu_{50}Ni_{50}$
Target to substrate distance	: 50 mm
Ultimate pressure	: 5×10^{-4} Pa
Oxygen partial pressure (pO_2)	: 2×10^{-2} Pa
Sputtering pressure	: 4 Pa
Substrate bias voltage (V_b)	: 0 to - 90 V
Sputter power	: 100 W
Deposition time	: 90 min

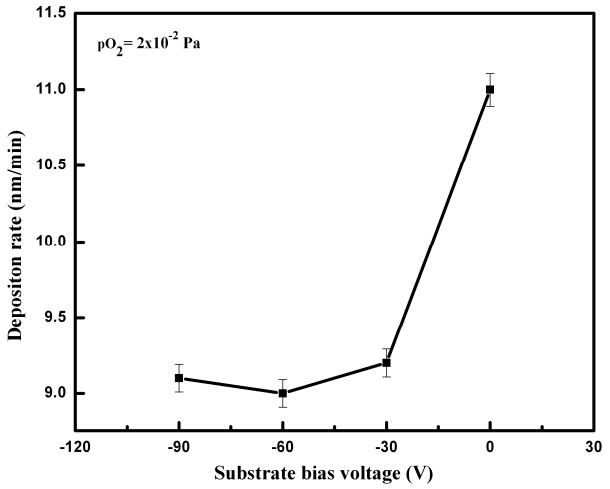

Figure 1. Variation of deposition rate with substrate bias voltage of $CuNiO_2$ films.

analyzed by atomic force microscope taken on Seiko Instruments Inc. (Model SPA 400). The electrical resistivity, carrier concentration and carrier mobility of the films were determined with an ECOPIA Hall measurement system (HMS - 3000 VER 3.51.3).

3. Results and Discussion

The thickness of the deposited copper nickel oxide films was measured with depth profilometer in the range from 800 - 990 nm. The deposition rate of the films was calculated from the film thickness and deposition time. Figure 1 shows the deposition rate of $CuNiO_2$ films as a function of substrate bias voltage (V_b). The deposition rate of the films was highly influenced by the bias voltage applied to the substrate during its growth. As can be seen that the deposition rate was 11 nm/min when the films formed on unbiased substrate and almost linearly decrease in the deposition rate to 9.2 nm/min with increase of V_b to -30 V. At higher substrate bias voltage of -60 V it decreased to 9.0 nm/min and remained almost constant at higher substrate bias voltage of -90 V. Such a decrease in the deposition rate with the substrate bias voltage was also reported in aluminum oxide films formed by DC reactive magnetron sputtering [15]. The ion energy (E) is proportional to the applied negative substrate bias voltage (V_b) as given by the relation [16],

$$E = KV_b / P^m; \qquad 0 \le m \le 1 \qquad (1)$$

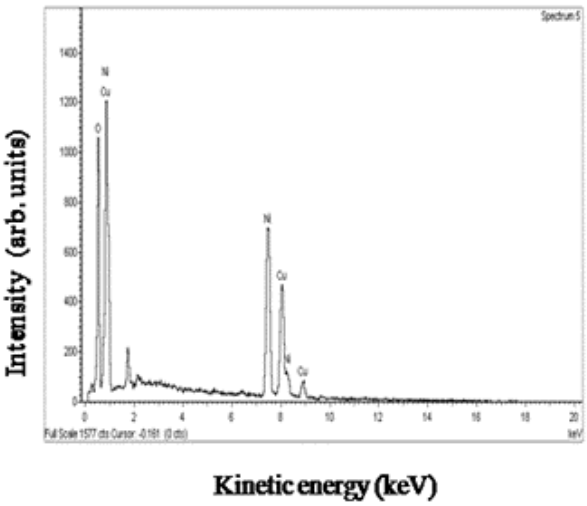

Figure 2. EDAX spectrum of $CuNiO_2$ film formed on unbiased substrate.

where K is a constant, P the pressure in the sputter chamber during the deposition and m a coefficient. According to this relation, the ion energy would be proportional to V_b when other parameters are kept constant during the film growth and the ion flux incident on the growing film was constant because of the constant sputtering power of 100 W. Hence increase in the V_b caused the enhancement in the adatom mobility and the affects the ion bombardment resulting in the ion pining effect and subsequent re-sputtering of the films, which may be the cause for falling of deposition rate of the films at higher substrate bias voltages.

3.1. Energy dispersive X-ray analysis

Figure 2 shows the representative EDAX spectrum of copper nickel oxide films formed on unbiased substrates. The chemical composition of the copper nickel oxide films was determined by using energy dispersive X-ray analysis. The chemical composition of the elements present in the films were 50.8 at.% of oxygen, 24.0 at.% of nickel and 25.2 at.% of copper, which is nearly equal to the elements present in the ternary compound of $CuNiO_2$. There was no much variation in the chemical composition of the films with the increase of substrate bias voltage which indicated that the films were of $CuNiO_2$.

3.2. Structural properties

Figure 3 shows the X-ray diffraction profiles of $CuNiO_2$ films formed at different substrate bias voltages ranging from 0 to -90 V. It was observed that the films formed at unbiased condition showed a weak diffraction peak at $2\theta = 36.6^0$ corresponding to the (111) reflection of Cu_2O [JCPDS Card no. 77-0199] and a broad peak at $2\theta = 41.4^0$ corresponds to the (002) reflection of $CuNiO_2$ [JCPDS Card no. 06-0720]. It indicated that the films formed at unbiased substrates were mixed phase of Cu_2O and $CuNiO_2$. The broadness of (002) reflection of $CuNiO_2$ clearly shows that the grown films were nanocrystalline in nature. The (111) orientation related to Cu_2O disappeared at substrate bias voltages $\geq$ -30 V. It indicated that the films formed at substrate bias voltages $\geq$ -30 V were of single phase $CuNiO_2$. Mallikarjuna Reddy et al. [17] reported that the improvement of the crystallinity of the DC magnetron sputtered NiO films formed at substrate bias voltage of -60 V due to the enhancement of the energy to the

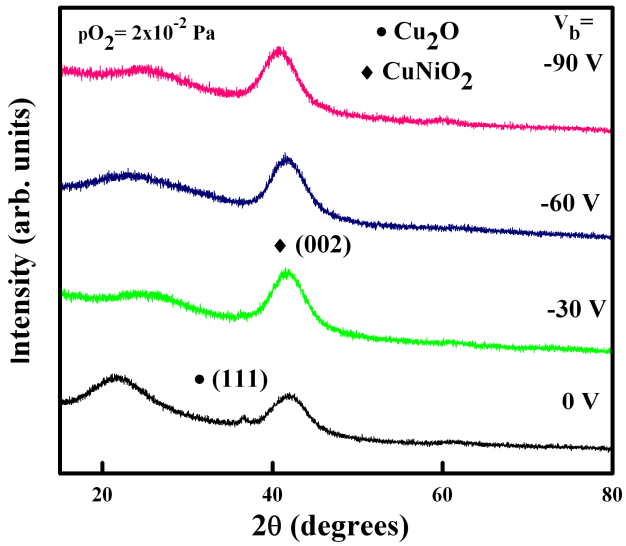

Figure 3. X-ray diffraction profiles of $CuNiO_2$ films formed at different substrate bias voltages.

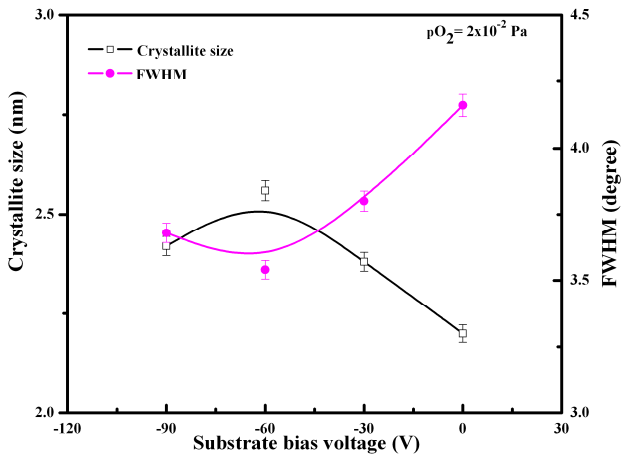

Figure 4. Variation of crystallite size and FWHM of $CuNiO_2$ films with substrate bias voltage.

molecules which increase the diffusion mobility of the sputtered particles. The crystallite size (L) of the $CuNiO_2$ films was calculated by using the Debye - Scherrer's equation [18],

$$L = K\lambda / \beta \cos\theta \qquad (2)$$

where K a constant which is a correction factor for Cu K_α radiation with a value of 0.89, β the full width at half maximum intensity correspond to the diffraction angle. Figure 4 shows the variation of crystallite size and full width at half maximum intensity of X-ray diffraction peak of $CuNiO_2$ films with the substrate bias voltage. It is seen from the Figure that the full width at half maximum of the $CuNiO_2$ films decreased from 4.16 to 3.54° with increase of substrate bias voltage from 0 to -60 V, thereafter it increased to 3.68° at higher substrate bias voltage of -90 V. The crystallite size of the films increased from 2.2 to 2.5 nm with increase of substrate bias voltage from 0 to -60 V. At higher substrate bias voltages it was decreased to 2.4 nm. The growth of nanocrystalline films was due to the adatom mobility on the substrate surface where the substrates were maintained at room temperature. It is to be

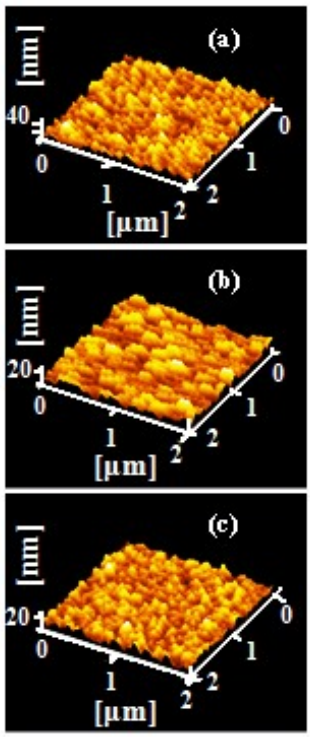

Figure 5. Three dimensional AFM images of $CuNiO_2$ films formed at various substrate bias voltages: (a) 0 V, (b) -60 V and (c) -90 V.

noted that the copper doping in NiO increased the crystallinity and the nanorods growth of sol-gel dip coated films formed on fluorine doped tin oxide coated glass substrates [14].

3.3. Atomic force microscopic studies

The surface morphology of the $CuNiO_2$ films was analyzed with the atomic force microscope. Figure 5 shows the three dimensional atomic force micrograph images of $CuNiO_2$ films formed at various substrate bias voltages. The variation in grain size and root mean square surface roughness of the $CuNiO_2$ films at various substrate bias voltages are shown in the Figure 6. The grain size of the films increased from 80 to 95 nm with the increase of substrate bias voltage from 0 to -60 V and then it decreased to 60 nm at V_b of -90 V. Increase in the grain size of the films with increase of substrate bias voltage was due to the fact that the ion bombardment enhanced the surface mobility of the adatoms thereby accelerated the nucleation growth and coalescence of nuclei, hence of larger size grains. The surface roughness of the $CuNiO_2$ films increased from 3.17 to 3.77 nm with increase of substrate bias voltage from 0 to -60 V, further increased of V_b to -90 V it increased to 4.6 nm.

3.4. Electrical properties

The electrical properties of the copper nickel oxide films were highly influenced by the substrate bias voltage. Figure 7 shows the dependence of electrical resistivity of the films on substrate bias voltage. The electrical resistivity of the films decreased from 67 to 1.5 Ωcm with increase of bias voltage from 0 to -60 V. The high electrical resistivity of 67 Ωcm in unbiased films was due to the growth of mixed phase of Cu_2O and $CuNiO_2$. The low resistivity at substrate bias voltage of -60 V was due to the growth of single phase nanocrystalline $CuNiO_2$. Thereafter, it increased to 5.5 Ωcm at

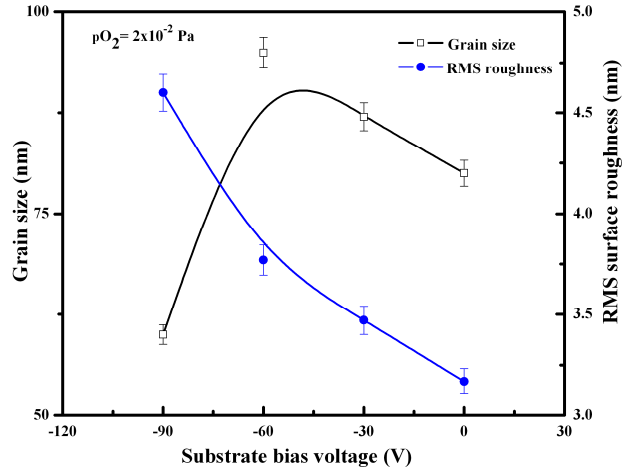

Figure 6. Variation of grain size and RMS roughness of $CuNiO_2$ with substrate bias voltage.

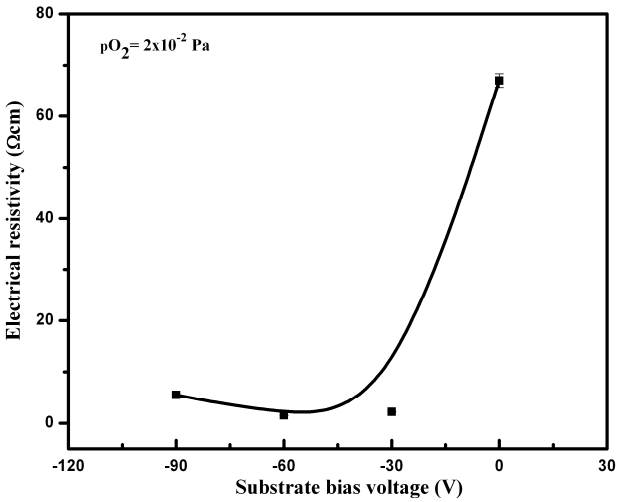

Figure 7. Variation of electrical resistivity of $CuNiO_2$ films with substrate bias voltage.

higher substrate bias voltage of -90 V. At higher substrate bias voltage the increase in resistivity was due to entrapment of argon ions in the films [19]. It is to be noted in the literature that the electrical resistivity of $Ni_{0.9}Cu_{0.1}O$ films formed by pulsed laser deposition showed low value of 0.19 Ωcm [8]. Miyata et al. [9] achieved high electrical resistivity of $2x10^4$ Ωcm in RF magnetron sputtered Cu_2O - NiO films with nickel concentration of 50 at.% using sintered Cu_2O and NiO powdered target. Chen et al. [11] achieved electrical resistivity of $2x10^{-2}$ Ωcm in 0.18 at.% copper doped nickel oxide films using NiO – Cu composite target by RF magnetron sputtering in pure argon atmosphere. The large variation in the electrical resistivity values was mainly due to the difference in the composition of the deposited Cu-Ni-O films, the composition of sputter target used, and the method of deposition and process parameters maintained during the growth of the films.

Hall measurements showed that the $CuNiO_2$ films were of p-type in conductivity. Figure 8 shows the dependence of charge carrier concentration and Hall mobility of $CuNiO_2$ films on substrate bias voltage. Hall mobility of the films increased from 7 to 19 $cm^2V^{-1}sec^{-1}$ with increase of substrate bias voltage from 0 to -60 V, thereafter it decreased to 12 $cm^2V^{-1}sec^{-1}$. Similar variation in the Hall mobility was also reported by Sujatha et al. [20] in indium tin oxide films formed by bias DC magnetron sputtering, where the Hall

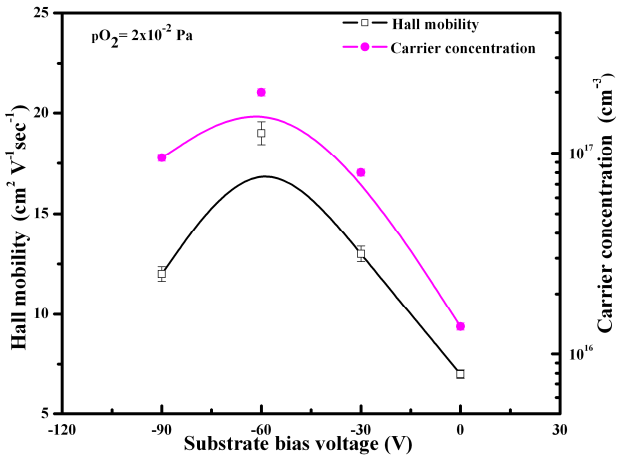

Figure 8. Variation of carrier concentration and Hall mobility of $CuNiO_2$ films with substrate bias voltage.

mobility increased up to 0 to -30 V and then decreased at higher substrate bias voltage of -70 V. The increase in the Hall mobility at low bias voltages was due to the improvement in the nanocrystallinity of the films. At higher bias voltages, the change in mobility was due to increase in the resistivity of the films. The carrier concentration of the films increased from $1.4x10^{16}$ to $2.0x10^{17}$ cm^{-3} with increase of substrate bias voltage from 0 to -60 V and it decreased to $9.5x10^{16}$ cm^{-3} with increase of substrate bias voltage to -90 V.

4. Conclusions

Nanocrystalline $CuNiO_2$ films were deposited on glass substrates by RF magnetron sputtering of $Cu_{50}Ni_{50}$ target at an oxygen partial pressure of $2x10^{-2}$ Pa, sputter pressure of 4 Pa and at various substrate bias voltages in the range from 0 to -90 V. The deposited films were characterized for chemical composition with energy dispersive X-ray analysis, crystallographic structure by X-ray diffraction, surface morphology using atomic force microscope and electrical properties by Hall measurement system. The substrate bias voltage significantly influenced the structural, chemical composition, surface morphological and electrical properties of the deposited $CuNiO_2$ films. Single phase nanocrystalline $CuNiO_2$ films were formed at substrate bias voltage ≥ -30 V. Films deposited showed the strong (002) reflection of nanocrystalline $CuNiO_2$. The electrical resistivity of the films decreased as the substrate bias voltage increased up to -60 V. Nanocrystalline $CuNiO_2$ films formed at substrate bias voltage of -60 V showed electrical resistivity of 1.5 Ωcm, grain size of 95 nm, Hall mobility of 19 $cm^2V^{-1}sec^{-1}$ and carrier concentration of $2x10^{17}$ cm^{-3}.

Acknowledgements

The authors thank Prof. J. F. Pierson, Institut Jean Lamour, Department CP2S, Nancy Universite, Nancy cedex, France, for sparing of sputter target and valuable discussion on the present work. One of the authors (A. Sreedhar) thankful to the University Grants Commission, New Delhi, India, for the award of UGC-RFSMS Junior Research Fellowship to carry out the present work.

References

1. T. J. Richardson, J. L. Slack, M. D. Rubin, Electrochim. Acta 46 (2001) 2281.
2. A. Mittiga, E. Salza, F. Sarto, M. Tucci, R. Vasanthi, Appl. Phys. Lett. 88 (2006) 163502.
3. M. Izaki, T. Shinagawa, K. T. Mizuno, Y. Ida, M. Inaba, A. Tasaka, J. Phys. D: Appl. Phys. 40 (2007) 3326.
4. T. Minami, T. Miyata, K. Ihara, Y. Minamino, S. Tsukada, Thin Solid Films 494 (2006) 47.
5. A. Martinez-Ruiz, M. G. Moreno, N. Takeuchi, Solid State Sci. 5 (2003) 291.
6. H. R. Liu, Y. Y. Zhong, B. X. Feng, J. Alloys Compd. 481 (2009) 385.
7. X. C. Lou, X. J. Zhao, X. He, Sol. Energy 83 (2009) 2103.
8. M. Yang, Z. Shi, J. Feng, H. Pu, G. Li, J. Zhou, Q. Zhang, Thin Solid Films 519 (2011) 3025.
9. T. Miyata. H. Tanaka H. Sato, T. Minami, Mater. Sci. 41 (2006) 5531.
10. Z. He, Z. Ji, S. Zhao, C. Wang, K. Liu, Z. Ye, Sol. Energy 80 (2006) 226.
11. S. C. Chen, T. Y. Kuo, Y. C. Lin, H. C. Lin, Thin Solid Films 519 (2011) 4944.
12. S. Moghe, A. D. Acharya, P. Richa, S. B. Shrivastava, G. Mohan, T. Shripathi, V. Ganesan, Renewable Energy 46 (2012) 43.
13. N. Kikuchi, K. Tonooka, E. Kusano, Vacuum 80 (2006) 756.
14. L. Zhao, G. Su, W. Liu, L. Cao, J. Wang, Z. Dong, M. Song, Appl. Surf. Sci. 257 (2011) 397.
15. X. Tang, F. Luo, F. Ou, W. Zhou, D. Zhu, Z. Huang, Appl. Surf. Sci. (2012) doi: 10.1016/ j.apsusc.2012.07.064.
16. A. Bubenzer, B. Dischler, G. Brandt, P. Koidl, J. Appl. Phys. 54 (1983) 4590.
17. A. Mallikarjuna Reddy, A. Sivasankar Reddy, P. Sreedhara Reddy, Mater. Chem. Phys. 125 (2011) 434.
18. B. D. Cullity, Elements of X-ray Diffraction (2nd ed.), Addison Wesley, London (1978).
19. P. Mohan Babu, G. Venkata Rao, P. Sreedhara Reddy, S. Uthanna, J. Mater. Sci.: Mater. Electron. 15 (2004) 389.
20. Ch. Sujatha, G. Mohan Rao, S. Uthanna, Mater. Sci. Eng. B 94 (2002) 106.

Cite this article as:

A. Sreedhar *et al.*: **Structural and electrical characteristics of nanocrystalline copper nickel oxide films formed by RF magnetron sputtering.** *Phys. Express* 2013, **3**: 15

Force induced unzipping of dsDNA: The solvent effect

Amar Singh*, Bhaskar Mittal, Navin Singh

Department of Physics, Birla Institute of Technology & Science, Pilani - 333 031, Rajasthan, India

Author for correspondence: Amar Singh, email: amarsinghbyamal@gmail.com
Received 25 Aug 2012; Accepted 14 Nov 2012; Available Online 14 Nov 2012

Abstract

The salt concentration of the solution plays an important role in the stabilization of double stranded DNA (dsDNA) molecule. In our work, the Hamiltonian in Peyrard-Bishop Dauxois (PBD) model of a heterogeneous chain has been modified with a stabilizing solvent interaction term. This term strengthens the base pair dissociation energy and stabilizes the hydrogen bonds between complementary strands of dsDNA. To study the effect of salt concentration we have modified the potentials appearing in this model. We investigated the influence of salt concentration on the force required to unzip the chain. The force induced unzipping is studied in both constant extension ensemble (CEE) and constant force ensemble (CFE). We found that the results are independent of choice of the ensembles and are in good agreement with the experimental results.

Keywords: Double stranded DNA; DNA unzipping; Peyrard-Bishop Dauxois model; Constant extension ensemble; Constant force ensemble

1. Introduction

The separation of double-stranded DNA (dsDNA) into single-stranded DNA (ssDNA) is fundamental to DNA replication in living organisms. In *vivo*, proteins apply forces to unzip and stretch DNA within the cell in living organism. In *vitro*, thermodynamically stable dsDNA can be denatured by increasing the temperature or by applying a force at one end of dsDNA [1-3]. In addition to this, the concentration of salt ($Na^{+} or\ Mg^{2+}$) present in the solution plays a crucial role in the stability of this molecule [4, 5]. Since the two strands of the dsDNA are negatively charged, to neutralize the Coulombic repulsion between the phosphates, the cations like sodium or magnesium ions are required. The concentration of these ions contributes not only to the stability of the molecule but also has important role in the folding kinetics of the molecule [6]. In recent years, using single molecule force spectroscopy (SMFS) experiments, some experimental groups have measured the force required to destabilize the dsDNA as a function of concentration of salt in the solution [7-9]. These experiments are preformed either in constant extension or in constant force ensemble. The microscopic features of unzipping may vary with the choice of ensemble one choose. When the separation between the two bases in a pair is fixed and force is allowed to fluctuate, it is CEE [10]. While in CFE, the force is fixed and the distance between two bases in a pair on which force is applied, is allowed to fluctuate [11]. We have investigated the effect of salt present in the solution, on the force induced unzipping of a heterogeneous dsDNA molecule using Peyrard Bishop and Dauxois (PBD) model [12, 13].

2. The PBD model

The Hamiltonian used in the Peyrard Bishop and Dauxois (PBD) model [12], which considers the stretching between corresponding bases only is,

$$H(y_i, y_{i+1}) = \sum_{i=1}^{N} \left[\frac{p_i^2}{2m} + W(y_i, y_{i+1}) + V_M(y_i)\right] \quad (1)$$

where y_i in eq. 1 denotes the stretching of the hydrogen bonds connecting the two bases of the i^{th} pair. $p_i = m\dot{y}_i$ represents the momentum part of the Hamiltonian and m is the reduced mass of a base pair (taken to be same for both A-T and G-C base pairs) [14]. W is the stacking interaction term or the stacking energy, between the two neighboring base pairs, is described by the anharmonic potential

$$W(y_i,\ y_{i+1}) = \frac{k}{2}\left(1 + \rho e^{-b(y_i + y_{i+1})}\right)(y_i - y_{i+1})^2 \quad (2)$$

where k represents the elasticity of a single strand, ρ is the anharmonicity and b is its range. In the stability of the dsDNA molecule the role of hydrogen bond is the key factor. With the change in the salt concentration of the solution, the electrostatic repulsive forces between these negatively charged groups change. This affects the overall rigidity of the dsDNA molecule and hence the helix to coil transition. The on-site potential $V_M(y_i)$ describes the interaction of the two bases of the n^{th} pair. To take care the effect of salt concentration of the solution and to study the effect of this on the stretching behavior of dsDNA molecule, we modify this Morse potential appearing in the model as $V = V_M + V_{sol}$ as done in Ref. [15, 16] where

$$V_M = D(e^{-ay} - 1)^2 \quad \& \quad V_{sol} = -\frac{1}{4}D[tanh(\gamma y_i) - 1] \quad (3)$$

As it was found that melting temperature T_m varies logarithmically with the salt concentration of the solution therefore we modify the potential depth D appearing in Morse potential as [16, 17]

$$D_i = D_0\left[1 + \lambda \ln\left(\frac{C}{C_0}\right)\right] \quad (4)$$

The concentration, C is expressed in moles per liter and C_0 is the reference concentration chosen to be 1 mole/liter. λ is solution constant and we choose its value as 0.01 [16]. V_{sol} is the solvent interaction term and γ is the solvent interaction factor, we found $\gamma = 1.0$ Å^{-1} is good choice for our calculation [15, 18]

Using this model Hamiltonian one can study the response of dsDNA molecule by defining the canonical partition function as,

$$Z = \int \prod_{i=1}^{N} \{dy_i dp_i \exp[-\beta H(y_i, y_{i+1})]\} = Z_p Z_c \quad (5)$$

where Z_p corresponds to the momentum part of the partition function while the Z_c contributes as the configurational part of the partition function. Since the momentum part is decoupled in the integration, it can be integrated out as a simple Gaussian integral. This will contribute a factor of $(2\pi m k_B T)^{N/2}$ in the partition function, where N is the number of base pairs in the chain. The configurational partition function, Z_c, is defined as [19],

$$Z_c = \int \prod_{i=1}^{N} dy_i K(y_i, y_{i+1}) \quad (6)$$

where $K(y_i, y_{i+1}) = \exp[-\beta H(y_i, y_{i+1})]$. For the homogeneous chain one can evaluate the partition function by transfer integral (TI) method by applying the periodic boundary condition. In case of heterogeneous chain with open boundary the configurational part of the partition function can be integrated numerically with the help of matrix multiplication method. Once the limit of integration has been chosen, the task is reduced to discretize the space to evaluate the integral numerically. We choose the limits as -5.0 Å to 200.0 Å, as the lower and upper limits of the integration, respectively. The space is being discretized using the Gaussian quadrature formula with number of grid points equal to 900. In our previous studies [19], we observed that to get precise value of melting temperature (T_m) one has to choose the large grid points. We found that 900 is quite sufficient number for this purpose. As all matrices in eq. 6 are identical in nature the multiplication is done very efficiently. The resulting partition function is used to calculate the free energy per base pair from the following relation:

$$f(T) = -\frac{1}{2}k_B T \ln(2\pi m k_B T) - \frac{k_B T}{N}\ln Z_c \quad (7)$$

The thermodynamics quantities such as entropy S, specific heat C_V of the system can be evaluated using the following relations:

$$S(T) = \frac{\partial f}{\partial T} \quad , \quad C_v(T) = -T\frac{\partial^2 f}{\partial T^2} \quad (8)$$

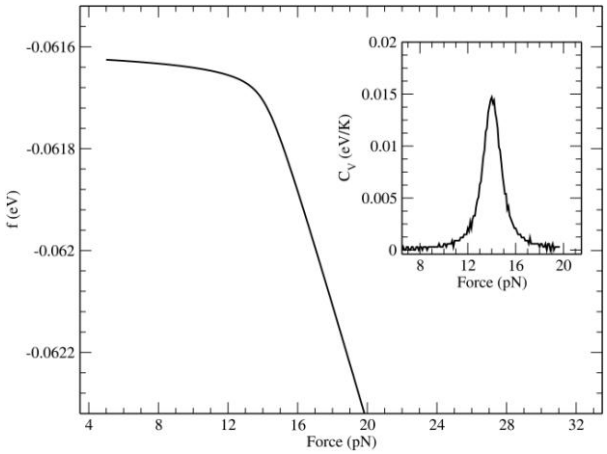

Figure 1. Variation in free energy and specific heat as function of force for salt concentration of 0.0621 M, with the value of D is 0.076.

3. Force induced transition

We take a heterogeneous chain having sequence as *5'-TACTTCCAGTGCTCAGCGTA-3'* and we repeate this sequence to make chain of 1000 base pairs. As the GC and AT base pairs have different bond strengths (~ 1.5 times), the heterogeneity in the model can be introduced via the Morse potential. Different values are found in the literature for the model parameters [2,13,18,20,21], we choose these as $\rho = 1.0$, $k_0 = 0.01$ eV/Å^2, $b = 0.35$ Å^{-1}, $T = 300$ K, $D_{AT} = 0.076$ eV and $a_{AT} = 4.2$ Å^{-1} With these parameters, the melting temperature T_m is about 350 K. The force induced unzipping is studied at 300 K, at these parameters chain will not open due to thermal fluctuation. We study the mechanical unzipping in two different ensembles, constant force and constant extension ensemble.

3.1. Constant force ensemble

In this ensemble the force is applied on the one end of the strand at constant rate keeping other end fixed. The modified Hamiltonian under the applied force can be written as

$$H_f = H - F.y_i \quad (9)$$

where F is the force applied to the one end and y_i is the extension due to this applied force. This approach may be more close to what happen in *vivo*, *i.e.* the strand separation in cells. For homopolymeric DNA, the unzipping transition is smooth with the constant applied rate once the constant applied force exceeds the threshold for separating the single base pairs. However, for heterogeneous chain, the transition from double stranded to single stranded is not smooth, but having several pauses and jumps depending on the distribution of weak (AT) and strong (GC) pairs.

Using free energy calculation as function of force we calculate the critical force. Figure 1 represents the variation in free energy with applied force at a particular salt concentration of 0.0621 M. The kink in the free energy curve correspond to the transition from dsDNA to ssDNA configuration.

3.2. Constant extension ensemble

We investigate the mechanical response of the molecule in the constant extension ensemble (CEE). In this ensemble, the separation between the end base pair of one of the ends in the dsDNA molecule is kept fixed. Average force needed to keep this separation is measured [10] by evaluating the change in free energy in displacing the first (end) base pair from a position to its next. The work done in stretching the base pair 1 to y distance apart is

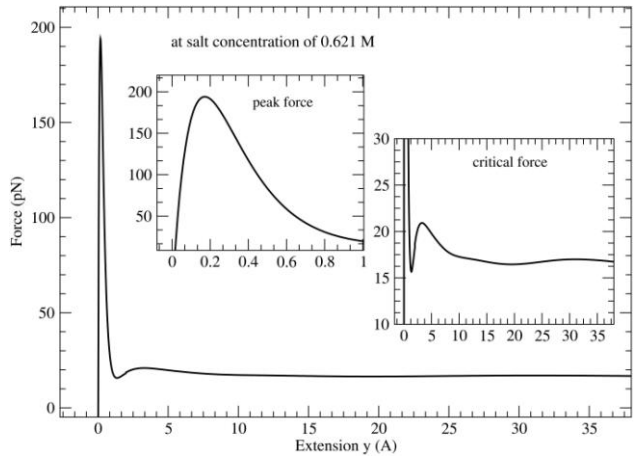

Figure 2. $F(y)$ as a function of extension y at temperature $300\,K$ with salt concentration of $0.621\,mM$. Figure shows the variation in peak force and in the critical force with extension.

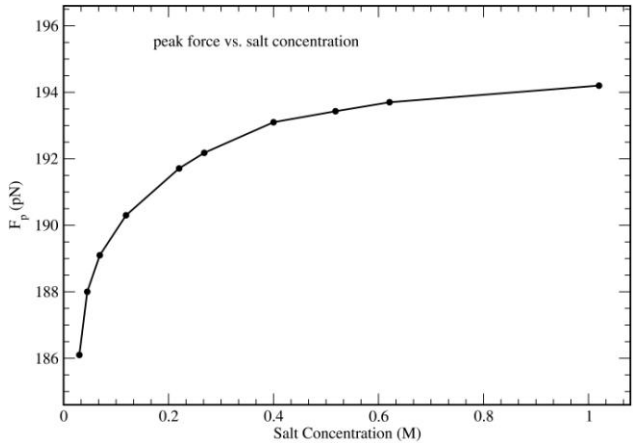

Figure 3. The graph showing the variation in peak force F_p as a function of salt concentration of the solution.

$$W(y) = \frac{1}{2}V(y) - k_B T[\ln Z_N^c(y) - \ln Z_N^c] \quad (10)$$

where

$$Z_N^c(y) = \int \prod_{i=1}^{N} dy_i \exp[-\beta H(y_i, y_{i+1})] \quad (11)$$

and Z_N^c is the partition function corresponding to unperturbed state. The force $F(y)$ as a function of extension y of first base pair, is found from the relation,

$$F(y) = \frac{\partial W(y)}{\partial y} \quad (12)$$

We plot the value of $F(y)$ as a function of extension y at temperature 300 K with salt concentration of 0.621 mM. We see from Figure 2 that at beginning a very high force is required to initiate the unzipping of the chain. This force is known as peak force. We calculate the peak force as well as the critical force required to unzip the chain. In all the cases we apply the force on the 3' end of the chain.

In CEE, we investigate the effect of salt concentration on the peak force in addition to the critical force. The variation in peak force with salt concentration is shown in Figure 3. The dependence of peak force on the salt concentration is in the same manner as for the critical force.

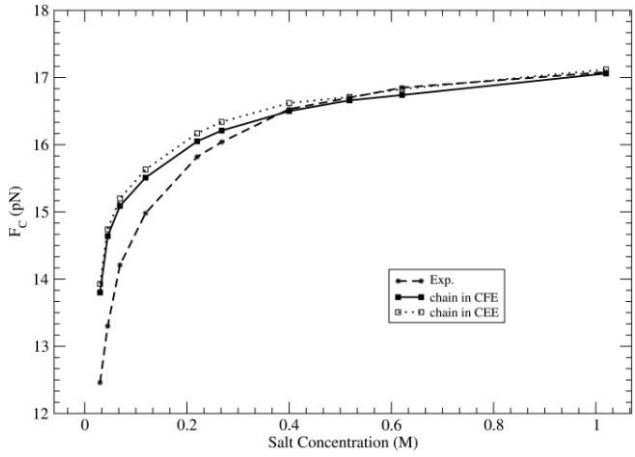

Figure 4. The graph showing the variation in critical force F_C as a function of salt concentration of the solution in both ensembles, Constant force and constant extension ensemble.

We calculated F_C and F_P at ten different salt concentrations 0.030 M, 0.045 M, 0.069 M, 0.119 M, 0.220 M, 0.268 M, 0.400 M, 0.518 M, 0.621 M & 1.02 M as for these concentrations the experimental values are available [9]. From Figure 4 we observe that the variation in critical force with salt concentration is having good match with the experimental values except the low salt concentration. We found that by increasing the salt concentration the critical force increases, or ions make the strand stronger.

4. Conclusions

We investigate the role of salt present in the solution on mechanical unzipping behavior of heterogeneous dsDNA molecule. With the suitable modifications in the PBD model, we observe the dependence of critical force of the system on the concentration of Na^+ or Mg^{2+} present in the solution. We found that the force required to unzip the chain varies non-linearly with the salt concentration of the solution. As predicted by Manning's counterion condensation theory [22], there is a layer of condensed counter ions on the DNA surface that neutralises the phosphate charges so that the electrostatic repulsion of inter-strand decreases and the interaction of hydrogen bond increases. This simply means that system needs more force to unzip the dsDNA molecule. The critical force and the peak force is found to vary with salt concentration. The addition of salt in the solution basically shields the repulsion between the phosphate groups in the dsDNA chain which, in result, needs more force to unzip the chain. We found that the dependence of critical force on salt concentration is in same manner in both the ensembles, and the results are in good agreement with the experimental observations [9].

Acknowledgements

We are thankful to Yashwant Singh and Sanjay Kumar, Department of Physics, Banaras Hindu University, India, for useful discussions and drawing our attentions to some experimental papers. We acknowledge the financial support provided by University Grant Commission, New Delhi, India.

References

1. S. M. Bhattacharjee, J. Phys. A 33 (2000) L423.
2. S. Srivastava and N. Singh, J. Chem. Phys. 134 (2011) 01510.
3. S. Kumar and M. S. Li, Phys. Rep. 486 (2010) 1.
4. J. SantaLucia Jr., Proc. Natl. Acad. Sci. U. S. A. 95 (1998) 146.
5. M. Ageno, E. Dore and C. Frontali, Biophys. J. 9 (1969) 128.
6. V. A. Bloomfield, D. M. Crothers and I. Tinoco Jr., Nucleic Acids: Structure, Properties and Functions, University Science Books, Sausalito CA (2000).
7. F. Ritort, J. Phys.: Condens. Mat. 18 (2006) R531.
8. K. Hatch, C. Danilowicz, V. Coljee, and M. Prentis, Nucleic Acids Res. 36 (2008) 29.
9. Josep M. Huguet et al, Proc. Natl. Acad. Sci. U. S. A. 107 (2010) 1543.
10. B. Essevaz-Roulet, U. Bockelmann, and F. Heslot, Proc. Natl. Acad. Sci. USA 94 (1997) 11935; U. Bockelmann, B. Essevaz-Roulet, and F. Heslot, Phys. Rev. E 58 (1998) 2386.
11. C. Danilcowicz et al, Proc. Natl. Acad. Sci. USA 100 (2003) 1694; J. D. Weeks et al, Biophys. J. 88 (2005) 2752.
12. M. Peyrard and A. R. Bishop, Phys. Rev. Lett. 62 (1989) 2755; T. Dauxois, and M. Peyrard, and A. R. Bishop, Phys. Rev. E 47 (1993) R44.
13. M. Peyrard, S. Cuesta-L pez, G. James, J. Biol. Phys. 35 (2009) 73.
14. R. D. Blake, S. G. Delcourt, Nucleic Acids Res. 26 (1998) 332.
15. Karen Drukker et al, J. Chem. Phys. 114 (2001) 579.
16. R. Dong, X. Yan, and S. Liu, J. Phys. A: Math. Gen. 37 (2004) 4977.
17. Nikos Theodorakopoulos, Phys. Rev. E 82 (2010) 021905.
18. Marco Zoli, J. Chem. Phys. 135 (2011) 115101.
19. N. Singh and Y. Singh, Eur. Phys. J. E 17 (2005) 7.
20. T. S. van Erp, S. Cuesta-L pez, M. Peyrard, Eur. Phys. J. E 20 (2006) 421.
21. S. Buyukdagli, M. Joyeux, Phys. Rev. E 77 (2008) 031903.
22. G. S Manning, Biopolymers 11 (1972) 937; G. S Manning, J. Chem. Phys. 90 (1989) 5704.

Cite this article as:

Amar Singh *et al.*: **Force induced unzipping of dsDNA: The solvent effect.** *Phys. Express* 2013, **3**: 18

Spin susceptibility: A study of anomalies due to Kondo effect and f-electron correlation in HF systems

P. C. Baral[a,*], G. C. Rout[b]

[a] *Dept. of Physics, B. J. B Junior College, Bhubaneswar-751014, Odisha, India*
[b] *Condensed Matter Physics Group, F. M. University, Vyasa Vihar, Balasore-756019, Odisha, India*

[*] *Author for correspondence: P. C. Baral, email: pbaral@iopb.res.in*
Received 29 Sep 2012; Accepted 6 Nov 2012; Available Online 6 Nov 2012 2012

Abstract

We report here a microscopic theory of the temperature dependence of the spin susceptibility in heavy fermion (HF) systems. The model Hamiltonian consists of c-f electron exchange term and Heisenberg type inter-site spin-spin correlation in addition to the conduction electron and f-electron terms. The Hamiltonian is treated in mean-field approximation (MFA) taking into account two mean-field parameters the Kondo singlet $\lambda = \langle f_{i,\sigma}^{\dagger} c_{i,\sigma} \rangle$ and f-electron correlation parameter $\Gamma = \langle f_{i,\sigma}^{\dagger} f_{j,\sigma} \rangle$. An attempt has been made in this present communication to calculate the temperature dependent dynamic spin susceptibility by using Zubarev's Green's function and to study resonance peaks at Kondo and correlation temperatures. The evolution of peaks are studied by varying the model parameters and comparing the relation of it to the experimental data.

Keywords: Heavy fermions; Kondo effect; f-electron correlation; Susceptibility

1. Introduction

It is well established that an anomalous behaviour is observed in many Cerium, Ytterbium, Uranium or other anomalous rare-earth (Europium, Samarium, Praseodymium and Thulium) and actinide (Neptunium and Plutonium) systems. There are different anomalous behaviours observed in such systems. A very important case concerns the intermediate valence systems, where the number of $4f-$electrons are generally not an integer and vary with the external pressure or the matrix concentration, like in the famous phase diagram of Cerium metal [1-6] or in $Eu(Pd_{1-x}Au_x)_2Si_2$ alloys [7] or $YbInCu_4$ [8]. Another interesting and well studied case concerns the so-called Kondo systems, which have a valence or a number of $f-$electrons close to an integer. However, there is an anomalous behaviour due to a strong $c-f$ hybridization. The Kondo systems have been studied experimentally and theoretically after the first explanation of the resistivity minimum of magnetic dilute alloys by Kondo [9] and the exact solution obtained within the normalization group technique for the single Kondo impurity [10].

In the case of lattice, there exists a strong competition between the Kondo effect and the magnetic order in many compounds or concentrated alloys containing rare-earths or actinides. This strong interplay between the Kondo effect on each site and the magnetic ordering arising from the Ruderman-Kittel-Kasuya-Yosida (RKKY) interaction between rare-earth atoms at different lattice sites is described earlier by the Doniach diagram [11], which gives the variation of the $Ne'el$ temperature and of the Kondo temperature with increasing antiferromagnetic (AFM) intrasite exchange interaction J_K between localized spins and conduction electron spins. It is well known that the ordering temperature T_N is increasing initially with increasing ρJ_K, then passes through a maximum and tends to zero at a critical value ρJ_K^c corresponding to a quantum critical point (QCP) in the Doniach diagram. Such a behaviour of T_N has been experimentally observed with increasing pressure in many Cerium compounds, such as $CeAl_2$ [12] or $CeRh_2Si_2$ [13]. A similar effect has been observed in $YbCu_2Si_2$ [14] or in related Ytterbium compounds, where the $Ne'el$ temperature starts from zero at a given pressure and increases rapidly with pressure, because pressure has an opposite effect in Ytterbium compounds than in Cerium compounds.

The dynamic spin susceptibility $\chi(\omega)$, which is related to the inelastic neutron scattering cross-section, gives important information about the low energy excitations of the system. In this work, we apply random phase approximation (RPA) theory [15] to calculate dynamical longitudinal magnetic susceptibility of conduction electrons in the Kondo model. The magnetic excitation in HF system provides valuable information for the nature HF states in Ce and Uranium compounds [15]. Aeppli et. al. [16] performed neutron scattering measurements on $CeCu_6$ which is a typical HF compound with an exceptionally large specific heat constant at low temperatures [17, 18]. The cross-section of the inelastic scattering for $k_BT \ll \hbar\omega$ is proportional to Im $\chi(q,\omega)$, where χ is the dynamical spin susceptibility. Some authors [19-23] have calculated $\chi(q,\omega)$ in Anderson model applying $\frac{1}{N_f}$ method, where N_f is degeneracy of $4f-$electrons. In above model, they could explain the Kondo peak but could not explain the f-electron correlation interaction peaks. In their calculation, they assumed f-f Coulomb interaction (U) to be infinity.

In the present work, we attempt to study the interplay between the Kondo effect and short range f-f correlations within the mean-field approximation. Therefore, we investigate the momentum and frequency dependent dynamical

spin susceptibility $\chi(q,\omega)$ for HF systems. In particular, we compare the formation of the resonant spin excitations (resonance peaks) with the resonance peak in the inelastic neutron scattering (INS) experiment. For this purpose, a model Hamiltonian is formulated in section 2. The mean- field Kondo parameter (λ) and magnetic correlation parameter (Γ) are calculated by minimizing the free energy of the systems. The calculation of dynamic spin susceptibility $\chi(q,\omega)$ is presented in section 3. Finally, the results and discussion are presented in section 4 and conclusions in section 5.

2. Formalism

The Kondo lattice model is the standard model to describe the HF systems. In this standard notation the model Hamiltonian [24-28] can be written as:

$$H_0 = \sum_{k,\sigma} \varepsilon_k c^{\dagger}_{k,\sigma} c_{k,\sigma} - J_K \sum_i \vec{s}_i^{\,c} \cdot \vec{S}_i^{\,f} - J_H \sum_{i,j} \vec{S}_i^{\,f} \cdot \vec{S}_j^{\,f} + E_0 \sum_{i,\sigma} f^{\dagger}_{i,\sigma} f_{i,\sigma} \quad (1)$$

The first term describes a half-filled band of conduction electrons of energy $\varepsilon_k = \varepsilon_0(k) - \mu$, with μ as chemical potential and $c_{k,\sigma}(c^{\dagger}_{k,\sigma})$ are the annihilation (creation) operators of conduction electrons. The second term represents the intrasite Kondo exchange interactions between the spin-half local moments $\vec{S}_j^{\,f}$ and the conduction electron spin $\vec{s}_i^{\,c} = \frac{1}{2} c^{\dagger}_{i,\sigma} \tau_{\sigma,\sigma'} c_{i,\sigma'}$ (with Pauli matrices τ) at site i and J_K is Kondo coupling parameter. The third term is the Heisenberg interaction and J_H is the interaction between the nearest neighbour spins and $J_H > 0$ for ferromagnetic and $J_H < 0$ for antiferromagnetic states. The last term represents the localized f-electron energy, where E_0 is the position of the f-electron level with respect to the Fermi level and $f_{i,\sigma}(f^{\dagger}_{i,\sigma})$ are the annihilation (creation) operators of f-electrons at site i.

In low temperatures phase, within the mean-field approximation (MFA), the f −excitations are weakly hybridized with conduction band and form Kondo hybridization with renormalized bands. Whereas, at high temperatures, f −excitations are completely decoupled from the conduction band. Both the complete decoupling found at high temperatures and the sharp phase transition are unphysical artifacts, but are expected to be corrected by treatments that incorporate the effects of fluctuations [29]. Although fluctuation effects are expected to yield important corrections to the MFA, we expect that the qualitative nature of the mean-field state would be maintained. Hence, within the MFA simillar to that used by Coleman and Andrei [30], the mean-field Hamiltonian is derived as:

$$H_0 = \sum_{k,\sigma} \varepsilon_k c^{\dagger}_{k,\sigma} c_{k,\sigma} + \sum_{k,\sigma} \varepsilon_f(k) f^{\dagger}_{k,\sigma} f_{k,\sigma} + V(\lambda) \sum_{k,\sigma} \left(c^{\dagger}_{k,\sigma} f_{k,\sigma} + f^{\dagger}_{k,\sigma} c_{k,\sigma} \right) - 2J_K \lambda^2 - Z J_H \Gamma^2 \quad (2)$$

The two mean-field parameters are $\lambda = \langle c^{\dagger}_{i,\sigma} f_{i,\sigma} \rangle$ and $\Gamma = \langle f^{\dagger}_{i,\sigma} f_{j,\sigma} \rangle$, where λ describe the intrasite Kondo correlation and Γ represents an inter-site correlation between the f-electrons of two neighbouring atoms. Within this mean-field approximations, the effective c-f hybridization appears as $V(\lambda) = J_K \lambda$ and the renormalized f-electron position appears as $\varepsilon_f(k) = E_0 + B\varepsilon_k$, where $B = 2ZJ_H/W$ with Z, W are the nearest neighbour coordination number and the conduction band width respectively. Thus, the Heisenberg coupling introduces a finite band width to the dispersion less f-electron position E_0, while the Kondo coupling J_K acts as the hybridization between the conduction band and the effective f-electron band. The temperature dependent two mean field parameters the Kondo singlet $\lambda(T)$ and correlation $\Gamma(T)$ and expression for the chemical potential $\mu(T)$ which are given in [31]. Then, the temperature dependence of $\Gamma(T)$, $\lambda(T)$ and $\mu(T)$ can be calculated self consistently. When λ equals to zero, the correlation function $(s_i^c \cdot S_j^f)$ becomes also zero, in our mean- field approximation. The temperature at which λ equals to zero, corresponds to the real Kondo temperature T_K. Similarly, the temperature T_{Cor} at which Γ becomes zero, corresponds to the temperature at which short range magnetic correlation (for nearest neighbours) disappears.

3. Calculation of susceptibility $\chi^{zz}(q,\omega)$

It is assumed that the solid is not in magnetic state (i.e. either ferromagnetic or anti-ferromagnetic). A weak magnetic field may change the magnetization and produce a linear response of the system. The dynamic longitudinal wave vector dependent magnetic spin susceptibility based on RPA theory is given by

$$\chi^{zz}(q,\omega) = \ll m_z(q,t); m_z(-q,t) \gg_{\omega} \quad (3)$$

where the z-component of magnetization $m_z(q,t)$ is given in terms of annihilation (creation) operators $c_{k,\sigma}(c^{\dagger}_{k,\sigma})$ of the conduction electrons.

$$m_z(q,t) = \mu_0 \sum_k \left(c^{\dagger}_{k+q\uparrow} c_{k\uparrow} - c^{\dagger}_{k+q\downarrow} c_{k\downarrow} \right)$$
$$m_z(-q,t) = \mu_0 \sum_k \left(c^{\dagger}_{k-q\uparrow} c_{k\uparrow} - c^{\dagger}_{k-q\downarrow} c_{k\downarrow} \right) \quad (4)$$

The susceptibility reduces

$$\chi^{zz}(q,\omega) = \mu_0^2 \sum_k \sum_{\alpha}^{4} \Gamma_{\alpha}(k,q,\omega) \quad (5)$$

where μ_0 is Bohr magnetron and $\Gamma_{\alpha}(k,q,\omega)$, for $\alpha = 1$ to 4, are the Fourier transformed two particle Green's functions which are defined by

$$\Gamma_1(k,q,\omega) = \ll \alpha_k^a; \beta_k^a \gg_{\omega}; \Gamma_2(k,q,\omega) = \ll \alpha_k^b; \beta_k^b \gg_{\omega}$$
$$\Gamma_3(k,q,\omega) = \ll \alpha_k^a; \beta_k^b \gg_{\omega}; \Gamma_4(k,q,\omega) = \ll \alpha_k^b; \beta_k^a \gg_{\omega} \quad (6)$$

The new two particle operator α_k and β_k are defined as

$$\alpha_k^a = c^{\dagger}_{k+q\uparrow} c_{k\uparrow}; \alpha_k^b = c^{\dagger}_{k+q\downarrow} c_{k\downarrow}$$
$$\beta_k^a = c^{\dagger}_{k-q\uparrow} c_{k\uparrow}; \beta_k^b = c^{\dagger}_{k-q\downarrow} c_{k\downarrow} \quad (7)$$

The Green's function $\Gamma_1(k,q,\omega)$ is coupled to other three Green's functions $A_{\alpha}(k,q,\omega)$ with $\alpha = 1$ to 3 and the coupled equations are solved to find the value of $\Gamma_{1,2}(k,q,\omega)$ as $\Gamma_{3,4}(k,q,\omega) = 0$. Hence, the longitudinal dynamic spin susceptibility $\chi(q,\omega)$ can be written as

$$\chi^{zz}(q,\omega) = \frac{\mu_0^2}{2\pi}\sum_k \frac{1}{|D_0(\omega)|}[|D_1(\omega)|(n_{k+q}-n_k) - |D_2(\omega)|\phi_k - |D_3(\omega)|\phi_{k+q}] \quad (8)$$

here $|D_0(\omega)|$, $|D_1(\omega)|$ etc are written as

$$|D_0(\omega)| = (\omega+\varepsilon_{1k})(\omega+\varepsilon_{2k})(\omega+\varepsilon_{3k})(\omega+\varepsilon_{4k}) - |D_4(\omega)|$$
$$|D_1(\omega)| = (\omega+\varepsilon_{2k})(\omega+\varepsilon_{3k})(\omega+\varepsilon_{4k}) - V^2(\lambda)(2\omega+\varepsilon_{2k}+\varepsilon_{3k})$$
$$|D_2(\omega)| = V(\lambda)(\omega+\varepsilon_{3k})(\omega+\varepsilon_{4k})$$
$$|D_3(\omega)| = V(\lambda)(\omega+\varepsilon_{2k})(\omega+\varepsilon_{4k})$$
$$|D_4(\omega)| = V^2(\lambda)(2\omega+\varepsilon_{2k}+\varepsilon_{3k})^2 \quad (9)$$

with

$$\varepsilon_{1k} = \varepsilon_{k+q} - \varepsilon_k, \varepsilon_{2k} = \varepsilon_{k+q} - \varepsilon_f(k)$$

$$\varepsilon_{3k} = \varepsilon_f(k+q) - \varepsilon_k, \varepsilon_{4k} = \varepsilon_f(k+q) - \varepsilon_f(k)$$

Further the c −electron occupation numbers are defined as

$$n_{k+q} = n_{k+q\uparrow} + n_{k+q\downarrow}, \phi_{k+q} = \phi_{k+q\uparrow} + \phi_{k+q\downarrow} \quad (10)$$

and

$$n_{k+q} = \frac{F_1(\omega_1)-F_2(\omega_2)}{\omega_1(k+q)-\omega_2(k+q)} \quad (11)$$

with

$$F_1(\omega_1) = (\omega_1(k+q)-\varepsilon_f(k+q))f(\beta\omega_1(k+q))$$
$$F_2(\omega_2) = (\omega_2(k+q)-\varepsilon_f(k+q))f(\beta\omega_2(k+q)) \quad (12)$$

$$\phi_{k+q} = \frac{V(\lambda)[f((\beta\omega_1(k+q))-f((\beta\omega_2(k+q))]}{\omega_1(k+q)-\omega_2(k+q)} \quad (13)$$

where the Fermi function in general can be written as $f(y) = (e^y+1)^{-1}$ where $y = \beta\omega_\alpha$ and $\alpha = 1,2$ with $\beta = (k_BT)^{-1}$. The very weak magnetic moment of slow neutron interacts via dipole-dipole interaction with the spin magnetic moment of the electrons in solid. This interaction leads to enhanced neutron scattering from the magnetic system. The inelastic cross-section for the magnetic neutron scattering from a solid system may be written in the form of the spin density correlation function $\chi(q,\omega)$ for a wave vector q and frequency ω of the applied field. The dynamic spin susceptibility is given by

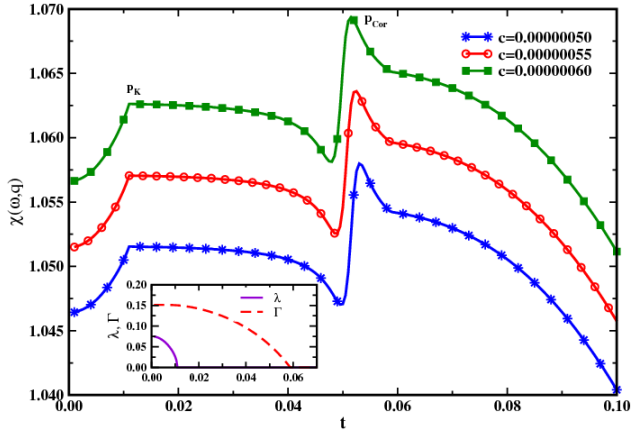

Figure 1. The temperature dependence of real part of spin susceptibility $\chi(q,\omega)$ for the different values of neutron frequency $c = 0.00000050,\ 0.00000055,\ 0.00000060$ and the self-consistent plots of λ vs. t and Γ vs. t for f −level position $d = 0.048$, the Kondo coupling $g_1 = 0.462$ and the correlation coupling $g_2 = 0.09$.

$$\chi(q,\omega) = \frac{2\pi}{\mu_0^2} Real[\chi^{zz}(q,\omega+i\eta)]_{\eta\to 0} \quad (14)$$

where η is finite width provided to the frequency to observe the resonance peaks. At $\omega = 0$, there can be no loss of energy so that Real $\chi^{zz}(q,\omega=0) = 0$ and any instability which occurs, then provides the signature of an instability in the ground state of the system. Thus the neutron scattering can be used as a direct experimental probe into the spectrum of the magnetic excitation of the system. The spin susceptibility $\chi(q,\omega)$ is calculated in the limit of small wave vector q. In this limit $\varepsilon_{k+q} \simeq \varepsilon_k + v_Fq$ where the velocity $v_F = (\frac{\partial\varepsilon_{k+q}}{\partial k})|_{q=0}$ is the velocity of the conduction electron near Fermi surface. The parameters involved in the calculations are the Kondo coupling (J_K), Heisenberg coupling (J_H), position of f-level (E_0), chemical potential μ, energy due to wave vector $q(\varepsilon_q = v_Fq)$, temperature (T), frequency (ω) and spectral width (η). These quantities are scaled with respect to conduction band width W. So, the parameters become dimensionless and are given by

$$g_1 = \frac{J_K}{W}, g_2 = \frac{J_H}{W}, B = 12g_2\Gamma, d = \frac{E_0}{W}, u = \frac{\mu}{W}$$

$$\tilde{\varepsilon}_q = \frac{v_Fq}{W}, t = \frac{k_BT}{W}, c = \frac{\omega}{W}, e = \frac{\eta}{W}$$

4. Results and Discussion

We have calculated real $\chi(q,\omega)$ based upon our model Hamiltonian given in Eq. (1). The temperature variation of Kondo singlet parameter λ and magnetic correlation Γ are solved self-consistently and are shown inset of in Figure 1. The Kondo coupling $g_1 = 0.462$ and the correlation coupling $g_2 = 0.09$ are so chosen that the reduced Kondo temperature $t_K = 0.011$ and the reduced correlation temperature $t_{Cor} = 0.058$. The condition that $t_{Cor} > t_K$ is satisfied for most of HF systems as observed by experiments i.e $T_K \simeq 125K$, $T_{Cor} \simeq 260K$ for $CeSn_3$, $T_K \simeq 150K$, $T_{Cor} \simeq 340K$ for $CeBe_{13}$ [32] and $T_{Cor} = 60-70K, T_K = 14-23K$ in $CeRu_2Si_2$ [33, 34] and $T_{Cor} = 10K, T_K = 5K$ in $CeCu_6$ [33].

The inset of Figure 1 shows that there is a very strong interaction between these two mean- field parameters, λ and Γ at low temperatures in their co-existence phases. The correlation parameter Γ is suppressed at low temperature after performing the self-consistent solutions. The position of f −level is fixed above the Fermi level at $d = 0.048$. The temperature dependence of λ and Γ are used for calculating temperature dependence of magnetic susceptibility $\chi(q,\omega)$ as shown in Figures 1 to 5. The dynamic longitudinal spin susceptibility is calculated within RPA to study the correlation and Kondo effect in HF systems. The Kondo correlation co-exists with the correlation at lower temperatures $T < T_K$. The pure f-electron correlation exists for the temperatures $T_K < T < T_{Cor}$ and paramagnetic phase exists for $T > T_{Cor}$. In order to investigate the two co-operative phenomena like the Kondo state and the magnetic state through the temperature dependence of dynamic spin susceptibility, we apply the the temperature dependence results of $\lambda(T)$ and $\Gamma(T)$. The

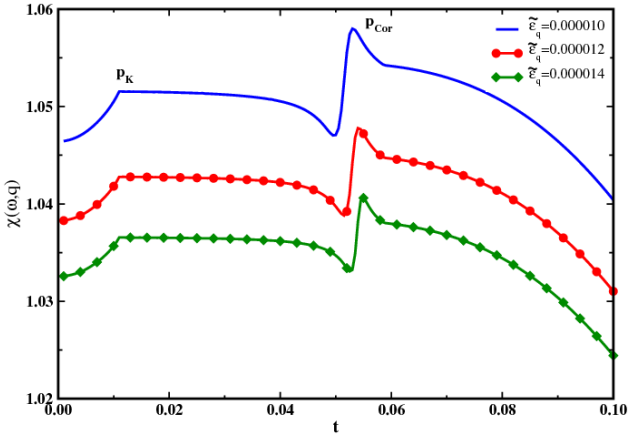

Figure 2. The plots of χ Vs. temperature t for f −level position $d = 0.048$, Kondo coupling $g_1 = 0.462$, correlation coupling $g_2 = 0.09$,for different reduced phonon energy $\tilde{\varepsilon}_q = 0.000010,\ 0.000012,\ 0.000014$.

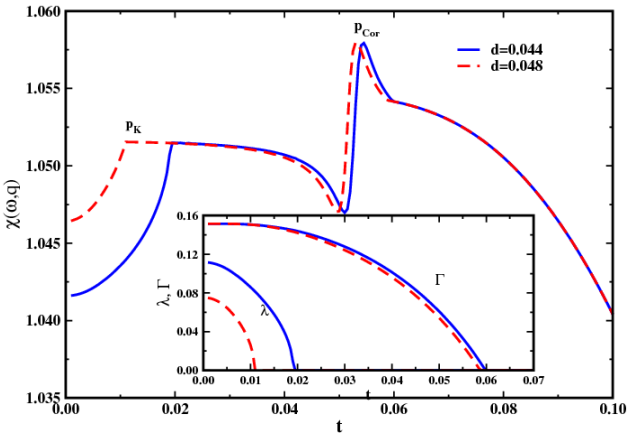

Figure 3. The plots of χ vs. reduced temperature t for Kondo coupling $g_1 = 0.462$, correlation coupling $g_2 = 0.09$, and reduced phonon energy $\tilde{\varepsilon}_q = 0.00001$ for different f −level position $d = 0.044$ and 0.048.

temperature dependent of dynamic spin susceptibility $\chi(q,\omega)$ are discussed in based on the Figure 1 to Figure 5.

The velocity (v_F) of conduction electron near Fermi surface is in order of $1\times10^5, 6.6\times10^6, 3.4\times10^6, 1.2\times10^5\ cm/s$ in heavy fermion systems (HFS) $CeCu_2Si_2, UPt_3, UBe_{13}, CeAl_3$ respectively [37] and the Fermi wave vector q is in order of $0.09A^{0-1}$ to $0.33A^{0-1}$ [38]. So, at present, we consider the phonon momentum transfer energy $\tilde{\varepsilon}_q = V_F q/W = 0.00001$ i,e $\varepsilon_q \simeq 0.01meV$ [37, 38]. During the numerical calculation the reduced phonon energy $\tilde{\varepsilon}_q = 0.00001$ and spectral width $\eta = 0.0000001$ to frequency are considered. The temperature variation of $\chi(q,\omega)$ for different reduced frequencies $c = 0.00000050$ to 0.00000060 for low frequencies $c < \tilde{\varepsilon}_q$ are shown in Figure 1 indicating that the susceptibility is enhanced with the increase of frequencies. This behaviour is observed experimentally for heavy fermion systems (HFS) like $CeCu_6, UPt_3$ [39, 40] for frequencies in order of MHz throughout the temperature range in ultrasonic measurement. For a fixed value of frequency, the susceptibility nearly remains constant at low frequencies in the f-electron correlation phase. However, with increase of temperature beyond magnetic correlation temperature T_{Cor}, the

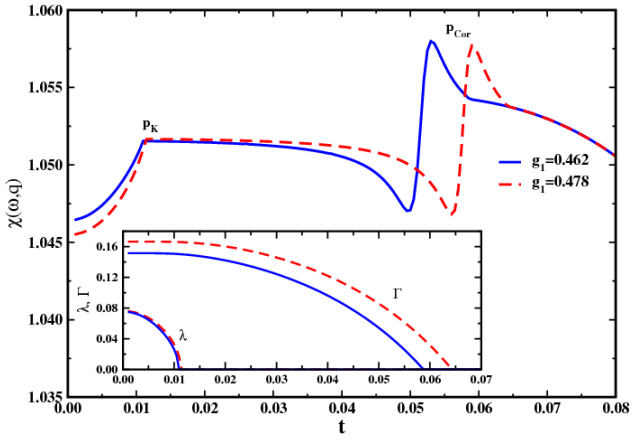

Figure 4. The plots of χ vs. reduced temperature t for f −level position $d = 0.048$, f-electron coupling $g_2 = 0.09$, for different Kondo coupling $g_1 = 0.462$ and 0.478.

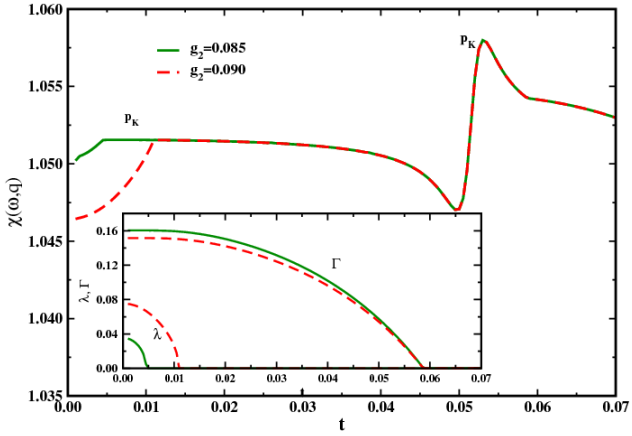

Figure 5. The plots of χ vs. reduced frequency c for f −level position $d = 0.048$, Kondo coupling $g_1 = 0.462$, for different f-electron coupling $g_2 = 0.85$ and 0.090.

susceptibility monotonically decreases in the paramagnetic phase showing mean field behaviour. As the temperature decreases below the Kondo temperature T_K, the susceptibility decreases to $0K$ in the Kondo phase. Since a sharp anomaly is seen at T_{Cor} for the susceptibility, there is possibility of magneto-striction effect due to the onset of the magnetic correlation. Lin et al. [39] have observed this type of signature in anti ferromagnetic (AFM) ordering through the ultrasound measurement. Since, in the Kondo singlet phase, localized f −electrons are hybridized with the conduction electrons, thereby decreasing the itinerant character of the conduction electrons.

When phonon of wave vector q is coupled to the conduction electrons, the conduction electron dispersion is modified to ε_{k+q} for the spin susceptibility in the solids. This energy dispersion ε_{k+q} can be expanded in the long wave length limit near the center of Brillouin zone boundary. As a result we find $\varepsilon_{k+q} \simeq \varepsilon_k + \frac{\partial\varepsilon_{k+q}}{\partial k}|_{q=0} q = \varepsilon_k + v_F q$, where v_F is the velocity of electron near the Fermi level. So, the energy due to phonon transfer is $\tilde{\varepsilon}_q = \frac{v_F q}{W}$. The effect of phonon transfer energy to the conduction electron band narrows down the conduction band and results in the reduction of the conduction band width. Thus, the phonon coupling to the conduction band is weakened. When phonon transfer energy

$\tilde{\varepsilon}_q$ increases from 0.000010 to 0.000014 in the low frequency range ($c < \tilde{\varepsilon}_q$), the susceptibility is suppressed due to weakening of EP coupling throughout the temperature range (see Figure 2). The phonon transfer energy has no effect on the correlation temperature T_{Cor} and the Kondo temperature T_K.

The effect of position of bare f-electron level with respect to the Fermi level $\varepsilon_F = 0$ on the temperature dependence of spin susceptibility is shown in Figure 3. As f −level position moves away from the Fermi level to higher energies, the formation of Kondo singlet is weakened. As a result, the Kondo temperature T_K decreases as shown in the self consistent plots of temperature dependent of $\lambda(T)$ and $\Gamma(T)$ as shown inset of Figure 3 with very small decrease in T_{Cor}. This is reflected in the temperature dependent spin susceptibility with the change of position of f −level. With the increase of f −level position from $d = 0.044$ to 0.048, the spin susceptibility is suppressed in the magnetic correlation phase for temperature $T_K < T < T_{Cor}$. However, the spin susceptibility is enhanced in the Kondo singlet region at low temperature $T < T_K$ resulting in the reduction of Kondo temperature T_K. It is to note further that the Kondo region will vanish, when f −level position will move far away from the Fermi level, finally $T_K = 0$. In paramagnetic phase $T > T_{Cor}$, the susceptibility does not change.

Figure 4 depicts the plots of $\chi(q,\omega)$ versus the temperature for the different values of the Kondo coupling $g_1 = 0.462$ and 0.478. As the Kondo coupling $g_1 = \frac{J_K}{W}$ increases for the given c-f hybridization, the Kondo singlet λ decreases and hence the Kondo temperature T_K. The increase of this coupling also enhances the correlation Γ in the temperature range $T_K < T < T_{Cor}$ in the correlation phase. This is reflected in the measurement of spin susceptibility. Our result is in good agreement with specific heat measurement by Peres et al. [41].

The effect of correlation coupling (g_2) in the temperature deprndence of spin susceptibility in shown in Figure 5. The effective f-electron band width is $\varepsilon_f(k) = E_0 + B\varepsilon_k$, where $B = 2ZJ_H/W$ with Z, W are the nearest neighbour coordination number and the conduction band width respectively. For a given $\varepsilon_f(k)$, as the f-electron coupling g_2 increases from 0.085 to 0.090, the magnetic correlation Γ decreases in the temperature range without change of correlation temperature T_{Cor}. But, it enhances the Kondo singlet as well as the Kondo temperature. The increase of correlation coupling decreases the susceptibility in Kondo correlation phase $T < T_K$. Coqblin et. al. [42] have shown three different regimes for different sets of values of correlation coupling J_H/W and occupation number n. They have not studied the interplay of Kondo effect and f-electron correlation. Here, we study that increase of correlation coupling $g_2 = J_H/W$ increases the Kondo temperature T_K.

5. Conclusions

Based on the model Hamiltonian described in Eq. 1, we have earlier investigated the Raman spectra, the modified BCS theory of HF superconductivty, the interplay of the Kondo effect and superconductivity, the anomalies in specific heat and the spectral density function in HF systems [25-28, 31]. The same microscopic theoretical model [25-28, 31] is applied here to study the frequency and temperature dependence of longitudinal spin susceptibility. The Kondo correlation and magnetic correlation are treated here within the mean-field approximation for which temperature dependent Kondo parameter λ, the correlation parameter Γ are solved self-consistently. The two particle Green's functions involved in the calculation of $\chi(q,\omega)$, are calculated by Zubarev's method [35]. The frequency and temperature dependent spin susceptibility $\chi(q,\omega)$ for different Kondo coupling g_1 and magnetic correlation coupling g_2 are studied and their effect on χ is presented in this paper in detail. Hence, the interplay between Kondo effect and magnetic correlation is studied extensively. It is observed that the correlation coupling strength enhances the correlation parameter as well as the correlation temperature, while suppressing the Kondo parameter and Kondo temperature. On the other hand, the Kondo coupling enhances the Kondo effect with increase in Kondo temperature, while suppressing the correlation effect and correlation temperature. The present calculation of spin susceptibility exhibits interplay of the Kondo effect and the correlation interaction which is displayed by the inelastic neutron scattering measurements [20, 22]. The two peak structure corresponding to the Kondo effect and the correlation interaction are reported by Citro et. al. [36] for their model calculation of specific heat and static magnetic susceptibility.

References

1. A. Jayaraman, Phys. Rev. 137 (1965) 179.
2. B. Coqblin, A. Blandin, Adv. Phys. 17 (1968) 281.
3. R. Ramirez, L. M. Falicov, Phys. Rev. B 3 (1971) 2425.
4. J. W. Allen, R. M. Martin, Phys. Rev. Lett. 49 (1982) 1106.
5. M. Lavagna, C. Lacroix, M. Cyrot, J. Phys. F 13 (1983) 1007.
6. A. Svane, Phys. Rev. B 53 (1996) 4275.
7. C. U. Segre, M. Croft, J. A. Hodges, V. Murgai, L. C. Gupta, R. D. Parks, Phys. Rev. Lett. 49 (1982) 1947.
8. J. L. Sarrao, Physica B 259-261 (1999) 128.
9. J. Kondo, Prog. Theor. Phys. 32 (1964) 37.
10. K. G. Wilson, Rev. Mod. Phys. 47 (1975) 773.
11. S. Doniach, Phys. Rev. B 91 (1977) 321.
12. B. Barbara, H. Bartholin, D. Florence, M. F. Rossignol, E. Walker, Physica B 86-88 (1977) 188.
13. T. Graf, J. D. Thompson, M. F. Hundley, R. Movshovich, Z. Fisk, D. Mandrus, R. A. Fischer, N. E. Phillips, Phys. Rev. Lett. 78 (1997) 3769.
14. K. Alami-Yadri, H. Wilhelm, D. Jaccard, Physica B 259-261 (1999) 157.
15. G. D. Mahan, Many particle physics, Plenum Press, New York (1990) p. 223.
16. G. Aeppli, H. Yoshizawa, Y. Endo, E. Bucher, H. Hufnagl, Y. Onuki, T. Komatsubara, Phys. Rev. Lett. 57 (1986) 122.
17. Y. Onuki, Y. Shimizu, T. Komatsubara, J. Phys. Soc. Jpn. 53 (1984) 1210.
18. G. R. Stewart, Z. Fisk, M. S. Wise, Phys. Rev. B 30 (1984) 482.
19. O. Gunnarsson, K. Schönhammer, Phys. Rev. Lett. 50 (1983) 604.
20. O. Gunnarsson, K. Schönhammer, Phys. Rev. B 28 (1982) 4315.
21. Y. Kuramoto, H. Kojima, Z. Phys. 57 (1984) 95.
22. N. E. Bickers, D. L. Coxs, Z. W. Wilkins, Phys. Rev. Lett. 54 (1985) 230.
23. J. W. Rasul, A. C. Hewson, J. Phys. C 16 (1983) L930.
24. J. R. Iglesias, C. Lacroix, B. Coqblin, Phys. Rev. B 56 (1997) 11820.
25. P. C. Baral, G. C. Rout, Prog. Theor. Phys. 126 (2011) 1101.
26. P. C. Baral, G. C. Rout, Indian J. Phys. 86 (2012) 431.
27. P. C. Baral, G. C. Rout, Indian J. Phys. 78 (2004) 797.
28. P. C. Baral, G. C. Rout, Mod. Phys. Lett. B 26 (2012) 12502.

29. P. S. Riseborough, Phys. Rev. B 45 (1992) 13984.
30. P. Coleman, N. Andrei, J. Phys: Condens Matter 1 (1989) 4057.
31. G. C. Rout, P. C. Baral, Physica B 404 (2009) 2051.
32. B. Lüthi, G. Bruls, P. Thameir, B. Wolf, D. Finsterbusch and I. Kouroudis, J. Low Temp. Phys. 95 (1994) 257.
33. J. Rossat-Mignod, L. P. Regnualt, J. L. Jacoud, C. Vettier, P. Lejay, J. Feouquet, E. Walker, D. Jaccard, A. Amato, J. Magn. Magn. Mater. 76-77 (1988) 376.
34. L. P. Regnault, W. A. C. Erkelens, J. Rossat-Mignold, P. lejay, J. Fouquet, Phys. Rev. B 38 (1988) 4481.
35. D. N. Zubarev, Sov. Phys. Uspekhi. 3 (1960) 320.
36. R. Citro, J. R. Iglesia, Physica B 259-261 (1999) 210.
37. A. Mourachkine, Room Temperature Superconductivity, Cambridge International Science Publishing (2004) p. 118.
38. N. R. Bernhoeft, G. G. Lonzarich, J. Phys. Condens. Matter 7 (1995) 7325.
39. S. -W. Lin, S. Adenwalla, J. B. Ketterson, M. Levy, B. K. Sarma, J. Low Temp. Phys. 89 (1992) 217.
40. V. Müller, D. Maurer, K. de Groot, E. Bucher, H. E. Bömmel, Phys. Rev. Lett. 56 (1986) 248.
41. N. M. R. Peres, P. D. Sacramento, M. A. N. Arau'jo, Phys. Rev. B 64 (2001) 113104.
42. B. Coqblin, C. Lacroix, M. A. Gusmã o, J. R. Iglesias, Phys. Rev. B 67 (2003) 064417.

Cite this article as:

P. C. Baral *et al.*: **Spin susceptibility: A study of anomalies due to Kondo efeect and f-electron correlation in HF systems.** *Phys. Express* 2013, **3**: 20

Comparative studies on magnetocrystalline anisotropy constant of $CoFe_{1.5}M_{0.5}O_4$, M=Al & Cr

Lawrence Kumar[a,b], Pawan Kumar[a], Manoranjan Kar[a,*]

[a] *Department of Physics, Indian Institute of Technology Patna, Patna-800013, India*
[b] *Centre for Nanotechnology, Central University of Jharkhand, Ranchi-835205, India*

[*] *Author for correspondence: Manoranjan Kar, email: mano@iitp.ac.in*
Received 28 Aug 2012; Accepted 30 Oct 2012; Available Online 30 Oct 2012

Abstract

Nanocrystalline $CoFe_{1.5}Al_{0.5}O_4$ and $CoFe_{1.5}Cr_{0.5}O_4$ have been synthesized by the standard citrate precursor method. Crystal structure and phase purity have been studied by X-ray powder diffraction method. All the XRD Patterns have been analyzed by Rietveld refinement technique using the $Fd\bar{3}m$ space group. Magnetic hysteresis loops measurement has been carried out at room temperature using a vibrating sample magnetometer (VSM) over a field range of ± 1.5 T. It has been observed that the saturation magnetisation, remanant magnetisation and magnetocrystalline anisotropy constants are larger in Cr substituted sample than that of Al substituted one irrespective of the particle size (almost same for both samples). The magnetic data in high field region have been analyzed by employing law of approach to saturation (LA) technique. The anisotropy constants have been obtained from the LA analysis and found to be dependent upon crystal structure parameters, crystallite sizes, bond lengths and bond angles. The coercivity is lower in Cr substituted sample than that of Al substituted one.

Keywords: Spinel; Ferrite; Magnetic anisotropy; XRD; Rietveld

1. Introduction

Spinel structure of crystalline materials has many degrees of freedom available which can tune physical properties. Spinel ferrite is an important class of mixed-metal oxides in spinel families which has the general chemical formula AB_2O_4 (A site = divalent cations and B site = Trivalent Fe ions). Cobalt ferrite ($CoFe_2O_4$) is a well known hard ferrimagnetic materials in its bulk form which crystallizes in mixed spinel structure with space group $Fd\bar{3}m$. Its empirical formulae is $(Co_x^{2+}Fe_{1-x}^{3+})[Co_{1-x}^{2+}Fe_{1+x}^{3+}]O_4$ where round and square brackets indicate A and B sites respectively and x depends on preparation conditions [1]. The antiparallel alignment of magnetic moments of A-site with B-site is coupled by superexchange interaction through the O^{2-} ions which induce ferrimagnetism [2]. It exhibits high coercivity, moderate saturation magnetization and good chemical stability [3]. Hence this material is a promising candidate for technological applications at room temperature such as memory devices, drug delivery, cancer treatment, medical diagnosis and high frequency applications etc. [4-9].

The cubic $CoFe_2O_4$ has large magneto crystalline anisotropy energy with positive anisotropy constant [10-12]. The large magneto crystalline anisotropy energy in this material is mainly attributed to the Co^{2+} ions on the B sites. It is a hard magnetic material as it has large multiaxial positive magneto crystalline anisotropy constant. This property can be tuned by substituting A site and/or B site by different transition and/or nontransition elements.

There are several substitutions of transition elements (Mn, Cr, Ga etc.) in Fe site [13-15]. However, according to our knowledge there is lack in the detailed comparative study on magnetic and nonmagnetic substitution in $CoFe_2O_4$ and its influence on magnetic anisotropy of these materials. As ionic sizes of Al^{3+} and Cr^{3+} are comparable to Fe^{3+} ions, doping these cations will leave the material with magnetic defects without changing its crystal structure. It is expected that doping of nonmagnetic Al^{3+} ion will affect the superexchange interactions more significantly than that of Cr^{3+} ion. The magnetic properties of Aluminium substituted cobalt ferrites have been reported by various groups [16-17]. Recently Ranvah *et al.* [17] synthesized the aluminium substituted cobalt ferrite by ceramic route and found that magneto crystalline anisotropy constant decreased with the increasing annealing temperature. Kwang *et al.* [18] synthesized the chromium substituted cobalt ferrite by micro-emulsion method and found that magnetic parameters decreased with the increase in Cr ion concentration. According to our knowledge, there is no report in detailed study on crystal structure and its correlation of the physical properties with different types of dopants. In this report we have compared the properties of $CoFe_{1.5}Al_{0.5}O_4$ and $CoFe_{1.5}Cr_{0.5}O_4$ samples.

2. Experimental Details

Nanocrystalline powder samples $CoFe_{1.5}Al_{0.5}O_4$ and $CoFe_{1.5}Cr_{0.5}O_4$ were synthesized by the citrate precursor method. Cobalt nitrate ($Co(NO_3)_2.6H_2O$), Iron nitrate ($Fe(NO_3)_3.9H_2O$), Aluminium nitrate ($Al(NO_3)_3.9H_2O$), Chromium nitrate ($Cr(NO_3)_3.9H_2O$) and Citric acid ($C_6H_8O_7.H_2O$) with 99.9% purity were used as starting materials. The details about method of preparation are followed as in ref. [19]. The resulting materials were annealed at 200 ^{0}C and 600 ^{0}C for 2 hours at each temperature. Literature survey shows that cobalt ferrite ($CoFe_2O_4$) samples starts nucleation at 200 ^{0}C i.e. samples are in amorphous phase annealed below 200 ^{0}C. Also, samples annealed above 600 ^{0}C are in bulk phase and do not show any nanocrystalline

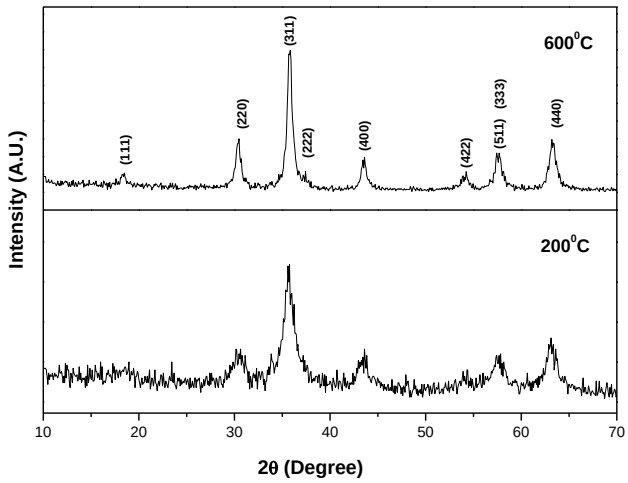

Figure 1. XRD patterns of the sample $CoFe_{1.5}Al_{0.5}O_4$ annealed at 200 ^{0}C and 600 ^{0}C.

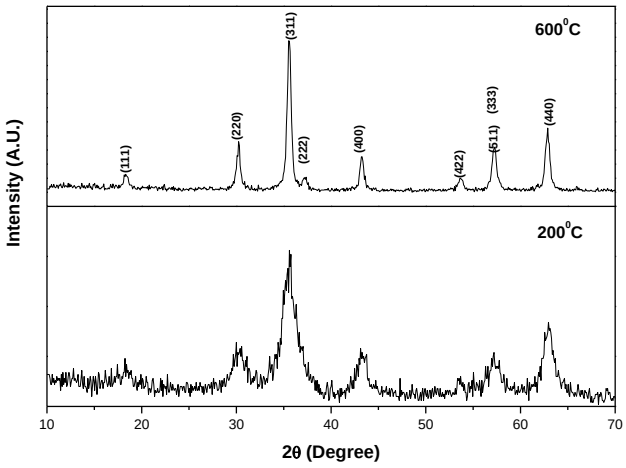

Figure 2. XRD patterns of the sample $CoFe_{1.5}Cr_{0.5}O_4$ annealed at 200 ^{0}C and 600 ^{0}C.

properties. Hence, we have chosen these two temperatures to prepare the nanocrystalline samples for the present study. The crystalline phase of the annealed samples was identified by the powder X-ray diffraction method (Rigaku Miniflex) using Cu K_α radiation. The compositional analysis has been carried out by EDS (Energy-dispersive spectroscopy) using the Hitachi S4800 Field Emission Scanning Electron Microscopy (FE-SEM). Surface morphology and particle size distribution was analysed by FE-SEM image. The magnetic hysteresis loops were recorded at room temperature (300 K) by using a LakeShore (Model No. 7410) Vibrating Sample Magnetometer (VSM). The maximum field of ± 1.5 T was used for this measurement.

3. Results and Discussion

3.1. Structural analysis

XRD patterns of the samples $CoFe_{1.5}Al_{0.5}O_4$ and $CoFe_{1.5}Cr_{0.5}O_4$ (annealed at 200 ^{0}C and 600 ^{0}C) are shown in Figure 1 and 2 respectively. All the XRD peaks have been indexed to $Fd\bar{3}m$ space group with cubic symmetry. The XRD patterns for the samples annealed at 200 ^{0}C shows very broad peaks which indicate the small crystallite size of the particles. The XRD patterns of the sample annealed at 600 ^{0}C shows an

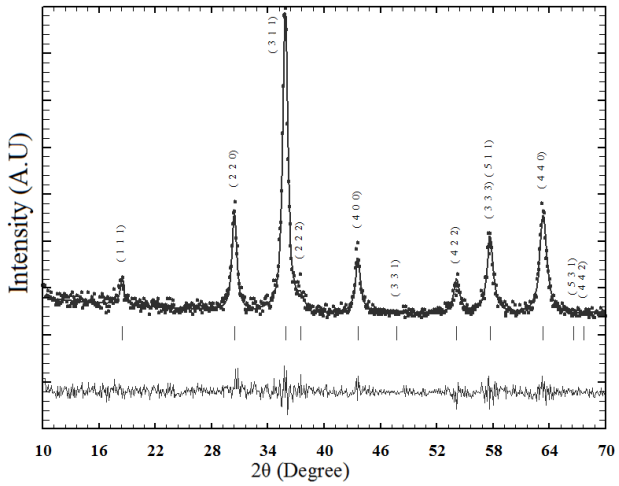

Figure 3. Rietveld refined XRD pattern for the sample $CoFe_{1.5}Al_{0.5}O_4$ annealed at 600°C. Solid circles represent experimental points and the solid line represents Rietveld refined data. The bottom line shows the difference between the experimental and refined data. The marked *2θ* positions are the allowed Bragg peaks.

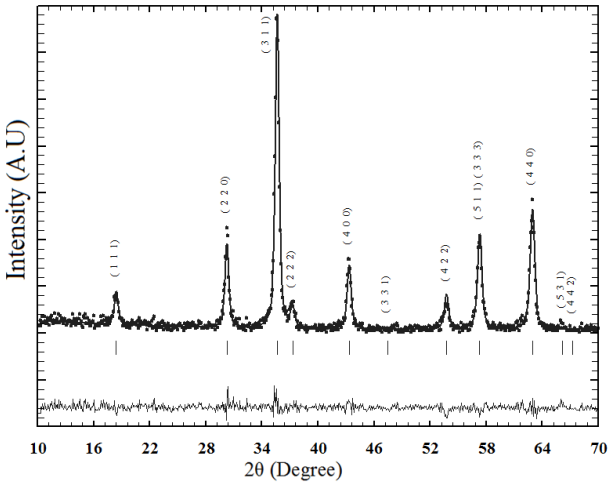

Figure 4. Rietveld refined XRD pattern for the sample $CoFe_{1.5}Cr_{0.5}O_4$ annealed at 600°C. Solid circles represent experimental points and the solid line represents Rietveld refined data. The bottom line shows the difference between the experimental and refined data. The marked *2θ* positions are the allowed Bragg peaks.

improvement in the sharpness of the XRD peaks due to increase in the crystallinity.

All XRD patterns have been analyzed by employing Rietveld method with the help of Fullprof Suite 2011 release programme [20]. XRD patterns along with Rietveld refinement for the samples $CoFe_{1.5}Al_{0.5}O_4$ and $CoFe_{1.5}Cr_{0.5}O_4$ (annealed at 600 ^{0}C) are shown in Figure 3 & 4 respectively. The allowed Braggs positions for the $Fd\bar{3}m$ space group are marked as vertical lines. All the observed peaks are allowed Bragg 2θ positions. The typical fractional positions and isothermal parameters of the atoms are given in Table 1 and 2 for $CoFe_{1.5}Al_{0.5}O_4$ and $CoFe_{1.5}Cr_{0.5}O_4$ respectively. Cation distributions are listed in Table 3. The oxygen positions (x = y = z) was taken as free parameter, however all other atomic fractional positions were taken as fixed. Lattice constant, isothermal parameter, occupancy, shape parameters and scale factor were taken as free parameters during the fitting. Background was corrected by pseudo voigt function.

Table 1. Values of fractional atomic coordinates and isothermal parameters for the sample $CoFe_{1.5}Al_{0.5}O_4$ (annealed at 600 ^{0}C).

Atoms	x	y	z	B_{iso}
Co/Fe/Al	0.1250	0.1250	0.1250	0.13740
Fe/Co/Al	0.5000	0.5000	0.5000	0.83793
O	0.25144	0.25144	0.25144	0.94900

Table 2. Values of fractional atomic coordinates and isothermal parameters for the sample $CoFe_{1.5}Cr_{0.5}O_4$ (annealed at 600 ^{0}C).

Atoms	x	y	z	B_{iso}
Co/Fe/Cr	0.1250	0.1250	0.1250	0.11283
Fe/Co/Cr	0.5000	0.5000	0.5000	0.64956
O	0.25233	0.25233	0.25233	0.93907

Occupancy variation shows that Al^{3+} and Cr^{3+} occupy both tetrahedral and octahedral sites. So, the present samples are in mixed spinel structure. The refined lattice parameters and the unit cell volume are listed in Table 4. The lattice parameters are comparable to that of literature values [21].

The analysis of the crystallite size has been carried out using the broadening of the XRD peaks. Peak broadening comes from several sources i.e. instrumental effect, finite crystallite size and strain effect within the crystal lattice [22]. A complete expression used in Rietveld method [20] is defined as,

$$FWMH^2 = (U+D^2_{ST})(tan^2\theta) + V(tan\theta) + W + IG/cos^2\theta \quad (1)$$

where U, V and W are the usual peak shape parameters, IG is a measure of the isotropic size effect, D_{ST} is the coefficient related to strain. The calculated crystallite size is enlisted in Table 4.

3.2. Elemental analysis

The FE-SEM image of the samples and the corresponding particle size distribution histogram with Gaussian fit has been shown in Figure 5(a), (b), (c) & (d). The image shows that the majority particles are spherical in shape and distributed homogeneously. The average size of the majority of particles in the sample $CoFe_{1.5}Al_{0.5}O_4$ and $CoFe_{1.5}Cr_{0.5}O_4$ (annealed at 600 ^{0}C) are in the range of 20-22 nm observed from the particle size distribution histogram. These values are close to the crystallite size (15.2 & 18.1 nm) obtained by XRD analysis. So, we conclude that particles are in the range of single domain size as crystallite size and particle size are same. The EDS spectrums of present samples have been shown in Figure 6(a) & (b). The EDS pattern indicates the presence of respective elements in the samples. There are no extra peaks except the Au peak. The gold peak is due to the thin coating of gold on the sample surface to make it conducting for FE-SEM measurements. We have not observed any contamination in the samples although the starting materials have 0.1% impurity. As 0.1% impurity is due to the presence of many compounds in the starting material, which is below the resolution of EDS.

3.3. Magnetic studies

The room temperature hysteresis loops for the samples $CoFe_{1.5}Al_{0.5}O_4$ and $CoFe_{1.5}Cr_{0.5}O_4$ (annealed at 600 ^{0}C) are shown in figure 7(a) and (b) respectively. The positive remanent magnetisation (M_r) was obtained from hysteresis loop at H = 0. The coercivity field (-ve value in H axis) was obtained from hysteresis loop at M = 0. The remanent magnetization (M_r) and coercivity (H_c) are listed in Table 5 for both samples.

Table 3. Cation distributions obtained using site occupancy of Rietveld analysis for the samples $CoFe_{1.5}Al_{0.5}O_4$ and $CoFe_{1.5}Cr_{0.5}O_4$ (annealed at 600^{o}C).

Sample Name	A-site			B-site		
	Fe	Co	Al/Cr	Fe	Co	Al/Cr
$CoFe_{1.5}Al_{0.5}O_4$	0.635	0.298	0.067	0.865	0.702	0.433
$CoFe_{1.5}Cr_{0.5}O_4$	0.665	0.222	0.113	0.835	0.778	0.387

Table 4. Parameters obtained from Rietveld analysis of XRD patterns for the samples $CoFe_{1.5}Al_{0.5}O_4$ and $CoFe_{1.5}Cr_{0.5}O_4$ (annealed at 600 ^{0}C). (R_p=Profile parameter, χ^2 =goodness fit factor and a=lattice constant).

Sample	R_p	χ^2	a=b=c (Å)	Volume (Å^3)	Rietveld method
$CoFe_{1.5}Al_{0.5}O_4$	13.5	1.16	8.309 (3)	573.6 (4)	15.2 (4)
$CoFe_{1.5}Cr_{0.5}O_4$	13.7	1.24	8.344 (1)	580.9 (2)	18.1 (0)

Magnetization at saturation has been analyzed by the "Law of Approach (LA)" to saturation which is described by the dependence of magnetization M on the applied magnetic field for $H>>H_c$. The magnetization near the saturation M_{sfit} can be written as [23],

$$M = M_{Sfit}\left[1-\frac{b}{H^2}\right]+\kappa H \quad (2)$$

where, $b = \frac{8}{105}\frac{K_1^2}{\mu_O^2 M_{Sfit}^2}$, M is the magnetization, H is the applied magnetic field, M_S is the saturation magnetization, μ_o is the permeability of the free space, K_1 is the cubic anisotropy constant and the term κH is known as the forced magnetization. The forced magnetization is caused by a linear increase in the spontaneous magnetization especially at high fields. The numerical coefficient 8/105 applies to cubic anisotropy of random polycrystalline samples. In general, the forced magnetization term was found to be necessary to fit the hysteresis curves at higher temperatures and higher fields, hence in the present case it has been neglected. Hence, M_{sfit} and K_1 are the only fitting parameters in the equation (2).

In the present samples the experimental data [M-H curve] above than 1T (high field parts) is fitted to equation 2. Typical fitting curve to LA are shown as inset in Figure 7 (a) & (b) for the samples $CoFe_{1.5}Al_{0.5}O_4$ and $CoFe_{1.5}Cr_{0.5}O_4$ (annealed at 600^{o}C) respectively. The values of M_s and b are obtained from fitting and, cubic anisotropy constant (K_1) was calculated using the equation,

$$K_1 = \mu_o M_{Sfit}\sqrt{105b/8} \quad (3)$$

The estimated value of M_{sfit} and K_1 are enlisted in Table 4. Value of saturation magnetization and K_1 in sample $CoFe_{1.5}Cr_{0.5}O_4$ is greater than that of $CoFe_{1.5}Al_{0.5}O_4$ and it can be explained as follows: The analysis of both samples magnetic hysteresis loops show that there are magnetic

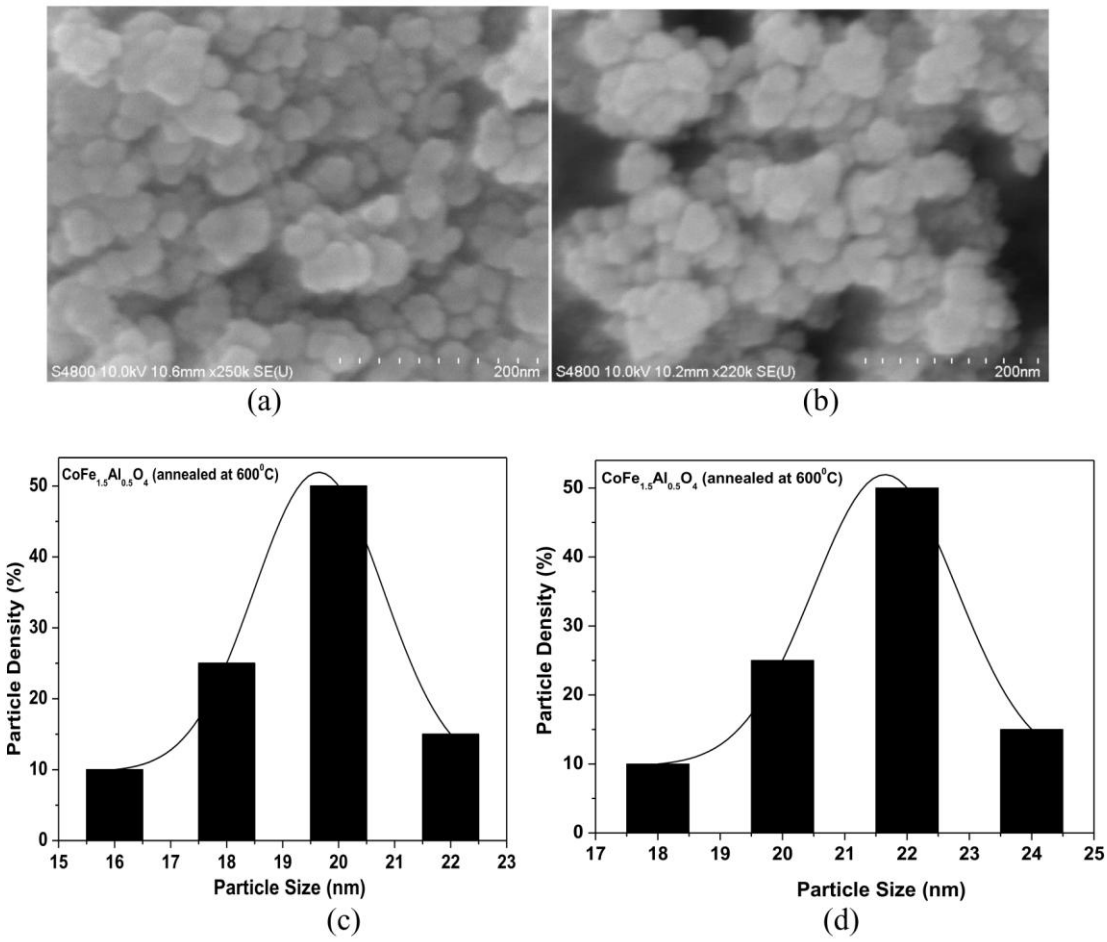

Figure 5. FE-SEM images and corresponding particle size distributions for the samples $CoFe_{1.5}Al_{0.5}O_4$ and $CoFe_{1.5}Cr_{0.5}O_4$.

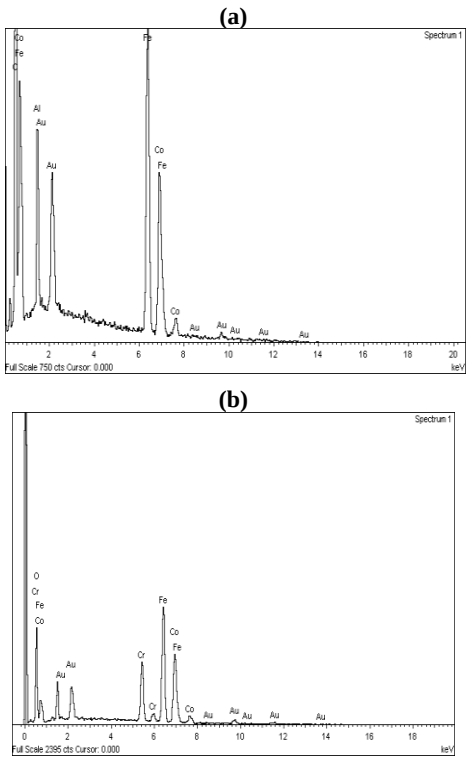

Figure 6. EDS patterns for the samples $CoFe_{1.5}Al_{0.5}O_4$ and $CoFe_{1.5}Cr_{0.5}O_4$ (annealed at 600 ^{0}C) (a) & (b) respectively. Au peak appears due to thin coating on the sample to make it conducting which is required for FESEM measurement.

interactions between Cr and Fe/Co ions whereas there is no magnetic interaction between Al and Fe/Co which is obvious as Al is a non-magnetic element. The saturation magnetization, remanant magnetization, coercivity, and magnetocrystalline anisotropy constant depend upon the magnetic properties of cations present on A (tetrahedral) and B (octahedral) sites of cobalt ferrite which affects the trahedral-octahedral superexchange interactions. The magnetic parameters are significantly less in case of nonmagnetic cation (Al^{3+}) substitution than magnetic cations (Cr^{3+}) because Al^{3+} ions do not take part in magnetic interactions due to its nonmagnetic nature. Hence there will be no crossover of magnetic moment when there is site exchange of cations in Al substituted cobalt ferrite.

For the sample $CoFe_{1.5}Al_{0.5}O_4$, more number of Al^{3+} ion replace Fe^{3+} from octahedral site which reveals that, more numbers of Fe^{3+} ions will have no magnetic neighbours and their spins will become uncoupled. Hence, the saturation magnetization decreases abruptly for $CoFe_{1.5}Al_{0.5}O_4$. The similar behaviour has been observed for Ga doped spinel ferrites [24].

According to the one-ion model, the strong anisotropy of cobalt ferrite is primarily due to the presence of Co^{2+} ions on the octahedral sites of the spinel structure [23]. As the crystal field (trigonal field) is not capable of removing the orbital degeneracy of Co^{2+} at the octahedral sites, the orbital magnetic moment is not quenched and, therefore there is a strong spin- orbit coupling which leads to strong anisotropy of cobalt ferrite ($CoFe_2O_4$). As we can see from Table 3 the concentration of Co^{2+} ion for B-sites in case of sample

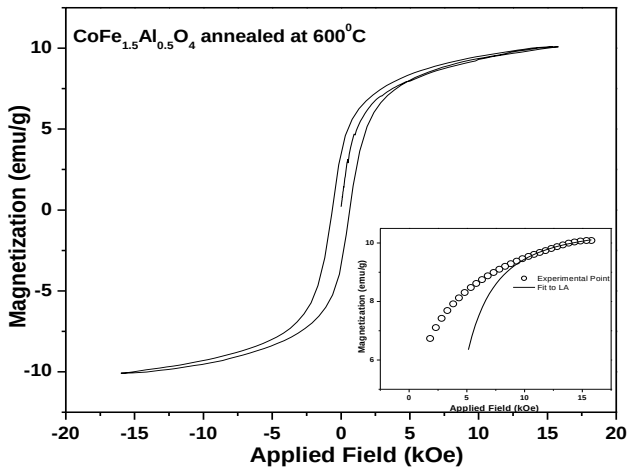

Figure 7(a). Magnetic hysteresis loops for the samples $CoFe_{1.5}Al_{0.5}O_4$ (annealed at 600 ^{0}C) and inset shows the LA fit.

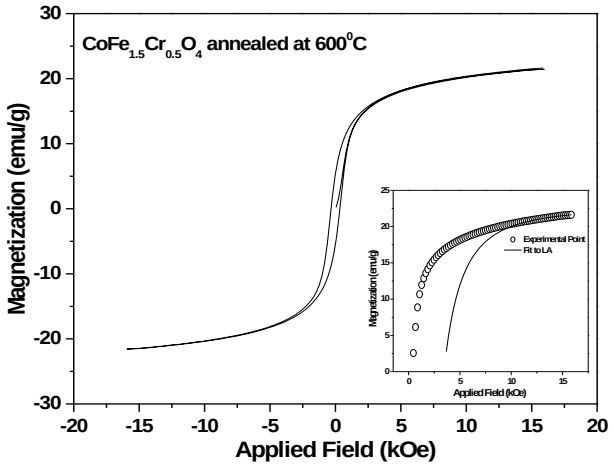

Figure 7(b). Magnetic hysteresis loops for the samples $CoFe_{1.5}Cr_{0.5}O_4$ (annealed at 600 ^{0}C) and inset shows the LA fit.

Table 5. Parameters obtained from magnetic hysteresis measurement at room temperature for the samples $CoFe_{1.5}Al_{0.5}O_4$ and $CoFe_{1.5}Cr_{0.5}O_4$ (annealed at 600 ^{o}C). M_{sfit}=saturation magnetization, M_r=remanent magnetization, H_c=coercivity, K_1=magnetocrystalline anisotropy constant.

Sample	M_{sfit} (emu/g)	M_r (emu/g)	H_c (k Oe)	K_1 (erg/cm^3)
$CoFe_{1.5}Al_{0.5}O_4$	10.52 (1)	3.371 (3)	0.623 (1)	0.61 x 10^6
$CoFe_{1.5}Cr_{0.5}O_4$	22.70 (4)	5.362 (0)	0.335 (2)	0.94 x 10^6

$CoFe_{1.5}Cr_{0.5}O_4$ is greater than that in $CoFe_{1.5}Al_{0.5}O_4$ which results in increase of the magnetocrystalline anisotropy constant in Cr doped sample.

4. Conclusions

Single phase nanocrystalline $CoFe_{1.5}Al_{0.5}O_4$ and $CoFe_{1.5}Cr_{0.5}O_4$ have been successfully synthesized by the citrate precursor method. The samples have been found to be in mixed spinel structure from Rietveld analysis of XRD patterns. Both samples are single domain nanocrystalline materials. The magnetic parameters decrease more significantly in case of nonmagnetic cation (Al^{3+}) substitution than magnetic cation (Cr^{3+}) because Al^{3+} ions does not take part in magnetic interactions due to its non-magnetic nature. There will be no crossover of magnetic moment when there is site exchange of cations. Hence, controlling magnetic properties become relatively easier in case of nonmagnetic substitution than that of magnetic substitution.

Acknowledgements

Authors are grateful to Department of Atomic Energy, Government of India (Sanction No. 2011/20/37P/ 03/BRNS/076) for financial support. Authors are thankful to the Centre of Instrumentation facility (CIF), Indian Institute of Technology Guwahati and Department of Physics, Patna University for extending the VSM and XRD facilities respectively.

References

1. K. Haneda, A. H. Morrish, J. Appl. Phys. 63 (1988) 4258.
2. Anthony R., West, Solid State Chemistry and its Application, Wiley India (2009).
3. A. Broese Van Groenou, P. F. Bongers and A. L. Stuyts, Mater. Sci. Eng. 3 (1968) 317.
4. Y. Yin, A. P. Alivisatos, Nature 437 (2005) 664.
5. M. A. El-Sayed, Acc. Chem. Res. 37 (2004) 326.
6. B. Y. Geng, J. Z. Ma, X. W. Liu, Q. B. Du, M. G. Kong, L. D. Zhang, Appl. Phys. Lett. 90 (2007) 043120.
7. S. Sun, C. B. Murray, D. Weller, L. Folks, A. Moser, Science 287 (2000) 1989.
8. R. C. Kambale, K. M. Song, Y. S. Koo, N. Hur, J. Appl. Phys. 110 (2011) 053910.
9. H. L. Yuan, Y. Q. Wang, S. M. Zhou, L. S. Liu, X. L. Chen, S. Y. Lou, R. J. Yuan, Y. M. Hao, N. Li, Nanoscale Res. Lett. 5 (2010) 1817.
10. H. Shenker, Phys. Rev. 107 (1957) 1246.
11. T. Hyeon, Chem. Commun. 8 (2003) 927.
12. M. Walker, P. I Mayo, K. O' Grady, S. W Charles, R. W. Chantrell, J. Phys. Condens. Matter 5 (1993) 2779.
13. Y. Melikhov, J. E. Snyder, D. C. Jiles, A. P. ring, J. A. Paulsen, C. C. H. Lo, K. W. Dennis, J. Appl. Phys. 99 (2006) 08.
14. Y. Melikhov, J. E. Snyder, C. C. H. Lo, P. N. Matlage, S. H. song, K. W. Dennis, D. C. Jiles, IEEE Trans. Magn. 42 (2006) 2861.
15. N. Ranvah, Y. Melikhov, D. C. Jiles, J. E. Snyder, A. J. Moses, P. I. Williams, S. H. Song, J. Appl. Phys. 103 (2008) 07.
16. S. Singhal, S. K. Barthwal, Kailash Chandra, J. Magn. Magn. Mater. 306 (2006) 233.
17. N. Ravah, I. C. Nlebedim, Y. Melikhov, J. E Snyder, P. I. Williams, A. J. Moses and D. C. Jiles, IEEE Trans. Magn. 45 (2009) 4261.
18. Kwang P. Chae, Y. B. Lee, J. G. Lee and S. H. Lee, J. Magn. Magn. Mater. 220 (2000) 59.
19. L. Kumar and M. Kar, J. Magn. Magn. Mater. 323 (2011) 2042.
20. R. Y. Young, The Rietveld Method (3rd ed.), Oxford University Press (1996).
21. Sonal Singhal, S. K. Barthwal, Kailash Chandra, J. Magn. Magn. Mater. 306 (2006) 233.
22. C. Suryanarayana, M. G. Nortan, X-ray Diffraction: A practical Approach, Plenum Publishing Corporation, New York (1998).
23. S. Chikazumi, Physics of Ferromagnetism (2nd ed.), Oxford University Press, New York (1997).
24. K. Krieble, M. Devlin, S. J. Lee, S. T Aldini and J. E. Snyder, J. Appl. Phys. 103 (2008) 07.

Cite this article as:

Lawrence Kumar *et al.*: **Comparative studies on magnetocrystalline anisotropy constant of $CoFe_{1.5}M_{0.5}O_4$, M=Al & Cr.** *Phys. Express* 2013, **3**: 21

DC electrical resistivity study of $YBa_2Cu_3O_{7-\delta}$ +x $BaTiO_3$-$CoFe_2O_4$ superconductor

M. Sahoo*, D. Behera

Department of physics, National institute of technology, Rourkela-769008, India

**Author for correspondence: M. Sahoo, email: sahoomousumi0@gmail.com*
Received 3 Sep 2012; Accepted 26 Oct 2012; Available Online 26 Oct 2012

Abstract

Polycrystalline $YBa_2Cu_3O_{7-\delta}$ + x $BaTiO_3$-$CoFe_2O_4$ (x = 0.0, 0.2, 0.4, 0.6 wt. %) superconductors were prepared by solid state route. With the increase of $BaTiO_3$-$CoFe_2O_4$ (BTO-CFO) addition it has been analyzed that the superconducting transition temperatures (T_c) determined from standard four-probe method was decreased and dropped sharply with higher wt. % addition of BTO-CFO. Excess conductivity fluctuation analysis using Aslamazov-Larkin model fitting reveals transition of two dominant regions (2D and 3D) above T_c. The decrease in 2D-3D crossover temperature T_{LD} (Lawerence-Doniach temperature) in the mean field region has been observed as a consequent dominance of 3D region to increase in wt. % in the composite. The increasing value of ρ_{wl} (weak link resistivity) and ρ_n (0) (residual resistivity) and the decreasing trend in the value of zero-resistance critical temperature (T_{c0}) indicates that the connectivity between grains decreases gradually with the addition of magneto-electric composite BTO-CFO. The increasing value of α_n (Percolation factor) and ΔT_C signifies the increase in grain size and degradation of sample quality in the composites.

Keywords: Paraconductivity; AL model; Percolation factor; M-E composite; Piezomagnetic

1. Introduction

Excess conductivity study of the para-coherence region of high temperature superconductors (HTSC) is a subject of interest for the past few years. Superconducting transition is a second order phase transition characterized by an order parameter, which is zero above the transition temperature T_c and grows to a finite value below T_c. The effect of fluctuations of this order parameter is a tool to understand the nature of the phase transition near T_c [1]. The resistive transition of sintered samples of the HTSC shows a characteristic two stage behavior. When the temperature is decreased, one first observes the pairing transition, where superconductivity is stabilized in some small and homogeneous regions of the sample. The superconducting grains may not necessarily be coincident with the crystallographic grains [2-6]. In lower temperatures, the resistivity is described by a percolation-like process related to the activation of weak links between the superconducting grains [7]. The resistivity becomes zero at the coherence transition that occurs in a critical temperature T_{c0} well below T_c. This transition is dominated by the fluctuating phases of the Ginzburg-Landau (GL) order parameter of individual grains that couple into a long range ordered state, leading to the zero resistance state.

It has been observed that superconductor composite materials have significantly improved electrical and magnetic properties [8]. The generated defects such as twins and inhomogeneous micro-defects can act as additional pinning centers. These defects decrease the number of weak-links and induce significant enhancement of the superconducting critical current density J_c in applied magnetic field [9-13]. Composite materials containing piezoelectric (ferroelectric) and piezomagnetic (ferrite) phases exhibit magneto-electric effect (ME) [14]. These composites have ME property, which is absent in their constituent phases. The ME effect couples two field effects: (i) magnetization due to application of electric field and (ii) electric polarization due to the application of magnetic field. The magneto-electric effect is due to the mechanical coupling between piezomagnetic (ferrite) and piezoelectric (ferroelectric) phases [15]. Magneto-electric materials are promising candidates for technological applications since the multiferroic coupling allows the interconnection between magnetic and electric fields. New memory devices that are electrically written and magnetically read have been based on ME materials [16]. $BaTiO_3$–$CoFe_2O_4$ (BTO-CFO) composites are interesting ME materials due to the individual properties of their components. $CoFe_2O_4$ has a spinel structure with large coercivity and magnetostriction [17]. $BaTiO_3$ exhibits polymorphs depending on the temperature, which is most interesting due to its ferroelectric and piezoelectric properties. BTO-CFO composite possesses enhanced flux pinning property [18]. In this paper, the electrical resistivity ρ (T) around the superconducting transition of YBCO + x BTO-CFO (x = 0.0,0.2,0.4,0.6 wt. %) is presented.

2. Experimental Details

YBCO, $CoFe_2O_4$ and $BaTiO_3$ were prepared separately by the solid state route method. YBCO powder is prepared by the solid state reaction route by mixing stoichiometries amount of Y_2O_3, $BaCO_3$, CuO followed by grinding, calcination at 880° C, sintering at 920° C and annealing at 500^0 C for 8 hrs for oxygen uptake, respectively. $CoFe_2O_4$ is prepared by mixing Co_3O_4 and Fe_2O_3 in 1:1 molar ratio and the mixed oxides were calcined in the temperature range of 1200^0 C for 4 hrs. $BaCO_3$ and TiO_2 have been used in 1:1 molar ratio as the precursor for the synthesis of $BaTiO_3$ powder. The mixed powder was calcined in temperature 1200° C for 4 hrs. Then, composite of $BaTiO_3$-$CoFe_2O_4$ was prepared in the ratio of 70 : 30 mole %. Then, a series of polycrystalline composite

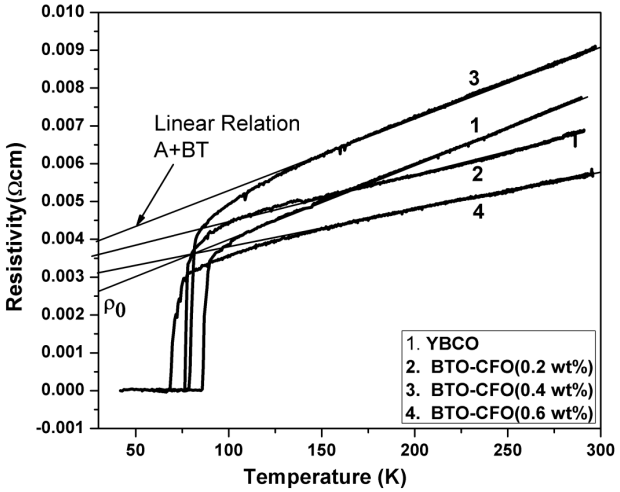

Figure 1. Resistivity dependences on the temperature for YBCO+ x BTO-CFO (x=0.0,0.2,0.4,0.6 wt. %) composites.

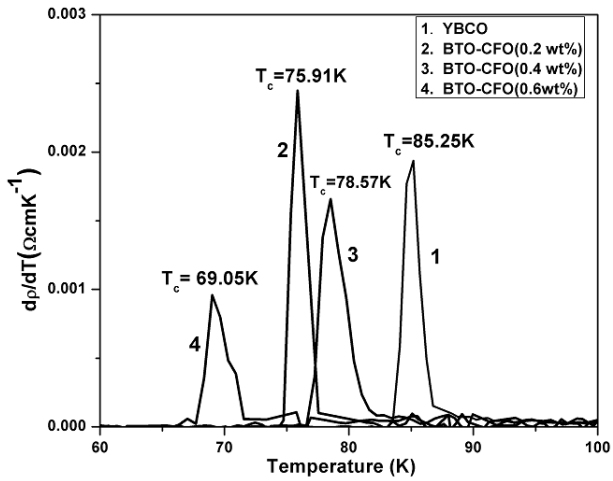

Figure 2. Temperature derivative of resistivity for YBCO + x BTO-CFO composites (x = 0.0, 0.2, 0.4,0.6 wt. %).

samples of (1-x) YBCO + x BTO-CFO (where x= 0.0,0.2,0.4,0.6 wt. %) were ground and pressed into pellets. The composite pellets were sintered at 920^0 C for 12 hrs and then cooled to 500^0 C where they were kept for 6 hours in an oxygen atmosphere for oxygen annealing. Temperature dependent resistivity ρ (T) was measured using standard four-probe technique with a Nanovoltmeter (Keithley- 2182A) and constant current source (Keithley 6221), with the voltage resolution of 10^{-8}V of the nanovoltmeter, a constant current source of 1 mA flowing through the samples. A closed cycle Helium refrigerators (JANIS) and a temperature controller (Lakeshore 332) having a temperature resolution of ±0.1 K was used for temperature variation. Computer controlled data acquisition system was used with LabView program.

3. Results and Discussion

3.1. Temperature dependence of resistivity

Measurements of the resistivity dependence of temperature for different samples with various amounts of BTO-CFO are shown in Figure 1. All samples show metallic behavior in the normal state (dρ/dT>0) and as superconducting transition to zero resistance. At higher temperature, both samples exhibited linear temperature dependence. The resistive transition exhibits two different regimes. The first is characterized by the normal state that shows a metallic behavior (above $2T_c$). The normal state resistivity is found to be linear from room temperature to a certain temperature, and follows Anderson and Zou relation $\rho_n(T) = A + BT$. Where ρ_n (T) is calculated by using the values of A and B parameters, which are obtained from the linear fitting of resistivity in the temperature range $2T_c$ to 300 K and extrapolation to 0 K gives resistivity slope (dρ/dT) and residual resistivity ρ_0 as seen from Figure 1.

The nonlinear region develops due to the contribution of Cooper pairs fluctuation to the conductivity above T_c. This is mainly due to the increasing rate of cooper pair formation on decreasing the temperature. Therefore, the fluctuation induced conductivity in this region follows the Aslamazov-Larkin (AL) model to yield the dimensional exponent appropriately to fluctuation-induced conductivity. The normal state resistivity of the composite samples is less than that of pure samples except the 0.4 wt. % composite sample ,which is tabulated in Table 1. At the temperature value T_{c0} the electrical resistivity vanishes and the phase of the order parameter acquired long range order between the grains of the system. This critical temperature characterizes the coherence transition. A finite tailing is observed in the superconducting transition for all the YBCO + x BTO-CFO composites before the resistance attains zero value. It indicates that the superconducting grains get progressively coupled to each other by Josephson tunneling across the grain boundary weak links. The zero-resistance at the temperature T_{c0}, characterizes the onset of global superconductivity in the samples where the long range superconducting order is achieved. The onset of global resistivity decreases with the addition of BTO-CFO indicates that BTO-CFO adheres to grain boundary forming weak links. Thus it is suggested that the BTO-CFO, being a magneto-electric material probably acts as a weak link, which causes the global resistivity transition temperature to decrease in addition to extra BTO-CFO.

The transition temperature from normal to superconducting state is severely damaged by the addition of ME composite BTO-CFO. From the temperature derivative of resistivity (Figure 2) firstly, we observe a sharp peak at T_c, which is related to intragranular fluctuation (fluctuations in the amplitude of the order parameter). These characteristic fluctuations define the so-called pairing transition [5]. The temperature values of this maximum are close to the bulk critical temperature value T_c followed by hump or secondary peak which broadens for composite samples. This is due to the M-E composite BTO-CFO affecting the intergranular percolation of cooper pairs of YBCO matrix. The transition width (ΔT_c) defined as full width half maxima increases with doping concentration. This may be due to the gradual occurrence of non-superconducting additional phases and the effect of microscopic inhomogeneity.

The weak-link resistivity (ρ_{wl}) across the grain boundaries and the percolation factor (α_n) arising due to current frustration caused by misalignment of anisotropic grains and sample defects such as voids and cracks are estimated from the residual resistivity $\rho_n(0)$ and the temperature coefficient of resistivity dρ/dT (shown in Table 1). This factor contributes to percolate conduction in granular copper oxides. Generally in the normal state electrical conduction of granular samples, current path frustration and

Table 1. Variation of normal state and superconducting parameters in the Composites with different BTO-CFO wt.%.

BTO-CFO (wt.%)	T_{C0} (K)	T_C (K)	ΔT_C (K)	ρ_N (290K) (μΩ.cm)	ρ_{wl} (μΩ.cm)	α_n	$\rho_n(0)$ (μΩ.cm)
0.0	82.99	85.20	1.6	7000	52.25	0.025	2090
0.2	74.27	75.94	1.7	6000	120.9	0.039	3100
0.4	76.73	78.55	2.3	8000	89.44	0.026	3440
0.6	67.71	68.99	1.8	5000	144.84	0.051	2840

meandering of current may occur due to two mechanisms. One is associated with the orientational disorder of anisotropic grains [19]. It depends on the degree of texturization, and has its origin in the extreme anisotropy of the copper oxides, the in-plane resistivity ρ_{ab} being orders of magnitude less than the out of plane resistivity ρ_c [20]. Due to the extreme conduction anisotropy, current blocks along the pathways with misaligned grains and current percolates through the sample along unobstructed paths, which results in a cross section reduction and path lengthening [21] that increases resistivity by a multiplicative factor, denote as 1/f ($0<f\leq1$). Another source of resistivity enhancement comes from structural defects of the grains (i.e pores, isolating boundaries, microcracks etc.) denoted as $1/\alpha_{str}$ ($0<\alpha_{str}\leq1$). Besides the percolative processes, a contribution to resistivity coming from the intergrain barriers ρ_{wl} is to be added. So the observed resistivity can be written as,

$$\rho_n = 1/\alpha_n (\rho_{ab}+\rho_{wl}) \quad (1)$$

where α_n is a shorthand for

$$\alpha_n = f \cdot \alpha_{str} \quad (2)$$

and it may be referred to as the normal-state percolative factor. The normal-state resistivity of polycrystalline HTS is linear with temperature. This linearity of ρ_n enables determination of the two sample parameters α_n and ρ_{wl} . Taking temperature derivatives of the equation (1) and assuming ρ_{wl} constant we can get [22,23]

$$\alpha_n = \rho'_{ab}/\rho'_n \quad (3)$$

where the primes stand for temperature derivatives. Similarly from Eqs. (1) and (3)

$$\rho_{wl} = \rho'_{ab}/\rho'_n \rho_n(0) = \alpha_n \rho_n(0) \quad (4)$$

where $\rho_n(0)$ is the extrapolation of the normal state resistivity to zero temperature. Based on single crystal measurements ρ_{ab} is assumed [24] to vary linearly with temperature (ρ'_{ab}= 0.5 $\mu\Omega.cm.K^{-1}$) with a negligible zero-temperature intercept. For typical polycrystalline Y-based HTS α_n is in the range 0.2–0.05 (also seen from Table 1 value). The increasing value of ρ_{wl} and $\rho_n(0)$ and the decreasing trend in the value of zero-resistance critical temperature (T_{c0}) indicate that the connectivity between grains decreases gradually with the addition of ME composite BTO-CFO. The increasing value of α_n and ΔT_C signifies the increase in grain size and degradation of sample quality in the composites. All these effects are due to increased inhomogeneities in the intergranular regions. Point defects and chemical dopants may occupy various positions in a real crystal forming substituent or interstitial impurities. Because of the grain boundary is a structurally distorted region in crystals, an extra energy form in the grain boundary region due to the distortion. As a result of the existence of grain boundary energy as well as the Coulomb interaction between the boundaries and the impurity atoms, they tend to attract impurity atoms in order to decrease the grain boundary energy. Therefore, the chemical dopant has a higher probability to stay in the grain boundary region than to stay inside the crystal.

3.2. Excess conductivity

3.2.1. Theoretical background

In the absence of an external magnetic field, the total conductivity above T_{c0}, can be expressed in a combination of three terms as follows:

$$\sigma = \sigma_n + \sigma_{AL} + \sigma_{MT} \quad (5)$$

The above eqn. states that, above T_{c0}, the conductivity is enhanced above the normal state conductivity (σ_n) by the fluctuation conductivity of both the Aslamzov-Larkin (LD) term (σ_{AL}) and the Maki-Thompson term (σ_{MT}). The MT term has been usually ignored in the analysis of various zero-field fluctuation conductivity measurements, because of the general belief that the intrinsic large inelastic scattering rates in these materials would reduce significantly the contribution of the MT term to the fluctuation conductivity. Also as the ceramic HTSC are in the dirty superconductor limit, the MT contribution is probably negligible in zero-applied magnetic field [25-27]. Since it has been well known that YBCO has a quasi two-dimensional nature as well as the characteristics of dimensional crossover as a function of temperature, we adopt Aslamazov-Larkin (AL) model to analyze the excess conductivity. The density of states (DOS) at the Fermi energy contribution introduced by Tewordt and coworkers by using a quasi two-dimensional tight binding model is better adapted to copper-oxide HTSC. But this may introduce variations in the excess conductivity amplitude 'A'. But all these effects are being taken directly into account in our approximation for normal state resistivity (ρ_n). According to AL theory the excess-conductivity ($\Delta\sigma$) above T_c generated by the thermodynamic fluctuations [8,28] diverges as a power-law given by

$$\Delta\sigma = A\varepsilon^{\lambda} \quad (6)$$

$\Delta\sigma$ is defined by

$$\Delta\sigma = (1/\rho - 1/\rho_R) = \sigma(T) - \sigma_R(T) \quad (7)$$

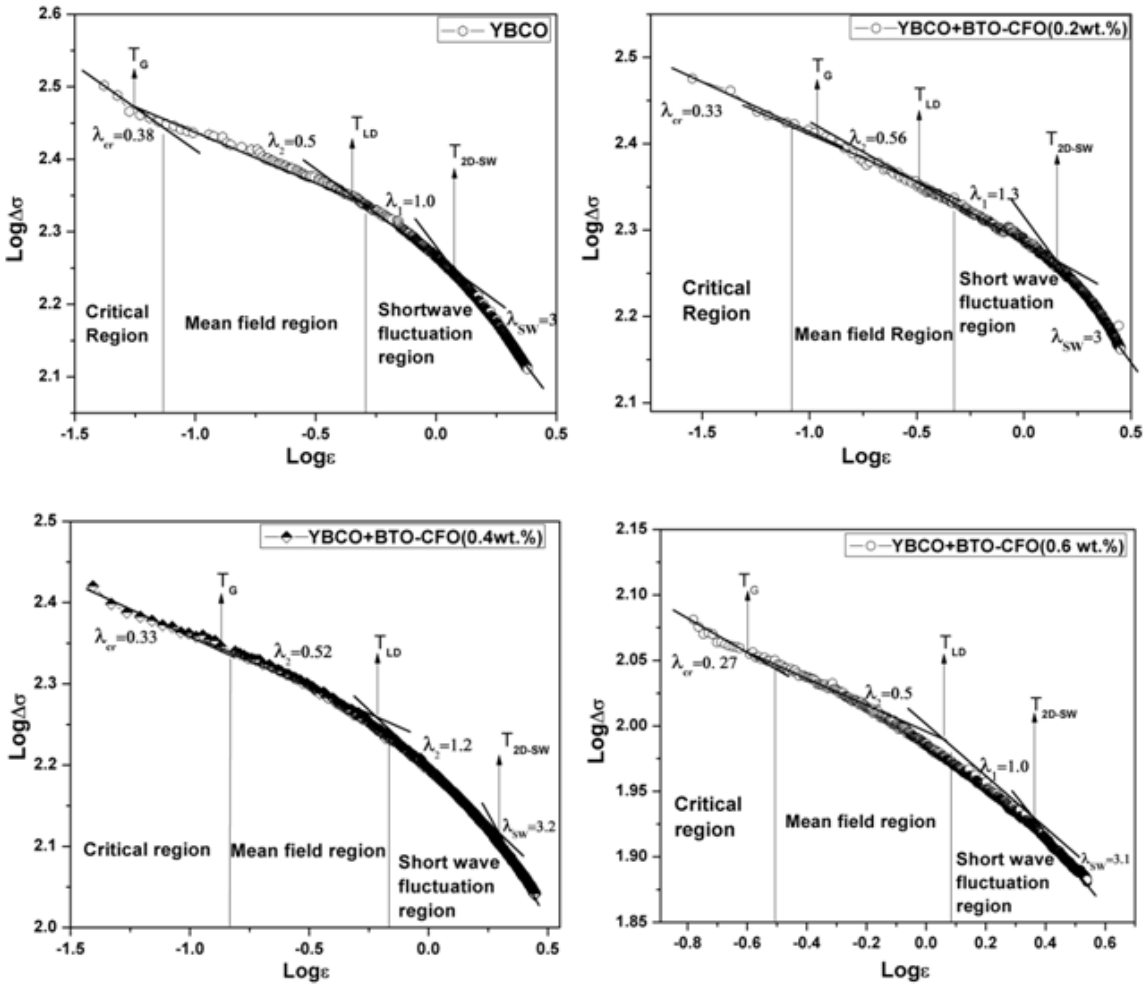

Figure 3. Log–Log plot of excess conductivity $1/\rho - 1/\rho_R$ as a function of reduced temperature $\epsilon = (T-T_c)/T_c$ in YBCO+ x BTO-CFO composite.

where ρ and ρ_R are the measured and normal resistivity, σ (T) is the measured conductivity and σ_R (T) is the extrapolated conductivity under the assumption of a linear behavior of temperature dependent resistivity. The reduced temperature $\varepsilon = (T-T_c)/T_c$, defined with respect to the mean field critical temperature (T_c) of the normal to superconducting transition. λ is the Gaussian critical exponent depending on the dimensionality of the HTSC system. The dimensionality D of the fluctuation system is related through the expression,

$$\lambda = 2 - D/2. \quad (8)$$

The effective value of the critical exponent for 3D and 2D are λ = 0.5 and λ= 1 respectively [29]. A is a temperature dependent parameter and its values for 3D and 2D are $A = e^2/32\hbar\xi(0)$ and $e^2/16\hbar d$ respectively. 'ξ (0)' is the zero-temperature coherence length or GL correlation length and 'd' is the effective separation of CuO_2 layers. These relations are based on GL theory and are valid only for the mean field temperature region ($1.01T_c$ to $1.1T_c$). Lawrence and Doniach (LD) [30] extended the AL model for layer superconductors, where conduction occurs mainly in 2D CuO_2 planes and these planes are coupled by Josephson tunneling. The excess conductivity parallel to the layers in the LD Model is given by

$$\Delta\sigma(T)_{LD} = e^2/16\hbar d\varepsilon\{1+(2\xi(0)/d)^2\,\varepsilon^{-1}\}^{-1/2} \quad (9)$$

From equation (4) at temperature close to T_c, $2\xi(0)/d >> 1$ and $\Delta\sigma(T)$ diverges as $\varepsilon^{-1/2}$ which corresponds to 3D behavior, whereas at $T >> Tc$, $2\xi(0)/d << 1$ and $\Delta\sigma(T)$ diverges as ε^{-1} which corresponds to 2D behaviour.

Figure 3 displays the logarithmic plot of excess conductivity as a function of reduced temperature (ε). In order to explain the experimental data with theoretical predicted ones, the different regions of the plot were linearly fitted and the exponent values were determined from the slopes. The plot reveals three distinct regimes i.e. mean-field region or the Gaussian fluctuations, critical fluctuations and short wave fluctuation region.

4. Gaussian fluctuations

In the mean-field region we represent two fits, one with slope value 1.0 and the other with value 0.5. The different exponents corresponding to crossover temperatures are as follows: the first exponent is in the normal region at log ε ($-0.6 \geq \log\varepsilon \geq -1$) and its values are close to 1, which indicates that the order parameter dimensionality (OPD) are two dimensional (2D). The second exponent is in the critical field region at log ε ($-1 \geq \log\varepsilon \geq -2$) and its values are close to 0.5, which signifies that the OPD are three dimensional (3D). 3D and 2D behavior of superconducting order parameter fluctuation dominates in YBCO composite. The temperature at which dimensionality fluctuation occurs from 3D to 2D is

Table 2. BTO-CFO content dependence of different cross over temperatures (Ginzburg Landau, Lawrence–Doniach and Shortwave fluctuation).

BTO-CFO (wt.%)	T_G (K)	T_{LD} (K)	$T_{2D\text{-}SW}$(K)
0.0	109.53	145.07	177.88
0.2	105.60	123.21	164.16
0.4	110.91	130.84	173.18
0.6	104.26	122.07	163.91

denoted by T_{LD}. T_{LD} values are higher than the T_c values. It reveals that the thermodynamically activated Cooper pairs are generated within the grain at comparatively higher temperatures, but due to the intragranular disturbances the mean field critical temperature comes down to lower value. It is possible to infer that this 3D Gaussian regime, determines the spatial limit for the obtainment of long range order of the superconductivity in the material bulk. When the temperature is diminished near T_c, first superconductivity is established in the CuO_2 planes, as a 2D regime, and crosses up to a well defined 3D regime [31].

5. Critical fluctuations

In superconducting grains Josephson coupling occurs between the grains. In the absence of magnetic field, their interaction is two dimensional. Considering the Drude like formula for excess conductivity and dynamical scaling theory for coherence length, the critical exponent of excess conductivity is obtained as [32,33]

$$\lambda_{cr} = \nu\,(2\text{-}D\text{-}\eta+z) \qquad (10)$$

where z is the dynamical exponent, η is the exponent of the order parameter correlation function, D is the dimensionality of the fluctuations and ν is the critical exponent for the coherence length. Using this relation for the fluctuation conductivity data in the critical region, one can estimate the dynamical exponent z. The CuO_2 planes as a common structural element of HTSCs are responsible for their dimensionality and their anisotropic properties [34,35]. According to renormalization group calculations, $\nu = 0.67$ and $\mu = 0.03$ are expected and $z = 0.32$ being predicted by the theory of dynamical critical scaling [36]. Using these values with D = 3 yields $\lambda_{cr}= 0.33$, which is called as the 3D-XY-E because of the model-E dynamics [37]. The critical fluctuation and 3D fluctuation regions intersect at temperature T_G. Still closer to T_G, a critical scaling regime beyond 3D-XY is observed, labeled by the exponent $\lambda_{cr} = 0.16$ [38-40]. The regime beyond 3D-XY with $\lambda_{cr} = 0.17$ was first observed in YBCO single crystal [41]. This exponent is known to characterize the critical resistive transition in classical granular arrays formed by metallic superconducting particles embedded in a poorly conducting matrix.

6. Shortwave fluctuations

The excess conductivity varies sharply with exponent value 3 with $\log \varepsilon$ ($-0.5 \geq \log \varepsilon \geq -0.1$) which highlights the presence of short wave fluctuations. The crossover temperature from 2D to short wave fluctuations ($T_{2D\text{-}SW}$) is indicated in Table 2. Short-wavelength fluctuations (SWF) effects appear when the characteristic wavelength of the order parameter becomes of the order of coherence length [42].

From the above data it is clear that the different regions observed are the critical region at $T < T_c$, the mean field region at T close to T_c and the short wave fluctuations at $T > T_c$. The different crossover temperatures T_G, T_{LD}, $T_{2D\text{-}SW}$ decrease with an increase in wt. % except 0.4 wt.% added sample. Generally the high temperature superconductors originate from Mott insulator and as such behave as a strong coupling system. It has been reported [43] that the strongly coupled supercurrent across the grain boundary is restricted to channels between the grain-boundary dislocation cores or their strain fields. Since the dislocation spacing becomes smaller with increasing angle, it is natural to postulate that no strongly coupled superconducting path across the boundary should exist above some critical misorientation angle. This model provides a conceptually reasonable explanation of why grain boundaries of increasing misorientation angle undergo a transition from strong to weak coupling with increasing misorientation angle. So the system can behave strongly coupled or weakly coupled depending the superconducting grain alignment and angle between them. In the regime of strong coupling between grains, tunneling conductance g >>1, electrons propagate easily through the granular sample and the Coulomb interaction is screened. As in our system the 3D fluctuation region is dominated so it is strongly coupled.

7. Conclusions

The effect of ME inhomogeneity BTO-CFO on the fluctuation conductivity of YBCO is studied. The different regions observed are the critical region at $T < T_c$, the mean field region at temperature close to T_c and the short wave fluctuations at $T > T_c$. The experimental data fit with theoretical predicted ones. The increasing value of ρ_{wl} and ρ_0 and the decreasing trend in the value of zero-resistance critical temperature (T_{c0}) indicate that the connectivity between grains decreases gradually with the addition of ME composite BTO-CFO. The increasing value of α and ΔT_C signifies the increase in grain size and degradation of sample quality in the composites. The different crossover temperatures T_G, T_{LD}, $T_{2D\text{-}SW}$ decrease gradually as compared to the pristine sample.

Acknowledgments

The authors gratefully acknowledge the Department of Science and Technology, Govt. of India for providing fellowship to carry out this work.

References

1. M. K Marhas, K. Balakrishlnan, V. Ganesan, R. Srinivasan, D. Kanjilal, G. K. Mehta, G. K Muralidhar, G. M. Rao, Senthil Nathan, S. Mohan, Bull. Mater. Sci. 17 (1994) 585.
2. M. Daeumling, J. M. Seuntjens, D. C. Larbalestier, Nature 346 (1990) 332.
3. A. Gerber, T. Grenet, M. Cyrot, J. Beille, Phys. Rev. Lett. 65 (1990) 3201.
4. P. Pureur, J. Schaf, M. A. Gusmao, J. V. Kunzler, Physica C 176 (1991) 357.
5. J. Roa-Rojas, R. Menegotto Costa., P. Pureur, P. Prieto, Phys. Rev. B 61 (2000) 12457.
6. A. Raboutou, P. Peyral, C. Lebeau, J. Rosenblatt, J. P. Burin, Y. Fouad, Physica A 207 (1994) 271.

7. J. Rosenblatt, P. Peyral, A. Raboutou, C. Lebeau, Physica B 152 (1988) 95.
8. L . G. Aslamazov, A. I. Larkin, Sov. Phys. Solid State 10 (1968) 875.
9. Y. Zhao, C. H. Cheng, J. S. Wang, Supercond. Sci. Technol. 18 (2005) S43.
10. T. A. Campbell, T. J. Haugan, I. Maartense, J. Murphy, L. Brunke, P. N. Barnes, Physica C 423 (2005) 1.
11. Z. H. He, T. Habisreuther, G. Bruchlos, D. Litzkendorf, W. Gawalek, Physica C 356 (2001) 277.
12. Z. Q. ang, X. D. Su, G. W. Qiao, Y. C. Guo, S. X. Dou, F. R. deBoer, Physica C 325 (1999) 136.
13. B. A. Albiss, N. Alrawashdeh, A. A. Jabal, M. Gharaibeh, I. M. Obaidat, M. K. Hasan (Qaseer), K. A. Azez, J. Supercond. Nov. Magn. 23 (2010) 1333.
14. J. Van Suchetelene, Philips Res. Rep. 27 (1972) 28.
15. A. M. J. G. Van Run, D. R. Terrel, J. H. Scholing, Mater. Sci. 9 (1974) 1710.
16. J. F. Scott, Nat. Mater. 6 (2007) 256.
17. J. B. Silva, W. Brito, N. D. S. Mohallem, Mater. Sci. Eng. B 112 (2004) 182.
18. S. H Wee, J. Shin, C. Cantoni, Y. L Zuev, S. Cook, A. Goyal,, Supercond. Sci. Technol. 23 (2010) 014007.
19. J. W. Ekin, A. I. Braginski, A. J. Panson, M. A. Janocko, D. W. Capone, N. J. Zaluzec, B. Flandermeyer, O. F. de Lima, M. Hong, J. Kwo, S. H. Liou, Appl. Phys. 62 (1987) 4821.
20. T. A. Friedmann, M. W. Rabin, J. Giapintzakis, J. P. Rice, D. M. Ginsberg, Phys. Rev. B 42 (1990) 6217.
21. J. Halbritter, Int. J. Mod. Phys. B 3 (1989) 719.
22. S. S. Bungre, R. Meisels, Z. X. Shen, A. D. Caplin, Nature 341 (1989) 725.
23. E. Babic, M. Prester, Z. Marohnic, T. Car, N. Biskup, S. A. Siddiqui, Solid State Commun. 72 (1989) 753.
24. B. Batlogg, In: Sadamichi Maekawa, Masatoshi Sato (Eds.), Physics of high-temperature superconductors, Springer-Verlag, Berlin, Vol. 106 (1992) p. 219.
25. S. Hikami and A. I. Larkin, Mod. Phys. Lett. B 2 (1988) 693.
26. A. G. Aronov, S. Hikami and A. I. Larkin, Phys. Rev. Lett. 62 (1989) 965.
27. K. Maki and R. S. Thomson, Phys. Rev. B 39 (1989) 2767.
28. M. Sahoo, B. Bhol, A. Kujur and D. Behera, AIP Conf. Proc. 1461 (2012) 342.
29. X. G. Tang, Q. X. Liu, J. Wang, H. L. W. Chan, Appl. Phys. A 96 (2009) 945.
30. J. Lawrence, S. Doniach, In: E. Kanda (Ed.), Proceedings of 12th Conference on Low Temperature Physics, Kyoto (1970) pp. 361
31. A. Kujur, D. Behera, Thin Solid Films 520 (2012) 2195.
32. V. N. Vieira, P. Pureur, J. Schaf, Phys. Rev. B 66 (2002) 224506.
33. A. Esmaeili, H. Sedghi, M. Amniat-Talab, M. Talebian, Eur. Phys. J. B 79 (2011) 443.
34. S. W. Tozer et al, Phys. Rev. Lett. 59 (1987) 1768.
35. T. R. Dinger, T. K. Worthington, W. J. Gollagher, R. L. Sandstorm, Phys. Rev. Lett. 58 (1987) 2687.
36. J. C. Le, J. Guillou Zinn-Justin, Phys. Rev. B 21 (1980) 3976.
37. C. Hohenberg, B. I. Halperin, Rev. Mod. Phys. 49 (1977) 435.
38. A. R. Jurelo, P. Rodrigues Jr., R. M. Costa, Mod. Phys. Lett. B 23 (2009) 1367.
39. R. Jurelo, P. R. Junior, A. E. Carrillo, T. Puig, X. Obradors, J. Barbosa, Physica C 399 (2003) 87.
40. A. Mohanta, D. Behera, Physica C 470 (2010) 295.
41. R. M. Costa, P. Pureur, M. Gusmao, S. Senousi, K. Behnia, Solid State commun. 113 (1999) 23.
42. A. Harabor, N. A. Harabor, M. Deletter, J. Optoelectron. Adv. Mater. 8 (2006) 1072.
43. N. F. Heinig, R. D. Redwing, J. E. Nordman, and D. C. Larbalestier, Phys. Rev. B 60 (1999) 1409.

Cite this article as:

M. Sahoo *et al.*: **DC electrical resistivity study of $YBa_2Cu_3O_{7-\delta}$ +x $BaTiO_3$-$CoFe_2O_4$ superconductor.** *Phys. Express* 2013, **3**: 22

Synthesis and characterization of yellow light emitting $Na_5Dy(MoO_4)_4$ double molybdate phosphor

S. Dutta, S. Som, R. K. Mukherjee, S. K. Sharma*

Department of Applied Physics, Indian School of Mines, Dhanbad-826004, India

Author for correspondence: S. K. Sharma, email: sksharma.ism@gmail.com
Received 30 Sep 2012; Accepted 14 Nov 2012; Available Online 14 Nov 2012

Abstract

$Na_5Dy(MoO_4)_4$ double molybdate phosphor was synthesized by solid state reaction method. Characterization of the prepared phosphor was carried out by X-ray diffraction, photoluminescence, absorption, diffuse reflectance, thermoluminescence and dielectric studies. X-ray diffraction studies confirm the tetragonal structure with average crystallite size of 60 nm. Photoluminescence spectrum shows intense emission peak at 579 nm corresponding to the transition $^4F_{9/2} \rightarrow {}^6H_{13/2}$ for bright yellow light. Thermoluminescence measurements show a broad glow curve with maximum centered at 107ºC after irradiating the phosphor by γ-rays. The dielectric properties such as permittivity, dielectric loss and a.c. conductivity were studied as a function of frequency. The structural, colour coordinates, band gap and trapping parameters were calculated from X-ray diffraction and optical studies.

Keywords: XRD; Photoluminescence; Band gap; Thermoluminescence

1. Introduction

In recent years, solid-state lighting technology has been in high demand due to the replacement of conventional fluorescent lamps by light emitting diodes (LED). White LEDs have been widely used as a backlight of liquid crystal display (LCD) and traffic signals [1]. These LEDs have attracted much attention due to their high reliability, long lifetime, low energy consumption and environment-friendly characteristics [2]. The luminescence emission from any phosphor converted LED becomes more intense if the band gap between the excited state and the highest component of the ground state multiplet of this phosphor becomes larger. So, a detailed study of band gap is necessary for the understanding of the practical applications of LEDs. The electronic and optical properties of the luminescent materials are markedly influenced by the presence of intrinsic and extrinsic defects. Thermoluminescence (TL) technique plays a vital role in getting the information about the distribution of defects / traps within the forbidden gap present in a material [3]. An important feature of the luminescent material to be used in display devices is that the material should preferably have a high dielectric constant and low dielectric loss, so that there will be a high electric field within the phosphor particles at a sufficiently low operating voltage. Due to this high electric field, a sufficient number of electrons from occupied meta-stable states excited to conduction band, and subsequently the electrons from conduction band fall into vacant meta-stable states. This results in an increase in radiative and non-radiative transitions. So, the dielectric properties of the phosphor were measured in order to see the applications of this phosphor for optoelectronic applications.

Double alkali rare-earth molybdates are an interesting class of luminescent materials because of their excellent thermal and chemical stability [4]. Their structural diversity and possible substitution in the structure provide these materials with numerous physical properties [5]. When Dy^{3+} ions are doped in these lattices, the phosphor emits intense yellow light and weak blue lights [6].

In this work, sodium-dysprosium double molybdate $Na_5Dy(MoO_4)_4$ phosphor has been synthesized in order to achieve a novel long wavelength yellow light. The structural, optical and dielectric studies of this phosphor were investigated in detail. The thermoluminescence studies with computerized glow-curve deconvolution procedure were applied to gain complete insight of the kinetic behavior for the synthesized host matrix doped with Dy^{3+} ions.

2. Experimental Details

$Na_5Dy(MoO_4)_4$ phosphor was prepared by solid state reaction method taking sodium bicarbonate ($NaHCO_3$), ammonium molybdate [$(NH_4)_6Mo_7O_{24}.4H_2O$] and dysprosium oxide (Dy_2O_3) as the starting raw materials in stoichiometric ratio. The concentration of Dy^{3+} ions was taken as 1 mol%. These raw materials were mixed with absolute ethyl alcohol and grounded thoroughly in an agate mortar for several hours to achieve uniform mixing. The obtained homogeneous mixture was put into a quartz crucible and prefired at 500°C for 2 hours, and then it was again fired at 700°C for two hours. Finally, a grey colour powder phosphor was obtained.

X-Ray diffractogram of the prepared phosphor was recorded in a wide range of Bragg angle 2θ (10°≤ 2θ ≤60°) using Bruker D8 X-Ray diffractometer with CuK_α radiation (λ = 0.154056 nm). The photoluminescence studies were carried out using Hitachi F-2500 Fluorescence spectrophotometer in the wavelength range 220 nm - 650 nm. Thermoluminescence studies were carried out on Harshaw make thermoluminescence analyzer after irradiation by ^{60}Co γ- rays. Absorption spectra were recorded using Shimadzu UV-VIS-2101 spectrophotometer in the wavelength range 200 nm - 800 nm. The diffuse reflectance studies were performed on Perkin Elmer Lambda 35 UV-VIS spectrophotometer. The dielectric properties were measured by Novo-control Impedance

Table 1. Miller indices, lattice constants and inter-planar spacing of the phosphor.

2θ (degree)	(hkl) (calculated)	Lattice constants (Å) (JCPDS)		(calculated)		Inter-planer spacing (Å) (JCPDS)	(calculated)
		a	c	a	c		
10.97	(101)					8.2002	8.07
17.94	(211)					4.7281	4.941
24.44	(301)					3.6614	3.817
26.00	(222)	11.57	11.62	11.75	11.80	3.3455	3.424
28.92	(132)					3.0967	3.084
30.47	(004)					2.9050	2.930
46.10	(424)					1.9324	1.967
57.94	(712)					1.5754	1.59

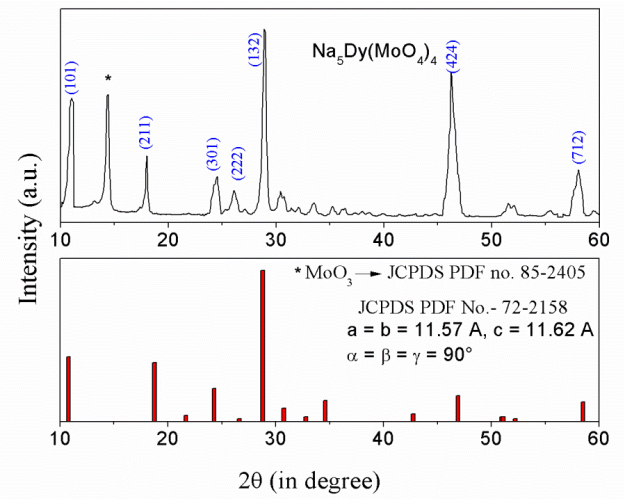

Figure 1. XRD pattern of $Na_5Dy(MoO_4)_4$ phosphor.

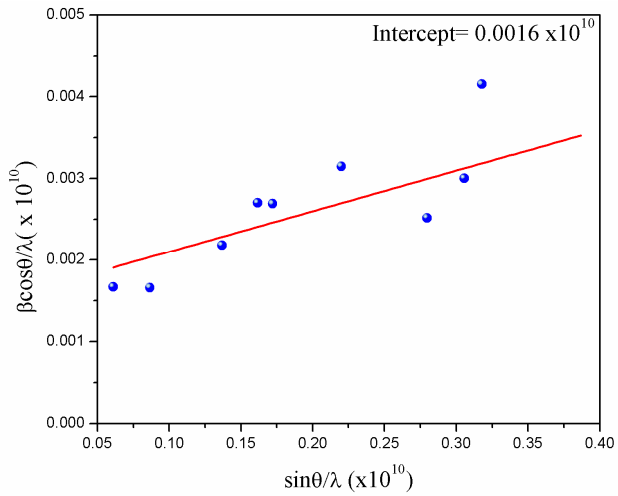

Figure 2. Crystallite size from Hall-Williamsons equation.

analyzer in the frequency range 1 Hz to 10 MHz. All the studies were carried out at room temperature.

3. Results and Discussion

3.1. X-Ray diffraction studies

The X-ray diffractogram of sodium-dysprosium double molybdate phosphor is shown in Figure 1. The phosphor exhibits tetragonal structure with space group $I4_1/a$ (88). The (h k l) values of the prominent peaks are shown in the XRD pattern. The lattice parameters of the unit cell were a = b = 11.57A, c = 11.62 A with α = β = γ =90° which is in correspondence with the JCPDS database of pdf number 72-2158. The peak at 12.92 is due to molybdenum oxide MoO_3 confirmed from the JCPDS database file number 85-2405 of molybdenum oxide. This is due to the fact that at high temperature ammonium molybdate decomposes to molybdenum oxide according to the reaction [7]:

$$(NH_4)_6Mo_7O_{24}.4H_2O \rightarrow 3(NH_4)_2MoO_4 + 4MoO_3 + 4H_2O$$

Calculation of structural parameters

The structural parameters such as miller indices, lattice constants, inter-planar spacing, crystallite size, dislocation density and microstrain were calculated from XRD data. The miller indices and lattice constants were determined using the following formula [8]:

$$\sin^2\theta = \frac{\lambda^2}{4a^2}(h^2 + k^2) + \frac{l^2}{c^2} \quad (1)$$

Here, θ is the diffraction angle, a and c are the lattice constants, (hkl) are the miller indices and λ is the wavelength of X-rays. This equation was used for indexing the XRD pattern for tetragonal structure. The calculated values of the Miller indices from the above equation [8] were found in agreement with the standard JCPDS values.

The inter-planar spacing was calculated using the following formula [8]:

$$d = \frac{1}{\sqrt{\frac{h^2 + k^2}{a^2} + \frac{l}{c^2}^2}} \quad (2)$$

The Miller indices, lattice constants and inter-planar spacing are given in Table 1.

For estimating the crystallite size (D) of the phosphor, Debye-Scherrer formula [9] and Hall-Williamsons [10] equation were used as given below:

$$D = 0.9\lambda / \beta\cos\theta \quad \text{(Debye-Scherrer formula)} \quad (3)$$

$$\beta\cos\theta/\lambda = 1/D + \varepsilon\sin\theta/\lambda \text{ (Hall-Williamsons equation)} \quad (4)$$

where, β is the full-width at half maximum (FWHM) and ε is the microstrain. Figure 2 shows the Hall-Williamsons plot. Here, ε and 1/D represents the slope and intercept of the straight line. The reciprocal of intercept on the βcosθ/λ axis

Table 2. Crystallite size, dislocation density and microstrain of the phosphor.

Crystallite size D (nm)		Dislocation density (δ)($x10^{14}/m^2$)	Microstrain ε ($x\ 10^{-3}$)	
Debye-Scherrer	Hall-Williamsons		Hall-Williamsons	$\varepsilon = \beta \cos\theta/4$
20-60	62.5	25.60	2.07	0.67

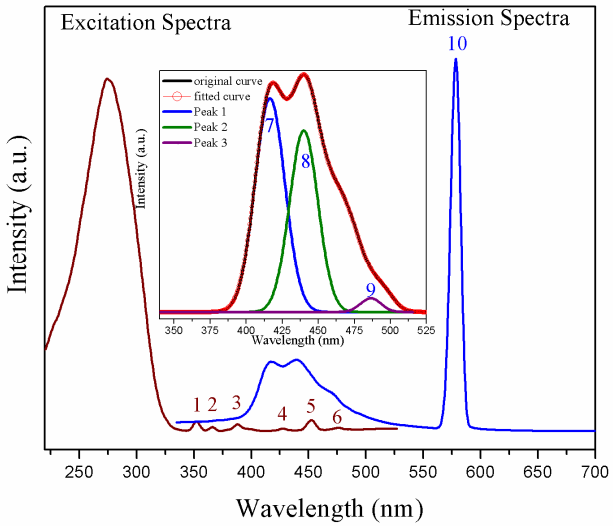

Figure 3. Photoluminescence spectra of the phosphor.

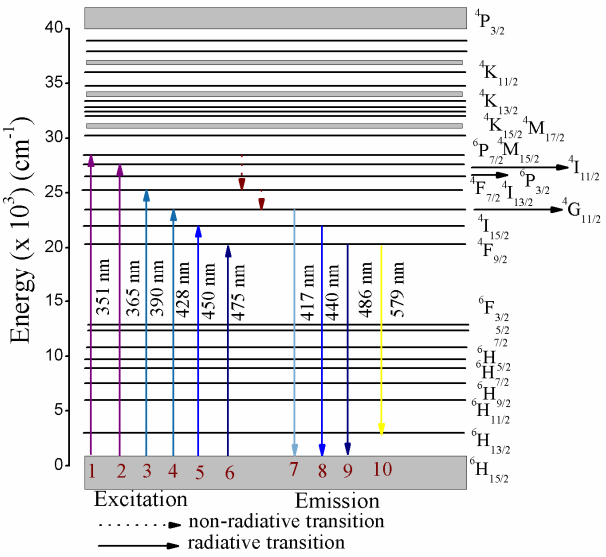

Figure 4. Energy level diagram of Dy^{3+} ion.

gave the average crystallite size which is in good agreement with that calculated by Scherrer formula.

The dislocation density and microstrain were calculated using following relations [10]:

$$\delta = 1/D^2 \quad (5)$$

$$\varepsilon = \beta \cos\theta/4 \quad (6)$$

The crystallite size, dislocation density and microstrain are given in Table 2.

3.2. Optical studies

3.2.1. Photoluminescence

The emission spectra of the $Na_5Dy(MoO_4)_4$ phosphor was recorded by keeping excitation wavelength fixed at 351 nm (Figure 3). A strong yellow emission at 579 nm due to $^4F_{9/2} \rightarrow {}^6H_{13/2}$ transition along with a weak blue emission band extending from 340 to 525 nm was observed. This weak blue band is composed of three bands (417, 440 and 486 nm) fitted by the Gaussian curves. These blue emissions were due to $^4G_{11/2} \rightarrow {}^6H_{15/2}$, $^4I_{15/2} \rightarrow {}^6H_{15/2}$ and $^4F_{9/2} \rightarrow {}^6H_{15/2}$ of Dy^{3+} respectively. The $^4F_{9/2} \rightarrow {}^6H_{13/2}$ transitions are hypersensitive electronic dipole transitions, which are greatly affected by the coordination environment while $^4F_{9/2} \rightarrow {}^6H_{15/2}$ transitions are magnetic dipole transitions and are much less sensitive to the coordination environment. The $^4F_{9/2} \rightarrow {}^6H_{13/2}$ transitions are forced electric dipole transition being allowed only at low symmetries with no inversion centre [11]. When Dy^{3+} is located at low symmetry local site (without an inversion centre), the yellow emission (transition $^4F_{9/2} \rightarrow {}^6H_{13/2}$) is often prominent in its emission spectrum as compared to blue emission (transition $^4F_{9/2} \rightarrow {}^6H_{15/2}$). As the radius of Dy^{3+} and Na^+ are comparable, Dy^{3+} can easily enter into the four fold coordination Na^+ low symmetry sites (without an inversion centre).

The excitation spectrum of the phosphor was recorded at emission wavelength 579 nm (Figure 3). An intense peak at 285 nm was observed due to the O→ Mo charge transfer (CT) [9]. Other smaller peaks at 351 nm, 365 nm, 390 nm, 428 nm, 450 nm and 475 nm were also observed due to the intra-configurational f–f transition of Dy^{3+} ions in the host lattice. The existence of these small peaks indicates that the phosphor can be well excited by UV and visible light.

The energy level diagram of Dy^{3+} with all possible transitions is shown in Figure 4.

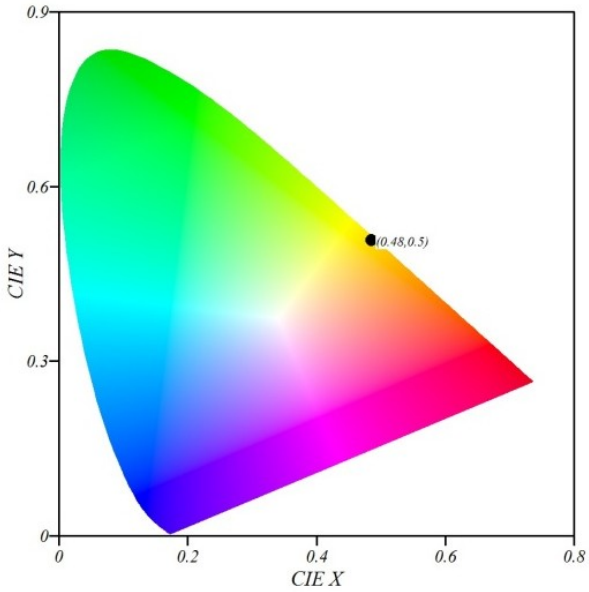

Figure 5. CIE Chromaticity diagram of the phosphor.

Calculation of colour coordinates

Figure 5 illustrates the CIE chromaticity diagram [12] depicted on 1931 chart. The colour coordinates were

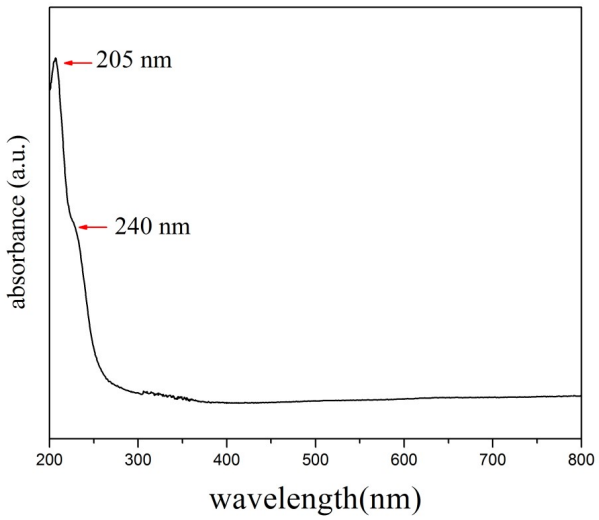

Figure 6. Optical absorption spectra of the phosphor.

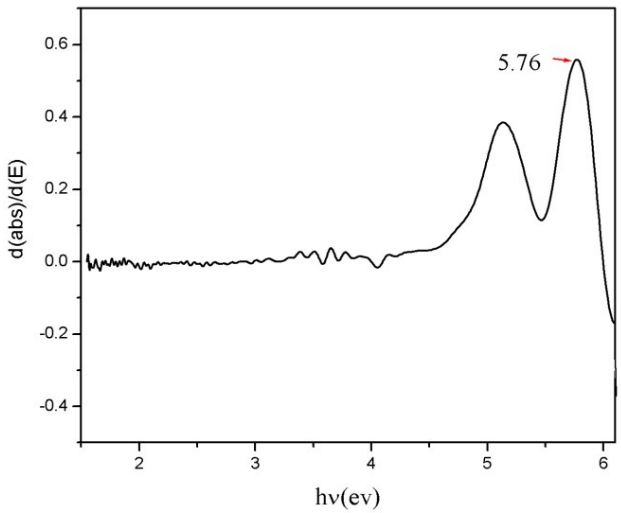

Figure 8. First derivative absorption spectrum.

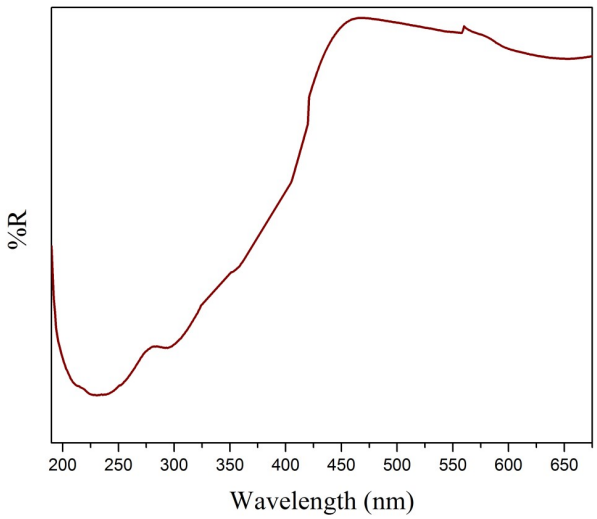

Figure 7. Diffuse reflectance spectra of the phosphor.

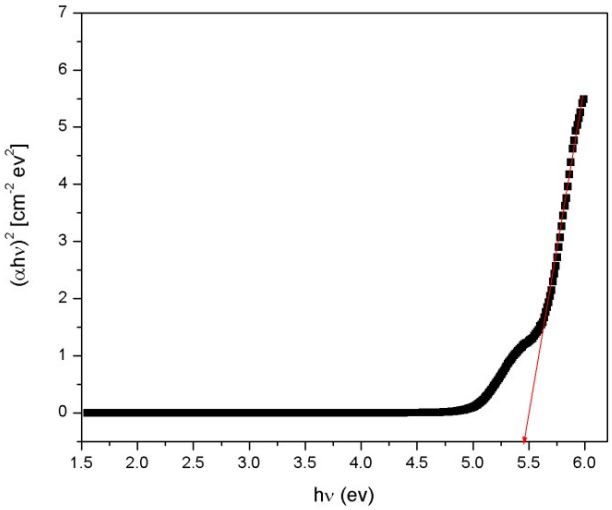

Figure 9. Plot of $(\alpha h\nu)^2$ versus photon energy (hν).

calculated by the spectrophotometric method using the spectral energy distribution. The colour coordinates for the $Na_5Dy(MoO_4)_4$ phosphor was calculated as (0.48, 0.50).

From the diagram it is evident that the colour coordinates lies in the yellow region which implies that the prepared phosphor can be used for yellow light emissions in various display devices.

3.2.2. Absorption

An optical absorption spectrum of the phosphor is shown in Figure 6. The spectrum shows an intense absorption peak at 205 nm which is attributed to the band gap of the phosphor. A shoulder at 240 nm appears due to charge transfer (CT) from oxygen ions to neighboring molybdenum ions.

3.2.3. Diffuse reflectance

The diffuse reflectance spectrum of the phosphor (Figure 7) was measured against a reference standard $BaSO_4$ compound. A sharp band at 235 nm indicates that light having this particular wavelength was absorbed. This band is due to band gap of the phosphor. The other weak bands beyond 300 nm were due to meta-stable energy states formed between valence band and conduction band by the Dy^{3+} ions.

Calculation of band gap

The band gap (Eg) is an important parameter for determining the application of phosphor materials in optoelectronic devices. In the present paper, the band gap of the phosphor was calculated from absorption and diffuse reflectance studies. The first derivative of the absorption spectrum with respect to photon energy (hν) was plotted (Figure 8). The maxima in the first derivative spectrum at the higher energy side provide the value of band gap [13]. From the plot the band gap of this phosphor was calculated as 5.76 eV.

The above calculated value of optical band gap was also verified by using the Tauc and Menth's relation [14]. According to this relation, the absorption coefficient (α) of the phosphor has the following energy dependence:

$$\alpha = A(h\nu - E_{gap})^2 / h\nu$$

where A is a proportionality constant and E_{gap} is the Tauc optical band gap.

In the high energy region of the spectrum, the plot of $(\alpha h\nu)^2$ vs hν varies linearly (Figure 9). The absorption spectrum deviated from the straight line plot in the low energy

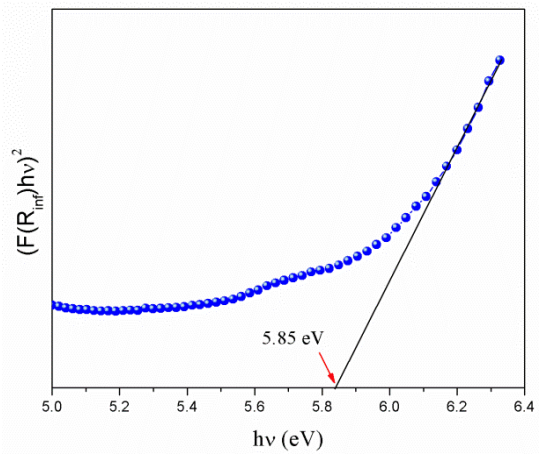

Figure 10. Plot of $[FR_{\infty}(h\nu)]^2$ versus photon energy (hν).

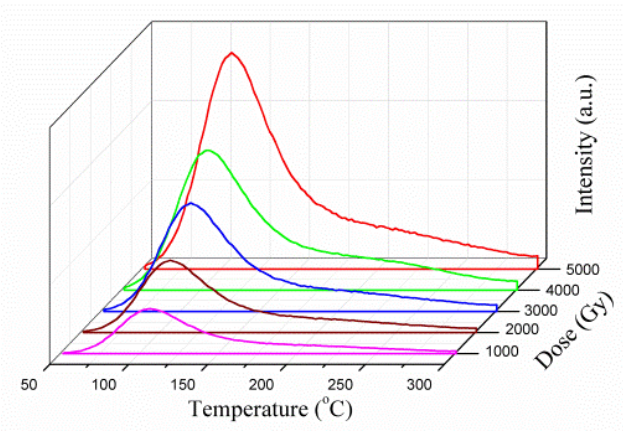

Figure 11. Thermoluminescence glow curves of the phosphor.

region. This straight line character of the graph in the high energy region is a good evidence of the direct band gap. So the band gap was therefore determined by extrapolating the linear portion of the plot relating, $(\alpha h\nu)^2$ vs. hν to $(\alpha h\nu)^2 = 0$. The optical band gap of the phosphor was obtained nearly 5.45 eV.

The Kubelka-Munk theory was used to calculate the band gap of double molybdate phosphor using diffuse reflectance spectrum [15,16]. In a diffuse reflectance spectrum, the ratio of the light scattered from a thick layer of sample and an ideal non-absorbing reference sample is measured as a function of the wavelength λ , $R_{\infty}= R_{sample} /R_{reference}$. The relation between the diffuse reflectance of the sample (R_{∞}), absorption coefficient (K) and scattering coefficient (S) is given by the Kubelka-Munk function $F(R_{\infty})$:

$$F(R_{\infty}) = \frac{(1-R_{\infty})^2}{2R_{\infty}} = \frac{K}{S} \quad (7)$$

The band gap E_g and linear absorption coefficient α of a material is related through the well-known Tauc relation:

$$\alpha h\nu = C_1(h\nu - E_g)^{1/2} \quad (8)$$

here ν is the photon energy and C_1 is a proportionality constant. When the material scatters in perfectly diffuse

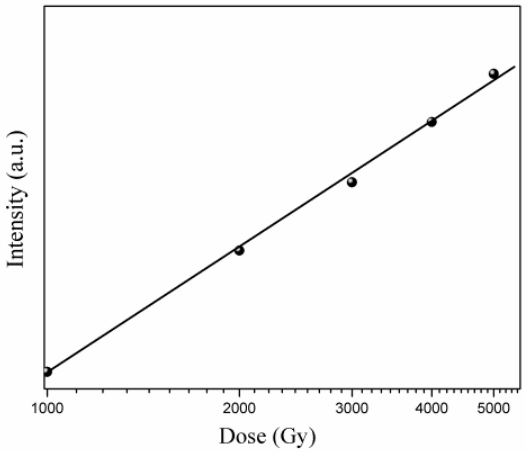

Figure 12. TL-dose response curve of the phosphor.

manner (or when it is illuminated at 60° incidence), the absorption coefficient K becomes equal to 2α. Considering the scattering coefficient S as constant with respect to wavelength, and using Equations 7 and 8, the following expression can be written:

$$[F(R_{\infty})h\nu]^2 = C_2(h\nu - E_g) \quad (9)$$

From the plot of $[F(R_{\infty})h\nu]^2$ versus hν, the value of E_g was obtained by extrapolating the linear fitted regions to $[F(R_{\infty})h\nu]^2 = 0$. The curve of Figure 10 exhibits nonlinear and linear portions, which is the characteristic of direct allowed transition. The nonlinear portion corresponds to a residual absorption involving impurity states and linear portion characterizes the fundamental absorption. The band gap calculated from the diffuse reflectance spectra using K-M function $F(R_{\infty})$ was found to be 5.85 eV.

As the absorption peak is not well resolved, the use of derivative of absorption spectra for calculating the band gap does not guarantee the exact estimation of band gap and can lead to erroneous conclusions. Diffuse reflectance takes advantage of the enhanced scattering phenomenon in powder materials and so the bandgap calculated from diffuse reflectance spectra is more reliable [16].

3.2.4. Thermoluminescence

Thermoluminescence glow curves of $Na_5Dy(MoO_4)_4$ phosphor were recorded after the irradiation by γ-rays with different doses at a constant heating rate of 5ºC/s and is shown in Figure 11. The phosphor was irradiated with different gamma doses ranging from 1 KGy-5 KGy to see the dose dependence of the glow curves. The gamma radiated glow curves exhibit a single glow peak at around 107°C with a variation of ±1°C for different gamma doses. The shape of the glow peak did not alter significantly with an increased γ-dose. The only effect observed is the increase in intensity of glow peaks with dose. Incident γ-rays create trapping centers, the number of which increases with increasing dose and thereby increases the intensity of glow peaks. These traps release the charge carriers on thermal simulation to finally recombine with their counterparts, thus giving rise to different glow peaks [17]. The variation in the intensity of glow peaks with irradiation dose is shown in Figure 12. The peak height increases almost linearly with the increase of irradiation dose.

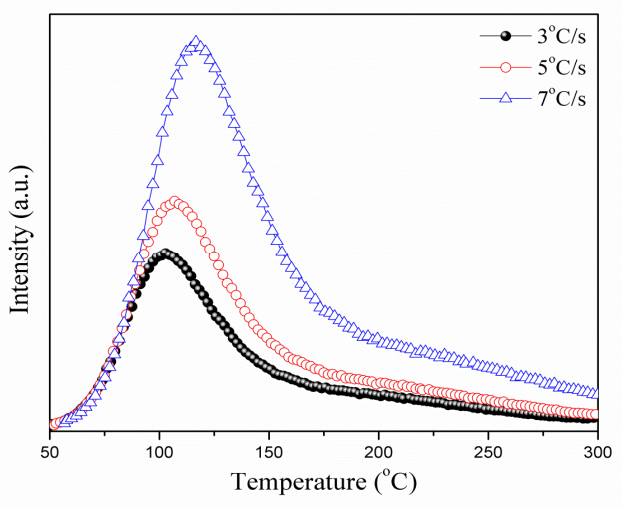

Figure 13. Thermoluminescence glow curves at different heating rates.

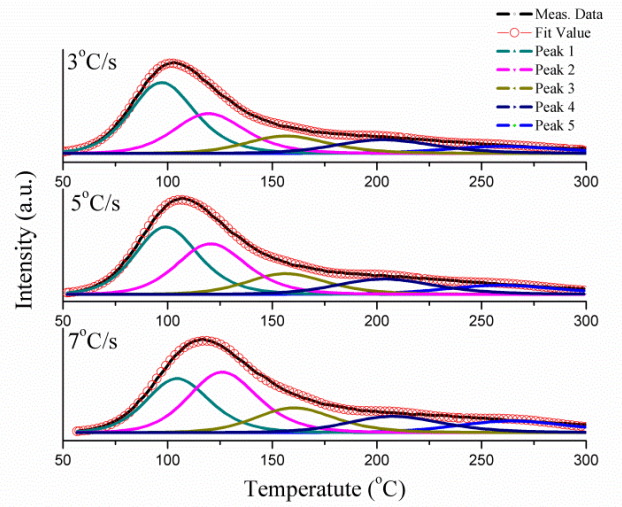

Figure 14. Deconvoluted glow curves at different heating rates.

Figure 13 shows the glow curve of the double molybdate phosphor, at different heating rates (3ºC/s, 5ºC/s, 7ºC/s) for the gamma dose of 5 KGy. The shift in peak temperature of the glow peaks was observed around 7ºC with heating rates and the peak shifts towards higher temperature.

Calculation of trapping parameters

Trapping is a fundamental process of energy storage in almost all electronically active solids. This energy storage is accompanied by the spatial localization of an excited electron or hole in such a way that the charge carrier is prohibited from moving freely through the crystal unless supplied with thermal or optical energy. The information regarding the trapping levels (namely trap depth E and frequency factor s) can be obtained by thermoluminescence (TL) measurements, in which, irradiation transfers charge carriers to their respective traps [18]. Hence, trapping parameters of trap levels are investigated by different methods.

It is observed that the trap depth can only be calculated with prior knowledge of order of kinetics that the system follows. According to Chen [19] method the shape of glow curve acts as a deciding factor for the kinetic order. This method utilizes the following shape parameters to determine the order of kinetics: the total half intensity width ($\omega = T_2 - T_1$) and the high temperature half width ($\delta = T_2 - T_m$). Here T_m is the peak temperature, T_1 and T_2 are the temperatures on either side of T_m corresponding to half peak intensity. A symmetry factor (μ_g) was introduced to differentiate between first and second order TL glow peaks:

Table 3. Shape parameters of the composite glow peaks.

Heating rate (β)	$\tau = T_m - T_1$	$\delta = T_2 - T_m$	$\omega = T_2 - T_1$	μ_g
3	22	32	54	0.59
5	22	33	55	0.60
7	25	36	61	0.58

$$\mu_g = \delta/\omega = (T_2 - T_m)/(T_2 - T_1) \quad (10)$$

$\mu_g = 0.42$ for first order kinetics

$\mu_g = 0.52$ for second order kinetics

In the present case, the value of μ_g at three different heating rates of the phosphor was found to be greater than 0.52 which confirms that the peaks are composite. So, deconvolution of the peaks was performed. The values of shape parameters are given in Table 3.

Computerized glow curve deconvolution (CGCD)

The recorded glow curves of the double molybdate phosphor exposed to 5KGy gamma radiation with different heating rates 3, 5 and 7º C/s were deconvoluted by TLanal computer program [20] in order to obtain the isolated peaks. The trapping parameters of trap states were then determined for each deconvoluted peak by this program. The fitted TL glow curves at the different heating rates are shown in the Figure 14. The order of kinetics for each deconvoluted peaks was found to be second order (b = 2). The trapping parameters of the five deconvoluted peaks for the phosphor at heating rates (β) 3, 5 and 7 ºC/s calculated by Tlanal program are summarized in Table 4.

Glow curve shape methods

The various methods based on the shape of the glow curve were used to verify the above calculated trap depth (E). General formulae [21] for calculating trap depth by these methods are given by:

$$E_\gamma = c_\gamma \left(k\frac{T_m^2}{\gamma}\right) - b_\gamma (2kT_m) \quad \text{(Chen)} \quad (11)$$

$$E_\gamma = c_\gamma \frac{kT_mT_1}{\gamma} \quad \text{(Grossweiner)} \quad (12)$$

$$E_\gamma = c_\gamma \frac{kT_m^2}{\gamma} \quad \text{(Luschik)} \quad (13)$$

where γ in all the equations is τ, δ or ω. The constants c_γ and b_γ for the three methods for second order kinetics are given in Table 5.

Table 4. Trapping parameters by CGCD method.

β (°C/s)	Peak 1		Peak 2		Peak 3		Peak 4		Peak 5		FOM (%)
	E (eV)	s(s^{-1}) x10^{14}	E (eV)	s (s^{-1}) x10^{14}	E (eV)	s (s^{-1}) x10^{13}	E (eV)	s (s^{-1}) x10^{11}	E (eV)	s (s^{-1}) x10^{10}	
3	1.09	2.03	1.12	0.5	1.14	0.45	1.15	2.75	1.19	2.89	2.48
5	1.13	8.08	1.14	1.73	1.16	1.63	1.18	7.84	1.23	9.58	2.05
7	1.15	15.8	1.18	4.74	1.21	6.59	1.23	32.5	1.26	20.9	1.83

Table 5. Values of constants used in the equations of glow curve shape methods.

Chen			Grossweiner			Luschik		
c_τ=1.81	c_δ=1.706	c_ω=2.52	c_τ=1.68	c_δ=1.8313	c_ω=3.5217	c_τ=1.5651	c_δ=3.2808	c_ω=1.706
b_τ=2.00	b_δ= 0	b_ω=1						

Table 6. Trap depths (E) by glow curve shape methods.

Methods	Peak 1			Peak 2			Peak 3			Peak 4			Peak 5		
	3	5	7	3	5	7	3	5	7	3	5	7	3	5	7
Chen	1.06	1.14	1.14	1.10	1.12	1.17	1.09	1.15	1.19	1.11	1.13	1.19	1.16	1.21	1.22
Grossweiner	1.05	1.13	1.16	1.11	1.19	1.16	1.05	1.06	1.23	1.14	1.15	1.21	1.17	1.20	1.19
Luschik	1.04	1.12	1.11	1.08	1.09	1.15	1.09	1.14	1.18	1.10	1.12	1.18	1.16	1.21	1.22

Table 7. Frequency factor (s) by glow curve shape methods.

Methods	Peak 1			Peak 2			Peak 3			Peak 4			Peak 5		
	3	5	7	3	5	7	3	5	7	3	5	7	3	5	7
Chen	7.4 x 10^{15}	1.36 x 10^{15}	1.15 x 10^{15}	3.49 x 10^{13}	9.79 x 10^{13}	3.63 x 10^{14}	1.22 x 10^{12}	10.1 x 10^{12}	3.68 x 10^{13}	1.01 x 10^{11}	2.63 x 10^{11}	1.30 x 10^{12}	1.29 x 10^{10}	7.07 x 10^{10}	9.02 x 10^{10}
Gross-weiner	5.4 x 10^{15}	0.98 x 10^{15}	2.17 x 10^{15}	4.74 x 10^{13}	82.9 x 10^{13}	2.69 x 10^{14}	0.4 x 10^{12}	0.82 x 10^{12}	11.1 x 10^{13}	2.17 x 10^{11}	4.37 x 10^{11}	1.30 x 10^{12}	1.62 x 10^{10}	5.63 x 10^{10}	7.20 x 10^{10}
Luschik	3.9 x 10^{15}	0.71 x 10^{15}	0.44 x 10^{15}	1.89 x 10^{13}	3.92 x 10^{13}	1.99 x 10^{14}	1.22 x 10^{12}	7.62 x 10^{12}	2.78 x 10^{13}	0.78 x 10^{11}	19.9 x 10^{11}	1.01 x 10^{12}	1.29 x 10^{10}	0.91 x 10^{10}	9.02 x 10^{10}

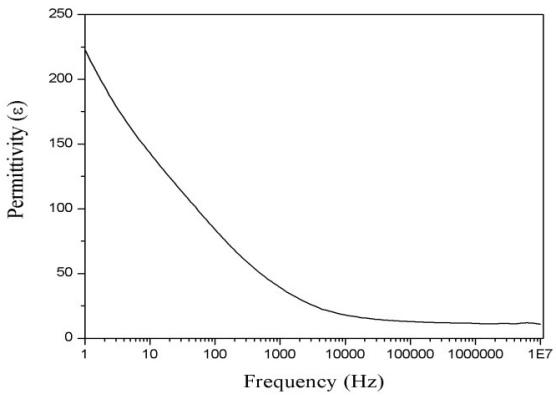

Figure 15. Plot of permittivity with frequency.

Frequency factor (s) was calculated by Chen and Winer equation [22]:

$$\frac{\beta E}{kT_m^2} = s\left[1+(b-1)2\frac{KT_m}{E}\right]\exp\left(\frac{-E}{kT_m}\right) \quad (14)$$

where s is the frequency factor and β is the heating rate. The values of trap depths and frequency factors calculated by the above glow curve shape methods are summarized in Table 6 and 7 respectively.

The arbitrary change in frequency factor indicates the dependency of frequency factor on temperature described by the relation as [23]:

$$s(T) = s_o T^a;\ -2 \le a \le 2 \quad (15)$$

where s_o is a constant having unit of sec^{-1} K^{-a} and a is the temperature exponent.

3.3. Dielectric studies

An important feature of the phosphor material to be used in optoelectronic devices is that the material should preferably have a high dielectric constant and low dielectric loss. The various dielectric parameters such as permittivity, dielectric loss and a.c. conductivity were studied as a function of frequency.

Permittivity

The variation of permittivity with frequency for the molybdate phosphor is shown in the Figure 15. High dielectric constant was observed in the frequency range upto 10^3 Hz and beyond which it was found to be stable. This was due to the

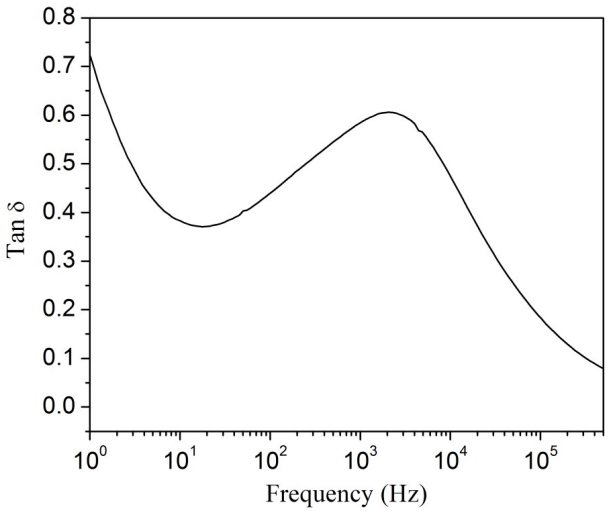

Figure 16. Plot of dielectric loss with frequency.

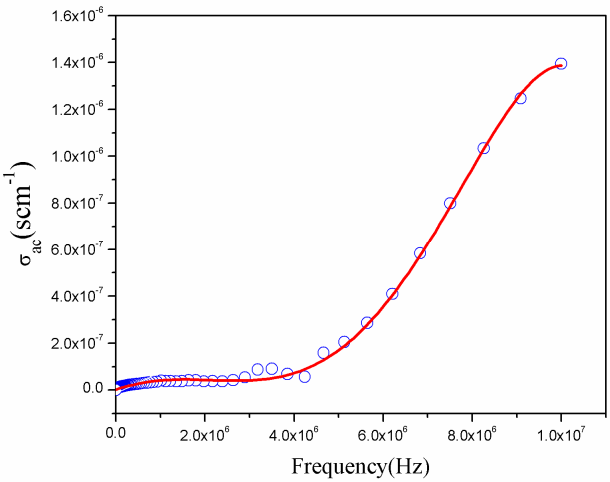

Figure 17. Plot of A.C. conductivity with frequency.

presence of rotational and space charge polarizations in the low frequency region [24].

Dielectric loss

From Figure 16, it was observed that the dielectric loss (tan δ) decreases with the increase in frequency. The high losses in lower frequency range are due to space charge polarization relaxation [17]. The existence of peak near 1 KHz suggests the presence of relaxing dipoles in this phosphor [25]. The low loss at the high frequency region implies that this material can be used for the high frequency applications.

A. C. conductivity

The a.c. conductivity pattern (Figure 17) shows frequency independent plateau in the low frequency region and exhibits dispersion at the higher frequencies. This behaviour follows the polynomial relation:

$$\sigma(\omega) = \sigma_0 + \sigma_1\omega + \sigma_2\,\omega^2 + \sigma_3\,\omega^3 + \sigma_4\,\omega^4 + \sigma_5\,\omega^5 \qquad (16)$$

where σ_0 is the dc conductivity which is frequency independent specially in the low frequency region, σ_i (i= 1-5) are the pre-exponential factor [26].

4. Conclusions

A new yellow emitting phosphor was successfully synthesized using solid state reaction method. The wide optical band gap of the phosphor indicates its application in various optoelectronic devices. The simple and sharp glow peaks of the phosphor and good linear behavior of TL dose response indicates that the prepared phosphor may have application as thermoluminescence dosimeter (TLD). All the deconvoluted peaks were found to obey second order kinetics indicating the occurrence of retrapping phenomena. The trapping parameters calculated by both the methods show a close agreement. Moreover, the dielectric studies indicate that the phosphor may have application in making display devices, which are more resistive to high frequency damages.

Acknowledgments

The authors are thankful to Department of Science and Technology, New Delhi (Government of India) for funding this work under the Project SR/ FTP/ PS-087/2010. The authors are also thankful to Dr. S. K. Rout, BIT Mesra for dielectric measurements.

References

1. R. Singh, S. J. Dhoble, Bull. Mater. Sci. 34 (2011) 557.
2. V. Morozov, A. Arakcheeva, B. Redkin, V. Sinitsyn, S. Khasanov, E. Kudrenko, M. Raskina, O. Lebedev, G. Van Tendeloo, Inorg. Chem. 51 (2012) 5313.
3. S. Som, A. Choubey, S. K. Sharma, Physica B 407 (2012) 3515.
4. A. P. A. Marques, M. T. S. Tanaka, E. Longo, E. R. Leite, I. L. V. Rosa, J. Fluoresc. 21 (2011) 893.
5. N. Xue, X. Fan, Z. Wang, M. Wang, Mater. Lett. 61 (2007) 1576.
6. Wei-Wei Zhou, Bo Wei, Wang Zhao, Guo-Fu Wang, Xia Bao, Yong-Hong Chen, Feng-Wu Wanga, Jian-Ming Du, Hai-Jun Yu, Opt. Mater. 34 (2011) 56.
7. Kh. M. Kadiev, A. M. Gyul'maliev, M. Ya. Shpirt, and S. N. Khadzhiev, Pet. Chem. 50 (2010) 312.
8. B. D. Cullity, Elements of X- Ray Diffraction (3rd ed.), Addison-Wesley Publishing Company, USA (1956).
9. P. Singh, A. Kumar, A. Kaushal, D. Kaur, A. Pandey, R. N. Goyal, Bull. Mater. Sci. 31 (2008) 573.
10. Z. Lin-Li, G. Chang-Xin, Z. Jun-Jing and H. Jun-Tao, Chin. Phys. Lett. 22 (2005) 1225.
11. A. Vij, R. Kumar, A. K. Chawla, S. P. Lochab, R. Chandra N. Singh, Opt. Mater. 33 (2010) 58.
12. D. Gao, Y. Li, X. Lai, Y. Wei, J. Bi, Y. Li, M. Liu, Mater. Chem. Phys. 126 (2011) 391.
13. M. Jayasimhadri, B. V. Ratnam, K. Jang, H. S. Lee, B. Chen, S. -S. Yi, J. -H. Jeong, L. R. Moorthy, J. Am. Chem. Soc. 93 (2010) 494.
14. A. Choubey, S. Som, R. Kumari, S. K. Sharma, Mod. Phys. Lett. B 25 (2011) 685.
15. J. H. Ryu, B. G. Choi, J. -W. Yoon, K. B. Shim, K. Machi, K. Hamada, J. Lumin. 124 (2007) 67.
16. A. E. Morales, E. S. Mora, U. Pal, Revista Mexicana de F´isica S 53 (2007) 18.
17. A. Choubey, S. K Sharma, S. P. Lochab, D. Kanjilal, J. Phys. Chem. Solids 72 (2011) 136.

18. S. S. Pitale, S. K. Sharma, R. N. Dubey, M. S. Qureshi, M. Manzar Malik, Opt. Mater. 31 (2009) 923.
19. R. Chen, S. W. S. McKeever, Theory of thermoluminescence and related phenomena, World Scientific Publishing (1997).
20. K. S. Chung, H. S. Choe, J. I. Lee, J. L. Kim, S. Y. Chang, Radiat. Prot. Dosim. 115 (2005) 345.
21. C. Furetta, Handbook of thermoluminescence (1st ed.), World Scientific Publishing (2003).
22. R. Chen, S. A. A. Winer, J. Appl. Phys. 40 (1970) 5227.
23. M. Karmakar, B. Sarkar, Sk. Azharuddin, P. S. Mazumdar, S. D. Singh, W. S. Singh, M. Bhattacharya, Indian J. Phys. 84 (2010) 529.
24. C. R. Indulal, G. S. Kumar, A. V. Vaidyan, R. Raveendran, Indian J. Pure Appl. Phys. 48 (2010) 893.
25. S. K. Rout, S. Panigrahi, P. K. Barhai, I. W. Kim, J. Electroceram. 23 (2009) 37.
26. D. K. Pradhan, R. N. P. Choudhary, B. K. Samantaray, Int. J. Electrochem. Sci. 3 (2008) 597.

Cite this article as:

S. Dutta *et al.*: **Synthesis and characterization of yellow light emitting $Na_5Dy(MoO_4)_4$ double molybdate phosphor.** *Phys. Express* 2013, **3**: 24

Theoretical study of velocity of sound in cuprates in normal state

K. C. Bishoyi[a,*], S. P. Mohapatra[b], G. C. Rout[c]

[a] *N. C. College (Autonomous), Jajpur - 755001, India*
[b] *Anandapur College, Anandapur - 758021, India*
[c] *Condensed Matter Physics Group P. G. Dept. of Applied Physics and Ballistics, F. M. University, Balasore - 756019, India*

[*] *Author for correspondence: K. C. Bishoyi, email: bishoyi@iopb.res.in*
Received 15 Sep 2012; Accepted 26 Oct 2012; Available Online 26 Oct 2012

Abstract

We address a microscopic theoretical calculation of temperature dependence of velocity of sound in cuprates in normal state in under-doped region. The model Hamiltonian contains the anti-ferromagnetism (AFM) in the conduction band, the hybridization between the conduction and f-electrons and the impurity atom kinetic energy. Here the phonon is coupled to the hybridization between the conduction electrons and the f-electrons of the system in presence of bare phonon energy. The Green's functions are calculated by Zubarev's technique from which the velocity of sound is calculated and studied in the finite temperature limit taking into account the temperature dependence of AFM. It is observed that the velocity of sound decreases (or softens) from a higher temperature upto Néel temperature (T_N) in the paramagnetic phase. The velocity of sound shows a sharp fall at T_N and decreases further, as temperature is lowered in the AFM phase. The effect of electron-phonon (e-p) coupling, the position of f-electron level and hybridization on velocity of sound is reported.

Keywords: Anti-ferromagnetism; Electron-phonon interaction; High-T_c superconductors

1. Introduction

The ultrasonic measurement is a sensitive technique to probe all kinds of phase transitions including superconductivity, magnetic and structural ones in condensed matter physics. The temperature dependent sound velocity has been measured for high-T_c systems both in normal and superconducting states for different values of frequencies and applied fields [1-4]. The longitudinal sound velocity shows softening effects due to phonon coupling to the sound velocities. Zhang et. al. [5] have measured the sound velocity as a function of temperature. The ultrasonic measurements on $YBa_2Cu_3O_{7-x}$ shows an inflation at nearly 235K indicating the characteristic of a phase transition [6]. In $La_{1-x}Ba_xCuO_4$ (x=0.15), a phase transition from tetragonal to orthorhombic phase has been observed at 180K by neutron scattering experiment [7] and a drastic decrease in sound velocity at 24 MHz due to structural phase transition has also been observed [8]. The ultrasonic peak and minimum in sound velocity are indicated in the non-superconducting sample Nd-Ce-Cu-O at 260K [9] and a similar behaviour of ultrasonic attenuation is shown to exit in La-Sr-Cu-O at 200K [10]. The role played by the electron-phonon (e-p) interaction in high-T_c superconductors is much debated. Hence it is important to study both experimentally and theoretically the velocity of sound for a wide range of frequencies and magnetic fields in order to evaluate the strength of the electron-phonon coupling and to test various models. Several phenomenological relaxation models have been proposed to explain the ultrasonic anomalies. Recently, Rout. et al. [11] have proposed a microscopic model consisting of charge density wave and spin density wave interactions to explain the ultrasonic anomaly in normal state of the high-T_c superconductors. Earlier Rout and co-authors [12, 13] have reported a model study of temperature dependent velocity of sound based upon a model consisting of antiferromagnetism and impurity f-electron interactions in presence of the hybridization between the conduction and f-electrons. In the present communication, we apply the same model to investigate the anomaly in the velocity of sound below the anti-ferromagnetic transition temperature in the normal state of the high-T_c superconductors by taking into consideration the role of temperature dependent staggered field. The formalism of the model is described in Section 2. The velocity of sound is calculated in Section 3, while Section 4 has been devoted to results and discussion. Finally, we conclude the paper in Section 5.

2. Formalism

The anti-ferromagnetic (AFM) spin fluctuations are present in the two dimensional Cu-O planes of the high-T_c systems due to the conduction electrons below the Néel temperature. Since the exchange interactions between the rare earth ions and their nearest neighbour Cu ions cancel because of the AFM alignment of Cu spins, we consider here the next nearest neighbour hybridization between the conduction and impurity f-electrons; besides the f-electron kinetic energy term in the doped systems, the AFM long range order is destroyed due to doping. In order to study the elastic properties, we consider the phonon interaction only to the hybridization between the conduction and f-electron for simplicity of calculation.

Based upon the earlier model [13], the pure electronic Hamiltonian is written as

$$H_0 = H_d + H_s + H_v + H_f \quad (1)$$

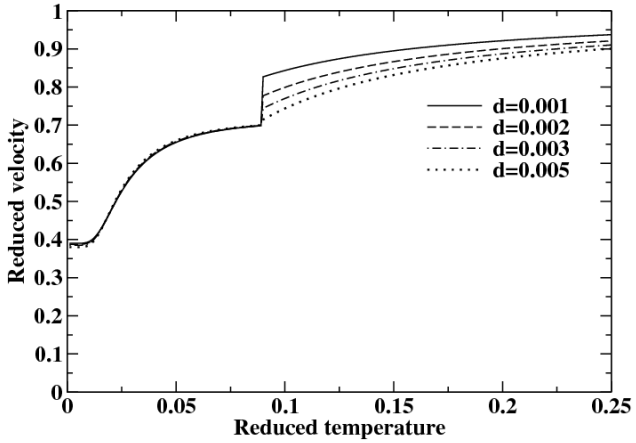

Figure 1. The plot of reduced velocity ($\tilde{v}$) vs. reduced temperature (t) for different values of the position of f-electron level d=0.001, 0.002, 0.003, 0.005 and for fixed values of spectral width e=0.001, bare phonon frequency p=0.1, e-p coupling s=0.0032, hybridization strength v=0.075, static ultrasonic frequency c=0, anti-ferromagnetic coupling g_1=0.1.

The first term represents the kinetic energy interaction between the electrons due to two different types of staggered lattices with band energy dispersion of $\varepsilon_0(k) = -2t_0(cosk_x + cosk_y)$, where t_0 is the nearest neighbour hopping integral. Here $a^{\dagger}_{k,\sigma}$ is the creation operator of the conduction electron at one lattice site with spin up and $b^{\dagger}_{k,\sigma}$ is the creation operator at another lattice site electron with spin down. The second term represents the staggered magnetic field interaction with AFM staggered field, where σ stands for +1 (-1) for spins up (down). The third term stands for the hybridization between the electrons with operators a and b and the impurity f-electron, where V is the momentum independent hybridization strength. The last term represents the kinetic energy term for the impurity f-electrons with impurity f-electron level at ε_f. The Fourier transformed phonon interaction to the hybridization is written as

$$H_{e-p} = \Sigma_{k,q,\sigma} f(q)\left[\left(a^{\dagger}_{k+q,\sigma} f_{k,\sigma} + b^{\dagger}_{k+q,\sigma} f_{k,\sigma}\right) + h.c\right] A_q \quad (2)$$

where $A_q = b_q + b^{\dagger}_{-q}$, with $b^{\dagger}_q(b_q)$ is the creation (annihilation) phonon operator with wave vector q. Here f(q) is the electron-phonon (e-p) coupling constant. The free phonon Hamiltonian in harmonic approximation is written as $H_p = \Sigma_q \omega_q b^{\dagger}_q b_q$, where ω_q is the phonon energy.

3. Expression for velocity of sound

Phonon Green's function involving phonon displacement at two different times is calculated by using Zubarev's Green's function technique [14]. Applying Dyson's approximation the phonon Green's function in general appears in closed form as

$$D_{qq}(\omega) = \frac{\omega_q}{\pi}\left[\omega^2 - \omega_q^2 - \Sigma(q,\omega)\right]^{-1} \quad (3)$$

where the phonon self energy is written as

$$\Sigma(q,\omega) = 4\pi f^2(q)\omega_q \chi_{qq}(\omega). \quad (4)$$

The electron response function $\chi_{qq}(\omega)$ is written as

$$\chi_{qq}(\omega) = \Sigma_{k,\sigma}[\chi_1 + \chi_2 + \chi_3 + \chi_4] \quad (5)$$

Here the χ_i(i=1,2,3,4) are the two particle electron's Green's functions involving only conduction electrons, pure impurity f-electrons and a mixture of conduction and f-electrons. The calculation of these Green's functions involve other higher order Green's functions. In order to simplify the calculation, the approximations are taken such that the terms upto V^2 are retained without loss of much physics. Finally the denominator of the phonon Green's function given in equation (3) is equated to zero to get

$$\omega^2 - \omega_q^2 - Re\Sigma(q,\omega) = 0 \quad (6)$$

In the long wavelength limit $(q \to 0)$, we find $\omega = vq$ and $\omega_0 = v_0 q$ and finally the expression for the reduced velocity ($\tilde{v}$) can be written as

$$(\tilde{v})^2 = \left(\frac{v}{v_0}\right)^2 = 1 + Re\Sigma(\omega, q = 0) \quad (7)$$

The different dimensionless parameters are scaled with respect to $2t_0$ and are written as: e-p coupling $s = f^2(0)N(0)/\omega_0$, the position of f-electron level $d = \varepsilon_f/2t_0$, the hybridization strength v = $V/2t_0$, the staggered field $h_1 = h/2t_0$, the temperature $t = k_B T/2t_0$, the ultrasound frequency $c = \omega/2t_0$, the spectral width $e = \eta/2t_0$ and the bare phonon frequency $p = \omega_0/2t_0$.

4. Results and Discussion

At the outset, we calculate the temperature dependent staggered field defined as $h = \Sigma_{k,\sigma}\sigma[\langle a^{\dagger}_{k,\sigma} a_{k,\sigma}\rangle - \langle b^{\dagger}_{k,\sigma} b_{k,\sigma}\rangle]$ and compute numerically its (h_1) temperature dependent behaviour. Incorporating the temperature dependence of h_1 and other physical parameters in the velocity of sound, we plot the temperature dependence of velocity of sound and discuss the results. Figure 1 shows the temperature dependence of reduced velocity for different values of the position of the f-electron level (d). For a given value of d, as temperature is decreased the reduced velocity decreases in the paramagnetic phase from $\tilde{v}$ =1 at $t = \infty$ upto the Néel temperature $t_N \approx 0.1$. The reduced velocity sharply drops to a lower value at t_N and then gradually decreases towards lower temperatures and reaches a minimum value at temperature t=0 for a given set of parameters. Similar temperature dependence of velocity of sound is observed experimentally for non-superconducting $Nd_{2-x}Ce_xCuO_{4-y}$ compound both in cooling and heating conditions [9]. The frequency and doping effects on the temperature dependent velocity of sound in the superconducting phase of the cuprate systems is in progress and will be reported elsewhere. As f-level position is increased above the Fermi level i.e., from d=0.001 to d=0.005, the velocity of sound is suppressed in the paramagnetic phase upto t_N. It is further observed that the sudden jump is reduced with increase of d. The velocity of sound is slightly increased in the low temperature AFM phase, when d is increased. Figure 2 shows the effect of hybridization on the velocity of sound. When the strength of hybridization increases, the impurity f-electrons are strongly hybridized with the conduction

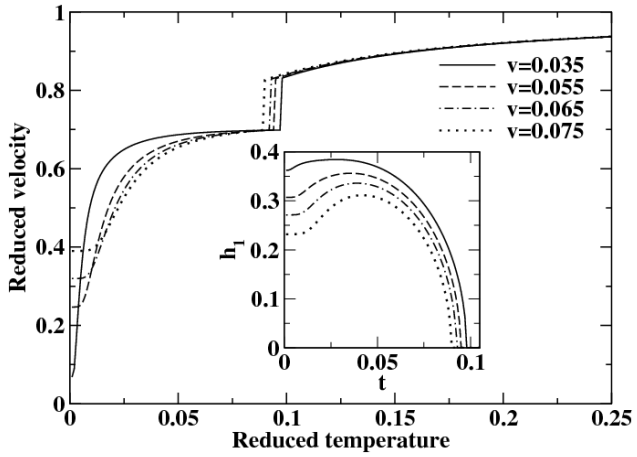

Figure 2. The plot of reduced velocity ($\tilde{v}$) vs. reduced temperature (t) for different values of the hybridization strength v=0.035, 0.055, 0.065, 0.075 and for fixed values of e=0.001, p=0.1, s=0.0032, d=0.001, c=0, g_1=0.1. The inset shows the self-consistent plot of the staggered field (h_1) vs. reduced temperature (t) for the values of the parameters mentioned above.

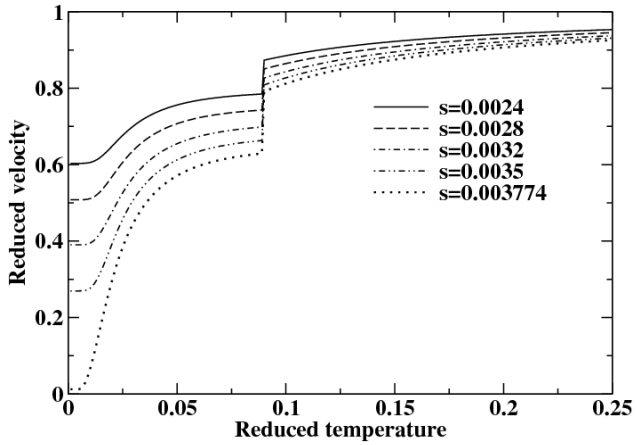

Figure 3. The plot of reduced velocity ($\tilde{v}$) vs. reduced temperature (t) for different values of e-p coupling s=0.0024, 0.0028, 0.0032, 0.0035, 0.003774 and for fixed values of e=0.001, p=0.1, d=0.001, v=0.075, c=0, g_1=0.1.

electrons. As a result, the long range AFM is destroyed and the AFM Néel temperature is suppressed. The similar effect is observed in the temperature dependent velocity of sound. The hybridization has no effect at high temperature paramagnetic phase except near the Néel temperature t_N. With the increase of hybridization, Néel temperature is suppressed as shown in Figure 2. Further, the velocity of sound is suppressed at low temperatures with increase of the strength of hybridization. Figure 3 shows the effect of e-p coupling (s) on the temperature dependent velocity of sound. The increase of e-p coupling implies the electrons are strongly coupled to the crystal lattice. With the increase of e-p coupling the velocity of sound is suppressed throughout the temperature range. However, the suppression of velocity of sound is more in low temperature AFM phase than the high temperature paramagnetic phase. Further, the sharp depression at Néel temperature is also more for the higher values of the e-p coupling. Figure 4 shows the effect of AFM coupling (g_1) on the velocity of sound. With increase of AFM coupling, the staggered field h_1 is enhanced throughout the temperature

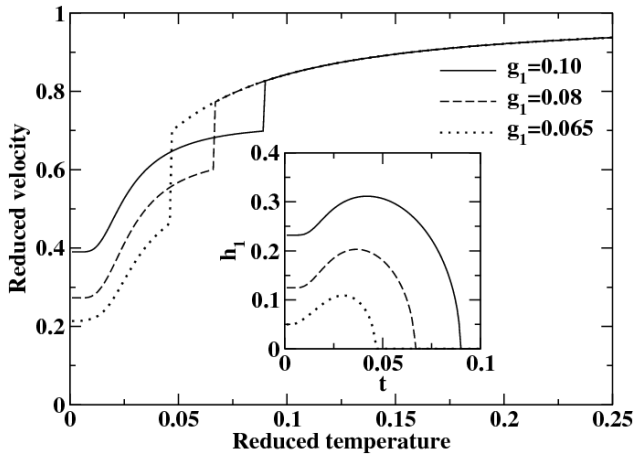

Figure 4. The plot of reduced velocity ($\tilde{v}$) vs. reduced temperature (t) for different values of anti-ferromagnetic coupling g_1=0.065, 0.08, 0.1 and for fixed values of e=0.001, p=0.1, c=0, s=0.0032, d=0.001, v=0.075. The inset shows the self-consistent plot of the staggered field (h_1) vs. reduced temperature (t) for the values of the parameters mentioned above.

range resulting in the enhancement of Néel temperature t_N. These results are observed in temperature dependent velocity of sound. The AFM coupling has great bearing on the velocity of sound at low temperature AFM phase. With increase of AFM coupling the velocity of sound increases throughout the temperature range in AFM phase and simultaneously the Néel temperature is shifted towards high temperature.

5. Conclusions

We have proposed a model consisting of AFM interaction due to the conduction electrons besides the hybridization between the conduction electrons and the impurity f-electrons. For simplicity, phonon coupling to the hybridization is considered and the velocity of sound is calculated from the phonon Green's function. The effect of position of f-level, hybridization, the e-p coupling and AFM coupling are investigated to explain the sharp depression at Néel temperature and the suppression of velocity of sound in the low temperature AFM phase of the high-T_c system in normal phase.

Acknowledgements

The authors gracefully acknowledge the research facilities offered by the Institute of Physics, Bhubaneswar, India during their short stay.

References

1. Y. Horie, T. T. Fukami, S. Mose, Physica B 165-166 (1990) 1277.
2. M. Nohara, T. Suzuki, Y. Maeno, T. Fujita, I. Tanaka, H. Kojima, Physica B 185-189 (1991) 1397.
3. M. Nohara, S. Nishigori, T. Suzuki, Y. Maeno, T. Fujita, I. Tanaka, H. Kojima, Physica B 194-196 (1994) 2167.
4. Y. Satoh, M. Yamaguchi, M. Suzuki, Y. Yokuda, Y. Hidaka, Physica C 185-189 (1991) 1381.
5. H. Zhang, M. J. McKenna, Carsten Hucho, B. K. Sarma, Moises Levy, T. Kimura, K. Kisho, K. Kitazawa, Physica B 223-224 (1996) 554.

6. G. Canneli, R. Cantelli, F. Cordero, G. A. Costa, M. Ferretti, G. L. Olcesc, Phys. Rev. B. 36 (1987) 8907.
7. D. McK. Paul, G. Balakrishnan, N. R. Bernhoeft, W. I. F. David, W. T. A. Harrison, Phys. Rev. Lett. 58 (1987) 1976.
8. K. Fossheim, T. Laegreid, E. Sandvold, F. Vassenden, K. A. Mueller, J. G. bednorz, Solid State Commun. 63 (1987) 531.
9. He. Yusheng, Sun Xiangzhong, Physica B 165-166 (1990) 1291.
10. J. Y. Prieur et al., Physica B 165-166 (1990) 1285.
11. G. C. Rout, S. K. Panda, Physica C 471 (2011) 121.
12. G. C. Rout, B. N. Panda, S. N. Behera, Solid State Commun. 106 (1998) 469.
13. K. C. Bishoyi, G. C. Rout, S. N. Behera, Physica B 395 (2007) 48.
14. D. N. Zubarev, Sov. Phys. Usp. 95 (1960) 71.

Cite this article as:

K. C. Bishoyi *et al.*: **Theoretical study of velocity of sound in cuprates in normal state.** *Phys. Express* 2013, **3**: 25

Effect of staggered field on the temperature dependent ultrasonic attenuation in cuprates

S. P. Mohapatra[a,*], K. C. Bishoyi[b], G. C. Rout[c]

[a] *Anandapur College, Anandapur - 758021, India*
[b] *N. C. College (Autonomous), Jajpur - 755001, India*
[c] *Condensed Matter Physics Group P. G. Dept. of Applied Physics and Ballistics, F. M. University, Balasore - 756019, India*

[*] *Author for correspondence: S. P. Mohapatra, email: shakti@iopb.res.in*
Received 16 Sep 2012; Accepted 26 Oct 2012; Available Online 26 Oct 2012

Abstract

The ultrasonic measurement is an important experimental technique to study the elastic properties of the condensed matter systems. We present here a microscopic theoretical model to study the effect of staggered magnetic field on the temperature dependent ultrasonic attenuation coefficient (α). We consider a model Hamiltonian consisting of staggered magnetic field in the conduction band of the cuprate systems. The effect of temperature dependent staggered field on α is investigated. In order to study its effect on the ultrasonic attenuation (α), we have calculated the phonon Green's function. The imaginary part of its self-energy directly gives the attenuation coefficient (α). As temperature is lowered, the attenuation coefficient increases, forms a peak at the Néel temperature (T_N) and then the coefficient α shows large suppression in the anti-ferromagnetic (AFM) phase in the lower temperature region. The effect of the model parameters of the system on α are reported in the present communication.

Keywords: Anti-ferromagnetism; Electron-phonon interaction; High-T_c superconductors

1. Introduction

The ultrasonic measurements are a powerful tool to investigate structural imperfections, phase transformations and electron-phonon (e-p) interaction in solids. The sound waves are absorbed strongly in metals due to the interaction of elastic waves with the conduction electrons. If the metal exhibits anti-ferromagnetism (AFM) the absorption of sound wave markedly decreases below the Néel temperature. Hence high frequency ultrasonic measurements are made on the high-T_c materials to study different phase transitions. The ultrasonic peak and minimum in sound velocity are observed at the the Néel transition temperature T=260K in superconducting sample Nd-Ce-Cu-O [1]. The structural phase transition from orthogonal to tetragonal is observed in La-Sr-Cu-O [2], so that the sound attenuation increases with decreasing temperature and frequency due to phase transition. The ultrasonic measurement on La-Sr-Cu-O shows that the superconducting transition occurs at T_c=37.9K and magnetic phase transition occurs at T_N=27K [2]. The measurements on Tl-Ba-Ca-Cu-O for the temperature range 50-200K shows a sharp drop in ultrasonic attenuation at temperature $T_m \approx 220K$ [3-6] possibly due to distortion of magnetic orders and another sharp drop at superconducting transition temperature T_c120K [4, 6].

The role played by electron-phonon (e-p) interaction in high-T_c superconductors is much debated. Therefore, it is pertinent to perform sound absorption in wide range of frequencies in order to evaluate the strength of e-p coupling and to explain the anomalies observed at different phase transition temperatures in superconducting and normal phases of high-T_c systems. Several theoretical models have been proposed earlier. Recently, Rout. et al. [7] have proposed a model consisting of charge density wave and spin density wave to explain temperature dependent sound velocity in high-T_c systems in normal state. Earlier Rout et al. have proposed a model consisting of AFM interaction in presence of hybridization between conduction and f-electrons to interpret the elastic properties and Raman spectra of cuprates [8, 9]. In the present communication, we apply the same model to investigate the cause of anomaly near the AFM transition temperature in cuprates taking into account the temperature dependence of staggered field (h). The formalism is presented in section 2, the expression for sound attenuation coefficient is given in section 3, while section 4 has been devoted to results and discussion. Finally, we conclude the paper in section 5.

2. Formalism

The low temperature measurements of the specific heat and magnetic susceptibility demonstrate the existence of heavy quasi-particle excitations in the electron doped system Nd-Ce-Cu-O [10]. For impurity concentration x=0.2, the system exhibits heavy fermion behaviour with specific heat coefficient, $\gamma = 4J/(mol - K^2)$. Similar heavy fermion behaviour is observed in other high-T_c systems. In the two dimensional Cu-O planes there exists anti-ferromagnetic fluctuations with Néel temperature $T_N \approx 270K$ for un-doped Nd-Cu-O. Because of next nearest neighbour spin interaction between the spins of copper and rare-earth atoms, the anti-ferromagnetic long range order is destroyed by doping of impurity atoms. To describe the physics of high-T_c cuprates the anti-ferromagnetic fluctuation of the Cu spins are replaced by a static staggered field acting on them. This symmetry breaking field reduces strongly the charge fluctuation between Cu sites and also accounts for the strong correlation in the Cu-O planes. The heavy fermion behaviour can be extracted by a

term containing hybridization between copper 3d and rare-earth 4f orbitals. Such a Hamiltonian [9, 11] is written as

$$H_0 = -t_0\Sigma_{\langle tj\rangle\sigma}(a^\dagger_{i\sigma}a_{j\sigma} + h.c) + h\Sigma_{i,\sigma}\sigma e^{i\vec{Q}.\vec{R_i}}a^\dagger_{i\sigma}a_{i\sigma} + V\Sigma_{i,\sigma}(a^\dagger_{i\sigma}f_{i\sigma} + h.c) + \varepsilon_f\Sigma_{i,\sigma}f^\dagger_{i\sigma}f_{i\sigma} \quad (1)$$

The first term in the Hamiltonian represents the hopping of the conduction electron in the copper oxide plane between the nearest neighbour sites with nearest neighbour hopping integral $2t_0$. The second term in the Hamiltonian represents the staggered field interaction with a phase factor of $\vec{Q}.\vec{R_i}$. The third term shows the hybridization between the itinerant conduction electrons and the localized f-electrons. Finally, the last term represents the onsite hopping between the impurity f-electrons. Here $\vec{Q} = (\pi, \pi)$ is a reciprocal lattice vector, $\vec{R_i}$ denotes the positions of the Cu ions and h is the size of the staggered field. The operators $a^\dagger_{i\sigma}$, $f^\dagger_{i\sigma}$ create an electron in the Cu $3d_{x^2-y^2}$ and rare-earth 4f orbitals respectively. The f-electron energy ε_f and the hybridization strength V are strongly renormalized quantities because of the 4f electron correlations. In order to study the elastic properties of the materials we include an electron-phonon Hamiltonian (H_{e-p}) in which phonons are coupled to only the hybridization between conduction electrons and f-electrons [9]. Finally, the free phonon Hamiltonian in harmonic approximation is given by $H_p = \Sigma_q\omega_q b^\dagger_q b_q$. Here ω_q and $b^\dagger_q$ are the phonon energy and phonon creation operator with phonon wave vector q.

3. Calculation of attenuation coefficient

The double time phonon Green's function of Zubarev [12] technique is defined as

$$D_{q,q'}(t-t') = \ll A_q(t); A_{q'}(t') \gg \quad (2)$$

Applying Dyson's approximation the Fourier transformed phonon Green's function reduces to a closed form as given below.

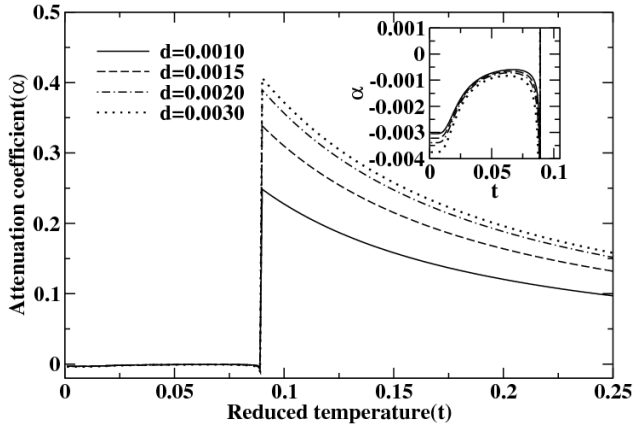

Figure 1. The plot of ultrasonic attenuation coefficient (α) vs. reduced temperature(t) for different values of the position of f-electron level d=0.001, 0.0015, 0.002, 0.003 and for fixed values of spectral width e=0.001, bare phonon frequency p=0.1, e-p coupling s=0.0032, hybridization strength v=0.075 and anti-ferromagnetic coupling $g_1 = 0.1$ in the static limit. The plot of α vs. t in the AFM phase is magnified in the inset for the values of the parameters mentioned above.

$$D_{q,q}(\omega) = \frac{\omega_q}{\pi}[\omega^2 - \omega_q^2 - \Sigma(q,\omega)]^{-1} \quad (3)$$

The phonon self energy is given by

$$\Sigma(q,\omega) = 4\pi f^2(q)\omega_q\chi_{qq}(\omega). \quad (4)$$

where the phonon response function χ involves four two particle electron Green's function which in turn involve higher order Green's functions. In the earlier calculation [8] the authors have considered distinctly two sub-lattices with conduction electron operators $a_{i\sigma}$ and $b_{i\sigma}$ to simulate staggered field effects in copper oxide plane. Hence the phonon response function χ in [8] has involved eight two particle Green's functions instead of four Green's functions in the present case. The complete solution of χ in the present case involves sixteen Green's functions. Hence the Hartree-Fock mean field approximation is applied to simplify the problem. The decoupling schemes are applied to keep second order terms in parameters like f-level position, staggered field, hybridization strength and phonon coupling. The dynamic ultrasonic attenuation coefficient at finite temperature is given by the imaginary part of the self-energy. Mathematically, it is written as

$$\alpha(\omega,T) = -\frac{2\pi}{\omega_0}Im\chi(q=0,\omega). \quad (5)$$

where $\chi(q=0,\omega)$ is the phonon response function for the long wavelength longitudinal phonons ($q \to 0$). Finally, $\chi(q=0,\omega)$ is computed numerically for different model parameters of the system. The dimensionless parameters are scaled with respect to the hopping integral $2t_0$ and are written as e-p coupling, $s = f^2(0)N(0)/\omega_0$, the position of f-level, $d = \varepsilon_f/2t_0$, the hybridization strength, v=$V/2t_0$, the staggered field $h_1 = h/2t_0$, the temperature $t = k_BT/2t_0$, the ultrasound frequency $c = \omega/2t_0$, the bare phonon frequency $p = \omega_0/2t_0$ and the spectral width $e = \eta/2t_0$.

4. Results and Discussion

The temperature dependent ultrasonic attenuation is shown in Figure 1 for different values of the position of the impurity f-electron with respect to the Fermi level ($\varepsilon_F = 0$). With decrease of temperature, the ultrasonic attenuation gradually increases in the paramagnetic phase upto the AFM Néel temperature $t_N \approx 0.088$. Then the ultrasonic attenuation sharply drops to a lower value at the temperature t_N indicating a phase transition from paramagnetic to AFM phase. Similar sharp fall in attenuation coefficient is observed in the ultrasonic sound measurement of Tl-Ba-Ca-Cu-O arising due to lattice distortion accompanied by a distortion of the magnetic order [6]. This is one of the striking features of the phonon coupling properties of the strong correlation systems like high-T_c cuprates [13]. On further decreasing the temperature the attenuation suddenly increases and then slowly decreases towards the low temperature (inset of Figure 1). It is observed that the ultrasonic attenuation is negative in the AFM phase indicating the hardening behaviour of the ultrasound wave. The hardening behaviour in the AFM phase arises since phonon is coupled to the strong magnetic correlation of the electron. When the f-electron level (d) moves away from the

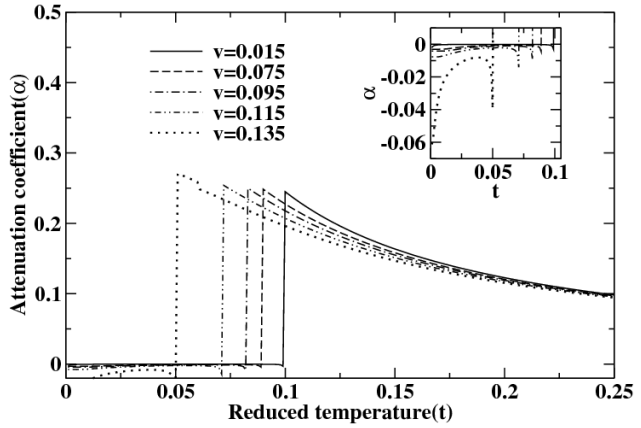

Figure 2. The plot of ultrasonic attenuation coefficient (α) vs. reduced temperature (t) for different values of the hybridization strength v=0.015, 0.075, 0.095, 0.115, 0.135 and for fixed values of e=0.001, p=0.1, s=0.0032, d=0.001 and $g_1 = 0.1$ in the static limit. The plot of α vs. t in the AFM phase is magnified in the inset for the values of the parameters mentioned above.

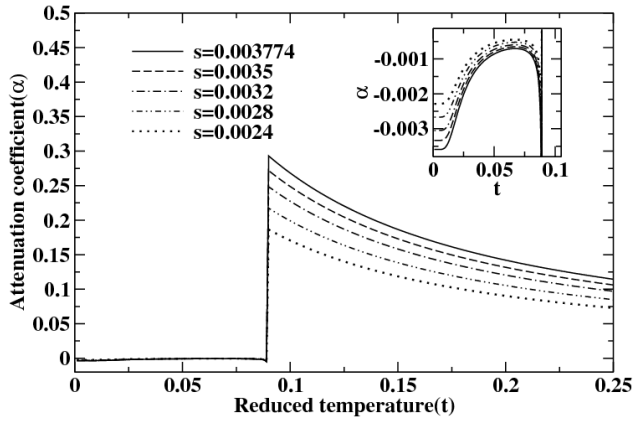

Figure 3. The plot of ultrasonic attenuation coefficient (α) vs. reduced temperature (t) for different values of e-p coupling s=0.0024, 0.0028, 0.0032, 0.0035, 0.003774 and for fixed values of e=0.001, p=0.1, d=0.001, v=0.075 and $g_1 = 0.1$ in the static limit. The plot of α vs. t in the AFM phase is magnified in the inset for the values of the parameters mentioned above.

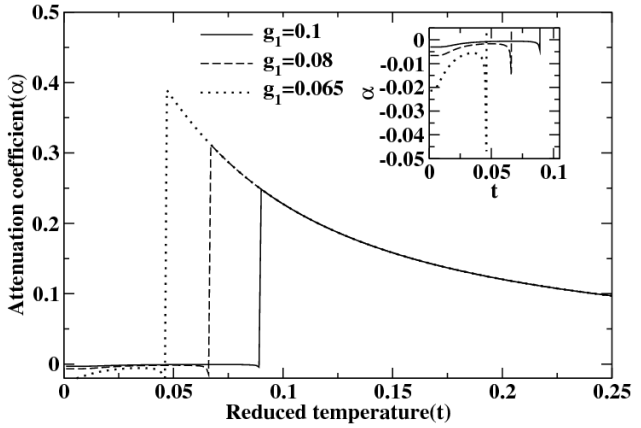

Figure 4. The plot of ultrasonic attenuation coefficient (α) vs. reduced temperature (t) for different values of anti-ferromagnetic coupling $g_1 = 0.065, 0.08, 0.1$ and for fixed values of e=0.001, p=0.1, s=0.0032, d=0.001 and v=0.075 in the static limit. The plot of α vs. t in the AFM phase is magnified in the inset for the values of the parameters mentioned above.

Fermi level in upward direction, the attenuation is enhanced in the paramagnetic phase indicating the weak hybridization of the conduction electrons with the localized f-electrons. On the other hand, with upward shift of the position of f-electron level the attenuation coefficient is reduced in the AFM phase indicating that the staggered field becomes more robust in presence of weak hybridization. However, the effect of shifting the f-electron position is very small in AFM phase than that in the paramagnetic phase. The effect of hybridization between conduction electrons with the localized f-electrons is shown in Figure 2. The increase of the strength of hybridization implies the overlap of the localized f-electron with the conduction electron is more. The increase of hybridization destroys the AFM order and suppresses the AFM Néel temperature as is shown in Figure 2. As the hybridization strength increases from v=0.015 to v=0.135, the Néel temperature is suppressed from t_N=0.1 to 0.05. Further, with increase of hybridization, the ultrasonic attenuation coefficient is suppressed more and more and this is shown clearly in the inset of the Figure 2. Figure 3 shows the effect of electron-phonon interaction (s) on the temperature dependent ultrasonic attenuation. When the phonons are strongly coupled to the electrons, the strength of the e-p interaction increases. As a result, ultrasound energy is absorbed more and more with the increase of the strength of the e-p interaction as is shown in Figure 3. When the e-p interaction increases from s=0.0024 to 0.003774, the attenuation coefficient is enhanced in the high temperature paramagnetic phase. On the other hand the attenuation coefficient is reduced with the increase of e-p coupling in the low temperature AFM phase (inset of Figure 3). Figure 4 shows the effect of AFM coupling (g_1) on the ultrasound attenuation coefficient. It is known that the magnetic order decreases with decrease of AFM coupling. Hence the Néel temperature is suppressed accompanied by the staggered field h_1 throughout the temperature range. This is reflected in the temperature dependent ultrasonic attenuation as shown in Figure 4. With decrease of AFM coupling from g_1=0.1 to 0.065 the Néel temperature is suppressed from t_N=0.088 to 0.048. Further, the attenuation coefficient is also suppressed more and more with decrease of the AFM coupling as shown clearly in the inset of Figure 4.

5. Conclusions

The effect of impurity f-electron position with respect to the Fermi level, the strength of the hybridization between the copper 3d electrons, the e-p coupling and the AFM coupling on the temperature dependent ultrasonic attenuation in the AFM phase is substantially large. The attenuation coefficient shows a sharp drop at the Néel temperature indicating an anti-ferromagnetic phase transition from high temperature paramagnetic to low temperature ferromagnetic phase as shown by ultrasound measurements on Tl-Ba-Ca-Cu-O [6]. In the low temperature AFM phase the attenuation coefficient is suppressed as the f-level moves away from the Fermi level, it is also suppressed with the increase of the strength of hybridization (v), with increase of the e-p coupling (s) and also with the decrease of the AFM coupling (g_1). The work to study the effect of interplay of anti-ferromagnetism and structural distortion on the ultrasonic attenuation is in progress.

Acknowledgements

The authors gracefully acknowledge the research facilities offered by the Institute of Physics, Bhubaneswar, India during their short stay.

References

1. He Yusheng, Sun Xiangzhong, Physica B 165-166 (1990) 1291.
2. Tetsuo Fukase et al., Physica B 165-166 (1990) 1289.
3. Y. H. Kim et al., Phys. Rev. B. 38 (1988) 6478.
4. B. H. Toby et al., Phys. Rev. Lett. 64 (1990) 2414.
5. W. Dmowski et al., Phys. Rev. Lett. 61 (1988) 2608.
6. Y. N. Huang, T. N. Wang, Z. X. Zhao, Phys. Rev. B. 49 (2) 1994.
7. G. C. Rout, S. K. Panda, Physica C 471 (2011) 121.
8. G. C. Rout, B. N. Panda, S. N. Behera, Solid State Commun. 106 (1998) 469.
9. K. C. Bishoyi, G. C. Rout, S. N. Behera, Physica B 395 (2007) 48.
10. Brugger T, Schreiner T, Royh G, Adelmann P, Czjzek G, Phys. Rev. Lett. 71 (1993) 2481.
11. P. Fulde, J. Low Temp. Phys. 95 (1994) 45.
12. D. N. Zubarev, Sov. Phys. Usp. 95 (1960) 71.
13. K. L. Nagi, S. L. Peng, Kwok Yeung Tsang, Physica A 191 (1992) 523.

Cite this article as:

S. P. Mohapatra *et al.*: **Effect of staggered field on the temperature dependent ultrasonic attenuation in cuprates.** *Phys. Express* 2013, **3**: 26

Crystal-field and molecular-field in ferromagnetic Mott-insulator $Y_2V_2O_7$ pyrochlore

A. Ali Biswas, Y. M. Jana*

Department of Physics, University of Kalyani, Kalyani -741235, Nadia, W.B., India

*Author for correspondence: Y. M. Jana, email: yatramohan@yahoo.com
Received 28 Aug 2012; Accepted 1 Nov 2012; Available Online 1 Nov 2012

Abstract

The observed dc magnetic susceptibility of ferromagnetic vanadate pyrochlore $Y_2V_2O_7$ is simulated using a D_{3d} crystal-field and mean-field approach and taking into the effect of spin-orbit coupling and anisotropic covalency overlap. The g-tensors and the exchange interactions among V^{4+}-ions are found to be anisotropic. The ^2D term of $3d^1$ V^{4+}-ion is split into 5 doublets with overall splitting $\Delta_1 \approx 2$ eV and the total splitting of the $^2T_{2g}$ state $\Delta_0 \approx 0.4$ eV under combined action of octahedral crystal-field, trigonal distortion at V-site and spin-orbit coupling. The V^{4+} ion has a substantial easy-axis single-ion anisotropy along local <111> axis of a given V_4 tetrahedron, particularly below $T_m = 170 \pm 10$ K. The temperature T_m may be associated with the initiation of ferromagnetic clusters embedded in the paramagnetic matrix that gradually develop a temperature dependent spin-like gap of the lowest Kramers doublet of $Y_2V_2O_7$, as also found for $Lu_2V_2O_7$.

Keywords: Crystal field; Exchange interactions; Spin-orbit coupling

1. Introduction

Magnetic pyrochlore oxides, $R_2M_2O_7$ (R^{3+} = rare-earth, M^{4+} = transition metals), have drawn much interest recently due mostly to their low-temperature spin-frustrated magnetic properties [1]. The pyrochlore structure is characterized by an infinite network of corner sharing tetrahedra of magnetic R and/or M ions, resulting in geometrical frustration (GF) of spins when the nearest-neighbour (n.n.) magnetic spins are coupled *via* anti-ferromagnetic Heisenberg exchange interactions. The n.n. coupling alone cannot select a unique ground state (GS) of this system and remain macroscopically degenerate down to $T \rightarrow 0$ K. However in real systems, unique GS should occur due to few other weaker perturbations like dipolar, further n.n. exchange interactions, single-ion anisotropy, Dzyaloshinskii-Moriya interactions etc. which relieve the effect of frustration and drive the magnetic systems from the paramagnetic phase to any of the quantum states, viz., spin-liquid, spin-ice, spin-glass or long-range ordered in the GS configurations [1].

Recently, vanadate pyrochlore $Y_2V_2O_7$ provides an additional interest in the GF systems, since Y^{3+} ($4d^0$) is a non-magnetic ion at R-site and consequently, electronic and magnetic properties of the said compound are simply driven by the magnetic V-ions ($3d^1$) at M-sublattice. This vanadate pyrochlore is unique in the sense that it is a $3d$ ferromagnet with magnetic ordering temperature $T_c \approx 68$ K [2] and it is also a Mott-insulator, contrary to the common belief that ferromagnetism leads usually to metallic character. The electronic configuration of V^{4+}-ion in $Y_2V_2O_7$ is $(t_{2g})^1(e_g)^0$. The orbital ordering pattern showed that each orbital is extended toward the centre of mass of the V_4 tetrahedron. Such an orbital structure is expected in a trigonal (D_{3d} symmetry) crystal-field (CF) due to an oxygen lattice distortion [3]. The D_{3d} CF anisotropy along or perpendicular to the local <111> directions of the V_4 tetrahedra plays a significant role in the low-temperature magnetic properties of $Y_2V_2O_7$ along with other perturbations, like exchange, magnetic dipolar coupling among spins depending on their relative strength and magnitudes.

It is, therefore, aimed in this study *firstly* to simulate the observed thermal dependence of dc susceptibility χ of $Y_2V_2O_7$, and *secondly*, to determine the CF parameters, CF energies and corresponding wave-functions, g-tensors of V^{4+} ions and anisotropy of the local magnetic susceptibility at V-site. For this purpose, we construct a single-ion Hamiltonian within the framework of appropriate CF theory and a mean-field approximation [4, 5] by introducing effective anisotropic molecular field tensors and also taking account of appreciable spin-orbit coupling and analyze their effects on the magnetic properties of $Y_2V_2O_7$.

2. Theoretical Details

The electronic configuration of V^{4+} ion is $3d^1$, so the ground term is ^2D ($L = 2$, $S = 1/2$) and it is five-fold orbital degenerate. The degeneracy is removed by the actions of intra-atomic spin-orbit coupling (SOC) $H_{\text{s.o.}} = \zeta L \cdot S$ where ζ is a SOC constant, and in a solid by the CF interactions, $H_{\text{CF}} = H_{CF}^{octahedra} + H_{CF}^{trigonal}$, where $H_{CF}^{octahedra}$ represents the CF at the site of V^{4+}-ion arising due to six surrounding O^{2-}- ions in regular octahedral arrangement (VO_6-octahedra in $Y_2V_2O_7$) and $H_{CF}^{trigonal}$ represents trigonal (D_{3d}) distortion of the VO_6-octahedra, and also by the internal Weiss molecular field, H_{dd}, originated from intersite spin-spin interactions at the magnetic V-site. The total Hamiltonian for a $3d^1$ V-ion in presence of the Zeeman interaction term H_Z due to the external magnetic field B_{ext} can, therefore, be written as [6]

$$H_d = H_{\text{CF}} + H_{\text{s.o}} + H_{dd} + H_Z \quad (1)$$

The operator equivalent crystal-field Hamiltonian with predominantly cubic (octahedral) field and a small trigonal distortion is represented as [6],

$$H_{CF} = -\frac{2}{3}B_4(O_4^0 + 20\sqrt{2}O_4^3) + B_2^0 O_2^0 + B_4^0 O_4^0 \qquad (2)$$

where O_k^m's are Steven equivalent operators and B_k^m's are CF parameters expressed in energy units (either K, meV or cm^{-1}). The first term of Eq. 2 represents the octahedral field at V-site and the next two terms define trigonal distortion. The cubic term having CF parameter B_4 splits the ^2D state into a lower triplet $^2T_{2g}$ and an upper doublet ^2E_g and the total splitting is $10D_q = 120\ B_4$. Under the trigonal D_{3d} distortion, B_2^0 and B_4^0, the $^2T_{2g}$ state splits into a lower orbital singlet $^2A_{1g}$ and an excited orbital doublet $^2E'_g$.

To determine the energy levels and wave-functions of the CF Hamiltonian, we have first diagonalized the matrix of $H_{CF}^{octahedra}$ in 5×5 (L, L_z) basis states and then find out the effect of trigonal symmetry by first-order perturbation method [6]. Thus we obtained

$$\begin{aligned}
&E_1 = -48B_4 - 6B_2^0 + 72B_4^0,\\
&|\psi_1> = |0> \equiv |\tilde{0}>\\
&E_2 = -48B_4 + 3B_2^0 - 8B_4^0,\\
&|\psi_2> = \pm\sqrt{2/3}\,|\mp 2> - \sqrt{1/3}\,|\pm 1> \equiv |\pm\tilde{1}>\\
&E_3 = 72B_4 - 28B_4^0,\\
&|\psi_3> = \sqrt{1/3}\,|\pm 2> - \sqrt{2/3}\,|\pm 1>
\end{aligned} \qquad (3)$$

Under the D_{3d} CF, the original five-fold degenerate free-ion state of $3d^1$ system splits up into a lower singlet (E_1) and two upper doublets (E_2, E_3). Note that in the method of Abragam and Pryce [6], the singlet state $|\psi_1>$ and the doublet state $|\psi_2>$ coming from the $^2T_{2g}$ state were referred to as $|\tilde{0}>$ and $|\pm\tilde{1}>$, respectively, corresponding to 'pseudo' angular momentum state $\tilde{l} = 1$.

Since the spin-orbit (S.O.) interaction has no effect in the first order on the lowest orbital singlet state $|\psi_1>$, we adopt the Pryce's spin-Hamiltonian formalism [7-9] for the calculation of g-values and magnetic susceptibilities. Here the S.O. interaction and the external magnetic field are treated as simultaneous perturbations. In the case of a V^{4+}-ion, such a treatment seems to be reliable – because of its small S.O. coupling constant [8] and also because of the fact that the dc magnetic susceptibilities are approximately ground-state properties when the next upper states are at very high energies compared to the experimental temperature zone, as observed for the V-compounds [6, 8, 9].

The Pryce's spin-Hamiltonian [7] is given by

$$\begin{aligned}
H_S =& <\psi_1|H'|\psi_1> - \sum_{n\neq 1}\frac{<\psi_1|H'|\psi_n><\psi_n|H'|\psi_1>}{E_n - E_1}\\
&+ \sum_{m\neq 1}\sum_{n\neq 1}\frac{<\psi_1|H'|\psi_m><\psi_m|H'|\psi_n><\psi_n|H'|\psi_1>}{(E_n - E_1)(E_m - E_1)}\\
&- \sum_{n\neq 1}\frac{<\psi_1|H'|\psi_n><\psi_n|H'|\psi_1><\psi_1|H'|\psi_1>}{(E_n - E_1)^2}
\end{aligned} \qquad (4)$$

with perturbation Hamiltonian is: $H' = H_{s.o} + H_Z =$

$$R_i\zeta\vec{L}.\vec{S} + \mu_B\vec{H}.(k_i\vec{L} + 2\vec{S}) \qquad (5)$$

where $\zeta = 248\ cm^{-1} = 357$ K is the S.O. coupling constant for the free-ion V^{4+} [6,9], k_i and R_i (i = x, y, z) are the orbital reduction and S.O. coupling reduction factors, respectively, arising from the covalency effect and these are considered to partake of the symmetry of the ligand field. For simplicity, we assume $k_x = k_y = k_\perp$, $k_z = k_\parallel$ and $R_x = R_y = R_\perp$, $R_z = R_\parallel$. Evaluating the matrices occurring in Eq. (4) following usual procedure, we finally get the expression for spin-Hamiltonian in terms of spin variables only.

Thus for $H\|z$, spin-Hamiltonian becomes

$$H_s(z) = 2\mu_B H S_z\left[1 - \frac{\zeta^2 R_\perp^2}{(E_2 - E_1)^2} - \frac{\zeta^2 R_\perp^2 k_\parallel}{2(E_2 - E_1)^2} + \frac{2\zeta^2 R_\perp^2 k_\parallel}{(E_3 - E_1)(E_2 - E_1)} - \frac{2\zeta^2 R_\perp^2}{(E_3 - E_1)^2}\right] \qquad (6)$$

For $H\|x$, it becomes

$$\begin{aligned}
H_s(x) =\ & 2\mu_B H S_x\left[1 - \frac{k_\perp R_\perp \zeta}{E_2 - E_1} - \frac{2k_\perp R_\perp \zeta}{E_3 - E_1} + \frac{\zeta^2 R_\parallel k_\perp R_\perp}{2(E_2 - E_1)^2} - \right.\\
&\left. \frac{2\zeta^2 R_\parallel k_\perp R_\perp}{(E_3 - E_1)(E_2 - E_1)} - \frac{\zeta^2 R_\perp^2}{2(E_2 - E_1)^2} - \frac{\zeta^2 R_\perp^2}{(E_3 - E_1)^2}\right]\\
&- \frac{\mu_B^2 H^2 k_\perp^2}{E_2 - E_1} - \frac{2\mu_B^2 H^2 k_\perp^2}{E_3 - E_1}
\end{aligned} \qquad (7)$$

and a similar expression can be obtained for $H\|y$.

Operating H_s over the spin states $|\pm 1/2>$, we obtain (2×2) secular matrix which on diagonalization gives the following energy eigen-values and g-tensors for the lowest orbital level in presence of S.O. coupling:

$$W_\pm = \pm\frac{1}{2}g_\parallel\mu_B H \qquad \text{(for } H\|z\text{)} \qquad (8)$$

$$W_\pm = \pm\frac{1}{2}g_\perp\mu_B H - \frac{\mu_B^2 H^2 k_\perp^2}{E_2 - E_1} - \frac{2\mu_B^2 H^2 k_\perp^2}{E_3 - E_1} \qquad \text{(for } H\perp z\text{)} \qquad (9)$$

$$\text{with } g_{\parallel} = 2\left[1-\frac{\zeta^2 R_{\perp}^2}{(E_2-E_1)^2}-\frac{\zeta^2 R_{\perp}^2 k_{\parallel}}{2(E_2-E_1)^2}+\frac{2\zeta^2 R_{\perp}^2 k_{\parallel}}{(E_3-E_1)(E_2-E_1)}-\frac{2\zeta^2 R_{\perp}^2}{(E_3-E_1)^2}\right] \quad (10)$$

$$\text{and } g_{\perp} = 2\left[1-\frac{k_{\perp}R_{\perp}\zeta}{E_2-E_1}-\frac{2k_{\perp}R_{\perp}\zeta}{E_3-E_1}+\frac{\zeta^2 R_{\parallel}k_{\perp}R_{\perp}}{2(E_2-E_1)^2}-\frac{2\zeta^2 R_{\parallel}k_{\perp}R_{\perp}}{(E_3-E_1)(E_2-E_1)}-\frac{\zeta^2 R_{\perp}^2}{2(E_2-E_1)^2}-\frac{\zeta^2 R_{\perp}^2}{(E_3-E_1)^2}\right] \quad (11)$$

The general expression for the single-ion magnetic susceptibility [10] is given by

$$\chi_j^s = \frac{N_a k_B T}{H}\frac{\partial}{\partial H}\ln Z(i) \qquad (j = \parallel \text{ or } \perp) \quad (12)$$

$$\text{where } Z(i) = \sum_i \exp\left(-\frac{W_i}{k_B T}\right)$$

$$\ln Z(i) = -\frac{\overline{W_i}}{k_B T} + \ln(2S+1) + \frac{<(W_i-\overline{W_i})^2>}{2k_B^2 T^2} - \frac{<(W_i-\overline{W_i})^3>}{6k_B^3 T^3} \quad (13)$$

On substituting the values of W_i obtained from Eqs. (8) and (9), we have from Eq. (12)

$$\chi_{\parallel}^s = \frac{N_a \mu_B^2}{4k_B}\frac{g_{\parallel}^2}{T} \quad (\text{for } H\parallel z), \quad (14)$$

and

$$\chi_{\perp}^s = 2N_a\mu_B^2\left[\frac{k_{\perp}^2}{E_2-E_1}+\frac{2k_{\perp}^2}{E_3-E_1}\right]+\frac{N_a\mu_B^2}{4k_B}\frac{g_{\perp}^2}{T} \quad (\text{for } H\perp z) \quad (15)$$

The χ_j^s is next used to *renormalize* the effective site-susceptibilities χ_j and calculate bulk susceptibility χ of these pyrochlores as a functions of CF parameters, ζ, reduction factors and exchange interactions $\lambda_{\parallel}$ and $\lambda_{\perp}$:

$$\chi_{\parallel} = \frac{\chi_{\parallel}^s}{\Delta}[1+(3\lambda_{\parallel}-\lambda_{\perp}+2q-p)\chi_{\perp}^s] \quad (16)$$

$$\chi_{\perp} = \frac{\chi_{\perp}^s}{\Delta}[1+(2\lambda_{\perp}+p-q)\chi_{\parallel}^s] \quad (17)$$

The bulk (observed) susceptibility is then given by

$$\chi = \frac{N_a}{3}(\chi_{\parallel}+2\chi_{\perp}) \quad , \quad (18)$$

where v and N_a are unit cell volume and the Avogadro number, respectively, and others have their usual meanings as defined in [4, 5].

3. Results and Analysis

Haghighirad et al. [2] measured the temperature dependence of the dc susceptibility χ_{dc} of poly-crystalline sample of $Y_2V_2O_7$ in the temperature range 2-300 K at external field H = 1T. The susceptibility rises sharply below 100 K and magnetic ordering has occurred at $T_c \approx 68$ K. The high temperature data (150-300 K) obeys a Curie-Weiss (CW) behaviour with paramagnetic Curie temperature θ_{CW} = 86 (±1) K indicating the dominance of the ferromagnetic exchange interactions between V^{4+} moments. The effective paramagnetic moment p_{eff} is 1.76 μ_B/V^{4+} which is close to the spin-only value of 1.734μ_B for $3d^1$ ion. The thermal variation of χ_{dc}, particularly above T_c is due to the coordinated effect of CF interactions, spin-orbit coupling, exchange and dipolar interactions among magnetic V-spins.

The parameters best suited to simulate the observed results of χ_{dc} are given by B_4 = 181.3 ±2 K, B_2^0 = 791.3 ±5 K, B_4^0 = 30.2 ±1 K, $k_{\parallel}$ = 0.92, $k_{\perp}$ = 0.91, $R_{\parallel}$ = 0.67, $R_{\perp}$ = 0.65. Calculated localized states of the $3d^1$ configuration of the V^{4+}-ions in $Y_2V_2O_7$ originated from the 5-fold degenerate ^2D term are drawn in Figure 1. Under the cubic field B_4, the $^2T_{2g}$ – ^2E_g splitting is 21756 K. It is to mention that for another vanadium compound $Na_2V_3O_7$, this splitting was found to be 24000 K [11]. Under the trigonal D_{3d} distortion, B_2^0 and B_4^0, the $^2A_{1g}$ – $^2E'_g$ splitting of the lower orbital triplet $^2T_{2g}$ is found to be Δ_0 = 4705 ±10 K (~0.4 eV) and the total $^2A_{1g}$– ^2E_g splitting is Δ' = 23481 ±15 K (~2.01 eV). The total splitting of the $^2T_{2g}$ state and the overall splitting of the ^2D term agree very well with the earlier results for $Y_2V_2O_7$ obtained from the Hubbard Hamiltonian approach [12]. The values of k's and R's indicate appreciable anisotropic covalency overlap of the ligand charges with the charge cloud of V^{4+}-ions. The spin-orbit coupling

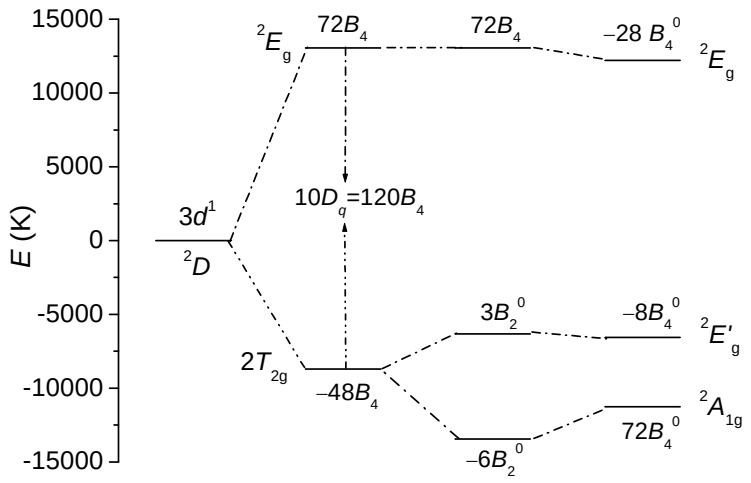

Figure 1. Calculated localized states of the $3d^1$ configuration of the V^{4+}-ions in $Y_2V_2O_7$ originated from the 5-fold orbitally degenerate ^2D term under the actions of the octahedral crystal-field (B_4 = 181.3 ±2 K), trigonal (D_{3d}) distortion (B_2^0 =791.3 ±5 K and B_4^0 = 30.2 ±1 K) at V^{4+}-site.

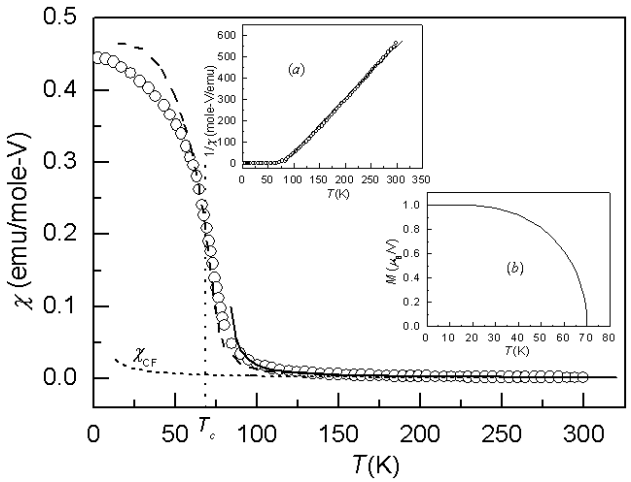

Figure 2. DC magnetic susceptibility χ of $Y_2V_2O_7$ – calculated values (solid curve), using anisotropic nearest-neighbor Heisenberg exchange interactions in the mean-field approach, match with the experimental results (O) measured in [2] in the temperature range 300–85±4 K. Below T_c the observed susceptibility is described (dashed curve) using single-ion ferromagnetic-like Heisenberg exchange Hamiltonian which creates a temperature dependent spin-like splitting of the ground CF doublet. Calculated susceptibilities (dotted curve) in the crystal-field (χ_{CF}) match with the experimental values down to 180 K only. Inset (a) shows the observed and calculated values of $1/\chi$. Inset (b) shows the variation of thermally averaged saturation magnetization of V^{4+}-ion with temperature, which vanishes at T_c (see text).

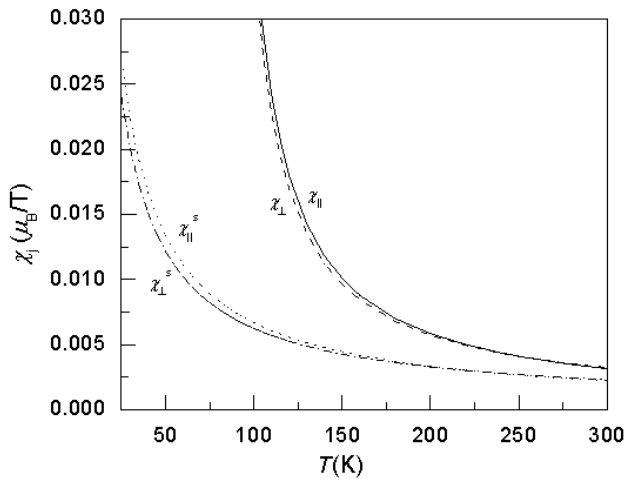

Figure 3. Calculated components of the single ion susceptibility ($\chi_{\parallel}^{s}$, $\chi_{\perp}^{s}$) in the CF and renormalized site susceptibility ($\chi_{\parallel}$ and $\chi_{\perp}$) tensors of $Y_2V_2O_7$ indicate that $Y_2V_2O_7$ is an easy-axis ($\chi_{\parallel} > \chi_{\perp}$) single-ion anisotropic system.

constant is reduced from its free-ion value to 235.6 K due to a factor R = 0.66 arising due to covalency effects [6, 9]. Orbital reduction factor is found to be k = 0.915 which agrees with other vanadate compounds [8, 9].

The CF single-ion susceptibility χ_{CF} calculated using the above parameters agrees appreciably with the observed data at T > 180 K in the paramagnetic region, but differs below 180 K (Figure 2). It is noted that single-ion susceptibility in CF are nearly isotropic above T = 170 ± 10 K but becomes anisotropic, $\chi_{\parallel}^{s} > \chi_{\perp}^{s}$ below 170 K as shown in Figure 3. But when we have introduced anisotropic values of ferromagnetic exchange constants $\lambda_{\parallel}$ = 22.0 T/μ_B and $\lambda_{\parallel}$ = 21.1 T/μ_B, the renormalized susceptibility (and its inverse) matches well with the experimental results down to the paramagnetic temperature ~ 86 K. Further the renormalized components of the site-susceptibility tensors ($\chi_{\parallel}$ and $\chi_{\perp}$) drawn in Figure 3 depict that the magnetic anisotropy of $Y_2V_2O_7$ is easy-axis type due to the coordinated effect of CF interactions, exchange and dipolar interactions among magnetic V-spins. Using the value of isotropic combination of exchange constants $\lambda_{iso} = (\lambda_{\parallel} + 2\lambda_{\perp})/3$ = 21.4 T/μ_B, we obtain corresponding exchange integral $J = (2\mu_B)^2\lambda_{iso}$ = 57.56 K. We have calculated dipolar contribution θ_{dip} to the CW temperature θ_{CW} using $\theta_{dip} = \frac{\mu_{eff}^2}{3k_B}\frac{16\pi(1-N)}{3v}$ ≈ 0 [4]. Using the value of the exchange contribution $\theta_{ex} = \theta_{CW} - \theta_{dip}$ = 86 K and putting θ_{ex} in $\lambda_{iso} = \frac{k_B}{2\mu_{eff}^2}\theta_{ex}$ [4], we get λ_{iso} = 20.66 T/μ_B. Further if we introduce Heisenberg exchange between the n.n. V-spins as $H_{12}^{ex} = -J\vec{S}_1 \cdot \vec{S}_2$, then $\theta_{ex} = z\,S(S+1)J/3$ gives J = 57.33 K, where z = 6 is no. of n.n. spins in the pyrochlore structure. Thus the values of λ_{iso} and J estimated independently from the observed value of θ_{CW} of $Y_2V_2O_7$ match very well with their corresponding fitted values.

The anisotropy of the Landé g-factor of the ground doublet is calculated to be $g_{\parallel}$ = 1.995 and $g_{\perp}$ = 1.876. The average g-value $\bar{g}$ = 1.916 is reduced from its free-spin value of g_e = 2.0023 by an amount ~ 0.086 due to spin-orbit coupling interaction.

4. Discussion

We have simulated and analyzed the observed results of dc magnetic susceptibility, paramagnetic Curie temperature θ_{CW} of ferromagnetic pyrochlore vanadate compound $Y_2V_2O_7$, consistently and simultaneously, assuming an appropriate CF theory and a mean-field approximation by introducing effective molecular-field tensors and also taking account of appreciable spin-orbit coupling. The total Hamiltonian is solved on perturbation method depending on the strength of different contributions, e.g., octahedral crystal-field and its trigonal distortion, spin-orbit coupling, Zeeman interaction of the magnetic V^{4+}-ion with the external-field.

Molecular field and spin-orbit coupling are found to be anisotropic along and perpendicular to the V-V bond distance due to anisotropic covalency overlapping effect. The temperature-dependent calculated site-susceptibilities show that V^{4+} ion has a substantial easy-axis single-ion anisotropy along local <111> axis of a given V_4 tetrahedron, particularly below 170 ± 10 K. It is appropriate to mention here that for another isomorphous compound $Lu_2V_2O_7$, the observed dc-susceptibility deviates from the CW behavior around T_m = 160 K at which formations of magnetic polarons [13] and ferromagnetic clusters [14] begin in $Lu_2V_2O_7$ marked by several features: (i) the magnetic specific heat starts to become anomalous around 160 K, (ii) the thermal conductivity is suppressed in the temperature range of 160-80 K, and (iii) an anomaly develops at 160 K in the power law behavior of the resistivity [15]. Assuming that the molecular-field at V-site lifts the degeneracy of the ferromagnetic ground doublet state

of V-ions, our calculation [16] for $Lu_2V_2O_7$ showed that the ground doublet state is split due to the spin-spin correlations among V_4-tetrahedra below T_c by an energy separation δ_0 = 166 ± 2 K which is very small in comparison to the total splitting of the $^2T_{2g}$ state of V^{4+}-ion and vanishes around T_m = 170 ± 10 K in the paramagnetic region. This spin-like gap may cause the sharp rise of the observed dc susceptibility below T_c ~70 K for $R_2V_2O_7$ (R = Y, Lu).

To address the steep rise of susceptibility below T_c, a single-ion ferromagnetic-like Heisenberg exchange Hamiltonian [17, 18] is defined in terms of thermally averaged total angular momentum $< \vec{J}_i >$ as

$$H_{\text{ex}} = -J_{av}\vec{J}\cdot<\vec{J}> + \frac{1}{2}J_{av}<\vec{J}>^2 \qquad (19)$$

where $J_{av} = J_{av}^{(i)} = \sum_{j=1}^{N} J(i,j)\alpha(i,j)$ is the averaged exchange interactions of the i-th ion with all others (j =1, N). The scaling factor $\alpha(i, j)$ contains information on the magnitudes and orientations of the neighboring j-th magnetic ion with respect to the considered i-th ion. Since the ground doublet state is well isolated from the upper states of V^{4+}-ion [8, 9, 16], it may be reasonable to assume that the magnetic properties of $Y_2V_2O_7$ can well be described by the ground CF state in the ferromagnetic region [18]. The ground-state wave function of V-ion in $Y_2V_2O_7$ was found to be Ψ_g = 0.9996 $|0, \pm1/2\rangle$ –0.0246 $|\pm1, \mp1/2\rangle$ ± 0.0148 $|\mp2, \mp1/2\rangle$ [16]. Diaginalizing the above Hamiltonian (19) in the vector space spanned by Ψ_g, we evaluate the average magnetization per V-ion $M = \mu_B < k_i\vec{L} + 2\vec{S} >$ and susceptibility $\chi = M/H$ by numerical approach. We took up the value of the effective exchange parameter J_{av} = 71 ±1 K for reproduction of the observed bulk magnetic properties of $Y_2V_2O_7$ below T_c. The value of J_{av} is found to differ from the n.n. Heisenberg exchange integral J ~ 57 K obtained above, since the former sums up the exchange interactions of a magnetic ion with all others in the magnetic system. If the calculations are restricted to the nearest-neighbor tetrahedra only, then $N = z = 6$ and the overall scaling factor $\alpha(i, j)$ becomes 1.25 which is comparable to the value of 1 for the ferromagnetic uniaxial system.

The calculated values of magnetization plotted in inset (b) of Figure 2 shows saturation at the value of ~1μ_B at zero external field as temperature goes down to T = 0K, which agrees very well with the observed saturated moment at 5 K [13, 15]. Further, the thermally averaged saturation magnetization decreases gradually as temperature rises and finally approaches zero at $T \sim T_c$, and the system then enters into the Curie-Weiss paramagnetic zone. Such behaviour appears due to the temperature dependence of the splitting of the ground doublet by ferromagnetic spin-spin exchange interactions. The calculated values of susceptibility (shown in Figure 2) below T_c match with the observed results down to 50 K and shows very similar tendency with decreasing temperature.

We here describe the observed susceptibility below T_c by adjusting just only one parameter J_{av} and assuming only the ground doublet state. Considering the temperature zone, contribution of the higher levels which are above 4700 K for the vanadium compounds, if any, can be negligible and hence can be ruled out, and any drastic variation of CF parameters from the above best fitted values cannot yield any better description of the electronic level pattern of V^{4+}-ion and hence the observed susceptibility. Therefore to simulate the observed susceptibility down to T = 0K, one may need to take care of magnitudes and different local ordering directions of the neighboring magnetic ions in terms of more exchange constants to describe the detailed magnetic structure in the ordered phase [17], and also have to distinguish between the spins of n.n. V_4-tetrahedra which are vertex-sharing and interpenetrating. Further, it is worth to mention that Hubbard Hamiltonian approach and the density-functional theory plus the onsite electron-electron repulsion and Dzyaloshinskii-Moriya (DM) interactions method [19] within 3d orbitals demonstrated that the electron hopping from the t_{2g} orbitals to the e_g orbitals between n.n. spins within the V_4-tetrahedron stimulates the ferromagnetic ground state below T_c as well as the semi-conducting properties for these vanadate pyrochlores $R_2V_2O_7$. The DM interaction, which is a consequence of S.O. coupling and only 6-7% of n.n. exchange interaction [16,19], must feed into the parametrization of electonic and magnetic properties of $Y_2V_2O_7$ to model a clear picture of ferromagnetism in these Mott insulators.

5. Conclusions

We conjecture that in $Y_2V_2O_7$ and also in $Lu_2V_2O_7$ (a) above T = 200 K, the paramagnetic (PM) state of V^{4+}-ions reigns with effectively no spin-spin correlations, such that CF susceptibility matches with the observed susceptibility and obeys the CW law; (b) ferromagnetic clusters with short-range spin-spin correlations among V^{4+}-ions develop around T_m ~170 K and coexist with the PM phase, having appreciable single-ion anisotropy which favours spins to be along the <111> easy-axes over the hard-axes, down to $T \sim \theta_{CW}$; and (c) ferromagnetic ground state of V^{4+}-ion is an well-isolated spin-1/2 state which is split by a temperature-dependent spin-like gap $O(T_m)$ at T = 0K due to ferromagnetic spin-spin exchange interactions and causes sharp rise in the magnetic susceptibility below T_c.

Acknowledgements

This work is done under UGC MRP Fund (F. No.: 41-886/2012 (SR)) sanctioned to YMJ by University Grants Commission, Government of India.

References

1. J. S. Gardner, M. J. P. Gingras, J. E. Greedan, Rev. Mod. Phys. 82 (2010) 53.
2. A. A. Haghighirad, C. Gross, W. Assmus, J. Cryst. Growth 310 (2008) 2277.
3. H. Ichikawa, L. Kano, M. Saitoh, S. Miyahara, N. Furukawa, J. Akimitsu, T. Yokoo, T. Matsumura, M. Takeda, K. Hirota, J. Phys. Soc. Jpn. 74 (2005) 1020.
4. B. Z. Malkin, T. T. A. Lummen, P. H. M. van Loosdrecht, G. Dhalenne, A. R. Zakirov, J. Phys. Condens. Matter 22 (2010) 276003.
5. A. Ali Biswas, Y. M. Jana, J. Magn. Magn. Mater. 323 (2011) 3202.
6. A. Abragam, B. Bleaney, Electron Paramagnetic Resonance of Transition Ions, Clarendon, Oxford (1970).
7. M. H. L. Pryce, Proc. Phys. Soc. A 63 (1950) 25.

8. B. D. Bhattacharyya, Phys. Stat. Sol. B 71 (1975) 427.
9. C. J. Ballhausen, Introduction to Ligand Field Theory, McGraw-Hill Book Company, New York (1962).
10. J. H. Van Vleck, The Theory of Electric and Magnetic Susceptibilities, Oxford University Press (1932).
11. Z. Ropka, R. J. Radwanski, Czech. J. Phys. 54 (2004) D427.
12. S. Miyahara, A. Murakami, N. Furukawa, J. Mol. Struct. 838 (2007) 223.
13. H. D. Zhou, E. S. Choi, J. A. Souza, J. Lu, Y. Xin, L. L. Lumata, B. S. Conner, L. Balicas, J. S. Brooks, J. J. Neumeier, C. R. Wiebe, Phys. Rev. B. 77 (2008) 020411.
14. K. Y. Choi, Z. Wang, P. Lemmens, H. D. Zhou, J. van Tol, N. S. Dalal, C. R. Weibe, Phys. Rev. B. 82 (2010) 054430.
15. Y. Onose, T. Ideue, H. Katsura, Y. Shiomi, N. Nagaosa, Y. Tokura, Science 329 (2010) 297.
16. A. Ali Biswas, Y. M. Jana, J. Magn. Magn. Mater. 329 (2013) 118.
17. Z. -S. Liu, M. Diviš, V. Sechovsky, Physica B 367 (2005) 48.
18. Z. -S. Liu, M. Diviš, V. Sechovsky, Physica B 403 (2008) 3439.
19. H. J. Xiang, E. J. Kan, M. -H. Whangbo, C. Lee, S. -H. Wei, X. G. Gong, Phys. Rev. B. 83 (2011) 174402.

Cite this article as:

A. Ali Biswas *et al.*: **Crystal-field and molecular-field in ferromagnetic Mott-insulator $Y_2V_2O_7$ pyrochlore.** *Phys. Express* 2013, **3**: 27

Theoretical study of pseudogap effect on the interplay of SDW and superconductivity in cuprates

K. L. Mohanta[a,*], S. K. Panda[b], B. K. Raj[c], G. C. Rout[d]

[a] *Department of Physics, Institute of Technical Education and Research, Siksha 'O' Anusandhan University, Bhubaneswar-751030, India*
[b] *K. D. Science College, Pochilima, Hinjilicut-761101, Odisha, India*
[c] *Dept. of Physics, Govt. Autonomous College, Angul-759122, India*
[d] *P. G. Dept. of Applied Physics and Ballistics, F. M. University, Balasore-756 019, India*

[*] *Author for correspondence: K. L. Mohanta, email: kamal@iopb.res.in*
Received 15 Sep 2012; Accepted 7 Dec 2012; Available Online 7 Dec 2012

Abstract

The pairing mechanism in high-T_c superconductors still remains an intriguing mystery. We present here a microscopic model calculation of the interplay of spin density wave (SDW) and superconductivity (SC) in high-T_c systems. Further the charge density wave (CDW) is incorporated in the Hamiltonian as a pseudogap interaction. The pseudogap co-exists in the superconducting state and extends to normal phase above T_C. These three temperature dependent order parameters corresponding to CDW, SDW, and SC are calculated by the Green's function technique by using the model Hamiltonian and are solved self-consistently. Finally, the conduction electron density of states (DOS) are calculated to interpret the scanning tunneling microscopy experimental data to explain the tunneling conductance of the system. The dip-hump structure as observed by the experiment is explained by our model calculation.

Keywords: Superconductivity; Charge density wave; Spin density wave

1. Introduction

The pairing mechanism of high temperature superconductivity is not yet clear. The pseudogap phase appearing in the phase diagram above superconducting transition temperature, t_c and below a characteristic temperature, T^* in the under-doped region appears to play a vital role in explaining the pairing mechanism [1, 2]. The theoretical approaches to relate pseudogap and superconductivity can be classified into two groups. According to the first group pseudogap is considered as an independent phase which competes with superconductivity and the pseudogap becomes dominant over superconductivity on reducing the hole doping concentration [3 - 5]. A variety of density waves like charge, spin and orbital currents fall under this group. In this scenario the pseudogap and superconducting gap compete with each other. According to the second category the pseudogap phase is a cooperative precursor to superconductivity. In this view superconducting pairs preform in pseudogap phase before the on-set of superconductivity [5, 6]. The scanning tunneling microscopy (STM) has revealed some unusual properties of high-T_c superconductors i.e the pseudogap and its relation to superconductivity and the unusual large gap values. The pseudogap appears in the electronic excitation spectra at temperature T^* above the superconducting transition temperature (T_c) in the under doped-region [7, 8]. A definite origin of the pseudogap is still lacking. The break junction tunneling by Ekino et. al [9] on Bi2212 compound shows the following facts. The pseudogap closing temperature, T^* distributes at $110-190K$ even though transition temperature lies between $86-89K$. They found the SC gap at $77.3K$ to be 4Δ ($T_c = 77.3K$) $\simeq$ 100 meV. The scanning tunneling microscopy (STM) study on $La_{2-x}Sr_xCuO_4$ (LSCO) reveals two gap structures Δ_1 and Δ_2 consisting of two energy scales [10]. Out of the two gaps, the low energy gap, Δ_2 is associated with nodal (in the vicinity of Fermi level) electronic states, whereas the high energy gap, Δ_1 is associated with antinodal (near the gap edge) electronic states. In case of LSCO ($T_C^{max} = 38K$), Δ_2 $\simeq$5meV and Δ_1 $\simeq$10meV depending on the doping levels [10], whereas Δ_2 $\simeq$10meV in optimally doped La-Bi2201 ($T_c = 34K$) [11]. The authors [10] agreed that Δ_2 represents the energy scale where the coherent quasi-particles persist. Angle Resolved photo emission spectroscopy (ARPES) measurements on LSCO and $Bi_2Sr_2CaCu_2O_8$(Bi2212) have revealed the presence of two distinct energy scales for the nodal and anti-nodal regions in the heavily under-doped regime [12, 13]. Several early STM measurements reveal dip-hump structure in the conductance spectra of several cuprate superconductors [14 - 16]. Jenkins et. al. [17] have demonstrated through their STM study that the dip feature in the conductance spectra of Bi-based superconductor originates from a collective excitation most likely the antiferromagnetic spin resonance detected by neutron scattering [18] and this collective mode is related to superconductivity. In view of the above experimental observations, we attempt here to formulate a model for pairing mechanism in high-T_C cuprates taking charge density wave (CDW) and spin density wave (SDW) as pseudogaps.

The occurrence of charge density wave (CDW) in Cu-O plane of $YBa_2CuO_{7-\delta}$ is observed in STM [19 - 21]. Further the structural and electronic phase transitions occur for the compounds $La_{2-x}Sr_xCuO_4$, $YBa_2CuO_{7-\delta}$ and Bi-Sr-Ca-Cu-O [22, 23]. At low dopant concentrations the cuprates exhibit the antiferromagnetic phase. Due to the low dimensional character of the cuprates there exists the antiferromagnetic spin density wave (SDW) [24, 25]. The CDW and SDW states arise from the nesting property of the Fermi-surface in the low dimensional cuprates. Ghosh et. al [26] have reported that the

interplay of SDW and superconductivity of the cuprates. Recently Panda et. al [27] have reported the theoretical study of tunneling conductance exhibiting the interplay of CDW, SDW and superconductivity. In this communication, we assume the CDW and SDW interactions as pseudogaps and attempt to investigate their interplay with superconductivity by varying the model parameters of the high-T_c systems. Then this model calculation is applied to interpret the tunneling conductance data. The theoretical model is presented in the section 2. Calculation of electron Green's functions is presented in section 3 and the expressions for the CDW, SDW and SC gap equations in section 4. The results and discussion are given in section 5 and conclusion in section 6.

2. Theoretical Model

In high-T_c systems , the oxygen atoms surrounding the central Cu-atom form an octahedron. The structural evidences show that the neighboring Cu-O octahedra are enlarged and contracted alternately. As a result Cu-atoms acquire disproportionate charges, because of the two different Cu-O bond lengths. This indicates the existence of strong electron-phonon interaction. The presence of the nested pieces of Fermi surface and the disproportionate charges of Cu-site stabilizes the system with Fermi surface instability by the formation of the charge density wave (CDW). Long range anti-ferromagnetic order present in cuprates owes its origin to itinerant electrons in the system. The presence of the Fermi surface instability due to the existence of the nested pieces of Fermi surface results in the formation of a spin density wave (SDW). Based upon our mean-field model [27], the Hamiltonian is written as

$$H = \sum_{k\sigma} \varepsilon_k c^{\dagger}_{k\sigma} c_{k\sigma} + \Delta_c \sum_{k\sigma} c^{\dagger}_{k\sigma} c_{k+Q\sigma} + \Delta_s \sum_{k\sigma} \sigma c^{\dagger}_{k\sigma} c_{k+Q\sigma} + \Delta \sum_{k} (c^{\dagger}_{k,\uparrow} c^{\dagger}_{-k,\downarrow} + c_{-k,\downarrow} c_{k,\uparrow}) \quad (1)$$

The first term in H describes the hopping of copper d-electrons between adjacent sites. Here $c^{\dagger}_{k\sigma}$ $(c_{k\sigma})$ is the creation (annihilation) operator of the conduction electrons of copper atoms. The hopping takes place between the neighbouring sites of copper with the dispersion $\varepsilon_k = -2t_0(cosk_x + cosk_y)$, where t_0 is the nearest-neighbour hopping integral. The second term represents the CDW interaction, where Δ_c is the CDW gap parameter which is defined as

$$\Delta_c = -V_1 \sum_{k\sigma} < c^{\dagger}_{k,\sigma} c_{k+Q,\sigma} > \quad (2)$$

where V_1 is attractive Coulomb interaction in presence of phonon coupling to the electron densities of the conduction band. The CDW interaction arises due to the Fermi surface instability due to nesting condition $\varepsilon_{k\pm Q} = -\varepsilon_k$. The third term represents the longitudinal spin density wave (SDW) interaction. The SDW interaction is a type of antiferro magnetic interaction arising due to the Fermi surface nesting. The SDW interaction originates from the repulsive Coulomb interaction among the electrons. The longitudinal SDW gap parameter is defined as

$$\Delta_s = +V_2 \sum_{k\sigma} \sigma < c^{\dagger}_{k,\sigma} c_{k+Q,\sigma} > \quad (3)$$

Here V_2 is the repulsive Coulomb interaction and the spin, $\sigma = \uparrow (\downarrow)$ corresponding to up (down) spin configuration of the electrons.

The last term represents the s-wave BCS type mean-field superconducting interaction present in the conduction band. The superconducting gap Δ is defined as

$$\Delta = -V_0 \sum_{k} < c^{\dagger}_{k,\uparrow} c_{-k,\downarrow} > \quad (4)$$

Here V_0 is the momentum independent effective attractive Coulomb interaction, which exists for the interval $-\omega_c \leq \varepsilon_k \leq \omega_c$, where ω_c is the cut-off energy.

3. Calculation of electron Green's Functions

In order to calculate the CDW, SDW and superconducting order parameters, we have to calculate their corresponding correlation functions from their corresponding single particle electron Green's functions. We define four electron Green's functions $A_j(k,\omega)$ for $j = 1$ to 4 for up-spin configuration of the electron spins.

$$A_1(k,\omega) = << c_{k,\uparrow}; c^{\dagger}_{k,\uparrow} >>_{\omega}; A_2(k,\omega) = << c^{\dagger}_{-k,\downarrow}; c^{\dagger}_{k,\uparrow} >>_{\omega} \quad (5)$$

$$A_3(k,\omega) = \ll c_{k+Q,\uparrow}; c^{\dagger}_{k,\uparrow} >>_{\omega}; A_4(k,\omega) = << c^{\dagger}_{-(k+Q),\downarrow}; c^{\dagger}_{k,\uparrow} >>_{\omega}$$

When these Green's functions are evaluated by the equations of motion of method of Zubarev [28], the four coupled electron Green's functions are found to be

$$A_1(k,\omega) = \frac{1}{2\pi}\left[\frac{(\omega+\varepsilon_k)(\omega^2-\varepsilon^2_{2k})}{|D(\omega)|}\right] \quad (6)$$

$$A_2(k,\omega) = \frac{1}{2\pi}\left[\frac{\Delta(\omega^2-\varepsilon^2_{2k}-2\Delta_s(\Delta_c-\Delta_s))}{|D(\omega)|}\right] \quad (7)$$

$$A_3(k,\omega) = \frac{1}{2\pi}\left[\frac{(\Delta_c+\Delta_s)(\omega^2-\varepsilon^2_{2k})+2\Delta^2\Delta_s}{|D(\omega)|}\right] \quad (8)$$

$$A_4(k,\omega) = \frac{1}{\pi}\left[\frac{(\omega+\varepsilon_k)\Delta_c\Delta_s}{|D(\omega)|}\right] \quad (9)$$

where $\varepsilon^2_{2k}=\varepsilon^2_k + (\Delta_c - \Delta_s)^2$ and $|D(\omega)|$ appearing in the denominator of these above Green's functions is given by

$$|D(\omega)| = \omega^4 - \omega^2(E^2_{1k} + E^2_{2k}) + E^2_{1k}E^2_{2k} - 4\Delta^2_s\Delta^2_c \quad (10)$$

Here the terms E_{1k} and E_{2k} appearing in Eq. (10) can be written as

$$E_{1k}, E_{2k} = \sqrt{\varepsilon^2_k + \Delta^2_c + (\Delta_s \pm \Delta)^2} \quad (11)$$

From the poles of the Green's functions given in Eq. (6) to Eq. (9), we find four quasi-particle energy bands i.e $\pm\omega_{1k}, \pm\omega_{2k}$ which are written as

$$\omega_{1k}, \omega_{2k} = \sqrt{\varepsilon_k^2 + (W \pm \Delta_s)^2} \quad (12)$$

Due to the interplay of CDW interaction and the superconductivity, the superconducting gap is renormalised to give an effective gap $W = \sqrt{\Delta^2 + \Delta_c^2}$. This indicates that the CDW and SC gaps appear together and they influence each other.

Thus it appears that the CDW gap acts as a pseudogap. Sometimes it becomes difficult to interpret the tunneling conductance spectra, Raman spectra and the neutron scattering spectra due to the co-existence of the CDW and SC interactions in the systems. In addition to this the SDW interaction again renormalises, the quasi-particle bands ω_{1k} and ω_{2k} by the presence of $\pm\Delta_s$ terms. We apply later on our model calculation to interpret the scanning tunneling microscopy experimental data.

4. The CDW, SDW and SC gap equations

In order to investigate the interplay of the CDW, SDW and SC interactions in their co-existence phase in the copper oxide superconductors, one has to calculate the gap equations from the Green's functions. The CDW gap (Δ_c) is calculated from the Green's function $A_3(k,\omega)$ given in Eq. (8) by using the definition of CDW gap defined in Eq. (2). The integral form of the CDW gap is written as

$$\Delta_c = -g_1 \int d\varepsilon_k [F_{11} + F_{12}] \quad (13)$$

where the CDW coupling is $g_1 = N(0)V_1$ with $N(0)$ as the density of states of the conduction band. The function F_{1j} (for j=1 to 2) can be written as

$$F_{1j} = \frac{\Delta_c(\omega_{jk}^2 - E_{3k}^2)}{\omega_{jk}(\omega_{1k}^2 - \omega_{2k}^2)} \tanh\left(\frac{1}{2}\beta\omega_{jk}\right) \quad (14)$$

where $E_{3k} = \sqrt{\varepsilon_k^2 + \Delta_c^2 - \Delta_s^2}$.

The expression for the SDW gap is calculated from the correlation functions derived from the Green's function $A_3(k,\omega)$ given in Eq. (8) by using the definition of the SDW gap in Eq. (3). The integral equation for the SDW gap is written as

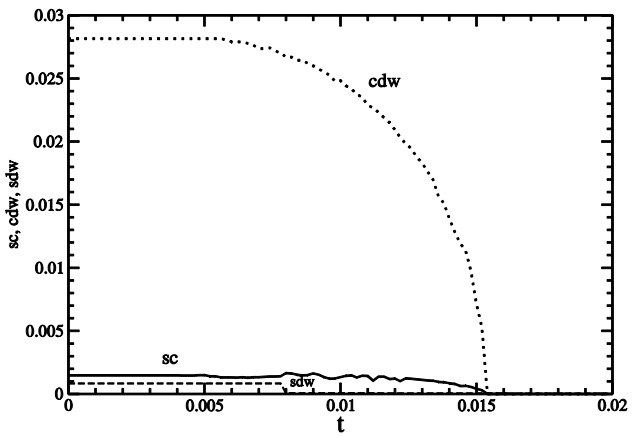

Figure 1. The self-consistent plot of SC gap parameter (z) vs. temperature (t), CDW gap parameter (z_1) vs. temperature (t), and SDW gap parameter (z_2) vs. temperature (t) for fixed values of g= 0.09994 , $g1$= 0.0445 , g_2= 0.0311.

$$\Delta_s = -g_2 \int d\varepsilon_k [F_{21} - F_{22}] \quad (15)$$

where the SDW coupling parameter is $N(0)V_0$. The functions F_{21} and F_{22} appearing in Eq. (15) are written as, the function F_{2j} for $j = 1$ to 2

$$F_{2j} = \frac{\Delta_s(\omega_{jk}^2 - E_{4k}^2 + 2\Delta^2)}{\omega_{jk}(\omega_{1k}^2 - \omega_{2k}^2)} \tanh\left(\frac{1}{2}\beta\omega_{jk}\right) \quad (16)$$

where $E_{4k} = \sqrt{\varepsilon_k^2 - \Delta_c^2 + \Delta_s^2}$.

The expression for superconducting gap is calculated from the correlation functions derived from the Green's function $A_2(k,\omega)$ given in Eq. (7). The integral form of the gap equation for the superconducting order parameter is written as

$$\Delta = -g \int_{-\omega_c}^{\omega_c} d\varepsilon_k [F_{31} + F_{32}] \quad (17)$$

where the SC coupling parameter $g = N(0)V_0$. The functions F_{3j} for $j = 1$ to 2 are written as

$$F_{3j} = \frac{\Delta(\omega_{jk}^2 - E_{3k}^2)}{\omega_{jk}} \tanh\left(\frac{1}{2}\beta\omega_{jk}\right) \quad (18)$$

To simulate the strong energy dependence of the conduction electron density of states around the center of the band in the system, we consider a model density of state $N(\varepsilon)$ as given below

$$N(\varepsilon) = N(0)\left(\sqrt{(1 - |\varepsilon/D|)}\right) ln|D^2/\varepsilon^2| \quad (19)$$

where 2D is the conduction band width. This form of the density of state also mimics that for a tight binding band of a two dimensional square lattice, thus justifying the choice for the copper oxide system. The physical quantities involved are made dimensionless by dividing them by the hopping integral $2t_0$. The reduced parameters are, the superconducting parameter $z = \frac{\Delta}{2t_0}$; the CDW parameter $z_1 = \frac{\Delta_c}{2t_0}$; the SDW parameter $z_2 = \frac{\Delta_s}{2t_0}$; the superconducting coupling $g = N(0)V_0$; the CDW coupling $g_1 = N(0)V_1$; the SDW coupling $g_2 = N(0)V_2$; reduced temperature $t = \frac{k_B T}{2t_0}$.

5. Results and Discussion

Based on our model, the gap equations for mutually competing orders i.e charge density wave (CDW), spin density wave (SDW) and superconductivity (SC), are calculated. The dimensionless CDW, SDW and SC parameters i.e. z_1, z_2 and z are involved integral functions and they are functions of each other and hence are solved self-consistently for a set of SC coupling $g = 0.09994$, the CDW coupling $g_1 = 0.0445$ and the SDW coupling $g_2 = 0.0311$. The temperature variations of the reduced SC parameter (z), CDW parameter (z_1) and the SDW parameter (z_2) are shown in Figure 1. As expected for cuprates, the SDW phase lies below the Nee'l temperature (t_N) $\simeq 0.008$ and the SDW gap magnitude is much reduced. The

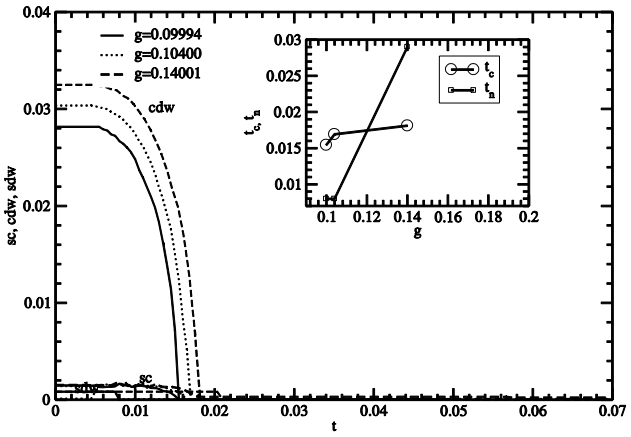

Figure 2. The self-consistent plot of SC gap parameter (z) vs. temperature (t), CDW gap parameter (z_1) vs. temperature (t) and SDW gap parameter (z_2) vs. temperature (t) taking different values of SC coupling g= 0.09994, 0.10400 and 0.14001.

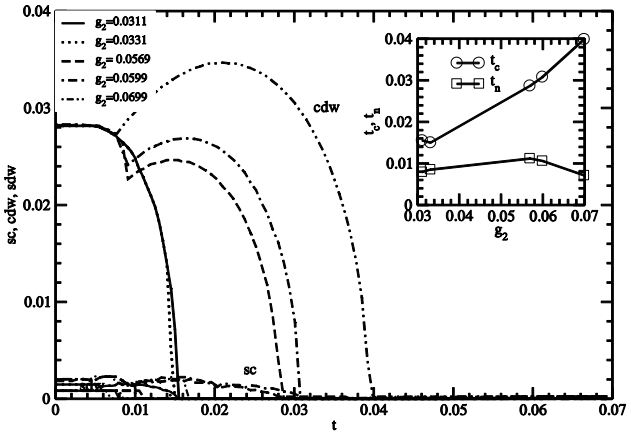

Figure 3. The self-consistent plot of SC gap parameter (z) vs. temperature (t), CDW gap parameter (z_1) vs. temperature (t) and SDW gap parameter (z_2) vs. temperature (t) taking different values of SDW coupling (g_2)= 0.0311, 0.0331, 0.0569, 0.0599 and 0.0699.

SC and CDW phases co-exist below a SC transition temperature $t_c \simeq 0.016$ which corresponds to the SC transition temperature of $T_C \simeq$ 40K for the hopping integral $2t_0 = 0.25eV$. This $T_C \simeq$ 40K is of the order of the SC transition temperature ($T_C^{max} \simeq$38K) for LSCO [10]. It is found the t_c and the CDW transition temperature t_d are equal. The pseudogap (CDW) merges with the superconducting gap showing that the superconducting gap is renormalised to give a higher gap value of $W = \sqrt{\Delta^2 + \Delta_c^2}$ as seen from the relation for the quasi-particle band energy given in Eq. (12). Earlier panda et. al. [27] have solved the gap equations for the SC, CDW and SDW parameters for a set of higher coupling constants [i.e g=0.4512, g_1=0.0941 and g_2=0.1095] compared to the present set of couplings and obtained the temperature dependent plots for z, z_1 and z_2 with three distinctly different transition temperatures. Moreover, the temperature dependent CDW order parameter resembles the plot obtained for the Bismuth based superconductor by Ekino et. al. [9]. It is to note further that the pseudogap phase (CDW) appears above the superconducting transition temperature ($T_c = 86 - 89K$) and below the pseudogap temperature ($T^* \simeq 120 - 130K$) for that system [9]. This type situation exists in the phase diagram of the under-doped high-T_c systems [1, 4]. In the present computation for the dimensionless order parameters z, z_1 and z_2, we have taken smaller values of the three couplings and particularly very small value of SC coupling, g=0.09994. For this situation the SC and CDW transition temperatures are equal and, the SC and CDW order parameters are of same order in magnitude and hence the SC order parameter is renormalized to give a higher magnitude the SC gap i.e W=$\sqrt{\Delta^2 + \Delta_c^2}$. Under the condition of t_c=t_d, the CDW and SC phases coexist in the phase diagram in the under-doped regime of the high-T_c cuprates [1, 2]. The effect of different couplings (i.e g, g_1, g_2) on the dimensionless parameters, z(t), z_1(t) and z_2(t) are presented in Figures 2 and 3.

The temperature dependences of the gap values z, z_1 and z_2 are shown in Figure 2 for different values of superconducting coupling parameter (g). It is found that with increase of SC coupling parameter, the magnitude of the SDW gap as well as the Nee'l temperature are suppressed considerably. Further with increase of SC coupling g, both the SC transition temperature (t_c) and the CDW transition temperature (t_d) are shifted together to a higher values. Under these conditions, the magnitude of the CDW gap is enhanced throughout the temperature range and, both the CDW and SC phases are extended to the higher temperature resulting in the enhancement of t_c due to the presence of the pseudogap (in this case CDW). This shows a strong interplay between the CDW and SC interactions. It is to note further that with increase of superconducting coupling (g), the CDW and the SC transition temperatures (t_c) are enhanced very slowly, while the SDW transition temperature (t_n) is enhanced rapidly and the magnitude of the SDW gap remains a low constant value throughout the temperature range (see the inset of Figure 2). In the present calculation, the SC transition temperature t_c = 0.16 ($T_c \simeq$40k for a hopping integral of $2t_0 \simeq$0.25 eV) for a given value of superconducting coupling g=0.14001. The SC transition temperature can still be enhanced by increasing the SC coupling. Due to the pseudogap (CDW phase in the present case) interaction with superconductivity, we can achieve higher T_c even with with lower SC coupling as compared to BCS type metallic superconductors. In the present calculation, we have considered BCS type weak SC coupling. It is to note here that there exists controversy regarding the electron-phonon pairing mechanism by Zhao [29, 30] and the spin fluctuation pairing mechanism [31] for high-T_c cuprates. Plakida [31] has agreed that the spin fluctuation pairing mechanism supports the experimental observations with negligible contribution of electron-phonon interaction. On the contrary, Zhao [29, 30] has shown that the strong electron-phonon interaction, rather than spin fluctuation, plays a dominant role in the microscopic pairing mechanism in cuprates. They further show that intrinsic pairing symmetry in the bulk is not d-wave, but extended s-wave in hole doped cuprates and node less s-wave in electron-doped cuprates.

The temperature dependences of z, z_1 and z_2 are shown in Figure 3 for different values of SDW coupling (g_2). With increase of SDW coupling, the SDW parameter is reduced and is finally suppressed completely. However, the effect of g_2 on CDW and SC gaps shows some new results. With the increase of SDW coupling, the CDW gap magnitude is enhanced considerably throughout the temperature range. Under this condition, the SC transition temperature (t_c) and CDW transition temperature (t_d) are shifted to new higher values and thereby extending the superconducting phase to a

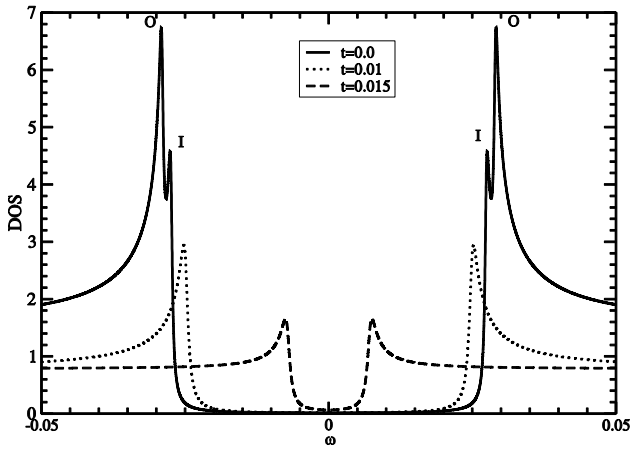

Figure 4. The conduction electron DOS at temperature t= 0.0, 0.01, and 0.015. The temperature dependence of the gap parameters z , z_1 and z_2 are taken from Figure 1.

higher temperatures. This shows that the SDW coupling plays an important role in enhancing the SC transition temperature and the magnitude of the pseudogap (CDW). With the increase of the SDW coupling (g_2), the CDW and the SC transition temperatures (t_c) are enhanced considerably, but the SDW transition temperature (t_n) nearly remains constant with gradual suppression of the SDW gap magnitude (see the inset of Figure 3). The present study shows that the SDW coupling plays a vital role in the pairing mechanism of cuprates. The spin fluctuation pairing mechanism is emphasized by several authors [17, 31].

The density of states (DOS) of the system represent the tunneling conductance measured by STM technique. Therefore, we have calculated the density of states from the spectral density function which is defined as $\rho_{k,\sigma}(\omega) = -2\pi ImG(k,\omega)$ where G is the conduction electron Green's functions. The plot of DOS is shown in Figure 4 for different temperatures, t=0, 0.01, 0.015. All the three phases such as SC, CDW and SDW co-exist at temperature $t = 0$. It is seen from Figure 4 that there appears two gaps at temperature t=0 i.e the outer gap, O-O with gap edges at $\pm(W + z_2) \simeq 0.0291$ and the inner gap, I-I with gap edges at $\pm(W - z_2) \simeq 0.0275$. These two gap edge values can be measured from the conductance data from the superconductor-insulator junction, STM or ARPES measurements. Applying our model calculation, the reduced SDW gap z_2 and the renormalised SC gap, $W \simeq \sqrt{z^2 + z_1^2}$ can be calculated. However, the individual magnitudes of the SC gap (z) and the CDW gap (z_1) cannot be calculated from our model calculation. The STM measurements [10] on the doped system LSCO with doping x=0 gives $\Delta_2 \simeq$ 5meV and $\Delta_1 \simeq$ 10meV. Our model calculation is applied to the system with $W + z_2 = 10meV$ and $W - z_2 = 5meV$. This gives the renormalised SC gap of $W = \sqrt{z^2 + z_1^2}$=7.5 meV and the smaller SDW gap z_2=2.5 meV. The renormalised SC gap (W) obtained from any tunneling measurements is higher than the actual SC gap. This is in agreement with the remarks made by the authors [10]. They have observed that the magnitude of the superconducting gap is not in simple agreement with the SC transition temperatures. Our model calculation can be applied similar to the tunneling measurements on other cuprate systems [11 - 13]. For the temperature range $t_N < t < t_c$ i.e at the temperature 0.01, the SDW phase disappears, but the CDW and SC phases co-exist. Therefore, we observe a single gap at t=0.01 in the DOS with gap edges at $\pm W = \sqrt{z^2 + z_1^2} = 0.0253$. Since the CDW and SC gaps are renormalised in the co-existence phase, it is not possible to find out the individual components of the two gap values. Thus, pseudogap (CDW) interferes with the SC gap, providing thereby an uncertainty in the measurement of the SC gap magnitude. Similarly a single gap structure with reduced gap size appears at temperature $t = 0.015$ in the vicinity of the SC transition temperature. The CDW state in cuprate systems acts as a pseudogap which exists in the normal state up to a temperature $t_d \simeq t_c$ as shown by the tunneling measurement for Bi-Sr-Ca-Cu-O system [9]. In the earlier model calculation by Panda et. al. [27], the SC and the CDW phases have competed with each other with the CDW transition temperature (t_d) being higher that of the SC transition temperature (t_c). The CDW phase lie in the region above t_c and below the pseudogap (CDW) transition temperature (t_d). They have shown that a gap (CDW pseudogap) still exists above t_c. In the present model calculation the pseudogap (CDW) phase lies inside the SC state and gives rise to a renormalized higher SC gap.

6. Conclusions

In the present communication, we consider the strong interplay between the charge density wave, spin density wave and superconducting order parameters within a mean-field approximation. The expressions for these three order parameters are derived from the correlation functions calculated from the corresponding single particle electron Green's functions. The order parameters are solved self-consistently for a set of the CDW coupling g_1=0.0445 and the SDW coupling g_2=0.0311 and the SC coupling g=0.09994 satisfying the experimental condition, $\Delta_s < \Delta < \Delta_c$. In this model the SDW and CDW gap are assumed to act as pseudogaps. The pseudogap (CDW) gap merge with the superconducting gap, thereby giving rise to a renormalised superconducting gap $W = \sqrt{z + z_c}$ which becomes higher than the pure superconducting gap. Rightly the authors [10] have found from their tunneling measurements that the magnitude of the superconducting gap is not simple agreement with the SC transition temperatures. With the increase of SC coupling the SDW gap is suppressed, while the SC and CDW gaps are enhanced throughout the temperature range. It is to note further that both the SC and CDW transition temperatures are coincident and are shifted to higher value with the increase of SC coupling. This shows a strong interplay between the CDW (pseudogap) and the SC interactions. Due to the competition of the pseudogaps (CDW and SDW) in the present model calculation, a smaller SC couplings (i.e. as compared to BCS weak coupling for metallic superconductors) gives higher SC transition temperature. With the increase of the SDW coupling, the SDW gap is suppressed gradually, but the SC and CDW gaps are enhanced considerably. In this case also the SC and CDW transition temperatures shift together to new higher value. Thus it is clear that the SDW coupling plays an important role in the enhancement of the SC transition temperature. This conclusion supports the spin-fluctuation mediated pairing mechanism advanced by several authors [17, 31]. We have calculated the density of states (DOS) of the conduction electrons from the imaginary part of the Green's functions. The DOS is directly related to the tunneling

conductance spectra obtained from the scanning tunneling microscopy. The DOS displays two gap structures i.e outer gap O-O with the gap edges at $\pm(W + z_2)$ and the inner gap, I-I with gap edges at $\pm(W - z_2)$ where the renormalised SC gap is $W = \sqrt{z^2 + z_1^2}$. From the measured gap edge values of the tunneling spectra one can calculate independently the renormalised SC gap W and the SDW gap z_2. At temperature $t > t_N$ the CDW and the SC gaps co-exist. Since these two gaps merge together giving rise to a single renormalised SC gap, we obtain only a single gap structure with gap edge values at $\pm W = \sqrt{z^2 + z_1^2}$ in the co-existence phase. The renormalised SC gap W is certainly higher than the true SC gap. This anomaly in the SC gap magnitude arises due to the pseudogap effect (in this case CDW gap).

Acknowledgements

The authors would like to gracefully acknowledge the research facilities offered by the Institute of Physics, Bhubaneswar and Institute of Mathematics and Applications, Bhubaneswar, available to them.

References

1. Peter Wahl, Nat. Phys. 8 (2012) 514.
2. Chandra Varma, Nature 468 (2010) 184.
3. S. Sachdev, Science 288 (2000) 475.
4. T. Hanaguri, C. Lupien et. al., Nature 430 (2004) 1001.
5. W. D. Wise, M. C. Boyer et. al., Nat. Phys. 4 (2008) 696.
6. V. J. Emery and S. A. Kivelson, Nature 374 (1995) 434.
7. Ø. Fischer, M. Kigles, I. M. Aprile, and C. Berthod, Rev. Mod. Phys. 79 (2007) 353.
8. T. Timusk and B. Statt, Rep. Prog. Phys. 62 (1999) 61.
9. T. Ekino, Y. Sezaki, H. Fujji, Phys. Rev. B. 60 (1999) 6916.
10. T. Kato, T. Maruyama, S. Okitsu, and H. Sakata, J. Phys. Soc. Jpn. 77 (2008) 054710.
11. T. Machida, Y. Kamijo, K. Harada, T. Noguchi, R. Saito, T. Kato and H. Sakata, J. Phys. Soc. Jpn. 75 (2006) 083708.
12. T. Yoshida, M. Hashimoto, I. M. Vishik, Z. Shen and A. Fujimori, J. Phys. Soc. Jpn. 81 (2012) 011006.
13. K. Tanaka, W. S. Lee et. al., Science 314 (2006) 1910.
14. Q. Huang, J. F. Zasadzinski, et. al., Phys. Rev. B 40 (1989) 9366.
15. D. S. Dessau et. al., Phys. Rev. Lett. 66 (1991) 2160.
16. Ch. Renner and Ø. Fischer, Phys. Rev. B. 51 (1995) 9208.
17. N. Jenkins, Y. Fasano et. al., Phys. Rev. Lett. 103 (2009) 227001.
18. H. F. Fong et. al., Nature 398 (1999) 588.
19. H. L. Edwards, A. L. Barr, J. T. Markert and A. L. de Lozanne, Phys. Rev. Lett. 73 (1994) 1154.
20. H. L. Edwards, D. J. Derro, A. L. Barr, J. T. Markert and A. L. de Lozanne, Phys. Rev. Lett. 75 (1995) 1387.
21. A. L. de Lozanne, Supercond. Sci. Technol. 12R (1999) 43 .
22. R. S. Gonnelli, A. Morello, G. A. Ummarino, D. Daghero, L. Natale, V. A. Stepanov, F. Licci and G. Ubertalli, (2000) (http://arxiv.org/abs/cond-mat/0003100).
23. S. V. Lubenets, V. D. Natsik and L. S. Fomenko, Fiz. Nizk. Temp. 21 (1995) 475 .
24. D. C. Johnston, S. K. Sinha, A. J. Jacobson, J. M. Newsam, Physica C 153-155 (1988) 572 .
25. J. R. Schrieffer, X. G. Wen, S. C. Zhang, Phys. Rev. Lett. 60 (1988) 944.
26. H. Ghosh, S. Sil, S. N. Behera, Physica C 316 (1999) 34.
27. S. K. Panda and G. C. Rout, Physica C 469 (2009) 702.
28. D. N. Zubarev, Sov. Phys. Usp. 3 (1960) 320.
29. Guo-meng Zhao, Phys. Scr. 83 (2011) 038302.
30. Guo-meng Zhao, Phys. Scr. 83 (2011) 038304.
31. N. M. Plakida, Phys. Scr. 83 (2011) 038303.

Cite this article as:

K. L. Mohanta *et al.*: **Theoretical study of pseudogap effect on the interplay of SDW and superconductivity in cuprates.** *Phys. Express* 2013, **3**: 29

Theoretical study of the interplay of spin-charge and orbital orderings in manganites

Saswati Panda[a,*], P. Purohit[b], G. C. Rout[c]

[a] *Trident Academy of Technology, F2/A, Chandaka Industrial Estate, Bhubaneswar -751 024, India*
[b] *D. A. V. College, Titilagarh, Balangir, India*
[c] *Condensed Matter Physics Group, P. G. Department of Applied Physics and Ballistics, F. M. University, Balasore - 756 019, India*

[*] *Author for correspondence: Saswati Panda, email: saswatip7@gmail.com*
Received 25 Aug 2012; Accepted 10 Dec 2012; Available Online 10 Dec 2012

Abstract

The doped rare-earth manganites exhibit a rich phase diagram due to several competing orders like charge, spin, orbital and lattice degrees of freedom. In order to study the complex properties of these systems, we report here a microscopic theoretical model. The model consists of band Jahn-Teller (JT) splitting in the e_g band due to the orbital ordering and the charge density wave (CDW) in the same e_g band arising due to the charge ordering for Mn^{3+} and Mn^{4+} ions. In addition to this we consider a double exchange model describing the spin-spin interaction among the e_g and localized core t_{2g} electrons. Due to Hund's rule coupling, the core electrons provide strong ferromagnetism which aligns the e_g spins ferromagnetically. Further, the model consists of Heisenberg type direct spin-spin interaction among the t_{2g} core electrons. Thus the model provides a strong interplay among the JT distortion, charge-ordering and ferromagnetism in the conduction band and this finally gives rise to complex properties of the manganite system. It is observed that both the CDW coupling and the static JT coupling strongly change the CDW transition temperature and the lattice distortion temperature, while it enhances the magnitude of e_g magnetization at low temperatures keeping the ferromagnetic transition temperature (T_c) unchanged due to strong Hund's rule coupling. On the other hand, the double exchange coupling enhances ferromagnetic Curie temperature and also the magnitude of the induced magnetization in the e_g electron band increases to a large extent. It is expected that this interplay will influence the magnetoresistance of the system as observed by the experiments. These results will be reported.

Keywords: Colossal magneto-resistance; Jahn-Teller effect; Magnetization; Charge-density waves

1. Introduction

The family of rare-earth perovskite manganites [$R_{1-x}A_xMnO_3, R =$ rare-earth, A=Ba, Sr, Ca] has revealed very interesting features like complex interplay of charge, spin and orbital degrees of freedom [1, 2]. Like other strongly correlated systems, the orbital physics plays a crucial role in governing the charge transfer and the magnetic properties like the colossal-magnetoresistance (CMR) near the Curie temperature (T_c) of manganites [3]. The substitution of the rare-earth ion R^{3+} by a divalent cation A^{2+} generates Mn^{4+} ion leading to double exchange interaction and a simultaneous observation of metallic and ferromagnetic character [4, 5]. The strength of the double exchange (DE) interaction in the Nd-based systems is eventually weaker than in the La-based systems, due to possible larger lattice distortion produced by the smaller Nd ions [6]. Consequently, a closer competition would exist between the electron-phonon, electron-electron and double exchange interactions in a system like $Nd_{1-x}Ca_xMnO_3$(NCMO) [7,8]. The manganite $La_{1-x}Ca_xMnO_3$ (LCMO) [9,10] exhibits extremely rich phase diagram due to competition between the tendency of electrons to delocalize and the simultaneous presence of interactions like magnetism, Coulomb repulsion and electron-phonon coupling. The spectroscopic measurements on $Pr_{0.7}Ca_{0.3}MnO_3$ [11] show a peak at $25cm^{-1}$ and a broad shoulder at lower frequencies which attribute to the CDW collective excitations. In the optical conductivity of manganites with commensurate charge ordering, strong CDW excitation peak appears in meV range below T_{co} for frequency $\omega > 2\Delta$, with CDW gap of $2\Delta(T=0) \simeq 800cm^{-1}$ or 0.1 meV for LCMO, $\sim 0.2meV$ in $Nd_{1/2}Ca_{1/2}MnO_3$(NCMO) [12]. In several manganites, the CO phase can be described [13] in terms of charge density wave (CDW) model [14, 15], which assumes weak electron-phonon coupling.

In doped manganites, metallic ferromagnetic (FM), insulating paramagnetic (PM), antiferromagnetic (AFM) and charge/orbital ordered states are among the competing ground states [16]. To explain the CMR phenomenon, Zener has proposed the double exchange (DE) mechanism [17]. According to this model the itinerant e_g electrons can hop between Mn^{3+} and Mn^{4+} ions via O^{2-} ion. In order to do so the spins of the e_g electrons have to remain parallel to those of the core t_{2g} electrons, because the Hund's coupling makes the system behaving like a ferromagnetic metal. The ferromagnetic Hund's rule exchange coupling between the spins of itinerant e_g and the localized t_{2g} electrons, their interaction strength with Jahn-Teller (JT) phonons or the CDW state and the Coulomb correlations, are believed to be responsible for different phenomena observed in manganites, but that has so far not been very clear. Though double exchange (DE) interaction [17] can promote the ferromagnetic metallic state in manganites, this is not sufficient to explain the observed large resistivity near T_c. Millis et. al. [18, 19] and others [20-23] have proposed other effects like JT distortion, spin-phonon interactions and polaron effects in order to explain the insulating phase above the Curie temperature (T_c). In manganites, the band structure is anisotropic which leads to the splitting of the JT levels as shown by the calculations of Takahashi et. al. [24]. A review on co-operative JT effects and

its consequences on different systems has been reported earlier [25]. Kanamori has reported the splitting of JT levels due to co-operative JT effect and applied to specific systems taking into account the pseudo-spin operators in semi-classical approximations [26]. Recently Rout et. al. [27-30] have employed Jahn-Teller effect to explain magnetoresistivity above T_c. More recently, Rout and co-workers have reported the theoretical investigations of the effect of charge ordering on the physical properties like magnetization [31], velocity of sound [32], magnetic spin susceptibility [33] and Raman spectra [34] for the manganite systems. In the present communication, we consider the Kondo-Heisenberg interaction along with the JT distortion and CDW interaction as the extra mechanisms to account for the insulating phase just above T_c. The rest of the work is as follows: The model Hamiltonian is described in section 2. The gap equations are calculated in section 3. The results and discussion are presented in section 4, and finally the conclusion in section 5.

2. The model Hamiltonian

The general structure of the doped manganites, $R_{1-x}A_xMnO_3$ is a perovskite structure. The manganese ions sitting at the center of the cube and oxygen ions lying at the face centers form MnO_6 octahedron. The alkaline-earth metallic ion (A) is substituted at the rare-earth ionic site (R) with a concentration of x. In the manganite systems double exchange (DE) interaction can promote the ferromagnetic metallic state, whereas the JT distortion is likely to promote the insulating phase. It can be visualized that when $Mn-O-Mn$ bond bends it enhances the JT distortion thereby reducing the band width as well as the DE interaction. Also the JT distortion itself can get altered because of the DE interaction. When DE interaction is enhanced, the JT distortion is suppressed due to the straightening of the $Mn-O-Mn$ bond. This competition between the JT distortion and the DE interaction can cause metal-insulator transition in the doped manganites. Externally applied magnetic field enhances metallic behaviour of manganites by enhancing DE interaction and suppresses the JT distortion as well as the insulating phase. Further, Peierls type periodic lattice distortion in the system is associated with a spatially periodic modulation of the electronic charge density, called charge density wave (CDW). The formation of CDW opens up an insulating gap at the Fermi level, lowering the kinetic energy of the conduction electrons. In the model calculation, we consider the Jahn-Teller effect and the CDW interaction as the two extra mechanisms in addition to the Kondo-Heisenberg interaction to explain the CMR effect just above the Curie temperature. The electronic part of the model Hamiltonian consists of the e_g electron Hamiltonian, the $s-d$ type double exchange interaction and the t_{2g} electron Hamiltonian besides the JT interaction. The Hamiltonian is written as

$$H_{el}^{JT} = \sum_{\alpha,k,\sigma} \varepsilon_{k,\sigma} c_{\alpha,k,\sigma}^{\dagger} c_{\alpha,k,\sigma} - \sum_{\alpha,k,\sigma} (-1)^{\alpha} Ge c_{\alpha,k,\sigma}^{\dagger} c_{\alpha,k,\sigma} - J \sum_{\alpha,i} \sigma_{\alpha,i}.S_i + \sum_{k,\sigma} (\varepsilon_d - \mu^d B\sigma) d_{k,\sigma}^{\dagger} d_{k,\sigma} - J_H \sum_{<i,j>} S_i.S_j + \frac{1}{2}Ce^2. \quad (1)$$

The first term in the Hamiltonian H_{el}^{JT} describes two degenerate orbitals $(\alpha = 1,2)$ for conduction electrons with band energy $\varepsilon_{k,\sigma} = (\varepsilon_0(k) - \mu - \sigma\mu_B B)$, where μ, μ_B and B are the chemical potential, Bohr magneton and external magnetic field respectively with $\sigma = +1$ or -1 depending on spin up or spin down states and $c_{\alpha,k,\sigma}(c_{\alpha,k,\sigma}^{\dagger})$ being the annihilation (creation) operator for the electrons in the e_g band. The partially filled e_g band of the manganese ion gives rise to Jahn-Teller (JT) effect in the d-electrons. The two electron bands are separated by a JT gap of $2Ge$, where G is the static JT coupling and e represents the lattice strain. The third term represents the $s-d$ double exchange interaction. In the fourth term ε_d is the position of the t_{2g} core level with respect to Fermi level $(\varepsilon_F = 0)$, μ^d is the magnetic moment of the core electron and $d_{k,\sigma}^{\dagger}(d_{k,\sigma})$ is the creation (annihilation) operator of the core electron. The fifth term describes the nearest neighbour Heisenberg type spin-spin interaction for the t_{2g} electrons, which produces ferromagnetism in the crystal. The last term in Eq. (1) is the elastic energy which is minimized to find the temperature dependent lattice strain e in equilibrium condition. The Hamiltonian representing the charge density wave (CDW) in the e_g band is written as

$$H_{CDW} = \Delta \sum_{\alpha,k,\sigma} c_{\alpha,k,\sigma}^{\dagger} c_{\alpha,k+Q,\sigma} \quad (2)$$

where Δ is the CDW gap parameter. The CDW state has a super periodicity where Q becomes the new reciprocal lattice vector with a corresponding reduced Brillouin's zone. This satisfies the nesting property, i.e. $\varepsilon_{k+Q} = -\varepsilon_k$, with a periodic wave vector Q.

In the present calculation, this interaction is considered within Ising type mean-field approximation giving emphasis only to the strong ferromagnetic molecular magnetization (M^d) arising due to the localized core t_{2g} electrons. It will be shown that the magnetization M^c will be induced in the e_g band due to the ferromagnetism present in the core t_{2g} electrons. The origin of the magnetization M^c induced in the e_g band is due to the double exchange (DE) interaction. The total Hamiltonian of the e_g and t_{2g} band electrons is given by

$$H = \sum_{\alpha,k,\sigma} \varepsilon_{\alpha,k,\sigma} c_{\alpha,k,\sigma}^{\dagger} c_{\alpha,k,\sigma} + \Delta \sum_{\alpha,k,\sigma} c_{\alpha,k,\sigma}^{\dagger} c_{\alpha,k+Q,\sigma} + \sum_{k,\sigma} \varepsilon_{d,\sigma} d_{k,\sigma}^{\dagger} d_{k,\sigma} + \frac{1}{2}Ce^2 \quad (3)$$

Here the band energy $\varepsilon_{\alpha,k,\sigma} = (\varepsilon_0(k) - \mu - \sigma\mu_B B) + JM^d\sigma/2 - (-1)^{\alpha}Ge$, with J and M^d being the $s-d$ type double exchange (DE) coupling constant and magnetization in the t_{2g} band respectively. In the third term $\varepsilon_{d,\sigma} = \varepsilon_d - \sigma[B - (JM^c + J_H M^d)/2]$, where J_H and M^c are Heisenberg coupling constant and induced magnetization in the e_g band respectively. The e_g electron magnetization (M^c), the lattice strain (e), the CDW order parameter (Δ) and the core electron magnetization (M^d) are calculated from the electron Green's functions.

3. Calculation of gap equations

Using the total Hamiltonian, the double time single particle electron Green's functions are calculated by using the Zubarev's technique [35]. The Green's functions for the conduction electrons in e_g bands corresponding to the two orbitals $(\alpha = 1,2)$ and spins $(\sigma = \uparrow, \downarrow)$ are

$$A_1(\alpha,k,\omega) = << c_{\alpha,k,\sigma}; c^{\dagger}_{\alpha,k,\sigma} >>_{\omega} = \frac{1}{2\pi}\frac{(\omega-\bar{\varepsilon}_{\alpha,k,\sigma})}{2E_k}\{\frac{1}{\omega-\omega_{1\alpha\sigma}} - \frac{1}{\omega-\omega_{2\alpha\sigma}}\}$$

$$A_2(\alpha,k,\omega) = << c_{\alpha,k+Q,\sigma}; c^{\dagger}_{\alpha,k,\sigma} >>_{\omega} = \frac{1}{2\pi}\frac{\Delta}{2E_k}\{\frac{1}{\omega-\omega_{1\alpha\sigma}} - \frac{1}{\omega-\omega_{2\alpha\sigma}}\} \quad (4)$$

where

$$\bar{\varepsilon}_{\alpha,k,\sigma} = \varepsilon(k+Q) - \mu - \sigma\mu_B B + JM^d\sigma/2 - (-1)^{\alpha}Ge$$

$$E_k^2 = \varepsilon_k^2 + \Delta^2$$

$$\omega_{1\alpha\sigma} = -\mu - \sigma\mu_B B + JM^d\sigma/2 - (-1)^{\alpha}Ge + E_k$$

and

$$\omega_{2\alpha\sigma} = -\mu - \sigma\mu_B B + JM^d\sigma/2 - (-1)^{\alpha}Ge - E_k$$

The average occupation numbers of up and down spin e_g electrons are

$$n^c_{\alpha,k,\sigma} = \frac{1}{N}\sum_k < c^{\dagger}_{\alpha,k,\sigma}c_{\alpha,k,\sigma} >= \frac{1}{N}\sum_k \frac{1}{2E_k}[(\varepsilon_k + E_k)f(\omega_{1\alpha\sigma}) - (\varepsilon_k - E_k)f(\omega_{2\alpha\sigma})] \quad (5)$$

The induced mean-field magnetization in e_g electrons is defined as

$$M^c = Nm^c = -\sum_{\alpha}(n^c_{\alpha,\uparrow} - n^c_{\alpha,\downarrow}) = -\sum_{\alpha,k}\frac{1}{2}[(\varepsilon_k + E_k)\{f(\omega_{1\alpha\uparrow}) - f(\omega_{1\alpha\downarrow})\} - (\varepsilon_k - E_k)\{f(\omega_{2\alpha\uparrow}) - f(\omega_{2\alpha\downarrow})\}] \quad (6)$$

The temperature dependent static lattice-strain (e) is given by

$$e = -\frac{G}{C}\sum_{\alpha,k,\sigma}[-(-1)^{\alpha} < c^{\dagger}_{\alpha,k,\sigma}c_{\alpha,k,\sigma} >] = -\frac{G}{C}\sum_{k,\sigma}[(\varepsilon_k + E_k)\{f(\omega_{11\sigma}) - f(\omega_{12\sigma})\} - (\varepsilon_k - E_k)\{f(\omega_{21\sigma}) - f(\omega_{22\sigma})\}] \quad (7)$$

The charge density wave order parameter

$$\Delta = -V_0\sum_{\alpha,k,\sigma} < c^{\dagger}_{\alpha,k,\sigma}c_{\alpha,k+Q,\sigma} >= -V_0\sum_{\alpha,k,\sigma}\frac{\Delta}{2E_k}[f(\omega_{1\alpha\sigma}) - f(\omega_{2\alpha\sigma})] \quad (8)$$

The Green's function for the t_{2g} band electrons is

$$B(k,\omega) = << d_{k,\sigma}; d^{\dagger}_{k,\sigma} >>_{\omega} = \frac{1}{2\pi(\omega-\varepsilon_{d,\sigma})} \quad (9)$$

where $\varepsilon_{d,\sigma} = \varepsilon_d - \{B - (JM^c + J_H M^d)/2\}\sigma$

The average occupation numbers for up and down spin t_{2g} electrons are

$$n^d_{\sigma} = \frac{1}{N}\sum_{k,\sigma} < d^{\dagger}_{k,\sigma}d_{k,\sigma} >= \frac{1}{N}\sum_{k,\sigma} f(\varepsilon_{d\sigma}) \quad (10)$$

The magnetization M^d for the localized t_{2g} electrons is found to be

$$M^d = Nm^d = -(n^d_{\uparrow} - n^d_{\downarrow}) = -3\frac{1}{N}\sum_k [f(\varepsilon_{d\uparrow}) - f(\varepsilon_{d\downarrow})] \quad (11)$$

As three electrons are present in the t_{2g} level, 3 is multiplied to the expression for M^d. Here $f(x) = 1/\{1 + exp(x/k_BT)\}$ is the Fermi-Dirac distribution function. While calculating, the temperature dependent parameters like CDW gap (Δ), lattice strain (e) and the conduction electron magnetization (m^c), we have taken the sum over the spins and the sum over the wave vector k is replaced by an integration over the energy $\varepsilon(k)$ as $\Sigma_k = \int_{-D}^{+D} N(\varepsilon)d\varepsilon$, where $N(\varepsilon)$ is the density of states (DOS)[27] and $2D$ is the total band width W of the conduction band. Here, $N(\varepsilon)$ simulates its strong energy dependence around the center of the band due to a logarithm singularity. The model DOS is assumed to be of the form

$$N(\varepsilon) = N(0)\sqrt{1 - |\frac{\varepsilon}{D}|ln|\frac{D^2}{\varepsilon^2}|} \quad (12)$$

where, $N(0)$ is the unperturbed DOS of the conduction band electrons at the Fermi level. Since these temperature dependent physical quantities are integral equations and involved functions of each other, they are computed together self-consistently. All these physical quantities are made dimensionless by scaling with respect to the conduction band width W, and the dimensionless parameters are: the double exchange coupling $g = J/W$, the CDW coupling $g_1 = V_0N(0)/W$, the Heisenberg coupling of core electrons $g_2 = J_H/W$, the static JT coupling $g_3 = G/W$, the reduced CDW order parameter $z = \Delta/W$, the reduced temperature $t = k_BT/W$, the external magnetic field $b = B/W$, and reduced core level position $d = \varepsilon_d/W$. The variations of the dimensionless parameters z, m^d, m^c, e for dimensionless temperature are shown in Figures 1-3.

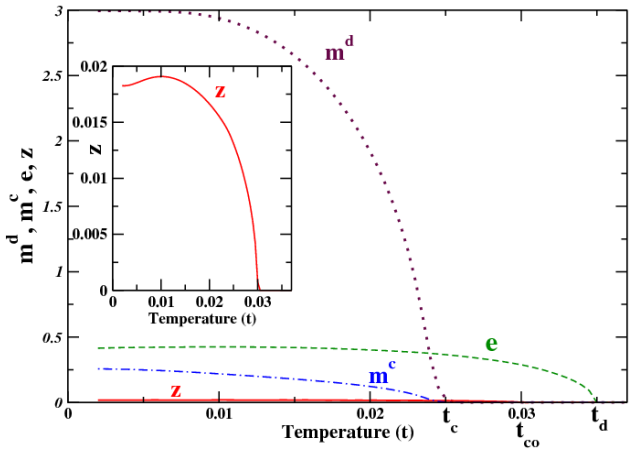

Figure 1. The self-consistent plot of core-electron magnetization (m^d) versus temperature (t), CDW gap (z) versus temperature (t), lattice strain (e) versus temperature (t) and induced magnetization (m^c) in the e_g band versus temperature (t) for fixed $s-d$ exchange coupling $g = 0.01$, CDW coupling $g_1 = 0.0515$, core-spin coupling $g_2 = 0.031$ and static JT coupling $g_3 = 0.0875$. The inset shows the magnified plot of z versus temperature.

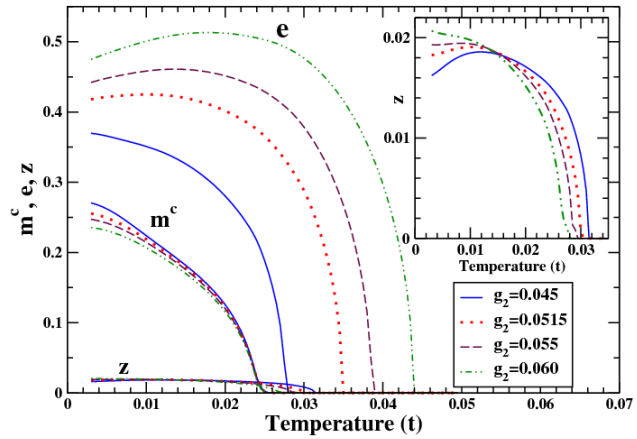

Figure 2. The temperature dependence of m^c, e and z in e_g band for different values of CDW coupling $g_1 = 0.045,\ 0.0515,\ 0.055, 0.060$ and other parameters being same as Figure 1. The inset shows the magnified plot of z versus temperature.

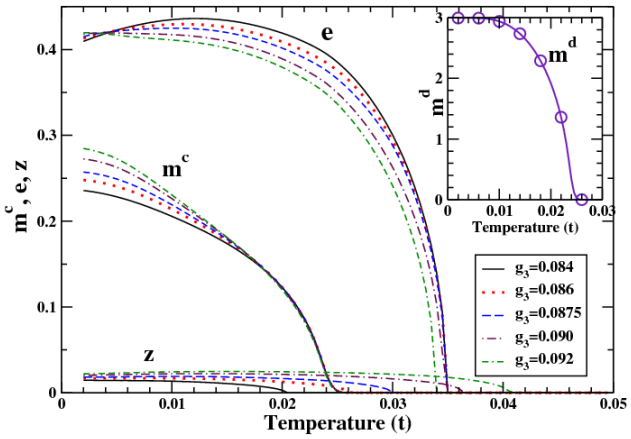

Figure 3. The temperature dependence of m^c, e and z for different values of static JT coupling $g_3 = 0.084,\ 0.086,\ 0.0875,\ 0.090,\ 0.092$ and other parameters being same as Figure 1. The inset figure shows the temperature dependence of m^d for the above values of g_3.

4. Results and Discussion

Temperature dependence of core electron magnetization (m^d), lattice strain (e), CDW gap (z), and the induced conduction electron magnetization (m^c) within this theoretical model can be studied by varying different model parameters of the manganite system. The temperature variation of m^d, m^c, e and z are used to study the interplay of these long range orders choosing a set of parameters of the system such as the double exchange coupling $g = 0.01$, the CDW coupling $g_1 = 0.0515$, the Heisenberg coupling $g_2 = 0.031$ and the static JT coupling $g_3 = 0.0875$ in absence of magnetic field (i.e. $b = 0$), with chemical potential $\mu = 0$ and core level position $d = 0$. In this model the Kondo-Heisenberg model is treated within a mean-field approximation in presence of the lattice strain and the CDW gap. It is assumed that there is one conduction electron and three core electrons in the system satisfying the constraint $n^c + n^d = 4 - x$. Here m^d, m^c, e and z are solved self-consistently and then their temperature dependencies are shown in Figure 1 for the fixed set of coupling constants. Such a phase change from paramagnetic to ferromagnetic state near T_c has been studied experimentally [36-38]. Similar CDW interaction gap appears at 0.1 meV for $La_{1-x}Ca_xMnO_3$, at 0.2 meV for $Nd_{1/2}Ca_{1/2}MnO_3$ [12], at 0.3 eV in $Nd_{0.5}Sr_{0.5}MnO_3$ [39]. In this model we have chosen the ferromagnetic Curie temperature $t_c = 0.025\ (i.e. T_c = 250K)$, the charge ordering temperature $t_{co} = 0.030\ (i.e. T_{co} = 300K)$ and the lattice distortion temperature $t_d = 0.035\ (i.e. T_d = 350K)$ for a band width (W) of $1eV$, such that $t_c < t_{co} < t_d$. The system displays pure lattice distortion phase for $t_{co} < t < t_d$, and the phase of interplay between CDW and lattice strain for $t_c < t < t_{co}$. Since ferromagnetism is induced in e_g electron band due to the ferromagnetism in t_{2g} core electrons through double exchange mechanism, the magnetic transition temperature is same for both e_g and t_{2g} electrons. However, the magnitude of m^c is much smaller compared to m^d. A strong interplay of m^d, m^c, e and z is expected below the Curie temperature. This interplay is studied below through Figures 2 and 3. Rout et. al. [30] have reported a very strong insulating phase just above t_c. Similar insulating phase is expected above the Curie temperature due to the presence of combined effect of CDW and lattice distortion just above the Curie temperature. The calculation for resistivity within the present model is in progress and will be reported elsewhere.

In the present model, the CDW interaction provides an extra mechanism to produce a strong insulating phase above the Curie temperature. The effect of CDW coupling g_1 on magnetization is shown in Figure 2. It is observed that with the increase of CDW coupling, both the CDW gap and the lattice strain are enhanced considerably at very low temperatures. As a result, the induced magnetization (m^c) is correspondingly suppressed at low temperatures. This type of suppression of magnetization at low temperatures is observed in the experimental datas on $Nd_{0.5}Sr_{0.5}MnO_3$ [40], $Pr_{0.5}Sr_{0.5}MnO_3$ [41] and $La_{1-x}Ca_xMnO_3$ at $x = 0.15$ [42]. Recently, theoretical model studies of large M-I transition near T_c in doped manganite systems is done separately considering CDW interaction [31] and band JT distortion [30] as extra mechanisms along with DE interaction. It is seen that due to strong interplay between charge ordering and ferromagnetism, the magnetization in e_g band is suppressed considerably at lower temperatures where the CDW gap is robust. Also, the CDW gap is found to be suppressed when magnetization in e_g electrons increases [31]. A similar effect is observed in the presence of JT interaction. The temperature dependence of both magnetization in e_g band and lattice strain due to JT distortion shows suppression at low temperatures [30], in the co-existence phase of ferromagnetism and JT distortion. This type of behaviour is also observed in the Jahn-Teller gap calculated based on a model Hamiltonian of Kondo model [43-45]. Above the Curie temperature in paramagnetic phase, with the increase of CDW coupling, the lattice strain as well as the lattice distortion temperature (t_d) are enhanced, whereas the CDW gap and the charge ordering temperature (t_{co}) are suppressed. However, the Curie temperature remains unchanged under this condition. It is expected that a strong insulating phase will appear above t_c and this will be strongly influenced by the interplay of lattice distortion and CDW interaction. Similar high resistivity arising due to lattice distortion has been reported earlier by Rout et. al. [29, 30].

In this present model the JT lattice distortion provides another extra mechanism to produce a strong insulating phase

just above the Curie temperature in the manganite systems. The effect of JT coupling (g_3) on the temperature dependent parameters i.e. m^d, m^c, e and z are shown in Figure 3. The interplay of lattice strain (e) and CDW gap (z) due to the variation of JT coupling shows very interesting effects. With increase of JT coupling (g_3), the lattice strain shows very small suppression at lower temperatures, whereas the CDW gap present in the conduction band is enhanced. Consequently, the induced magnetization (m^c) in the e_g electron band is enhanced at low temperatures. The JT coupling has no effect on the robust magnetization m^d arising due to the t_{2g} core electrons. It is to note further that the Curie temperature remains unchanged even due to the variation of JT coupling. On the other hand the effect of JT coupling on e and z is very profound above the Curie temperature in the paramagnetic phase. With increase of JT coupling the lattice strain above t_c and the lattice distortion temperature are suppressed, whereas the CDW gap is enhanced considerably throughout the temperature range and so also the charge ordering temperature (t_{co}). Thus the interplay shows that the charge ordering dominates over lattice distortion above t_c due to the variation of JT coupling. We expect that the resistivity arising above the Curie temperature will be strongly influenced by the interplay between the Jahn-Teller distortion and CDW interaction.

5. Conclusions

In the model calculation we have considered the JT effect and the CDW interaction as two extra mechanisms besides the double exchange interaction in order to study the CMR effects in manganites. The magnetic aspect of the system is considered within an Ising type mean-field approximation for ferromagnetism arising purely due to t_{2g} core electrons. The lattice strain, the CDW gap and the magnetization are calculated by Green's function technique and solved self-consistently. For a set of parameters we have fixed the JT distortion temperature (t_d) and the charge ordering temperature (t_{co}) above the Curie temperature. The effect of charge ordering coupling and the JT coupling on m^d, m^c, e and z are investigated. With the increase of CDW coupling, e and z are enhanced, while conduction electron magnetization (m^c) is suppressed at low temperatures as observed in several experiments [40-42] and theoretical model studies [30, 31]. Above Curie temperature the interplay of e and z are such that the charge ordering temperature is suppressed, but lattice distortion temperature is enhanced. With increase of JT coupling, the lattice strain is less suppressed at low temperatures, while the CDW gap is enhanced to a large extent. The e_g electron magnetization is enhanced at low temperatures with increase of JT coupling. Above Curie temperature, with increase of JT coupling, the lattice distortion temperature is suppressed, while the CDW gap and charge ordering temperature are enhanced considerably. The interplay of the charge ordering and the lattice strain is expected to have a great bearing on the magnetoresistivity above Curie temperature.

Acknowledgements

The authors would like to gracefully acknowledge the research facilities of the Institute of Physics, Bhubaneswar, available to them.

References

1. Y. Tokura (Ed.), Colossal Magnetoresistance oxides, Gordon and Breach, New York (2000).
2. M. B. Salamon, M. Jaime, Rev. Mod. Phys. 73 (2001) 583.
3. Y. Tokura, N. Nagaosa, Science 288 (2000) 462.
4. S. Jin, T. H. Tiefel, M. McCormack, R. A. Fastnatcht, R. Ramesh, L. H. Chen, Science 264 (1994) 413.
5. D. I. Khomskii, G. A. Sawatzky, Solid State Commun. 102 (1997) 87.
6. V. Caignaert, F. Millange, M. Hervieu, E. Suard, B. Raveau, Solid State Commun. 99 (1996) 173.
7. M. Tokunage, N. Miura, Y. Tomioka, Y. Tokura, Phys. Rev. B. 57 (1998) 5259.
8. S. Jandl, S. N. Barilo, S. V. Shiryaev, A. A. Mukhin, V. Yu. Ivanov, A. M. Balbashov, J. Magn. Magn. Mater. 264 (2003) 36.
9. C. H. Chen, S-W. Cheong, Phys. Rev. Lett. 76 (1996) 4042.
10. S. Mori, C. H. Chen, S-W. Cheong, Nature 392 (1998) 473.
11. N. Kida, M. Tonouchi, Phys. Rev. B. 66 (2002) 024401.
12. A. Nucara, P. Maselli, P. Calvani, R. Sopracase, M. Ortolani, G. Gruener, M. C. Guidi, U. Schade, J. Garcia, Phys. Rev. Lett. 101 (2008) 066407.
13. G. C. Milward, M. J. Calderon, P. B. Littlewood, Nature 433 (2005) 607.
14. P. A. Lee, T. M. Rice, P. W. Anderson, Solid State Commun. 14 (1974) 703.
15. G. Grüner, Rev. Mod. Phys. 60 (1988) 1129.
16. Y. Tokura, Rep. Prog. Phys. 69 (2006) 797.
17. C. Zener, Phys. Rev. 81 (1951) 440; C. Zener, Phys. Rev. 82 (1951) 403.
18. A. J. Millis, P. B. Littlewood, B. I. Shraiman, Phys. Rev. Lett. 74 (1995) 5144.
19. M. J. Calderon, J. A. Verges, L. Brey, Phys. Rev. B. 59 (1999) 4170.
20. H. Röder, J. Zang, A. R. Bishop, Phys. Rev. Lett. 76 (1996) 13569.
21. A. S. Alexandrov, G-M Zhao, H. Keller, B. Lorenz, Y. S. Wang, C. W. Chu, Phys. Rev. B. 64 (2001) 140404.
22. E. Granado, A. Garcia, J. A. Sanjurjo, C. Rettori, I. Torriani, F. Prado, R. D. Sanchez, A. Caneiro, S. B. Oseroff, Phys. Rev. B. 60 (1999) 11879.
23. A. J. Millis, B. I. Shraiman, R. Mueller, Phys. Rev. Lett. 77 (1996) 175.
24. A. Takahashi, H. Shiba, Eur. Phys. J. B 5 (1998) 413.
25. G. A. Gehring, K. A. Gehring, Rep. Prog. Phys. 38 (1975) 1.
26. J. Kanamori, J. Appl. Phys. 31 (1960) 14S.
27. G. C. Rout, N. Parhi, S. N. Behera, Int. J. Mod. Phys. B 20 (2006) 2093.
28. G. C. Rout, N. Parhi, S. N. Behera, Physica B 387 (2007) 259.
29. G. C. Rout, N. Parhi, S. N. Behera, Physica B 404 (2009) 2315.
30. G. C. Rout, S. Panda, S. N. Behera, J. Phys.: Condens. Matter 23 (2011) 396001.
31. G. C. Rout, S. Panda, S. N. Behera, Physica B 404 (2009) 4273.
32. G. C. Rout, S. Panda, J. Phys.: Condens. Matter 21 (2009) 416001.
33. G. C. Rout, S. Panda, Solid State Commun. 150 (2010) 613.
34. G. C. Rout, S. Panda, S. N. Behera, J. Phys.: Condens. Matter 22 (2010) 376003.
35. D. N. Zubarev, Sov. Phys. Usp. 3 (1960) 320.
36. R. W. Li, H. Wang, X. Wang, X. Z. Yu, Y. Matsui, Z. H. Cheng, B. G. Shen, E. W. Plummer, J. Zhang, PNAS 106 (2009) 14224.
37. A. Urushibara, Y. Moritomo, T. Arima, A. Asamitsu, G. Kido, Y. Tokura, Phys. Rev. B. 51 (1995) 14103.
38. P. Schiffer, A. P. Ramirez, W. Bao, S. W. Cheong, Phys. Rev. Lett. 75 (1995) 3336.

39. A. Biswas, A. K. Raychaudhuri, R. Mahendiran, A. Guha, R. Mahesh, C. N. R. Rao, J. Phys.: Condens. Matter 9 (1997) L355.
40. H. Kuwahara, Y. Tomioka, A. Asamitsu, Y. Moritomo, Y. Tokura, Science 270 (1995) 961.
41. Y. Tomioka, A. Asamitsu, Y. Moritomo, H. Kuwahara, Y. Tokura, Phys. Rev. Lett. 74 (1995) 5108.
42. M. Pissas, I. Margiolaki, G. Papavassiliou, D. Stamopoulos, D. Argyriou, Phys. Rev. B. 72 (2005) 064425.
43. G. G. Reddy, T. V. Rao, A. Ramakanth, S. K. Ghatak, S. N. Behera, Int. J. Mod. Phys. B 22 (2008) 423.
44. G. G. Reddy, A. Ramakanth, S. K. Ghatak, S. N. Behera, W. Nolting, T. V. Rao, Phys. Rev. B. 74 (2006) 134403.
45. M. Steir, W. Nolting, Phys. Rev. B. 75 (2007) 144409.

Cite this article as:

Saswati Panda *et al.*: **Theoretical study of the interplay of spin-charge and orbital orderings in manganites.** *Phys. Express* 2013, **3**: 30

First - principles calculations of electronic structure, optical properties and phase instability of potassium dihydrogen arsenate

G. Sriprakash[a,*], S. N. Prabhava[b], K. P. Ramesh[c], K. Rukmani[a]

[a] *Department of Physics, Bangalore University, Bangalore-560056, India*
[b] *CeNSE, Indian Institute of Science, Bangalore-560012, India*
[c] *Department of Physics, Indian Institute of Science, Bangalore-560012, India*

[*] *Author for correspondence: G. Sriprakash, email: sriprakash72@gmail.com*
Received 19 Nov 2012; Accepted 20 Dec 2012; Available Online 20 Dec 2012

Abstract

We have carried out first- principles calculations using density functional theory (DFT) and estimated electronic structure, optical properties and phase instability of tetragonal KDA. Born effective charges (Z^*) of different atoms in potassium dihydrogen arsenate (KDA) and potassium dihydrogen phosphate (KDP) have been evaluated and it is found that the zz component of Z^* for arsenic is smaller than that of phosphorous indicating the low contribution to the dipole moment due to distortion of AsO_4 ion compared to that of PO_4 ion. The reasons for deviation from linear relation between O-H--O bond distance (R) and T_c have been discussed. The negative phonon frequencies (B_2 and E) reveal instability of the tetragonal KDA. The Raman frequencies obtained from of density functional perturbation theory (DFPT) calculations are found to be in very good agreement with experimental data. The calculations made considering the pressure effect on KDA show the absence of unstable modes confirming the validity of DFPT.

Keywords: Electronic states; Reflectivity spectra; Born effective charge tensor; Phonon frequencies

1. Introduction

Hydrogen bonded ferroelectrics (HB) have attracted a lot of attention for the nature of phase transitions and their electro-optical applications [1]. Potassium dihydrogen phosphate (KDP) is the prototype of such hydrogen bonded ferroelectrics characterized by covalently bonded PO_4 units connected by a network of O-H---O hydrogen bonds and ionic bonding between potassium cations and H_2PO_4 anions. Potassium dihydrogen arsenate (KDA) is a member of the KDP family with a crystal structure isomorphic to tetragonal KDP at room temperature and belongs to space group D_{2d} with Z=2 as shown in Figure 1. At ferroelectric transition temperature T_c=94K, it undergoes transition from paraelectric (D_{2d}) to ferroelectric (C_{2v}) phase [2]. In the paraelectric phase hydrogen is disordered between two equivalent positions with equal probability along O-H---O bond [3]. In the proton tunneling model proposed by Blinc *et al* the equilibrium positions of H ion to the left or right of the centre of O-O bond are described by the pseudo spin S_Z, which takes values +1 and -1 respectively. The tunneling motion of hydrogen between these two positions and its propagation in the system can be described as pseudo spin wave. At phase transition temperature T_c, pseudospin wave condenses resulting in ferroelectric transition. The displacement of arsenate or phosphate ions along c axis is triggered by proton ordering in the basal plane as seen in the optical phonon mode at T_c [3] by Raman and IR measurements.

A linear correlation between T_c and O-H---O bond distance (R) for tetragonal KDP family is reported [4]. However, KH_2AsO_4 (KDA) and KD_2AsO_4 (KD^*A) show considerable deviation from such linear behavior [5]. Structural studies of KDA and KD^*A have revealed that the bond distance R is larger than that of KDP, in spite of having T_c lower than the other.

A systematic study of structural parameters influencing phase transition of KDP like systems has revealed

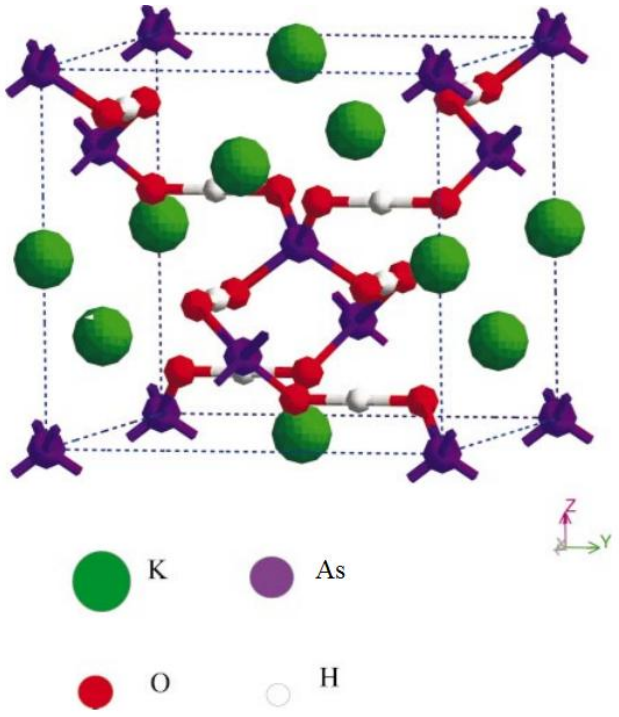

Figure 1. Crystal structure of tetragonal KDA. The hydrogen atoms are located at two equilibrium positions, which have two fold symmetry along *x* or *y* directions at the centre of O-H--O bond.

other parameters like degree of distortion and packing of cations contribute to the T_c in addition to the bond distance [5].

The first principles calculations of electronic structure of potassium dihydrogen phosphate (KDP) and proton transfer potential energy curve based on Hartree-Fock quantum mechanical calculation method was reported earlier [6]. Zhang *et al* reported similar calculations in KDP used density functional theory (DFT) [7]. They concluded that the spontaneous polarization in KDP like crystals is due to redistribution of electron charge density along P/As-O bond caused by proton ordering below T_c. The linear response functions such as Born effective charge tensors and phonon frequencies at the centre of Brillouin zone give insight into dynamics responsible for large spontaneous polarization at T_c [8]. Since the large values of Born effective charges of ions above their nominal values reflect the long range ionic interactions, ferroelectric instability is expected.

The aim of the present work is to understand the phase instability, electronic band structure, optical properties and lattice dynamics in tetragonal KDA using DFT calculations. Further, reasons for deviation of KDA from linear relation (T_c- R) (shown by KDP like crystals) is also addressed. The calculations of the phononic modes at high pressure show an evidence of phase stability.

2. Methods and Computational Details

2.1. Computational Details

The first - principles calculations of electronic structure and lattice dynamics of KDA reported here are carried out using CASTEP [9]. The energy cutoff for the plane wave basis was fixed at 750 eV. The total energy / atom convergence criterion was set below 0.01 meV. In order to calculate energy, band structure, density of states and optical spectra, generalized gradient approximation (GGA) with Perdew-Burke-Ernzerhof parametrization [10] was employed. Vanderbilt Ultrasoft pseudo potentials [11] were used for exchange-correlation.

We have performed structural relaxation of tetragonal KDA using BFGS algorithm employing delocalized internal optimization method with the starting geometry parameters taken from the crystallographic data [12]. In our calculations, the reciprocal space integration was done using Monkhorst-Pack (MP) special k-point integration method [13]. Integration is replaced by summation over 6X6X6 grid size at a band convergence tolerance of 0.001 meV. The linear response functions such as Born effective-charge tensors, the phonon frequencies and dielectric permittivity tensors are computed within the variational formulation of density functional perturbation theory [14]. The same method is followed to calculate the Born-effective charge tensors of atoms in KDP. Also phonon frequencies of KDA are calculated at a high hydrostatic pressure (20 GPa). In our density functional perturbation theory (DFPT) calculations, convergence criteria for maximal force between ions and maximum displacement are set at 0.002 eV/Å and 0.001 Å respectively.

3. Results and Discussion

3.1. Electronic structure

The results obtained after structural and atomic relaxation as shown in Table 1 and are found to be in agreement with the crystal structure obtained from neutron diffraction experiments [12]. The discrepancy between the calculated and experimental O(1)-H-O(2) distances (R) can be accounted for the symmetry constraints imposed in our calculations. The calculated partial density of states (PDOS) for tetragonal KDA as shown in Figure 2, showed energy gap (E_g) of 7.55 eV (scissor correction = 3eV) which is found to be in agreement with the reported values [15]. Table 2 lists the Mulliken charges and overlap populations which are calculated by Mulliken analysis using projection of plane wave basis onto LCAO basis [16]. Large value of overlap population in As-O bond in AsO_4 group suggests covalent nature of the bond. A very small value of overlap population along oxygen-potassium bond reveals weak ionic bonding between AsO_4 and potassium.

Valence levels are those occupied by low binding energy (0-20 eV) electronic states which are involved in de-localized or bonding orbitals. The spectrum in this region consists of many closely spaced levels giving rise to a band structure. The partial density of states (PDOS) of different

Table 1. Comparison of *ab initio* lattice parameters and atomic positions with the corresponding experimental values. All distances are in Å. Atomic positions are written in fractional co-ordinates.

	Calculated	Expt [24]
a	7.628	7.635
b	7.628	7.635
c	7.098	7.166
O/*x*	0.155	0.1594
y	0.092	0.0857
z	0.135	0.135
As-O(1)	1.674	1.687
O(1)-H-O(2)	2.420	2.513
O(1)-H	1.212	1.057
O(2)-H	1.212	1.052
H-H(δ)		0.404

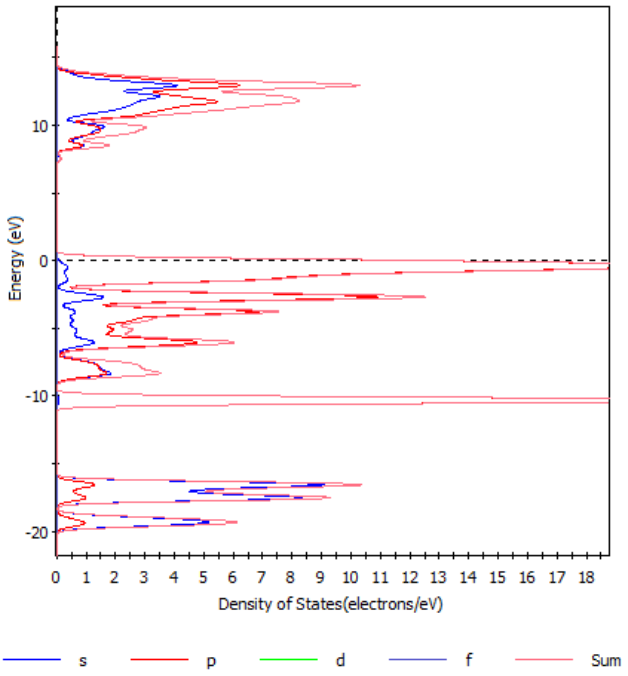

Figure 2. Partial density of states (PDOS) of tetragonal KDA.

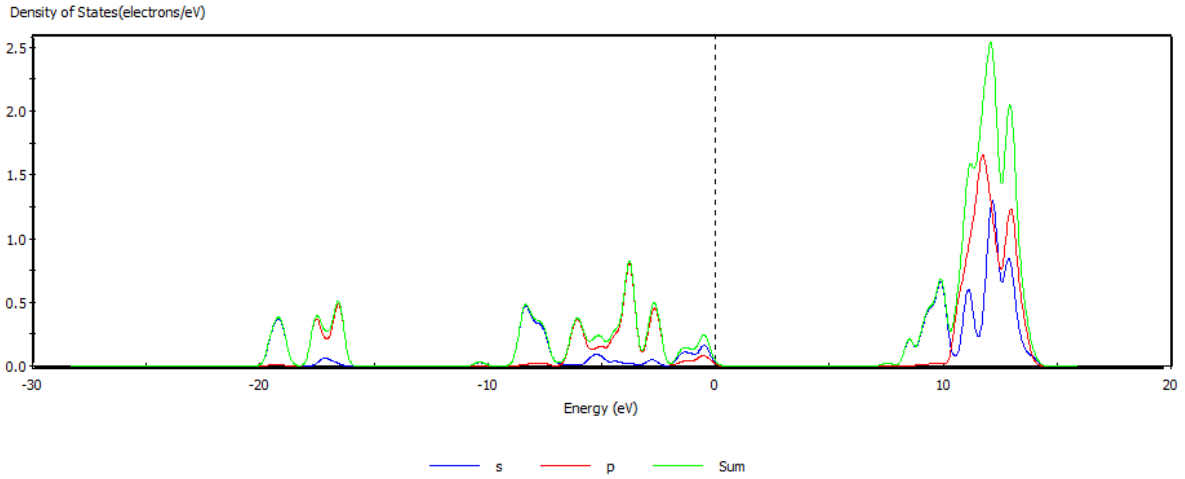

Figure 3. Partial density of states (PDOS) of As in KDA.

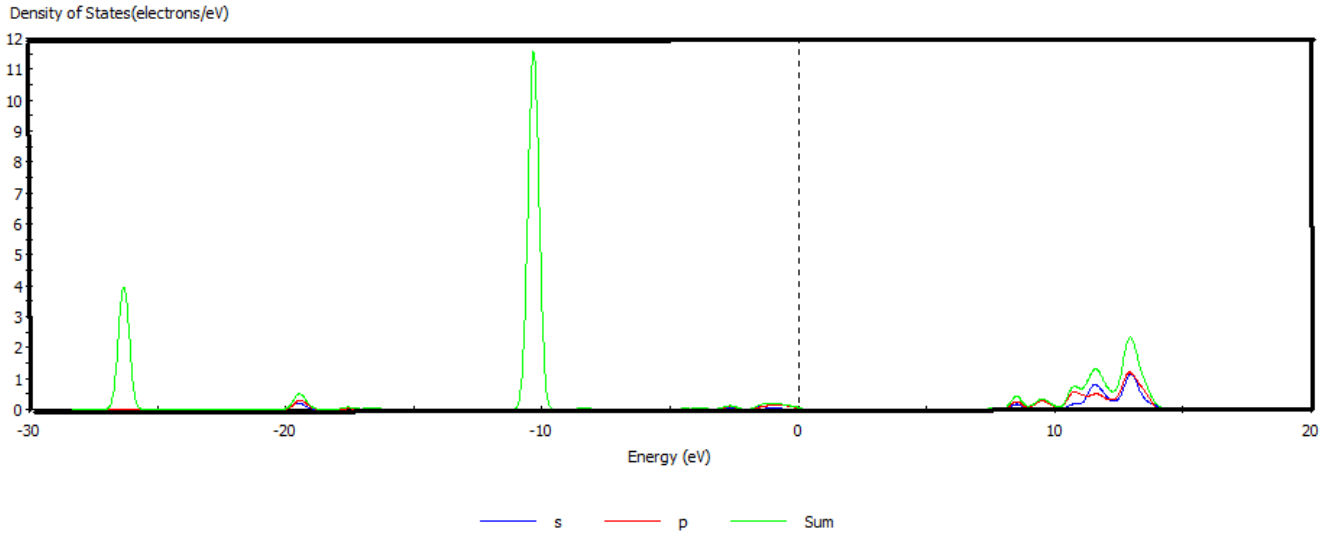

Figure 4. Partial density of states (PDOS) of K in KDA.

Table 2. List of charge of each atom and overlap population between atoms of tetragonal KDA.

Charge	O(1)	O(2)	H	As	K
	-0.92	-0.92	0.32	2.22	0.83
Overlap population		O(1)-O(2)	O(1)-H	O(1)-As	O(1)-K
		-0.20	0.39	0.59	0.07

atoms are shown in Figures 3-6. The highest occupied level (HOMO) at 0.0 eV in the calculated band structure can be ascribed to purely oxygen 2*p* in nature as reported in earlier molecular-orbital analysis calculations [17]. A prominent contribution from potassium *p* state is observed in our calculation at -10 eV. The conduction band mainly arising from the 4*p* and 4*s* character of As atoms and small contributions from H and K atoms is observed in our calculations.

3.2. Optical properties

The optical properties are determined by the dielectric function $\epsilon(\omega) = \epsilon_1(\omega) + j\epsilon_2(\omega)$, which is mainly contributed from electronic structures. The interaction of a photon with electrons in the system is described in terms of time dependent perturbation of the ground state electronic states. Then transitions between occupied and unoccupied states are caused by the electric field of the photon. From the Fermi Golden rule, it can be realized that the spectra resulting from these transitions will be joint density of states, weighted by appropriate matrix elements. The imaginary part of dielectric constant is given by

$$\epsilon_2 = \frac{2\pi e^2}{\Omega\epsilon_0}\sum_{k,v,c}|\langle\psi_k^c|u.r|\psi_k^v\rangle|^2\ \delta(E_k^c - E_k^v - E) \quad (1)$$

Where Ω is the volume of the unit cell, *E* and u are the energy and polarization of the photon respectively and $E_k^c, E_k^v, \psi_k^c, and\ \psi_k^v$ are energy values and wave functions of conduction and valence orbitals respectively in *k* space. The real and imaginary parts of the dielectric constant are related by Kramers-Kronig transform. In reciprocal space, the matrix elements are given by

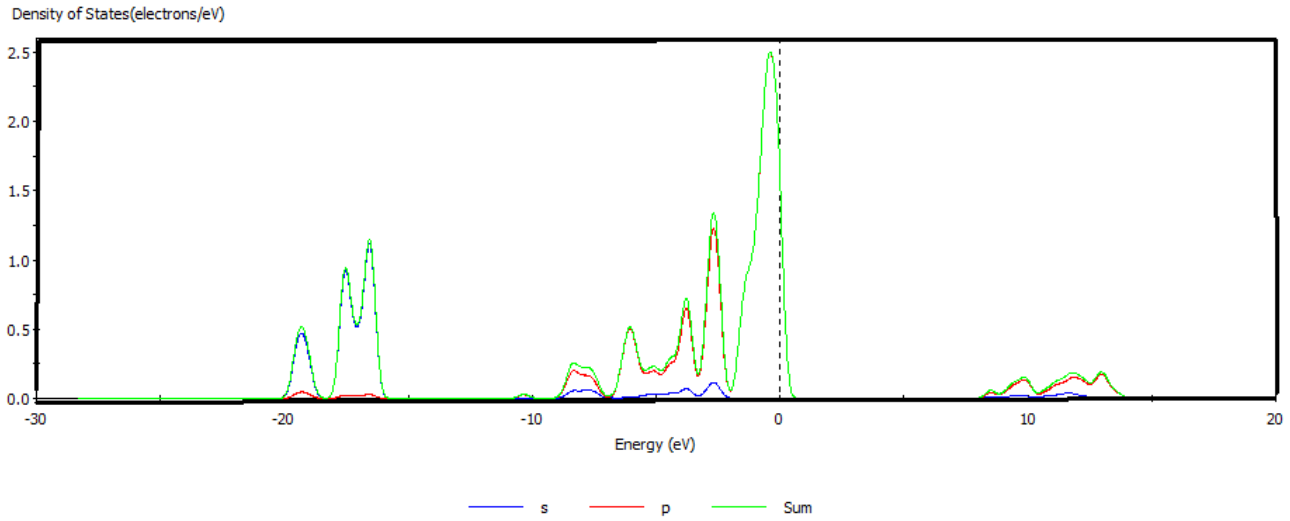

Figure 5. Partial density of states (PDOS) of O in KDA.

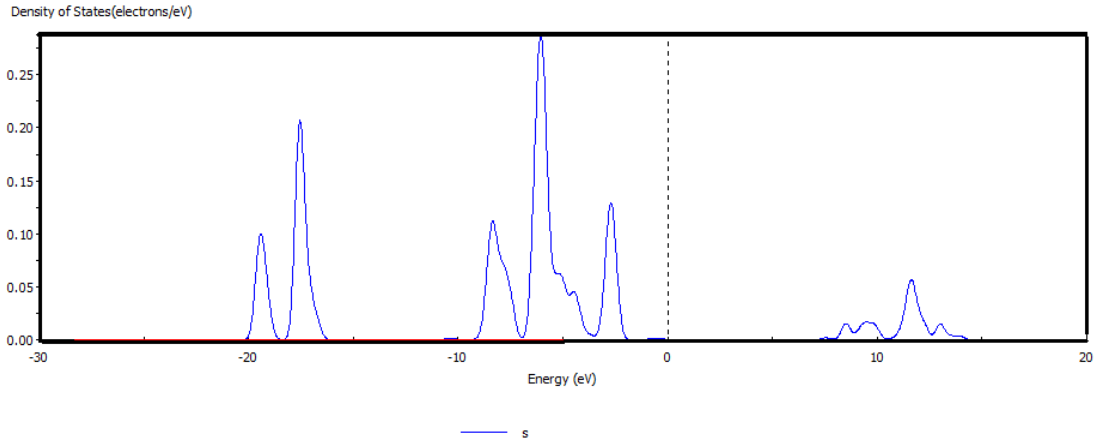

Figure 6. Partial density of states (PDOS) of H in KDA.

$$\langle \psi_k^c | r | \psi_k^v \rangle = \frac{1}{i\omega m} \langle \psi_k^c | p | \psi_k^v \rangle + \frac{1}{\hbar\omega} \langle \psi_k^c | V_{nl} | \psi_k^v \rangle \quad (2)$$

The second term corresponds to the non-local potentials used in DFT calculations. Drude correction term takes care of the intra-band contribution to the optical properties especially in the low frequency part of the spectra. Since KDA is an insulator, the Drude correction becomes insignificant. Other optical properties such as reflectivity R(ω), real part of refractive index n(ω) and imaginary part of refractive index k(ω) can also be obtained from $\epsilon_1(\omega)$ and $\epsilon_2(\omega)$ using the following formulae [18]

$$R(\omega) = \left| \frac{\sqrt{\epsilon_1(\omega) + j\epsilon_2(\omega)} - 1}{\sqrt{\epsilon_1(\omega) + j\epsilon_2(\omega)} + 1} \right|^2 \quad (3)$$

$$n(\omega) = \frac{\left[\sqrt{{\epsilon_1}^2(\omega) + {\epsilon_2}^2(\omega)} + \epsilon_1(\omega) \right]^{1\backslash 2}}{\sqrt{2}} \quad (4)$$

$$k(\omega) = \frac{\left[\sqrt{{\epsilon_1}^2(\omega) + {\epsilon_2}^2(\omega)} - \epsilon_1(\omega) \right]^{1\backslash 2}}{\sqrt{2}} \quad (5)$$

The calculated optical reflectivity spectra of KDA as shown in Figure 7 has revealed 6 bands in the energy range 5-30 eV for polarized light [001] at room temperature. The bands were named A-F for convenience; with bands A and B mainly ascribed to transitions of anions, namely H_2AsO_4 ions. This is also in agreement with the results of reflection spectra from synchrotron radiation and dielectric spectra of KDA [19]. The C and D bands can be attributed to transitions from valence bands of O-H bonds to conduction bands arising from the potassium ions. But E and F bands in reflection spectra of potassium phosphates and arsenates show different multiplet structures which clearly support the idea that the high energy transitions are due to cations, namely K^+ in case of KDA. Therefore, E band in the reflectivity spectra may be due to the intra-band transition of K^+ from 3*p* states to conduction band states derived from K^+ ion.

3.3. Linear response functions

The central idea of linear response method in DFT is to compute how the total energy E varies with respect to a given perturbation. The second derivative of total energy E with respect to external electric field (ε) is related to the dielectric permittivity of the system. Considering only the contribution from the energy of the electronic system (E_{el}), the

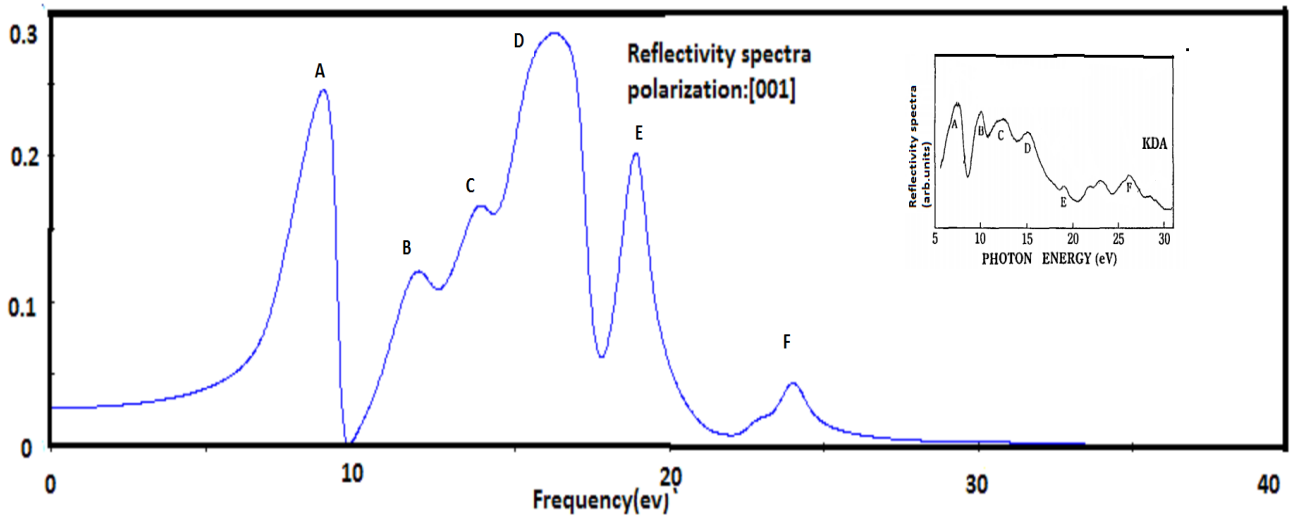

Figure 7. Theoretical reflection spectra (polarization along *c* direction) of tetragonal KDA. Inset: Experimental synchrotron radiation reflection spectra (polarization along *c* direction).

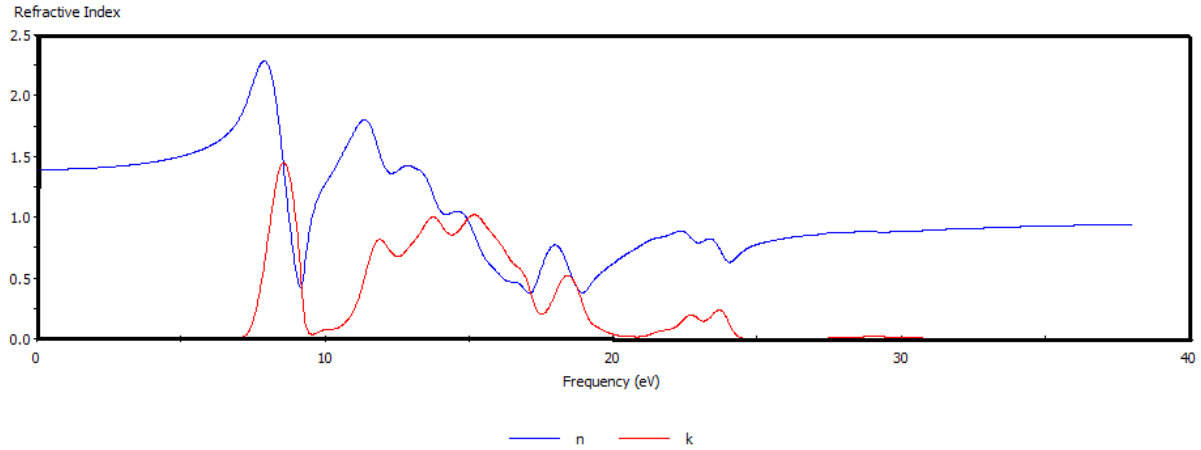

Figure 8. Variation of real and imaginary parts of refractive index with frequency.

Table 3. Optical frequency ($\omega \to \infty$) dielectric tensor of tetragonal KDA.

Tetragonal		
x	*y*	*z*
2.5279	0	0
0	2.5279	0
0	0	2.3274

dielectric response is purely an electronic dielectric permittivity tensor (ϵ_∞) given by

$$\epsilon_{\alpha\beta}^{\infty} = \delta_{\alpha\beta} - \frac{4\pi}{\Omega}\frac{\partial^2 E_{el}}{\partial\varepsilon_\alpha \partial\varepsilon_\beta} \quad (6)$$

Where α and β are indices to label Cartesian directions and Ω is the volume of the primitive unit cell. Using the variational formulation of density functional perturbation theory [20], we obtained electronic dielectric permittivity tensor (ϵ_∞) as given in Table 3. The tensor form is as expected from the crystal point group. It is diagonal with $\epsilon_{xx} = \epsilon_{yy} \neq \epsilon_{zz}$ and shows a small anisotropy (η) of 0.92 confirming the uni-axial nature of KDA crystal. The propagation of electromagnetic radiation through a give medium can be defined by a complex refractive index $N(\omega) = n(\omega) + jk(\omega)$. The variation of real and imaginary components of refractive index with respect to frequency is shown in Figure 8. Due to small anisotropy, no difference was observed in refractive index with respect to direction of propagation of electromagnetic waves. The calculated refractive index (n) at 1.1653 eV is found to be ~1.45 in proximity with reported values [15].

The calculation of ionic contribution to the static dielectric permittivity gives Born- effective charge tensors and zone centre phonon frequencies. Born-effective charge tensors $Z^*_{k,\alpha\beta}$ are defined as the induced polarization of the solid along direction α for a unit displacement of atoms along direction β belonging in sub-lattice *k*.

$$Z^*_{k,\alpha\beta} = \Omega_0 \frac{\partial P_\alpha}{\partial \tau_{k,\beta}^{q=0}} \quad (7)$$

Based on the mixed ionic-covalent character of the bonding in ABO_3 compounds (essentially B-O covalency), Harrison [21] suggested that the sensitivity of the hybridizations to the bond length should produce dynamic transfers of electrons when the atoms are displaced, resulting in an anomalous contribution to the Born effective charges Z^*.

Table 4. List of Raman frequencies of tetragonal KDA.

Raman shift (cm^{-1})			
Symmetry	Assignment	Experimental	Calculated
E			548.27*i*
B_2			536.80*i*
E	K^+-AsO_4 external	130	129.48
B_2	K^+- AsO_4 stretching	143	147.40
E	AsO_4 internal bending	368	357.55
B_2	AsO_4 internal bending	421	413
A_1	AsO_4 symmetric stretching	795	807
E	AsO_4antisymmetric stretching	885	862

Because of the mixed ionic-covalent character of their bonding, these materials show unusual transfer of charge when atoms are displaced. These large values of Z^*reflect correlated atomic displacements which lead to instability. Since KDA is a polar crystal with mixed ionic-covalent nature, displacement of ions induces non-rigid motion of associated electronic charges. In our DFPT calculations, the calculated Born effective charge tensors of atoms in KDA are

$$Z_H^* = \begin{pmatrix} 2.75 & 0.00 & 0.62 \\ 0.00 & 0.22 & 0.00 \\ -0.04 & 0.00 & 0.18 \end{pmatrix};$$

$$Z_O^* = \begin{pmatrix} -2.28 & -0.15 & 0.51 \\ -0.42 & -1.28 & 0.29 \\ 0.29 & 0.28 & -1.16 \end{pmatrix};$$

$$Z_K^* = \begin{pmatrix} 1.15 & -0.03 & 0.00 \\ 0.03 & 1.15 & 0.00 \\ 0.00 & 0.00 & 1.32 \end{pmatrix};$$

$$Z_{As}^* = \begin{pmatrix} 2.99 & 0.52 & 0.00 \\ -0.52 & 2.99 & 0.00 \\ 0.00 & 0.00 & 2.92 \end{pmatrix}$$

We notice that Z^* values of hydrogen, oxygen and K are much higher than their nominal ionic charge values (H: +1e, O:-2e, K: +1e). These values clearly indicate that the there is a strong dynamic charge transfer along O-H bond and z axis in KDA.

The calculated Z^* values of atoms in KDP are

$$Z_H^* = \begin{pmatrix} 2.59 & 0.00 & 0.57 \\ 0.00 & 0.29 & 0.00 \\ -0.121 & 0.00 & 0.28 \end{pmatrix};$$

$$Z_O^* = \begin{pmatrix} -2.22 & -0.17 & 0.52 \\ -0.48 & -1.35 & 0.37 \\ 0.39 & 0.34 & -1.26 \end{pmatrix};$$

$$Z_K^* = \begin{pmatrix} 1.13 & -0.01 & 0.00 \\ 0.01 & 1.13 & 0.00 \\ 0.00 & 0.00 & 1.33 \end{pmatrix};$$

$$Z_P^* = \begin{pmatrix} 3.14 & 0.58 & 0.00 \\ -0.58 & 3.14 & 0.00 \\ 0.00 & 0.00 & 3.12 \end{pmatrix}$$

The squares of phonon frequencies at zone center are obtained as eigenvalues of dynamical matrix

$$\mathcal{D}_{k\alpha,k'\beta} = \frac{\mathcal{C}_{k\alpha,k'\beta}}{(M_k M_{k'})^{1/2}} \quad (8)$$

Where k and k' run over all the atoms in the unit cell with ionic masses M_k and $M_{k'}$ respectively; and $\mathcal{C}$ is the Fourier transform of interatomic force constants which is a second derivative of total energy with respect to collective atomic displacements. By the group theoretical analysis of KDP like structure (which contain two molecular units in a primitive cell), it is known that 28 Raman active modes can be distributed among different irreducible representation of D_{2d}. i.e., Γ_{Raman} = $4A_1$+$6B_1$+$6B_2$+12E in paraelectric phase [22]. Table 4 lists the calculated Raman shifts of tetragonal KDA in comparison with the experimental values [23].

In our Raman calculations, phonon modes are assumed to be independent under harmonic approximation. The earlier reported Raman studies of hydrogen bonded arsenates in paraelectric and ferroelectric phase suggest that low frequency B_2 and E modes are due to collective protonic and deuteronic motion in paraelectric phase [23]. The two imaginary frequencies -546.34*i* (E) and -529.34*i* (B_2) in our calculations suggest that these modes in paraelectric phase may be responsible for instability. This B_2 mode has revealed significant atomic displacements of hydrogen along O-H--O bond, arsenic along z axis and potassium along -z axis. The displacement pattern of this mode is in agreement with the eigen vector proposed by Cochran for the soft mode associated with the ferroelectric phase transition in KDP [24]. The coupling of soft mode with the other optic phonon modes in KDP is also confirmed by the *ab initio* calculations [25]. Katiyar *et al* reported that the coupling between the soft mode and a zone center transverse optic mode of the same B_2 symmetry at ~160 cm^{-1} is responsible for spontaneous polarization along z direction [26]. We have identified a B_2 symmetry mode at 147 cm^{-1} in our calculation which is likely to be coupled to unstable B_2 soft mode. The atomic displacements in this B_2 mode at 144 cm^{-1} has revealed large displacement of K^+ ions along z axis and As along –z axis.

However, KDA which has the lowest O-H---O distance (R) among the members of the KDP family possess T_c higher than that of KDP. Bond geometry and distortion of arsenate or phosphate tetrahedron also play important role in defining the transition temperature of KDP system. It is also reported that the degree of distortion of PO_4/AsO_4 in KDP systems has a negative correlation with T_c [5]. In this work, the calculated zz component of Born effective charge tensor of Arsenic (2.92) is found to be lower than that of phosphorous. The low value of zz component of Z^* of As compared to that of phosphorous in KDP may suggest that dipole moment induced due to distortion of arsenate tetrahedron in KDA is

less than that of phosphate tetrahedron in KDP. This is also confirmed by the Raman studies on KDA by Tominaga *et al* [27]. The unit cell parameter ratio c/a of KDA (0.9385) is same as that of KDP (0.9359) [12]. Another reason for the low dipole moment in KDA can be attributed to less distortion of arsenate in KDA, due to its larger ionic radii in a unit cell with unit cell parameter ratio c/a same as that of KDP. Thus close packing and less distortion of arsenate ion in KDA may be the reasons for higher T_c compared to KDP.

The weakest link in KDP systems, O-H--O bond is known to be very sensitive to pressure variations [28]. The barrier height of the double-well potential along hydrogen bond is lowered, as the bond length of O-H--O decreases with pressure [29]. The bond length O-H—O is found to be 2.384 Å after the structural relaxation under hydrostatic pressure of 10 GPa. The presence of imaginary frequencies of symmetry B_2 and E at atmospheric pressure was ascribed to phase instability. The unstable B_2 and E modes which are mainly due to protonic motion are not observed in our high pressure calculations. This may be accounted for the disappearance of proton ordering at high pressure and hence the phase stability. The phonon frequencies have shown step-up behavior at high pressure. These observations warrant further investigations.

4. Conclusions

In this work, we have calculated band structure, optical properties, dielectric, Born effective charge tensors and various phonon modes in tetragonal KDA using DFT calculations. Main results are explanation for the observed deviation from the linearity of bond distance (O-H—O) vs. T_c. The estimated zz component of Born effective charge tensor for arsenic is found to be smaller than that of phosphorous indicating the low contribution to the dipole moment due to distortion of AsO_4 ion compared to that of PO_4 ion. The calculated negative frequencies of B_2 and E modes reveal the expected instability of the tetragonal phase. The Raman frequencies obtained from DFPT calculations are found to be in very good agreement with experimental data. The calculations also showed the disappearance of these modes at high pressure showing the stability of the phase.

Acknowledgements

Author (S. P) likes to thank U. G. C, Govt of India, New Delhi for providing the FIP fellowship. One of the authors (K. P. R) likes to thank SERC, I. I. Sc., Bangalore for software support.

References

1. R. Blinc and B. Zeks, Soft modes in Ferroelectrics and Antiferroelectrics, In: E. P. Wohlfarth (Ed.), Selected Topics in Solid State Physics, North-Holland, Amsterdam (1974).
2. M. E Lines and A. M. Glass, Principles and Applications of Ferroelectrics and related materials, Clarendon press, Oxford (1977).
3. K. K Kobayashi, J. Phys. Soc. Jpn. 24 (1968) 497.
4. M. Ichikawa, K. Motida and N. Yamada, Phys. Rev. B 36 (1987) 874.
5. M. Ichikawa, D. Amasaki, T. Gustaffson and I. Olovsson, Phys. Rev. B 64 (2001) 100101.
6. B. Silvi, Z. Latajak and H. Ratajczak, Ferroelectrics 150 (1993) 303.
7. Qing Zhang F. Chen, Nicholas Kioussis, S. G Demos and H. B. Radousky, Phys. Rev. B 65 (2001) 024108.
8. R. Resta, J. Phys. Chem. Solids 61 (2000) 153.
9. S. J. Clark, M. D. Seagall, C. J. Pickard, P. J. Hasnip, M. J. Probert and K. Refson, Z. Kristallogr. 220 (2005) 567.
10. J. P. Perdew, K. Burke, M. Ernzerhof, Phys. Rev. Lett. 77 (1996) 3865.
11. D. Vanderbilt, Phys. Rev. B 41 (1990) 7892.
12. Tatsuki Miyoshi, Tamoshi Akimoto and Hiroyuki Mashiyama, J. Phys. Soc. Jpn. 80 (2011) 074607.
13. H. J. Monkhorst and J. D. Pack, Phys. Rev. B 13 (1996) 5188.
14. R. Refson, S. J. Clark and P. R. Tulip, Phys. Rev. B 73 (2006) 155114.
15. V. G. Dimitriev, G. G. Gurzaddyan, and D. N. Nikogosyan, Handbook of Nonlinear Optical Crystals (2nd revised ed.), Springer, Berlin (1977).
16. D. Sanchez-Portal, E. Artacho and J. M. Soler, Solid State Commun. 95 (1995) 685.
17. Adam J. Bridgeman and German Cavigliasso, Polyhedron 20 (2001) 2269.
18. Sonali saha, T. P. Sinha and Abhijit Mookerjee, Phys. Rev. B 62 (2000) 13.
19. Setsoko Matsumoto, Masami Fujisawa and Shigemasa Suga, J. Electron Spec. 79 (1996) 54.
20. Xavier Gonze and Changyol Lee, Phys. Rev. B 55 (1997) 16.
21. W. A. Harrison, Electronic structure and properties of solids, W. H. Freeman and Co., San Francisco (1980).
22. P. Simon, Ferroelectrics 135 (1992) 169.
23. R. P. Lowndes, N. E. Tornberg and R. C. Leung, Phys. Rev. B 10 (1974) 3.
24. W. Cochran, Adv. Phys. 9 (1960) 387.
25. G. Colizzi, J. Kohanoff, J. Lasave and R. L. Migoni, Ferroelectrics 401 (2010) 200.
26. R. S. Katiyar, J. F. Ryan and J. F. Scott, Phys. Rev. B 4 (1971) 8.
27. Yasunori Tominaga and Keko Iizuka, J. Korean Phys. soc. 32 (1998) S493.
28. P. S. Peercy and G. A. Samara, Phys. Rev. B 8 (1973) 5.
29. B. Morosin and G. A. Samara, Ferroelectrics 3 (1971) 49.

Cite this article as:

G. Sriprakash *et al.*: **First - principles calculations of electronic structure, optical properties and phase instability of potassium dihydrogen arsenate.** *Phys. Express* 2013, **3**: 31